

Thermal stability of slot-die coated Organic Photovoltaics

By

Bradley Peter Kirk
Bachelor of Sciences (Honours)

Thesis
Submitted to Flinders University
for the degree of

Doctor of Philosophy
College of Science and Engineering
1st November 2023

TABLE OF CONTENT

ABSTRACT	VI
DECLARATION	VIII
ACKNOWLEDGEMENTS	IX
LIST OF PUBLICATIONS & CONFERENCES	XI
CONTEXTUAL STATEMENT	XIII
LIST OF FIGURES	XIV
LIST OF TABLES	XVIII
ABBREVIATIONS & ACRONYMS	XIX
CHAPTER 1 – INTRODUCTION	1
1.1. Global energy usage.....	1
1.2. Alternative energy sources.....	2
1.3. Photovoltaics.....	2
1.4. Organic photovoltaics.....	3
1.5. Printing fabrication of OPVs.....	4
1.6. Device stability.....	6
1.7. Aim of the thesis studies.....	7
1.8. References.....	9
CHAPTER 2 – PROGRESS WITH SCALABLE ORGANIC PHOTOVOLTAICS FABRICATION	12
2.1. Overview.....	12
2.1. Device structuring.....	12
2.1.1. Single layer OPV.....	12
2.2.2. Bilayer planar heterojunction OPV.....	13
2.2.3. Bulk heterojunction.....	14
2.3. Photocurrent generation in OPVs.....	15
2.4. Device architectures.....	16
2.4.1. Conventional device structure.....	17
2.4.2. Inverted device structure.....	17
2.5. Morphology.....	18
2.6. OPV performance characterisation and key parameters.....	18
2.6.1. Open-circuit voltage.....	19
2.6.2. Short-circuit current density.....	19
2.6.3. Fill-factor.....	20
2.6.4. Power conversion efficiency.....	20
2.7. Stability.....	20
2.7.1. UV irradiance.....	21
2.7.2. Oxygen and water.....	22
2.7.3. Mechanical.....	22
2.7.4. Thermal and storage.....	23

2.8.	Coating and printing techniques for OPV	24
2.8.1.	Vacuum and non-vacuum deposition	24
2.8.2.	OPV fabrication scalability via alternative printing and coating techniques.....	25
2.8.3.	Roll-to-roll fabrication	26
2.8.4.	Types of printing and coating methods.....	27
2.8.5.	Printing and coating method comparison	42
2.9.	Outlook	51
2.10.	Reference	52
CHAPTER 3 – RESEARCH METHODOLOGY.....	68	
3.1.	Overview.....	68
3.2.	Materials and ink preparation.....	68
3.2.1.	Synthesis of PPDT2FBT	68
3.2.2.	Synthesis of TQ1	69
3.2.3.	Synthesis of PDCBT	70
3.2.4.	Synthesis of ITIC	70
3.2.5.	Zinc Oxide nanoparticle synthesis and ink preparation	71
3.2.6.	Ink preparation of PEDOT:PSS.....	71
3.3.	Device fabrication	72
3.3.1.	Spin-coating.....	72
3.3.2.	Slot-die coating	73
3.4.	Device electrical analysis.....	78
3.4.1.	Electron and hole mobility measurements.....	78
3.4.2.	Charge Extraction by Linearly Increasing Voltage (CELIV)	80
3.4.4.	4-point probe.....	80
3.4.5.	Solar simulation	81
3.5.	Material characterisation techniques.....	81
3.5.1.	Neutral Impact Collision Ion Scattering Spectroscopy	81
3.5.2.	Atomic Force Microscopy.....	83
3.5.3.	X-ray Photoelectron Spectroscopy	83
3.5.4.	Grazing-Incidence Wide-Angle X-ray Scattering	83
3.5.5.	Ultraviolet Photoelectron Spectroscopy.....	84
3.5.6.	Stylus Profilometer.....	84
3.5.7.	Auger Electron Spectroscopy.....	84
3.5.8.	Dynamic Mechanical Thermal Analysis.....	85
3.6.	References	88
CHAPTER 4 – INTRODUCING NEAT FULLERENES TO IMPROVE THE THERMAL STABILITY OF SLOT-DIE COATED ORGANIC SOLAR CELLS.....	94	
4.1.	Overview.....	94
4.2.	Introduction.....	95
4.3.	Experimental section.....	98
4.3.1.	Materials	98

4.3.2.	Device fabrication	98
4.3.3.	Square-Wave Voltammetry	99
4.3.4.	Scanning Electron Microscopy	99
4.3.5.	Auger Electron Spectroscopy.....	99
4.3.6.	Dynamic Mechanical Thermal Analysis.....	100
4.4.	Results and Discussion.....	100
4.4.1.	Adjustment of the slot-die coating conditions	100
4.4.2.	Storage and thermal stability of PPDT2FBT:PC ₆₁ BM devices	101
4.4.3.	The influence of the additional C ₇₀ on the device performances.....	102
4.4.4.	Thermal stability at 120 °C.....	104
4.4.5.	Imaging of microcrystals at BHJ surface	105
4.4.6.	Elemental characteristics of microcrystals.....	107
4.4.7.	Thermal analysis.....	109
4.5.	Conclusion	111
4.6.	References	112
CHAPTER 5 – INVESTIGATING DEGRADATION PATHWAYS ASSOCIATED WITH WORKING AND ACCELERATED THERMAL CONDITIONS.....		117
5.1.	Overview.....	117
5.2.	Introduction.....	118
5.3.	Experimental section.....	120
5.3.1.	Materials	120
5.3.2.	Device fabrication	121
5.3.3.	Scanning Electron Microscopy	122
5.3.4.	Stylus Profilometry.....	122
5.3.5.	Auger Electron Spectroscopy.....	122
5.3.6.	Neutral Impact Collision Ion Scattering Spectroscopy (NICISS).....	122
5.3.7.	Dynamic Mechanical Thermal Analysis.....	123
5.4.	Results and discussion	123
5.4.1.	Device performance stability	123
5.4.2.	Bulk heterojunction degradation investigation	125
5.4.3.	Elemental characteristics of microfeatures.....	127
5.4.4.	Depth profiling of bulk-heterojunction surface containing microfeatures.....	129
5.4.5.	Thermal degradation behaviour	133
5.5.	Conclusion	138
5.6.	References	139
CHAPTER 6 – INTRODUCING NON-FULLERENE ADDITIVES TO IMPROVE THE THERMAL STABILITY OF SLOT-DIE COATED ORGANIC PHOTOVOLTAICS.....		144
6.1.	Overview.....	144
6.2.	Introduction.....	144
6.3.	Experimental section.....	149
6.3.1.	Materials	149
6.3.2.	Device fabrication	149

6.3.3.	Atomic Force Microscopy.....	150
6.3.4.	Scanning Electron Microscopy.....	150
6.3.5.	Charge Carrier Dynamics.....	150
6.3.6.	Dynamic Mechanical Thermal Analysis.....	150
6.4.	Results and discussion	151
6.4.1.	Device performance Influence due to additives in the Bulk Heterojunction.....	151
6.4.2.	Influence of solid additives over the Charge Carrier mobility	152
6.4.3.	Thermal stability of PPDT2FBT:PC61BM devices.....	154
6.4.4.	Bulk heterojunction degradation investigation at 120 °C and 85 °C.....	157
6.4.5.	Thermal Analysis	159
6.5.	Conclusion	162
6.6.	References	163
CHAPTER 7 – PRELIMINARY STUDY OF SCALABLE METHODS USED TO INFLUENCE THERMAL BEHAVIOUR OF OPVS		167
7.1.	Overview.....	167
7.2.	Introduction.....	167
7.3.	Experimental section.....	171
7.3.1.	Materials	171
7.3.2.	Inverted Device fabrication.....	172
7.3.3.	Conventional Device fabrication.....	173
7.3.4.	Solar simulator.....	174
7.3.5.	Scanning Electron Microscopy.....	174
7.4.	Results and discussion	174
7.4.1.	Inverted configuration OPVs	174
7.4.2.	Post-fabrication switching verses pre-aging silver electrode	175
7.4.3.	Conventional verses inverted OPVs.....	177
7.4.4.	Large area conventional devices.....	178
7.4.5.	Device stability under dark nitrogen conditions	180
7.4.6.	Device stability at elevated temperatures.....	181
7.4.6.	Influence of solid-additives over thermal degradation of conventional OPV	182
7.4.7.	Final discussion of stability of conventional OPV	183
7.5.	Conclusion	184
7.6.	Reference	185
CHAPTER 8 – CONCLUDING SUMMARY		192
8.1.	Summary of conclusions.....	193
8.2.	Potential for Future research.....	194
8.3.	References	196
APPENDICES		200
Appendix A – OPV device performances for cells that utilised different PPDT2FBT polymer batches.		200
A.1.	Experimental section.....	200

A.2.	Device performance results	201
Appendix B – Supporting Information for Chapter 4.....		202
B.1.	Active material costs	202
B.2.	Slot-die theoretical thickness	202
B.3.	Square-wave voltammetry	203
B.4.	Dynamic mechanical thermal analysis	203
B.5.	Solar simulation results.....	203
B.6.	Square-wave results	205
B.7.	Solar simulation light curves	205
B.8.	Scanning electron microscopy images.....	205
B.9.	Auger electron spectroscopy spectra	206
B.10.	References	209
Appendix C – Methodology and theoretical calculations.....		210
C.1.	Active layer material synthesis.....	210
C.2.	Slot-die theoretical thickness	210
C.3.	Dynamic mechanical thermal analysis	211
C.4.	References	211
Appendix D – Raw spectroscopy, microscopy, and analysis data.....		212
D.1.	Atomic Force Microscopy.....	212
D.2.	Scanning Electron Microscopy images from Auger Electron Spectroscopy samples..	213
D.3.	Auger Electron Spectra of surface features present on thermally aged PPDT2FBT:PC ₆₁ BM BHJ.....	214
D.4.	Charge carrier dynamics of inverted PPDT2FBT:PC ₆₁ BM devices.....	216

ABSTRACT

There is a large amount of interest towards the commercialisation of flexible solar cells, with several types that have gained traction, one such being organic photovoltaics (OPVs). Improving solar cell efficiency has dominated the OPV research field for several years, however, there has been less research aimed towards device stability, resulting majority of devices having poor lifetime under ambient and operating conditions. There has been even less research focused on the shift from research on lab-based spin-coated OPVs fabricated under protective nitrogen conditions to scalable and large-scale devices fabricated via coating/printing techniques under ambient conditions. This has led to the majority of OPV stability research to focus on reducing the degradation of bulk heterojunction (BHJ) of the active layer, with strategies for improving stability previously aimed at small-scale solar cells fabricated under nitrogen environment.

This thesis work has aimed at understanding the major thermal degradation pathways associated with slot-die polymer:fullerene-based OPV, with two temperatures being investigated, 85 °C and 120 °C. 85 °C is a thermal aging temperature that is accepted by the International Summit on OPV Stability (ISOS) community used for thermal degradation studies under dark storage conditions. Whereas 120 °C is one of several “accelerated” thermal aging temperatures that have been implemented in previous literature to increase the degradation rate. From our work, however, it was found that the two temperatures led to completely different degradation pathways, with 85 °C resulting in significant phase changes in the active layer, while 120 °C resulted in fullerene crystallisation and migration.

With this important observation in degradation pathway, a range of solid-based additives were extensively investigated, from neat fullerenes, cyclic-based small molecules and an insulating polymer, all having either been speculated to, or shown in previous literature to decrease thermal aging of the active layer. Though additives such as Piperazine (PP), 4,4'-Bipiperidine (BP) and Polyacacenaphthylene (PAN) were observed to reduce the crystallisation rate at 120 °C, the additives had a negative impact on degradation at 85 °C as they allowed for the formation of fullerene crystals that would otherwise have been observed at the lower temperature. Whereas for neat C₇₀, it was found to improve thermal stability at 120 °C and 85 °C, due to its ability to influence the thermal behaviour of the active layer itself.

Lastly, the thesis work aimed at demonstrating the scalability and translatability of the previously conducted work, using a device structure that has been demonstrated in roll-to-roll fabrication. For the additives that have been investigated in the thesis, they were found to have a negative impact on thermal degradation of the OPV devices, where it was suspected that by influencing the thermal behaviour and morphology of the active layer had led to increased interfacial degradation.

The work conducted in the thesis demonstrates a strategy, by implementing several spectroscopy, microscopy, and material analysis methods together, for investigating morphological changes associated with thermal degradation of the active layer of OPVs. The work has also shown the importance of investigating thermal degradation at appropriate annealing temperatures of OPVs, as well as further challenges associated with scalability and translatability between scalable and large-scale OPV fabrication.

DECLARATION

I certify that this thesis:

1. does not incorporate without acknowledgment any material previously submitted for a degree or diploma in any university
2. and the research within will not be submitted for any other future degree or diploma without the permission of Flinders University; and
3. to the best of my knowledge and belief, does not contain any material previously published or written by another person except where due reference is made in the text.

Signed: Bradley Peter Kirk.....

Date: 1st November 2023.....

ACKNOWLEDGEMENTS

I would like to show my appreciation and acknowledgement to the people and groups who have supported me throughout my PhD studies. Without them, I may have struggled to complete my research during these past 3 and half years.

I would firstly like to acknowledge the domestic Australian Government Research Training (RTP) scholarship for providing me with stipend through the duration of my PhD studies, as well as to Playford Trust for the PhD top-up scholarship. Also, to Flinders University, College of Science and Engineering, and the Flinders University Student Associated for providing me with financial assistance to be able to attend several conferences and symposiums in person. Without this support, I would not have been able to present my work to the international scientific community.

My supervisor Prof. Mats Andersson for the support and guidance throughout the project. He has strongly encouraged myself to present my research towards the OPV community, including the attendance of several conferences and symposiums. Has also provided me with opportunities to collaborate, especially with the University of Newcastle. His support has allowed me to become more confident in the field of OPV and material sciences, as well significantly improve my ability to communicate my research findings in front of a range of audiences.

My co-supervisor Prof. Gunther Andersson has help significantly with determining microscopy and spectroscopy methods that could help analysis the materials of interest. His suggestions and support helped with my confidence and understanding to pursue these analytical techniques which have proven fruitful in the studies.

Another co-supervisor, Prof. David Lewis has been both supportive, and challenged my findings throughout the project. This allowed for alternative conclusions to be considered and helped me think outside the box on several occasions.

Dr. Caroline Pan for her expertise in analysing the dynamic mechanical thermal Analysis results. Her support helped with gaining confidence with data interpretation. She has also been supportive throughout my research studies, as well as being very welcoming when I joined Mats Andersson's research team.

Dr. Jonas Mattiasson Bjuggren, both during his time at Flinders University and University of Newcastle. He was one of the first researcher to teach me about the field of OPVs, and has been incredibly supportive throughout my PhD studies, as well as helpful collaborator in later years of my studies.

Dr. Martyn Jevric, his work and expertise in organic material synthesis was what really kicked started my project, with his suggestions to try higher performing materials. He was able to synthesis several materials that I used throughout my project, as well as improved my understanding in polymer synthesis.

Dr. Matthew Griffith and Dr. Jessie Posar for the collaboration work on charge carrier dynamics in printed OPVs. Their work and knowledge in charge carrier mobility and lifetime allowed for considerable progress on understanding the influence of solid-based additives had on OPV efficiency.

Prof. Paul Dastoor and his research team for the collaboration work on large scale OPV fabrication, as well as providing significant knowledge and troubleshooting associated with slot-die coating. Members include Dr. Nathan Cooling and Dr. Jonas Mattiasson Bjuggren, who, without them, would have made progressing with the late-stage of my PhD studies near impossible.

To colleagues at the Flinders Institute for Nanoscale Science & Technology, both past and present. Many fun times were had away from my PhD studies, as well as made stressful times more manageable.

I also acknowledge the facilities, and the scientific and technical assistance of Microscopy Australia and the Australian National Fabrication Facility (ANFF) under the National Collaborative Research Infrastructure Strategy, at the South Australian Regional Facility, Flinders Microscopy and Microanalysis, Flinders University. Their facilities helped play a crucial role in the spectroscopy and microscopy measures that were necessary for the material analysis. Special mention goes to Dr. Christopher Gibson, Dr. Jason Gascooke, Dr. Liam Howard-Fabretto and Dr. Alex Sibley for their expertise, as well as assistance during instrumentation issues.

My parents, Duncan and Tania Kirk, as well as my brother, Luke Kirk, for their love and support throughout my project. Duncan has also provided support in terms of revising my presentation slides, posters, and written work, allowing for said work to be more professional and along for a clear message to be understood.

My partners parents, Bhavin and Pauravi Shah, for their love and support through my project. Bhavin and Pauravi also provided support in terms of revising my thesis, assisting in correcting spelling, grammar, and logical errors.

Lastly, but definitely not least, the loving support from my partner, Aniha Shah. She has been providing support and care due the entirety of my project, especially during the final months of studies. I could not have asked for a more loving and supportive partner. Again, thank you.

LIST OF PUBLICATIONS & CONFERENCES

The following is a list of accepted publications, as well as conference presentations performed throughout the author's candidature. The results that were presented were found from the projects associated with the candidature project. Co-author publications where the author was also a co-author is also listed, however, the data from these measurements are not present in the thesis (see Contextual Statement).

Journal Articles (Primary author)

Kirk, B., Pan, X., Jevric, M., Andersson, G., & Andersson, M. R., Introducing neat fullerenes to improve the thermal stability of slot-die coated organic solar cells. *Materials Advances*, **2022**. 3 (6), 2838-2849.

Journal Articles (Co-author)

Alghamdi, A. R., Kirk, B. P., Andersson, M. R., & Andersson, G. G., Chemical and Electronic Properties of PTB7-Th and ITIC on ZnO Interfaces in Organic Solar Cells. *ACS Sustainable Chemistry & Engineering*, **2023**. 11(32), 11811-11818.

Alghamdi, A. R., Kirk, B. P., Kocak, G., Andersson, M. R., & Andersson, G. G., Modification of the Surface Composition of PTB7-Th: ITIC Blend Using an Additive. *Molecules*, **2022**. 27(19), 6358.

Oral Presentations

Kirk, B., Pan, X., Jevric, M., Andersson, G., & Andersson, M. R., Investigating the thermal degradation pathways associated with organic photovoltaics. The 11th Annual Conference of The Flinders Institute of Nanoscale Science and Technology Conference, Adelaide, Australia, 14 June **2023**.

Kirk, B., Pan, X., Jevric, M., Andersson, G., & Andersson, M. R., Investigating the influence of molecular additives on the thermal stability of slot-die coated organic photovoltaics. The 17th Pacific Polymers Conference, Brisbane, Australia, 13 December **2022**.

Kirk, B., Pan, X., Jevric, M., Andersson, G., & Andersson, M. R., Influencing the active layer blend properties to improve the thermal stability of slot-die coated organic photovoltaics. The 22nd Australasian Community for Advanced Organics Semiconductors Symposium, Tweed Heads, Australia, 7 December **2022**.

Kirk, B., Pan, X., Jevric, M., Andersson, G., & Andersson, M. R., Introducing additives to improve the thermal stability of slot-die coated organic solar cell. International Symposium on Clean Energy Materials 2022, Gold Coast, Australia, 31 June **2022**.

Poster presentations

Kirk, B., Alghamdi, A., Jevric, M., Andersson, G. & Andersson, M. R., Introducing additives to improve the thermal stability of slot-die coated organic solar cells. International Conference on Science and Technology of Synthetic Metals 2022, Glasgow, Scotland, 18 July **2022**.

Kirk, B., Alghamdi, A., Jevric, M., Andersson, G. & Andersson, M. R., Introducing additives to improve the thermal stability of slot-die coated organic solar cells. The 10th Annual Conference of The Institute of Nanoscale Science and Technology Conference, Adelaide, Australia, 15 June **2022**.

Kirk, B., Alghamdi, A., Jevric, M., Andersson, G. & Andersson, M. R., Introducing Neat Fullerenes to Improve the Thermal Stability of Slot-die Coated Organic Solar Cells. The 33rd Australasian Colloid and Interface Society Student Conference, Adelaide, Australia (ONLINE), 31 January **2022**,

Kirk, B., Pan, X., Jevric, M., Andersson, G., & Andersson, M. R., Introducing Neat Fullerenes to Improve the Thermal Stability of Slot-die Coated Organic Solar Cells. Flinders University Molecular Science and Technology HDR Conference, Adelaide, Australia, 17 November **2021**.

Kirk, B., Pan, X., Jevric, M., Andersson, G., & Andersson, M. R. (2021). Introducing Neat Fullerenes to Improve the Thermal Stability of Slot-die Coated Organic Solar Cells. The 9th Annual Conference of The Institute for Nanoscale Science and Technology Conference, Adelaide, Australia, 16 June **2021**.

CONTEXTUAL STATEMENT

Majority of results presented in this thesis were from experimental measurements performed at Flinders University. Unless specified, results gathered, data analysis and manuscript prepared as first author was performed by the author of this thesis.

Chapter 4 is a reformatted text that has been published in *Material Advances*, with the author of this thesis being the first author, designer of experiments, preparation of the text. Other contributors of the text include Xun (Caroline) Pan, Martyn Jevric, Gunther Andersson, and Mats Andersson. Caroline conducted the initial DMTA measurements, and with cooperation with the author of this thesis, interpreted the data. Martyn synthesised the batch of PPDT2FBT polymer used in the experiments, as well as provided suggestions for the revised text. Gunther Andersson and Mats Andersson helped with experimentation design, as well as revision of the published text.

For Chapter 6, the measurement of charge carrier mobility and lifetime with the implementation of photo-CELIV, TPV and TRCE, devices fabricated at Flinders University were sent to Matthew Griffiths at the University of Sydney. The data collected from the technique was analysed by Matthew Griffith and Jessie Posar.

Chapter 7 involves an on-going collaborative project between the author and with the research group of Paul Dastoor at the University of Newcastle. Based on the organic photovoltaic structured by the research group, the author focused on small-area device testing and fabrication, while the collaborators focused on large-area testing. As such, manufacturing of Ag-grid covered PET, large-area electrode sputtering and large active area device testing was conducted by Nathan Cooling at University of Newcastle, PDCBT synthesis was conducted by Jonas Mattiasson Bjuggren. TQ1 synthesis was conducted by Caroline Pan at Flinders University.

Experimental work was also performed for one additional publication of which the author of this thesis was a co-author. As mentioned in the List of Publications & Conferences, the experimental results are not present in this thesis as the content of the measurements as they served to support the work of the collaborating researcher, and not directly related to the content of the thesis. The author of this thesis also contributed to revisions for the published version of the mentioned manuscript.

LIST OF FIGURES

Figure 1.1: Relative percentage of energy production type in 2019 [3].	1
Figure 1.2: A model of a simple architecture of an OPV.	3
Figure 1.3: Basic schematic of a roll-to-roll setup which slot-die coating deposition of film and post-heating treatment.	5
Figure 1.4: Basic schematic of slot-die coating on the MRC.	5
Figure 2.1: Chemical structure of C ₆₀ , C ₇₀ , PC ₆₁ BM, PC ₇₁ BM.	14
Figure 2.2: Schematic of photocurrent generation in OPVs: a) absorption of a photon to form an exciton, b) exciton diffusion towards the acceptor-donor interface, c) exciton dissociation, d) charge carrier separation, e) charge carrier movement through the active.	16
Figure 2.4: Schematic of conventional (left) and inverted (right) devices.	16
Figure 2.5: JV-curve (left) and PV curve (right), including markings of Short-circuit Current-density (J _{SC}), open-circuit voltage (V _{OC}), maximum power, as well as voltage and current density position of maximum power point (V _{MPP} & J _{MPP}), respectively.	19
Figure 2.6: Key areas of importance for OPV fabrication.	21
Figure 2.7: Basic schematics of the type of roll-to-roll fabrication procedures.	27
Figure 2.8: Basic schematic of spin-coating. Adapted from Krebs, 2009 [51].	28
Figure 2.9: Basic schematic of Rod coating. Adapted from Søndergaard <i>et al.</i> , 2012 [233].	29
Figure 2.10: Basic schematic of blade coater. Adapted from Søndergaard <i>et al.</i> , 2012 [233].	30
Figure 2.11: Basic schematic of slot-die coating. Adapted from Søndergaard <i>et al.</i> , 2012 [233].	32
Figure 2.12: Basic schematic of spray coating. Adapted from Søndergaard <i>et al.</i> , 2012 [233].	34
Figure 2.13: Basic schematic of two types of inkjet printing, Piezoelectric (LEFT) and continuous (RIGHT) [233].	36
Figure 2.14: Basic schematic of pad printing. Adapted from Krebs <i>et al.</i> , 2009 [285].	37
Figure 2.15: Basic schematic of Gravure printing. Adapted from Søndergaard <i>et al.</i> , 2012 [233].	38
Figure 2.16: Basic schematic of flexographic printing. Adapted from Søndergaard <i>et al.</i> , 2012 [233].	40
Figure 2.17: Basic schematic of screen printing, specifically flatbed and rotary. Adapted from Søndergaard <i>et al.</i> , 2012 [233].	41
Figure 3.1: Molecular structure of PPDT2FBT donor polymer.	68
Figure 3.2: Molecular structure of TQ1 donor polymer.	69
Figure 3.3: Molecular structure of PDCBT donor polymer.	70
Figure 3.4: Molecular structure of ITIC small-molecule acceptor.	71
Figure 3.5: Molecular structure of PEDOT and PSS ionomers.	72
Figure 3.6: Upstream and downstream ink flow with highlighted interaction of the pressure gradient and the shear force of the substrate-liquid interface [70].	74
Figure 3.7: Stable coating window based on Capillary Model for slot-die coating that allows for defect-free films [70].	75
Figure 3.8: Basic schematic of potential film defects from slot-die printing: Chattering (a), ribbing (b), neck-in (c), edge defects (d), bubble (e), and streaks (f).	75
Figure 3.9: Image of the MRC used throughout the thesis. Included in the image of active materials being deposited from the slot-die coating head.	78

Figure 3.10: Schematic of pulse response from the Photo-CELIV technique, showing for dark and light responses. Adapted from Mozer <i>et al.</i> , 2005 [70].	80
Figure 3.11: Basic schematic of NICISS instrument (LEFT) and elastic and inelastic energy loss due to projectiles colliding with the sample (RIGHT). Schematics adapted from Andersson, 2014 [10].	81
Figure 3.12: Sulphur spectra feature (4.5 μ s), with and without hydrogen background.	82
Figure 3.13: Spectra of raw AES data a) and data that has been smoothed and derived b). The AES spectra was from the surface of a PPDT2FBT:PC ₆₁ BM thin film.	85
Figure 3.14: Trends in the stress & strain of Ideal elastic, viscous and Viscoelastic behaviour materials.	86
Figure 3.15: Basic schematic of DMTA with tension clamps attachment. Adapted from Sharma <i>et al.</i> , 2019 [21].	87
Figure 4.1: (a) Chemical structure of PPDT2FBT, C ₆₀ , C ₇₀ , PC ₆₁ BM and PC ₇₁ BM; (b) schematic illustration of inverted OPV structure used in this work.	97
Figure 4.2: Device characteristic trends at room temperature aging and thermal aging at 85 °C under nitrogen of PPDT2FBT:PC ₆₁ BM based OPVs. The results are from an average of 6 cells, with an active area of 0.1 cm ² .	101
Figure 4.3: Illustration of energy levels of the active layer materials estimated from square-wave voltammetry measurements under identical conditions; PPDT2FBT (HOMO/LUMO), PC ₆₁ BM, PC ₇₁ BM, C ₆₀ & C ₇₀ (LUMO only).	103
Figure 4.4: Device characteristics trends at 120 °C thermal aging under nitrogen. The results are from an average of 6 cells, with an active area of 0.1 cm ² .	104
Figure 4.5: SEM images of PPDT2FBT:PC ₆₁ BM (1:2) (a,d), PPDT2FBT:PC ₆₁ BM:C ₇₀ (1:1.9:0.1) (b,e) & PPDT2FBT:PC ₆₁ BM:C ₆₀ (1:1.9:0.1) (c,f) before (a-c) and after (d-f) heated for 8 h at 120 °C under dark nitrogen conditions.	106
Figure 4.6: Flattened and smoothed Auger spectra of three positions that were measured on the PPDT2FBT:PC ₆₁ BM surface, including the predicted peak position of elements of interest. The spectra are an average of 5 different scanning areas.	108
Figure 4.7: DMTA plots of pristine PPDT2FBT (a), PPDT2FBT:PC ₆₁ BM (b), PPDT2FBT:PC ₆₁ BM:C ₆₀ (c) and PPDT2FBT:PC ₆₁ BM:C ₇₀ (d) before and after annealing (30 min).	110
Figure 5.1: (a) Chemical structure of PPDT2FBT & PC ₆₁ BM, (b) schematic illustration of inverted OPV structure used in this work.	120
Figure 5.2: Device degradation at 85 °C and room temperature.	123
Figure 5.3: Thermal degradation behaviour between devices that are annealed at either 85 °C or 120 °C.	124
Figure 5.4: SEM of PPDT2FBT:PC ₆₁ BM BHJ surface after either annealing at 85 °C for either 1 month, 3 months or 6 months.	126
Figure 5.5: Surface comparison of BHJ that was annealed at 85 °C for 6 months: a) Scanning electron microscopy, and b) stylus profilometry.	126
Figure 5.6: SEM of PPDT2FBT:PC ₆₁ BM BHJ surface before (a) and after (b) annealing 120 °C for 8 hours.	127
Figure 5.7: Smoothed and derived Auger spectra of specific features found on the surface of PPDT2FBT:PC ₆₁ BM annealed at either 85 °C or 120 °C. Highlighted are the predicted peak positions of elements suspected to be present at the surface. The spectra are an average of 5 different scanning locations.	128
Figure 5.8: NICISS ToF spectra of either pristine PPDT2FBT (black line) or PPDT2FBT:PC ₆₁ BM BHJ (coloured lines). The BHJ is either non-annealed (25 °C) (red line), aged at 85 °C for 6 months (blue) or aged at 120 °C for 24 hours (green line). Counts are normalised based on carbon	

peak height. Spectra features due to sulphur, fluorine, oxygen, nitrogen, and carbon are marked with vertical bars.	130
Figure 5.9: Concentration depth profiles of either pristine PPDT2FBT (black line) or PPDT2FBT:PC ₆₁ BM BHJ (coloured lines). The BHJ is either non-annealed (25 °C) (red line), aged at 85 °C for 6 months (blue) or aged at 120 °C for 24 hours (green line).....	131
Figure 5.10: SEM surface of PPDT2FBT:PC ₆₁ BM active layer aged at 85 °C for 6 months (LEFT), with highlighted area used for determining area of flat fullerene features.	132
Figure 5.11: DMTA of pure PPDT2FBT after thermal annealing: a) 40 °C for 30 minutes, b) 85 °C for 24 hours, and c) 120 °C for 24 hours.	133
Figure 5.12: DMTA of PPDT2FBT:PC ₆₁ BM samples after thermal annealing: a) 40 °C for 30 minutes, as well as b) 85 °C for 30 minutes, c) 8 hours, d) 15 hours, and e) 1 week.....	135
Figure 5.13: DMTA of PPDT2FBT:PC ₆₁ BM samples after thermal annealing: a) 40 °C for 30 minutes, as well as b) 120 °C for 30 minutes, c) 8 hours, d) 15 hours, and e) 1 week.....	137
Figure 5.14: DMTA of PPDT2FBT:PC ₆₁ BM sample after thermal annealing after annealing at 85 °C for 30 minutes (solid line), while the same sample was annealed at 120 °C for 30 minutes and measured again (dotted line)	138
Figure 6.1: Chemical structures of some solid additives that have been investigated in previously published worked.....	145
Figure 6.2: (a) Chemical structure of PPDT2FBT & PC ₆₁ BM, (b) schematic illustration of inverted OPV structure used in this work.	148
Figure 6.3: Chemical structure of Neat C ₇₀ , piperazine (PP), 4,4'-bipiperadine (BP), and polyacenaphthylene (PAN).	148
Figure 6.4: Charge carrier mobility in PPDT2FBT:PC ₆₁ BM devices as a function of light intensity, with the active layer either with or without various solid additives.....	153
Figure 6.5: Carrier Lifetime of PPDT2FBT:PC ₆₁ BM devices as a function of charge Density, with the active layer either with or without various solid additives.....	153
Figure 6.6: Device characteristics trends at 120 °C thermal aging under nitrogen. The results are from an average of 6 cells, with an active area of 0.1 cm ²	155
Figure 6.7: Device characteristics trends at 85 °C thermal aging under nitrogen. The results are from an average of 6 cells, with an active area of 0.1 cm ²	157
Figure 6.8: SEM images of PPDT2FBT:PC ₆₁ BM surface after annealing at either 120 °C for 24 hours (a-e) or 85 °C for 1 month (f-j). The active layer either contained no additives (a, f), 1.0% w/w PP (b, g), 0.1% w/w BP (c, h), 1.0% w/w PAN (d, i) or 3.3% w/w C ₇₀	158
Figure 6.9: SEM images of PPDT2FBT:PC ₆₁ BM surface after annealing at 85 °C for 1 month. The active layer either contained (a) 1.0% w/w PP, (b) 0.1% w/w BP or (c) 1.0% w/w PAN.....	159
Figure 6.10: DMTA plots of PPDT2FBT:PC ₆₁ BM, either (a) without additive, with (b) 1.0% w/w PP, (c) 0.1% w/w BP, or (d) 1.0% w/w PAN. All samples were pre-annealed at 40 °C for 30 minutes prior to measurements.	160
Figure 6.11: DMTA plots of PPDT2FBT:PC ₆₁ BM + 1.0% w/w PAN, which the blends having been pre-annealed at either (a) 40 °C for 30 minutes, (b) 120 °C for 30 minutes, (c) 85 °C for 30 minutes or (d) 24 hours. Pre-annealing was performed prior to measurements.....	161
Figure 7.1: Molecular structure of active layer materials, donor polymers and acceptor materials, as well as solid additives investigated in this thesis.	170
Figure 7.2: Schematic illustration of inverted (LEFT) and conventional (RIGHT) OPV structure used in this chapter.	171
Figure 7.3: JV-curve of PPDT2FBT:PC ₆₁ BM with different processing conditions, specifically, non-processed, switched and substrate-aged devices.	177
Figure 7.4: Conventional and Inverted PPDT2FBT:PC ₆₁ BM devices aging at room temperature under nitrogen conditions.....	180

Figure 7.5: Device stability of PPDT2FBT:PC ₆₁ BM conventional vs Inverted devices that are aged at 85 °C.....	181
Figure 7.6: PPDT2FBT:PC ₆₁ BM conventional device thermal aging at 85 °C for different additives. Additions include piperazine (PP), 4,4'-bipiperadine (BP) and polyacenaphthylene (PAN).....	183
Figure B1: Oxidation square-wave curve of PPDT2FBT (LEFT), as well as Reduction square-wave curves of PPDT2FBT, PC ₆₁ BM, PC ₇₁ BM, C ₆₀ , and C ₇₀ (RIGHT).....	205
Figure B2: Light current-density / Voltage (JV) curve of PPDT2FBT:PC ₆₁ BM (1:2) (LEFT), PPDT2FBT:PC ₆₁ BM:C ₆₀ (1:1.9:0.1) (MIDDLE) & PPDT2FBT:PC ₆₁ BM:C ₇₀ (1:1.9:0.1) (RIGHT) after experiencing different heating conditions, prior/post to MoO _x /Al deposition.	205
Figure B3: Scanning electron microscopy images of the PPDT2FBT:PC ₆₁ BM surface after 24 hours at 120 °C with marked locations of Auger electron spectroscopy was measured.	205
Figure B4: Raw Auger electron spectra of 3 positions (five different point scans per position). ...	206
Figure B5: Auger electron spectroscopy scans of 3 positions (five-point scan areas per position). Spectra has been smoothed (9-point Savitzky-Golay) and derived (5-point).	207
Figure D1: Atomic force microscopy images of surface of PPDT2FBT:PC ₆₁ BM a), with the addition of either 1.0% w/w PP b), 0.1% w/w BP c) or 1.0% w/w PAN d).....	212
Figure D2: Scanning electron microscopy images of the PPDT2FBT:PC ₆₁ BM surface after 8 hours at 120 °C with marked locations of Auger electron spectroscopy was measured. Position 1 & 2 is the spot scan location over the short and long crystals, respectively, while position 3 is over the surface of the BHJ.	213
Figure D3: Scanning electron microscopy images of the PPDT2FBT:PC ₆₁ BM surface after 6 months at 85 °C with marked locations of Auger electron spectroscopy was measured. Position 1 is the surface of the BHJ, while position 2 & 3 is the spot scan location of the flat surface feature.	214
Figure D4: Auger electron spectra of PPDT2FBT:PC ₆₁ BM surface after 8 hours at 120 °C with marked locations of Auger electron spectroscopy was measured. Position 1 & 2 is the spot scan location over the short and long crystals, respectively, while position 3 is over the surface of the BHJ. Position locations can be seen in Figure C2.	214
Figure D5: Auger electron spectra of PPDT2FBT:PC ₆₁ BM surface after 8 hours at 120 °C with marked locations of Auger electron spectroscopy was measured. Position 1 & 2 is the spot scan location over the short and long crystals, respectively, while position 3 is over the surface of the BHJ. Position locations can be seen in Figure C3.	215
Figure D6: Photo-CELIV results for inverted slot-die fabricated PPDT2FBT:PC ₆₁ BM devices, with and without solid additives. Additives include neat C ₇₀ , PP, BP, and PAN.....	216
Figure D7: : Transient photovoltage results for inverted slot-die fabricated PPDT2FBT:PC ₆₁ BM devices, with and without solid additives. Additives include neat C ₇₀ , PP, BP, and PAN.	217
Figure D8: Time-resolved current extration results for inverted slot-die fabricated PPDT2FBT:PC ₆₁ BM devices, with and without solid additives. Additives include neat C ₇₀ , PP, BP, and PAN.	218

LIST OF TABLES

Table 2.1: List of literature summary, including device architecture, which layers are printed, device area and device performance.....	43
Table 2.2: Technical comparison of different printing/coating techniques. Table was adapted from Krebs 2009 [1].	49
Table 4.1: Device characteristics of PPDT2FBT:fullerene devices with varying weight ratios of PC ₆₁ BM:C ₇₀	102
Table 4.2: Atomic Percentages of carbon and sulphur at three different locations. Percentages are calculated in relation to the presence of carbon and sulphur only.	108
Table 5.1: Calculated atomic percentages of carbon and sulphur at various locations based on Auger electron spectroscopy measurements. Percentages are calculated in relation to the presence of carbon and Sulphur only.....	128
Table 5.2: Step height of the count rate for sulphur and carbon, step height ratio and calculated material composition of polymer in the PPDT2DBT, as well as non-annealed and annealed BHJ. The material composition was calculated based on the C:S step height ratio of pristine PPDT2FBT.	131
Table 6.1: Device performance based on PPDT2FBT:PC ₆₁ BM devices with and without solid additives. Additives include neat C ₇₀ , piperazine (PP), 4,4'-bipiperadine (BP), polyacenaphthylene (PAN). The results are from an average of 6 cells, with an active area of 0.1 cm ²	151
Table 6.2: Charge carrier mobility, lifetime and PCE measurements of PPDT2FBT:PC ₆₁ BM based on BHJs either without or with solid additives.....	154
Table 7.1: Device performance of inverted OPVs, with the performance values based on the specific active layer blend per system. The results are from an average of 6 cells, with an active area of 0.1 cm ²	174
Table 7.2: Device performance of conventional PPDT2FBT:PC ₆₁ BM OPVs. The results are from an average of 6 cells, with an active area of 0.1 cm ²	176
Table 7.3: Device performance of inverted and conventional slot-die coated OPVs, with the performance values based on the specific active layer blend per system. The results are from an average of 6 cells, with an active area of 0.1 cm ²	177
Table 7.4: Device performance conventional OPVs for small and large active area, with the performance values based on the specific active layer blend per system. Small-area devices are an average of 6 cells, while large area is of the highest performance achieved.	179
Table A1: Device performance based on PPDT2FBT:PC ₆₁ BM devices with different PPDT2FBT batches (C143 & D173). The results are from an average of 6 cells, with an active area of 0.1 cm ² ..	208
Table B1: Estimated material cost of active layer materials based on a scale of 100 g. Prices gathered in December 2021, proved by Organic Nano Electronic (ONE=1) materials.....	202
Table B2: Device characteristics of PPDT2FBT:Fullerene devices under different coating conditions.....	203
Table B3: Device characteristics of PPDT2FBT:PC ₆₁ BM devices aging at room temperature under dark nitrogen conditions.	204
Table B4: Device characteristics of PPDT2FBT:PC ₆₁ BM devices aging at 85 °C under dark nitrogen conditions.....	204
Table B5: Device characteristics of PPDT2FBT:Fullerene devices aging at 120 °C under dark nitrogen conditions.....	208

ABBREVIATIONS & ACRONYMS

AES	Auger electron spectroscopy
AFM	Atomic force microscopy
AM	Air-mass coefficient
BHJ	Bulk-heterojunction
BP	4,4'-bipiperadine
bp	Boiling point
Ca	Calcium
CN	1-Chloronaphthalene
CTS	Charge transfer state
DSC	Differential scanning calorimetry
DMA	Dynamic mechanical analysis
DMTA	Dynamic mechanical thermal analysis
ETL	Electron transport layer
FF	Fill-factor
GIWAXS	Grazing-incidence wide-angle x-ray scattering
HOMO	Highest occupied molecular orbitals
HTL	Hole transport layer
ISOS	International summit on OPV stability
ITIC	3,9-bis(2-methylene-(3-(1,1-dicyanomethylene)-indanone))-5,5,11,11-tetrakis(4-hexylphenyl)-dithieno[2,3-d:2',3'-d']-s-indaceno[1,2-b:5,6-b']dithiophene
ITO	Indium tin oxide
J_{MPP}	Current density of maximum power point
J_{SC}	Short-circuit current density

LiF	Lithium fluoride
LUMO	Lowest unoccupied molecular orbital
MIES	Metastable induced electron spectroscopy
MoO _x	Molybdenum (VI) oxide
mp	Melting point
MRC	Mini-roll coater
NFA	Non-fullerene acceptor
NICISS	Neutral impact collision ion scattering spectroscopy
NiO _x	Nickel oxide
NP	Nanoparticles
NW	Nanowires
<i>o</i> -DCB	<i>ortho</i> -Dichlorobenzene
OPV	Organic photovoltaic
PAN	Poly acenaphthylene
PCE	Power conversion efficiency
PC ₆₁ BM	[6,6]-phenyl-C61-butyric acid methyl ester
PC ₇₁ BM	[6,6]-phenyl-C71-butyric acid methyl ester
PEDOT:PSS	Poly(3,4-ethylenedioxythiophene):poly(4-styrenesulfonate)
PEI	Polyethyleneimine
PEIE	Polyethyleneimine ethoxylated
PET	Polyethylene terephthalate
Photo-CELIV	Photo charge extraction by linearly increasing voltage
PP	1,4-piperazine

PPDT2FBT	Poly[(2,5-bis(2-hexyldecyloxy)phenylene)-alt-(5,6-difluoro-4,7-di(thiophen-2-yl)benzo[c]-[1,2,5]thiadiazole)]
PS	Polystyrene
PV	Photovoltaic
R2R	Roll-to-roll
SEM	Scanning electron microscopy
SiO ₂	Tin oxide
Sub-T _g	Sub-glass transition
T _g	Glass transition
TiO _x	Titanium oxide
ToF	Time-of-flight
TPV	Transient photovoltage
TQ1	poly[[2,3-bis(3-octyloxyphenyl)-5,8-quinoxalinediyl]-2,5-thiophenediyl]
TRCE	Time-resolved charge extraction
UPS	Ultraviolet photoelectron spectroscopy
UV	Ultraviolet
V ₂ O ₅	Vanadium oxide
Vis	Visible
V _{MPP}	Voltage of maximum power point
V _{OC}	Open-circuit voltage
XPS	X-ray photoelectron spectroscopy
ZnO	Zinc oxide

CHAPTER 1 – INTRODUCTION

In recent years, there has been increased interest towards the fabrication of printed and coated photovoltaics solar cells, allowing for the production of inexpensive and green energy. One promising type of solar cell is known as organic photovoltaics (OPVs) due to its cheap fabrication potential, flexibility, and increased performance; recently reaching beyond 19% efficiency [1, 2]. High performance has been achieved via lab-based small-scale fabrication, with some issues still associated with the lifetime of OPVs. This short lifespan can be associated with sources of PV degradation, including exposure to irradiance, mechanical, oxygen, moisture, and heating.

1.1. Global energy usage

Within the past century, energy security has been one of the most significant issues facing modern society. Currently, non-renewable energy sources, including coal and gas, have been the dominant energy sources as they are able to provide constant electricity to a large section of the population (as seen in *Figure 1.1*). As of 2022, fossil fuels make up the majority of the global energy market, with the three major energy sources being Oil, Coal, and Gas [3].

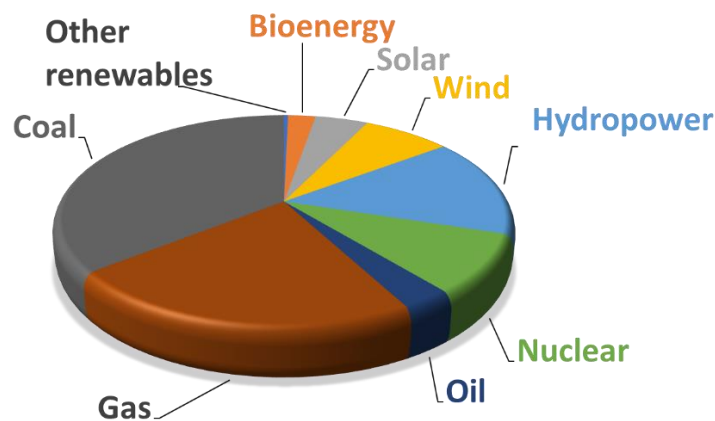


Figure 1.1: Relative percentage of energy production type in 2019 [3].

The issue with fossil fuels is that there are limited reserves that have been showing signs of depletions, while at the same time, have also been shown to have severe environmental impacts. As energy demands and the usage of fossil fuels increase, so too does the increase in greenhouse gas emissions [4]. With these increases in emissions, the frequency and severity of environmental issues such as climate change, smog, acid rain and human influenced natural disasters have increased [5].

1.2. Alternative energy sources

With the push towards environmentally friendly electricity production, there has been an increased interest towards the research and development of renewable energy sources. The goal for future energy sources is to provide indefinite power while minimising the environmental impact [6, 7].

Renewable energy is defined as an energy generated from sources that can be replenished on a human timescale [8].

Unlike fossil fuels; these sources have a low environmental impact, with renewables having minimal contribution towards the net increase of greenhouse gases [9]. Renewable energy can consist of a variety of types including wind, solar, geothermal and bioenergy. An issue with the use of renewable energy resources is consistency, mostly relying on external factors that are difficult to control (sun intensity, wind intensity). These effects can be reduced with the implementation of energy storage (battery, hydro-potential, solar thermal, solar fuels) and a combination of energy sources [10]. With the advancements in renewable energy technology, especially in relation to an increase in performance and their reduction in cost, there has been an overall increase in renewable energy generation.

In 2018, renewables made up 26.2% of the global electricity generation, with this number predicted to increase up to 45% by 2040 [11]. As for 2022, the projection is still fairly accurate, where the current percentage of renewable energy electricity production globally had reached 28.9% [3]. This current trajectory may not be sufficient, however, as international agencies and organisations, including the International Energy Agency, have goals of reaching net zero emissions by 2050. To reach this goal, theorised that 70% of electricity generation needs to be produced by renewable energy sources (including nuclear) [12]. For this transition to occur, it requires global cooperation to reduce energy demand and the improvement of energy production efficiency. It also requires a shift toward the production of renewable energy sources, carbon capture technology and nuclear energy, over sources such as coal and gas generators [13-16].

1.3. Photovoltaics

One such promising energy source, photovoltaic (PV) cells, utilises solar energy by directly converting the energy from sunlight into electricity. For nations with high average sun intensity such as Australia, converting solar energy into power with PV devices would allow for cheap and renewable energy to sustain many households. In the past ten years, there had been an average growth of 34% in solar energy consumption in Australia, whereas wind generation had an average increase of 15% [17]. This is due to the rise in popularity of PV installations for household usage and the ease of installation.

Currently, PV devices are produced with silicon-based materials, making up 90% of the commercial market associated with solar panels [18]. This is due to their relatively high performance, with record efficiencies reaching beyond 26% [19] and their maturity in the commercial market [20].

Due to their technological-maturity, however, silicon-based PVs has seen a minimal improvement in performance in the past decade, being evident from the National Renewable Energy Laboratory (USA) tracking the advancement of photovoltaic technology [21]. From these statistics, it is predicted that technology is not expected to significantly improve soon. Another issue associated with silicon solar cells is related to the method of device fabrication. To form these cells, elevated temperatures are required for both the purification of the silicon and to form the crystalline structure [22], resulting in the fabrication method being energy intense. Lastly, as crystalline silicon is fragile, stiff, and non-transparent, they are restricted to what surfaces they can be integrated with (i.e., windows, plastic sheets) [23].

As a result of the issues and limitations associated with silicon-based panels, there has been a push towards developing alternative technologies, with research now focusing on loosely referred to as third-generation photovoltaic cells. These involve solvent-based, thin devices that have the potential for energy-efficient PV manufacturing.

1.4. Organic photovoltaics

Organic photovoltaics (OPVs) are a type of third-generation solar cell which are devices that consists of an active layer component that contains a blend of semi-conducting organic materials. For the OPVs to generate electricity, the sunlight must pass through the substrate (as seen in *Figure 1.2*) and interact with the active layer. When the light is absorbed, it forms excitons which are split into free charge carriers, i.e., electrons and holes, at the donor-acceptor interface within the active layer.

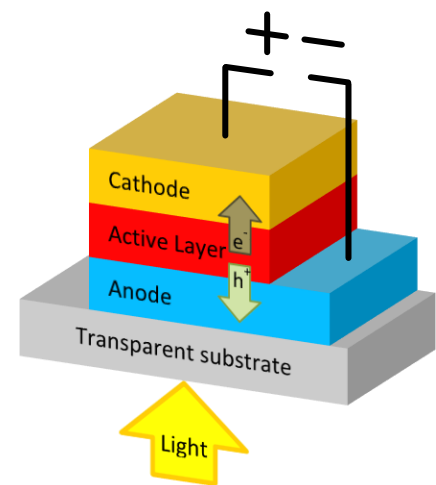


Figure 1.2: A model of a simple architecture of an OPV.

As electrons prefer to decrease in energy while holes prefer to increase in energy, high and low work function metals are used for the cathode and anode, respectively. Due to adjustment of energy levels between the materials, free charge carriers move towards their respective electrodes, electrons towards the cathode and the holes towards the anode. This flow of electrons and 'holes' in opposite directions generates electricity.

The advancement in OPV technology in the last decade has allowed for absorption of lower energy photons (due to decreasing the bandgap in active layers) which allows these devices to function better in indirect sunlight (i.e. cloud cover) [24] as well as under indoor conditions (artificial light) [25-27]. A higher efficiency cell means that there is a higher output of energy during daylight hours, resulting in a smaller area of solar panels required. Currently, record efficiencies for single-layered small-scaled devices have reached above 19% [1, 2].

1.5. Printing fabrication of OPVs

As the active materials can be dissolved in a variety of solvents, it allows for OPV to be fabricated using an array of non-vacuum-based thin-film coating methods. Methods that have been implemented in OPV fabrication include:

- Spin-coating [28-30]
- Blade-coating [31, 32]
- Slot-die coating [33-35]
- Screen printing [25, 36, 37]
- Spray-coating [38-40]
- Inkjet printing [26, 41, 42]
- Knife-over-edge coating [43-45]

Utilising these non-vacuum-based printing and coating methods, less energy is required for OPV fabrication, while simplifying the manufacturing procedure, thus, reducing the potential cost with producing these devices. With these benefits, researchers and industry has aimed the transition of OPV technology from laboratory-based fabrication to large-scale manufacturing. To achieve this, there has been a focus towards adjusting and optimising coating methods and conditions that can be applied to a roll-to-roll (R2R) printing/coating system.

What makes R2R processing an ideal system for large-scale OPV fabrication is due to its relatively low manufacturing cost, has minimal material waste, while allowing for the large-area production of flexible devices (as seen in *Figure 1.3*). This allow for the production of bendable, thin, and light weight solar cells, that can be integrated on a variety of surfaces that would otherwise be unable to support silicon-based solar panels [46].

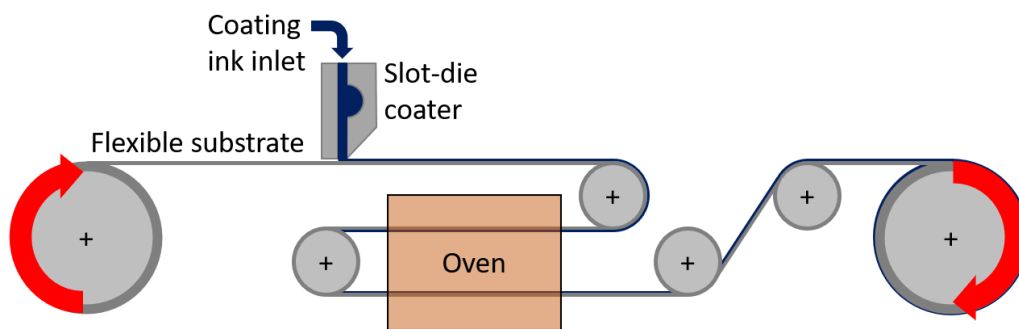


Figure 1.3: Basic schematic of a roll-to-roll setup which slot-die coating deposition of film and post-heating treatment.

For small-scaled, lab-based fabrication, spin-coating is one of the most used fabrication methods for OPV devices. This is due to the simplicity of use, allowing for ease of device fabrication, as well as the low machinery/instrument cost and implementation. The issue with this technique is that spin-coated films have a non-uniform thickness, with the films being thicker in the centre than at the edges. This problem worsens as the substrate size increases from 25 mm x 25 mm (small-scale device) to 156 x 156 mm (standard size of a silicon solar cell). Another issue with the technique is that most of the ink is spun off the substrate, resulting a large amount of material being wasted and thus, lead to an increased cost of manufacturing [47, 48]. Lastly, there is limited control over thickness [49]. Due to this issue, other methods have been investigated towards large-scale fabrication methods.

One such method, blade-coating, involves moving a blade to drag the ink across a substrate, allowing for the uniform coating of a thin-film. Recently, it has been found that they are able to yield similar efficiencies as compared to spin-coating, reaching up to 9.5% [50]. It is possible to produce large-scaled devices with this technique; however, they have limited control over printed strip width, and are not considered roll-to-roll compatible.

A more promising coating method, which is roll-to-roll compatible, is the use of a one-dimensional coating method known as slot-die coating. This involves forming a meniscus between the slot-die head and the substrate. This technique is well suited for producing multilayer solar cells, involving a variety of materials layered over each other [51] (seen in *Figure 1.4*). The thickness of each layer can be easily controlled by adjusting the flow rate of solution to the die-head, and the substrate movement rate. The method has also been shown to produce minimal material waste, thus, further reducing the production cost [52].

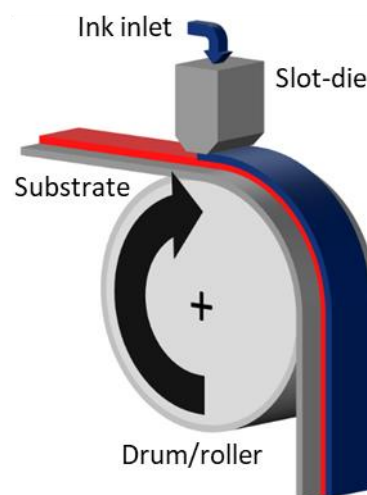


Figure 1.4: Basic schematic of slot-die coating on the MRC.

One downside to slot-die coating is the limitation to which solvents can be used for the coating process, especially when coating over the active layer. Ideally, the sequential deposition of thin films should not influence the film qualities of the underlying layer. In reality, there is a risk that the deposited wet film may either swell, or dissolve (partial or completely) the dry thin film underneath, which can result in non-ideal OPV device fabrication. It is worth noting that this limitation is not restricted to slot-die coating, and does impact other non-vacuum based deposition techniques, such as spin, blade and spray coating.

In 2019, by adjusting the drying kinetics in relation to slot-die coating of the active layer, an efficiency above 12% were able to be achieved; which was comparable with optimal spin-coated and blade-coated OPV devices of the same device material and structure [34]. To achieve this, several factors need to be adjusted: including coating speed, coating gap, flow rate, substrate temperature, solution temperature, liquid viscosity, and surface tension. It is noted that this method had been optimised for a device area of 0.06 cm².

This is an issue as for large-area OPV fabricated using roll-to-roll fabrication methods have not been able to repeat these high performances found in devices prepared in laboratory conditions. To date, the current record efficiency for a single-layered OPV is above 19% [1, 2], whereas for large-area (194.8 cm²), rigid-based devices had reached above 12%. For flexible modules, the efficiencies of these devices are worse, with the highest performance achieved at 5.6% with an active area of 7.2 cm² [53]. Overall, there is a significant efficiency gap between small-scale devices fabricated in laboratory environments, large-area rigid devices, and large-scale, roll-to-roll fabricated modules.

1.6. Device stability

In the past decade, there have been huge advancements in improving performance of OPVs, however, another aspect of OPV research, device stability, has not had as much focus. This area of research is important for mass-produced OPVs, as it is commercially unviable to fabricate devices that have a very-short lifespan. There are four primary areas of OPV degradation that are currently being researched:

- Thermal [30, 54]
- Oxygen and moisture [55, 56]
- UV radiance [57, 58]
- Mechanical [33, 59]

A majority of stability issues stem from the degradation of the bulk-heterojunction (BHJ) of the active layer, with one such example being relating to thermal stability. As the OPV is heated, the BHJ can experience an increase in domain size that results in the decrease in current and efficiency [30]. It is also understood that UV radiation can induce photochemical degradation of the BHJ, resulting in photobleaching of the active layer components [58].

Another major area that effects stability, especially for flexible devices, is the bottom electrode. With the aim for producing flexible OPVs, it is important that the device can withstand bending and straining. Though Indium Tin Oxide (ITO) is common material utilised as an effective bottom electrode due to its high transparency and low sheet resistance, it has been demonstrated to be easy to fracture under mechanical stress leading to an increase in sheet resistance, and thus, resulting a reduction in device performance [33, 59].

The last area of stability issues is related to the interface of materials. If material diffusion or layer de-lamination occurs, a change in the V_{oc} can occur, relating to decrease in efficiency [60]. This is the least investigated area of stability due to difficulty in analysing the interface between materials and generally relies on in-direct or destructive methods and measurements.

There are several strategies to improve the stability of OPVs, however, a good majority have only been investigated with spin-coated devices, rather than for scalable and large-scale device fabricated under ambient conditions. While some strategies are aimed at improving the active layer, rather than the causes of degradation including material diffusion at the layer interface. The stability issues and the appropriate strategies will be discussed later in the literature review (*Section 2.9*).

1.7. Aim of the thesis studies

In this thesis, the purpose of the studies was to investigate the thermal degradation of slot-die fabricated OPVs, implementing a range of spectroscopy, microscopy, and material analysis techniques. The studies also aimed at determining the scalability of methods for influencing the thermal behaviour of the active layer blend, and how translatable the research is towards upscalable OPV devices.

Before discussing the findings in the thesis, *Chapter 2*, titled **Progress in research focus associated with scalable Organic Photovoltaics Fabrication**, provides an in-depth analysis of the OPV field, with a highlight on previously published work on major degradation sources, and the strategies for minimising their impact on the device lifespan. The chapter also investigates the development of scalable printing and coating techniques used over the past decade, as well as challenges that are required to be overcome.

The next chapter (*Chapter 3*), titled **Research Methodology**, provides background and information associated with the experimental techniques and instrumentation in relation to research conducted in this thesis. This chapter provides information associated with material and ink preparation for thin-film deposition, OPV fabrication and testing, spectroscopy and microscopy instrumentation, and material analysis methods. Specific experimental information for *Chapters 4-7* can be found in the *Experimental section* for each given chapter.

Chapter 4, titled **Introducing neat fullerenes to improve the thermal stability of slot-die coated organic solar cells**, is a reformatted published manuscript about the influence that the addition of neat fullerenes can have over the thermal behaviour of the active layer containing a polymer:fullerene blend. By aging at an accelerated thermal degradation temperature, devices with and without the additives were compared to determine the impact the neat fullerenes C₆₀ and C₇₀ had on potential changes to the active layer morphology.

Chapter 5, titled **Investigating degradation pathways associated with working and accelerated thermal conditions**, was aimed at investigating the difference in thermal degradation of polymer:fullerene-based OPVs when heated at two different aging temperatures; 85 °C (accepted thermal aging temperature) and 120 °C (accelerated thermal aging temperature). The study involved observing the thermal behaviour of thermally aged active layer blends and comparing this with the device degradation behaviour.

Chapter 6, titled **Introducing non-fullerene additives to improve the thermal stability of slot-die coated organic photovoltaics**, is associated with the influence of non-fullerene solid additives, piperazine (PP), 4,4'-bipiperadine (BP) and polyacenaphthylene had on the thermal behaviour of the active morphology of a polymer:fullerene blend, and its impact over the thermal stability of the OPV devices. The study also compared the two major degradation pathways that were observed in *Chapter 5*.

Chapter 7, titled **Preliminary study of scalable methods used to influence thermal behaviour of OPVs**, investigated the scalability and translatability of the research conducted throughout this thesis. To achieve this, an OPV architecture that has been shown to be roll-to-roll friendly is used, as well as a selection of different active layer blends previously studied. The study aimed to demonstrate the ability to translate the research conducted from a mini-roll coater setup to roll-to-roll fabrication, as well as the challenges that are crucial to overcome.

Lastly, *Chapter 8* provides a conclusion for the thesis, focusing on the major findings in the four research chapters (*Chapter 4-7*). The chapter also discusses potential future work associated with the thesis studies, and direction that can be taken to further enhance the field of OPV thermal degradation and ways to allow for bridging the research conducted between small-scale laboratory environments, to large-scale roll-to-roll industry settings.

1.8. References

1. Zhu, L., Zhang, M., Xu, J., Li, C., Yan, J., Zhou, G., Zhong, W., Hao, T., Song, J., Xue, X., Zhou, Z., Zeng, R., Zhu, H., Chen, C.-C., MacKenzie, R. C. I., Zou, Y., Nelson, J., Zhang, Y., Sun, Y., and Liu, F., Single-junction organic solar cells with over 19% efficiency enabled by a refined double-fibril network morphology. *Nature Materials*, **2022**. 21 (6), 656-663.
2. Ding, G., Chen, T., Wang, M., Xia, X., He, C., Zheng, X., Li, Y., Zhou, D., Lu, X., Zuo, L., Xu, Z., and Chen, H., Solid Additive-Assisted Layer-by-Layer Processing for 19% Efficiency Binary Organic Solar Cells. *Nano-Micro Letters*, **2023**. 15 (1), 92.
3. Ritchie, H., Roser, M., and Rosado, P., Energy. *Our World in Data*, **2022**.
4. World Bank, World development indicators. 2014.
5. Newell, R. G. and Iler, S., The global energy outlook. **2013**, National Bureau of Economic Research.
6. European Environment Agency, Renewable energy in Europe – 2017 Update, in *EEA Report*. **2017**.
7. Johansson, T. B., Kelly, H., Reddy, A. K., and Williams, R. H., Renewable energy: sources for fuels and electricity. **1993**.
8. Herzog, A., Lipman, T., and Kammen, D., Renewable energy sources, Encyclopedia of Life Support Systems (EOLSS). *Forerunner Volume-Perspectives and Overview of Life Support Systems and Sustainable Development*, **2001**.
9. Eisenberg, R. and Nocera, D. G., Preface: Overview of the forum on solar and renewable energy. *Inorganic chemistry*, **2005**. 44 (20), 6799-6801.
10. Phuangpornpitak, N. and Tia, S., Opportunities and Challenges of Integrating Renewable Energy in Smart Grid System. *Energy Procedia*, **2013**. 34, 282-290.
11. REN21, Renewable 2019 Global Status Report. **2019**, REN21 Secretariat: Paris, France.
12. Bouckaert, S., Pales, A. F., McGlade, C., Remme, U., Wanner, B., Varro, L., D'Ambrosio, D., and Spencer, T., Net zero by 2050: A roadmap for the global energy sector. **2021**.
13. Blondeel, M., Bradshaw, M. J., Bridge, G., and Kuzemko, C., The geopolitics of energy system transformation: A review. *Geography Compass*, **2021**. 15 (7), e12580.
14. Wang, F., Harindintwali, J. D., Yuan, Z., Wang, M., Wang, F., Li, S., Yin, Z., Huang, L., Fu, Y., Li, L., Chang, S. X., Zhang, L., Rinklebe, J., Yuan, Z., Zhu, Q., Xiang, L., Tsang, D. C. W., Xu, L., Jiang, X., Liu, J., Wei, N., Kästner, M., Zou, Y., Ok, Y. S., Shen, J., Peng, D., Zhang, W., Barceló, D., Zhou, Y., Bai, Z., Li, B., Zhang, B., Wei, K., Cao, H., Tan, Z., Zhao, L.-b., He, X., Zheng, J., Bolan, N., Liu, X., Huang, C., Dietmann, S., Luo, M., Sun, N., Gong, J., Gong, Y., Brahushi, F., Zhang, T., Xiao, C., Li, X., Chen, W., Jiao, N., Lehmann, J., Zhu, Y.-G., Jin, H., Schäffer, A., Tiedje, J. M., and Chen, J. M., Technologies and perspectives for achieving carbon neutrality. *The Innovation*, **2021**. 2 (4), 100180.
15. Ram, M., Bogdanov, D., Aghahosseini, A., Gulagi, A., Oyewo, A. S., Odai Mensah, T. N., Child, M., Caldera, U., Sadovskaia, K., Barbosa, L. D. S. N. S., Fasihi, M., Khalili, S., Traber, T., and Breyer, C., Global energy transition to 100% renewables by 2050: Not fiction, but much needed impetus for developing economies to leapfrog into a sustainable future. *Energy*, **2022**. 246, 123419.
16. Holechek, J. L., Geli, H. M., Sawalhah, M. N., and Valdez, R., A global assessment: can renewable energy replace fossil fuels by 2050? *Sustainability*, **2022**. 14 (8), 4792.
17. Australian Government, Department of Climate Change, Energy, the Environment and Water, Australian Energy Update 2022. **2022**.
18. Mulvaney, D., Solar's green dilemma. *IEEE Spectrum*, **2014**. 51 (9), 30-33.
19. Yoshikawa, K., Kawasaki, H., Yoshida, W., Irie, T., Konishi, K., Nakano, K., Uto, T., Adachi, D., Kanematsu, M., and Uzu, H., Silicon heterojunction solar cell with interdigitated back contacts for a photoconversion efficiency over 26%. *Nature energy*, **2017**. 2 (5), 17032.
20. Pandey, A. K., Tyagi, V. V., Selvaraj, J. A. L., Rahim, N. A., and Tyagi, S. K., Recent advances in solar photovoltaic systems for emerging trends and advanced applications. *Renewable and Sustainable Energy Reviews*, **2016**. 53, 859-884.
21. National Renewable Energy Laboratory. Photovoltaic Research. **2017** [cited 2017 10 April]; Available from: <https://www.nrel.gov/pv/>.
22. Wurfel, P., Physics of Solar Cells: From Basics to Advanced Concepts. 1st ed. 2009, KGaA, Weinheim: WILEY-VCH Verlag GmbH & Co.

23. Polman, A., Knight, M., Garnett, E. C., Ehrler, B., and Sinke, W. C., Photovoltaic materials: Present efficiencies and future challenges. *Science*, **2016**. 352 (6283), aad4424.
24. Holliday, S., Li, Y., and Luscombe, C. K., Recent advances in high performance donor-acceptor polymers for organic photovoltaics. *Progress in Polymer Science*, **2017**. 70, 34-51.
25. Ylikunnari, M., Välimäki, M., Väisänen, K.-L., Kraft, T. M., Sliz, R., Corso, G., Po, R., Barbieri, R., Carbonera, C., Gorni, G., and Vilkmann, M., Flexible OPV modules for highly efficient indoor applications. *Flexible and Printed Electronics*, **2020**. 5 (1), 014008.
26. Alkhatib, H., Pasquinelli, M., Escoubas, L., Simon, J. J., Pierron, P., and Dkhil, S. B., Lifetime of inkjet printing OPV modules for indoor applications. **2019**.
27. Mainville, M. and Leclerc, M., Recent Progress on Indoor Organic Photovoltaics: From Molecular Design to Production Scale. *ACS Energy Letters*, **2020**. 5 (4), 1186-1197.
28. An, K., Zhong, W., Ying, L., Zhu, P., Fan, B., Li, Z., Li, N., Huang, F., and Cao, Y., Optimization of processing solvent and film morphology to achieve efficient non-fullerene polymer solar cells processed in air. *Journal of Materials Chemistry C*, **2020**. 8 (1), 270-275.
29. An, Q., Wang, J., Gao, W., Ma, X., Hu, Z., Gao, J., Xu, C., Hao, M., Zhang, X., Yang, C., and Zhang, F., Alloy-like ternary polymer solar cells with over 17.2% efficiency. *Science Bulletin*, **2020**. 65 (7), 538-545.
30. Zheng, N., Mahmood, K., Zhong, W., Liu, F., Zhu, P., Wang, Z., Xie, B., Chen, Z., Zhang, K., Ying, L., Huang, F., and Cao, Y., Improving the efficiency and stability of non-fullerene polymer solar cells by using N2200 as the Additive. *Nano Energy*, **2019**. 58, 724-731.
31. Zhang, L., Xu, X., Lin, B., Zhao, H., Li, T., Xin, J., Bi, Z., Qiu, G., Guo, S., Zhou, K., Zhan, X., and Ma, W., Achieving Balanced Crystallinity of Donor and Acceptor by Combining Blade-Coating and Ternary Strategies in Organic Solar Cells. *Advanced Materials*, **2018**. 30 (51), 1805041.
32. Pérez-Gutiérrez, E., Lozano, J., Gaspar-Tánori, J., Maldonado, J.-L., Gómez, B., López, L., Amores-Tapia, L.-F., Barbosa-García, O., and Percino, M.-J., Organic solar cells all made by blade and slot–die coating techniques. *Solar Energy*, **2017**. 146, 79-84.
33. Zimmermann, B., Schleiermacher, H.-F., Niggemann, M., Würfel, U., and Cells, S., ITO-free flexible inverted organic solar cell modules with high fill factor prepared by slot die coating. *Solar Energy Materials and Solar Cells*, **2011**. 95 (7), 1587-1589.
34. Wu, Q., Guo, J., Sun, R., Guo, J., Jia, S., Li, Y., Wang, J., and Min, J., Slot-die printed non-fullerene organic solar cells with the highest efficiency of 12.9% for low-cost PV-driven water splitting. *Nano Energy*, **2019**. 61, 559-566.
35. Zhao, H., Zhang, L., Naveed, H. B., Lin, B., Zhao, B., Zhou, K., Gao, C., Zhang, C., Wang, C., and Ma, W., Processing-Friendly Slot-Die-Cast Nonfullerene Organic Solar Cells with Optimized Morphology. *ACS Applied Materials & Interfaces*, **2019**. 11 (45), 42392-42402.
36. Krebs, F. C., Jørgensen, M., Norrman, K., Hagemann, O., Alstrup, J., Nielsen, T. D., Fyenbo, J., Larsen, K., and Kristensen, J., A complete process for production of flexible large area polymer solar cells entirely using screen printing—first public demonstration. *Solar Energy Materials and Solar Cells*, **2009**. 93 (4), 422-441.
37. He, P., Cao, J., Ding, H., Liu, C., Neilson, J., Li, Z., Kinloch, I. A., and Derby, B., Screen-Printing of a Highly Conductive Graphene Ink for Flexible Printed Electronics. *ACS Applied Materials & Interfaces*, **2019**. 11 (35), 32225-32234.
38. Susanna, G., Salamandra, L., Brown, T. M., Di Carlo, A., Brunetti, F., and Reale, A., Airbrush spray-coating of polymer bulk-heterojunction solar cells. *Solar Energy Materials and Solar Cells*, **2011**. 95 (7), 1775-1778.
39. Jiang, Z., Rahmanian, R., Soltanian, S., Nouri, R., and Servati, P. Single-pass Spray-coated Flexible Organic Solar Cells Using Graphene Transparent Electrodes. in *2019 IEEE International Flexible Electronics Technology Conference (IFETC)*. 2019.
40. Waheed, S., Pareek, S., Sharma, P., and Karak, S., Performance improvement of ultrasonic spray deposited polymer solar cell through droplet boundary reduction assisted by acoustic substrate vibration. *Semiconductor Science and Technology*, **2020**.
41. Angmo, D., Larsen-Olsen, T. T., Jørgensen, M., Søndergaard, R. R., and Krebs, F. C., Roll-to-Roll Inkjet Printing and Photonic Sintering of Electrodes for ITO Free Polymer Solar Cell Modules and Facile Product Integration. *Advanced Energy Materials*, **2013**. 3 (2), 172-175.
42. Maisch, P., Process Development for Inkjet Printing of Organic Photovoltaics. **2019**.

43. Krebs, F. C., Polymer solar cell modules prepared using roll-to-roll methods: knife-over-edge coating, slot-die coating and screen printing. *Solar Energy Materials and Solar Cells*, **2009**. 93 (4), 465-475.
44. Wang, G., Adil, M. A., Zhang, J., and Wei, Z., Large-Area Organic Solar Cells: Material Requirements, Modular Designs, and Printing Methods. *Advanced Materials*, **2019**. 31 (45), 1805089.
45. Park, J., Shin, K., and Lee, C., Roll-to-roll coating technology and its applications: A review. *International Journal of Precision Engineering and Manufacturing*, **2016**. 17 (4), 537-550.
46. Vogelbaum, H. S. and Sauv e, G., Recently developed high-efficiency organic photoactive materials for printable photovoltaic cells: a mini review. *Synthetic Metals*, **2017**. 223, 107-121.
47. Liao, H.-C., Ho, C.-C., Chang, C.-Y., Jao, M.-H., Darling, S. B., and Su, W.-F., Additives for morphology control in high-efficiency organic solar cells. *Materials today*, **2013**. 16 (9), 326-336.
48. Krebs, F. C., Fyenbo, J., and J rgensen, M., Product integration of compact roll-to-roll processed polymer solar cell modules: methods and manufacture using flexographic printing, slot-die coating and rotary screen printing. *Journal of Materials Chemistry*, **2010**. 20 (41), 8994-9001.
49. Sampaio, P. G. V., Gonz lez, M. O. A., de Oliveira Ferreira, P., da Cunha J come Vidal, P., Pereira, J. P. P., Ferreira, H. R., and Oprime, P. C., Overview of printing and coating techniques in the production of organic photovoltaic cells. *International Journal of Energy Research*, **2020**. 44 (13), 9912-9931.
50. Lin, Y., Jin, Y., Dong, S., Zheng, W., Yang, J., Liu, A., Liu, F., Jiang, Y., Russell, T. P., and Zhang, F., Printed nonfullerene organic solar cells with the highest efficiency of 9.5%. *Advanced Energy Materials*, **2018**. 8 (13), 1701942.
51. Krebs, F. C., Fabrication and processing of polymer solar cells: a review of printing and coating techniques. *Solar energy materials and solar cells*, **2009**. 93 (4), 394-412.
52. Chueh, C.-C., Yao, K., Yip, H.-L., Chang, C.-Y., Xu, Y.-X., Chen, K.-S., Li, C.-Z., Liu, P., Huang, F., Chen, Y. J. E., and Science, E., Non-halogenated solvents for environmentally friendly processing of high-performance bulk-heterojunction polymer solar cells. **2013**. 6 (11), 3241-3248.
53. Miranda, B. H., Corr ea, L. d. Q., Soares, G. A., Martins, J. L., Lopes, P. L., Vilela, M. L., Rodrigues, J. F., Cunha, T. G., Vila a, R. d. Q., and Castro-Hermosa, S., Efficient fully roll-to-roll coated encapsulated organic solar module for indoor applications. *Solar Energy*, **2021**. 220, 343-353.
54. Zhang, Z., Miao, J., Ding, Z., Kan, B., Lin, B., Wan, X., Ma, W., Chen, Y., Long, X., Dou, C., Zhang, J., Liu, J., and Wang, L., Efficient and thermally stable organic solar cells based on small molecule donor and polymer acceptor. *Nature Communications*, **2019**. 10 (1), 3271.
55. Meitzner, R., Faber, T., Alam, S., Amand, A., Roesch, R., B ttner, M., Herrmann-Westendorf, F., Presselt, M., Ciannaruchi, L., and Visoly-Fisher, I., Impact of P3HT materials properties and layer architecture on OPV device stability. *Solar Energy Materials and Solar Cells*, **2019**. 202, 110151.
56. Li, M., Zhang, W., Wang, H., Chen, L., Zheng, C., and Chen, R., Effect of organic cathode interfacial layers on efficiency and stability improvement of polymer solar cells. *RSC advances*, **2017**. 7 (50), 31158-31163.
57. Weng, C.-N., Yang, H.-C., Tsai, C.-Y., Chen, S.-H., Chen, Y.-S., Chen, C.-H., Huang, K.-M., Meng, H.-F., Chao, Y.-C., and Chang, C.-Y., The influence of UV filter and Al/Ag moisture barrier layer on the outdoor stability of polymer solar cells. *Solar Energy*, **2020**. 199, 308-316.
58. Doumon, N. Y., Wang, G., Chiechi, R. C., and Koster, L. J. A., Relating polymer chemical structure to the stability of polymer: fullerene solar cells. *Journal of Materials Chemistry C*, **2017**. 5 (26), 6611-6619.
59. Muhsin, B., Roesch, R., Gobsch, G., and Hoppe, H., Flexible ITO-free polymer solar cells based on highly conductive PEDOT:PSS and a printed silver grid. *Solar Energy Materials and Solar Cells*, **2014**. 130, 551-554.
60. Greenbank, W., Hirsch, L., Wantz, G., and Chambon, S., Interfacial thermal degradation in inverted organic solar cells. *Applied Physics Letters*, **2015**. 107 (26), 263301.

CHAPTER 2 – PROGRESS WITH SCALABLE ORGANIC PHOTOVOLTAICS FABRICATION

2.1. Overview

In this chapter, a literature review is present to provide the reader an overview of the history of the research field of organic solar cells, specifically an understanding of the operation of the solar cells as well as their device structuring and the materials utilised. The review will also cover the fabrication method for organic photovoltaics (OPVs), as well as investigate the causes of device degradation and the previous research aimed at improving OPV stability. Lastly, the review will extensively explore and compare several printing and coating processes that have been demonstrated in OPV fabrication.

Within recent years, there has been an increased interest towards OPVs, especially with the significant device performance reaching beyond 19% since 2022 [1, 2]. With these advances in device performance in laboratory scaled OPVs, there has also been more attention towards using printing and coating methods that are compatible with large-scale fabrication. Though large area fabricated OPVs have reached an efficiency of 15% [3], this is still behind that of small-scale OPVs. There also needs to be more focus on determining strategies of improving lifetime of OPVs that are suitable for scalable manufacturing, as well as methods for reducing material and manufacturing costs.

When investigating scalable printing and coating methods, there appears to be a growing interesting reducing the performance gap between small-scale spin-coated OPVs with scalable devices, as well as the fabrication of OPV modules with active areas greater than 100 cm². With that being said, there is still a lack of literature that investigated scalability of methods for improve OPV stability, especially in terms of thermal degradation. As for which printing and coating methods are recommended for OPV manufacturing, it has been found that blade coating and slot-die coating are ideal for active layer coating with sheet-to-sheet (S2S) and roll-to-roll (R2R), respectively. Though, for true large-scale OPV manufacturing to be successful, it needs to incorporate a variety of printing, coating, and post-processing techniques.

2.1. Device structuring

2.1.1. Single layer OPV

Over the decades, there has been an effort into improving the design of the physical structuring of devices, specifically the design of the active layer. The first generation of OPVs used single layer structure in-between two metal electrodes. It was found to yield extremely low efficiencies as the charge separation was insufficient for these devices [4].

Since then, there has been studies focusing on single layer materials that contain both donor and acceptor segments within the molecular structure [5-8]. To date, the highest efficiency achieved with this type of single layer material is just above 13% [8].

The initial development of active material in OPVs was first realised in 1977, where Shirakawa, MacDiarmid, and Heeger demonstrated that the conductivity of conjugated polymer can be controlled by doping with iodine [9], leading towards the path of OPVs. The electrical properties of conjugated polymers arise from the alternating single-double bond structuring of sp^2 hybridized carbon atoms present in the backbone of the polymer. Due to this structuring, conjugated polymers exhibit strong light absorption, allowing for the excitation of electrons from the ground state to an excited state.

By increasing the degree of conjugation splitting of energy levels occur, resulting in the formation of valence and conduction bands. Energy difference between the highest occupied molecular orbital (HOMO) and lowest unoccupied molecular orbital (LUMO) is defined as the bandgap. This gap is the lowest energy required to excite an electron from the valence to the conduction band. The bandgap can easily be altered through the tuning of the polymer structure [10, 11].

2.2.2. Bilayer planar heterojunction OPV

The second generation of OPVs employed a bilayer for their devices. First published in 1980, the bilayer planar heterojunction consists of donor and acceptor materials [4]. With the use of donor and acceptor materials, it allows for the separation of the electron-hole pair at the domain interface, resulting in the reduction of pair recombination, allowing for increased performance and higher output of energy. To achieve the bilayer planar heterojunction, the donor polymer was spin-coated onto the substrate, before fullerenes were evaporated on top [12]. Though an improvement over single layered devices was evident, efficiencies were still relatively low at 1%. This was associated with the exciton diffusion length limits of the number of excitons reaching the donor-acceptor interface and hence the charge carrier formation as well as efficiency [13].

The first fullerene structure, C_{60} (seen in *Figure 2.1*) was found by Harold Kroto *et al.*, also referred to as buckminsterfullerene [14], in which 60 carbons were bonded into conjugated rings to form a large ball. In 1992, Sariciftci *et al.* reported that C_{60} is able to accept electrons that were from conjugated polymers [15]. Fullerenes are great candidates as acceptor materials with conjugated polymers due to their high electron affinity and charge mobility. Currently, [6,6]-phenyl-C61-butyrac acid methyl ester (PC₆₁BM) [16] and [6,6]-phenyl-C71-butyrac acid methyl ester (PC₇₁BM) [17] (seen in *Figure 2.1*) are commonly used as fullerene acceptors due to their better solution-processability compared to C_{60} & C_{70} .

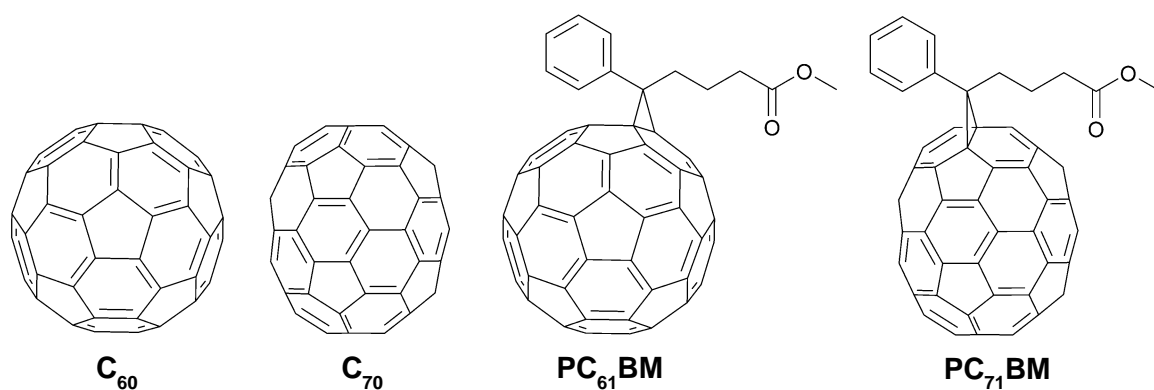


Figure 2.1: Chemical structure of C₆₀, C₇₀, PC₆₁BM, PC₇₁BM.

Other acceptor materials have also been investigated to allow for enhanced light absorption and to improve performance of OPVs. One such material, known as conjugated small molecule non-fullerene acceptors (NFA) have shown promising results with efficiencies reaching up above 19% [1, 2, 18]. It has also been shown that replacing fullerene with NFA can improve photo and thermal stability [19]. Such popular small molecule NFAs include, but not limited to 2,2'-[[6,6,12,12-Tetrakis(4-hexylphenyl)-6,12-dihydrodithieno[2,3-d:2',3'-d']-s-indaceno[1,2-b:5,6-b']dithiophene-2,8-diyl]bis[methyldiyne(3-oxo-1H-indene-2,1(3H)-diylidene)]]bis[propanedinitrile] (ITIC) [20-22] and 2,2'-[[12,13-Bis(2-ethylhexyl)-12,13-dihydro-3,9-diundecylbisthieno[2'',3'':4',5']thieno[2',3':4,5]pyrrolo[3,2-e:2',3'-g][2,1,3]benzothiadiazole-2,10-diyl]bis[methyldiyne(5,6-difluoro-3-oxo-1H-indene-2,1(3H)-diylidene)]]bis[propanedinitrile] (Y6) [23-25].

Another popular NFA acceptor material is polymer acceptors, with their increased interest due to their improved mechanical stability when compared with polymer:fullerene and polymer:small molecule NFA devices [26]. Recently, there have been interest towards designing polymer acceptors based on NFAs, with binary solar cells reaching up to 15% [27], reducing the performance gap between devices that use either polymer or NFA.

In terms of the bilayer planar heterojunction, there is a shift away from ideal bilayers, and towards pseudo-bilayers [28, 29] and sequentially deposited [2, 30-32] active layers. The advantage of this technique is that it allows for control over the interfacial area between the donor and accepted, depending on the solvent used in top active material ink and film processing. To date, the best performance that has been achieved by “bilayers” is currently above 7% [28], while sequential deposition has achieved an efficiency above 19% [2].

2.2.3. Bulk heterojunction

The third generation of OPVs had a bulk heterojunction (BHJ) structuring for the active layer, focusing on the intermixing of acceptor-donor domains. The BHJ layer involves the polymer donor and acceptor (Fullerene, NFA, polymer) materials being blended into a single film.

First developed in 1995, it had been shown that the BHJ was a superior design compared to a bilayer [33]; where the acceptor and donor materials appear in separate layers. The intermixing of materials allows for an increased interfacial surface area (seen in *Figure 2.*), which allows for an increased area where the separation of electron-hole pairs could occur. For the BHJ to work efficiently as an active layer, there must be both good mixing and good miscibility between the polymer and fullerene material [34]. This can be determined by investigating the morphology of the active layer.

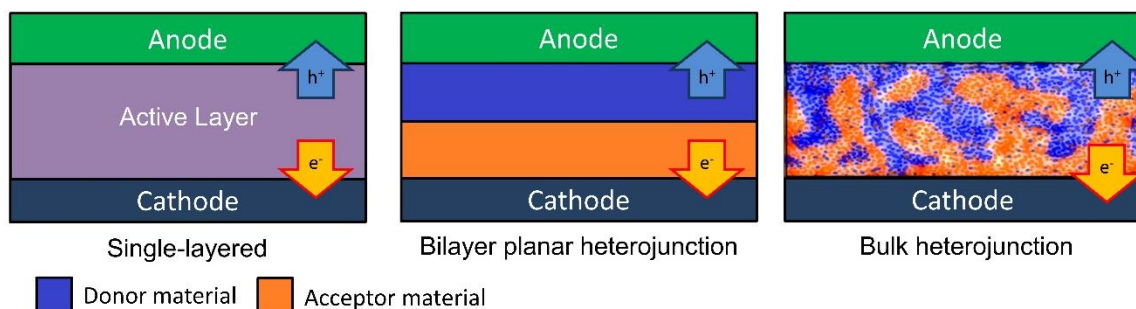


Figure 2.2: A basic model of types of junction structure; single, bilayer planar and bulk heterojunction solar cell.

As for 2023, the BHJ solar cell is still the most popular active layer structing for OPVs, however, its popularity is being challenged as the performance gap between BHJ and other structures such as pseudo-bilayer and singe-component reduces.

2.3. Photocurrent generation in OPVs

As mentioned in *Section 2.2*, a photo-induced current is generated by the light interaction with the material at the active layer. The process for the generation of photocurrent, as shown in *Figure 2.2* is (a) the photon is absorbed by the donor/acceptor material as the electron is excited from the HOMO to the LUMO energy states to form an exciton [35]. b) The exciton then diffuses towards the donor-acceptor interface; c) exciton diffusion then occurs, resulting in the electron in the LUMO of the acceptor material, while the hole is at the HOMO of the donor polymer. For an effective initial charge separation step, the LUMO offset at the donor-acceptor interface must be greater than the Coulomb binding energy of the exciton [36], or to form an effective intermolecular electric field by having a significant difference in electrostatic potential between the donor and acceptor materials [37, 38]. After diffusion, these excitons are still bounded by electric forces and thus, through the presence of the electric field or material disorder, the charge-pair is separated to form free charge carriers; e) allowing for the electron and hole to traverse to their respective electrodes.

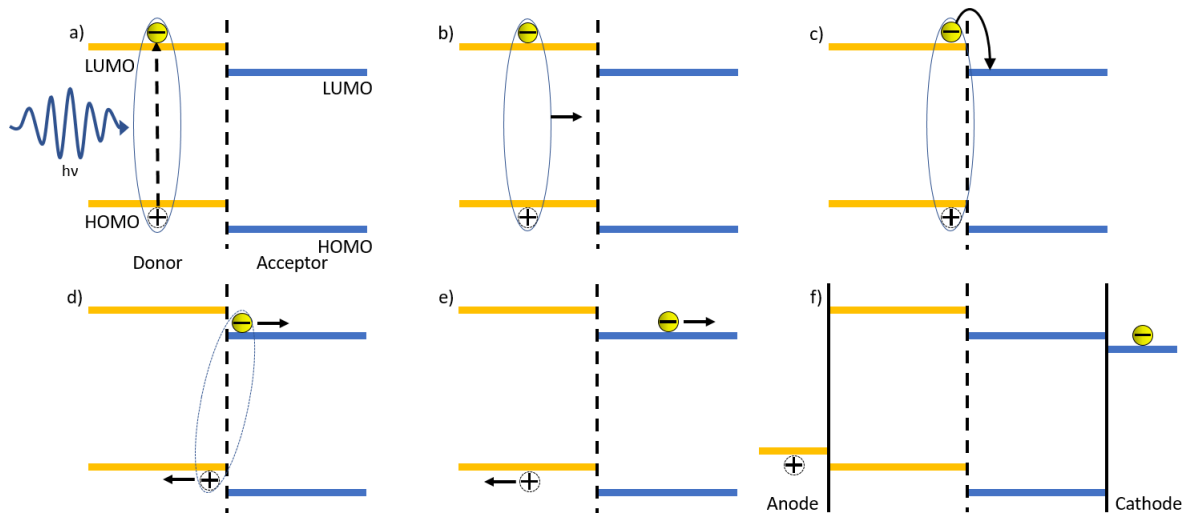


Figure 2.2: Schematic of photocurrent generation in OPVs: a) absorption of a photon to form an exciton, b) exciton diffusion towards the acceptor-donor interface, c) exciton dissociation, d) charge carrier separation, e) charge carrier movement through the active.

2.4. Device architectures

For the structuring of devices, there are two types: conventional and inverted devices structures, with both structures having photons through from the bottom (i.e., through the substrate). The structure order is as follows:

Conventional: *Substrate → Anode → Hole transport layer (HTL) → active layer → Electron transport layer (ETL) → Cathode*

Inverted: *Substrate → Cathode → Electron transport layer (ETL) → active layer → Hole transport layer (HTL) → Anode*

These two device structures can be seen in the schematic below (seen in *Figure 2.3*). It is noted that the transport layers can also act as a buffer or blocking layer.

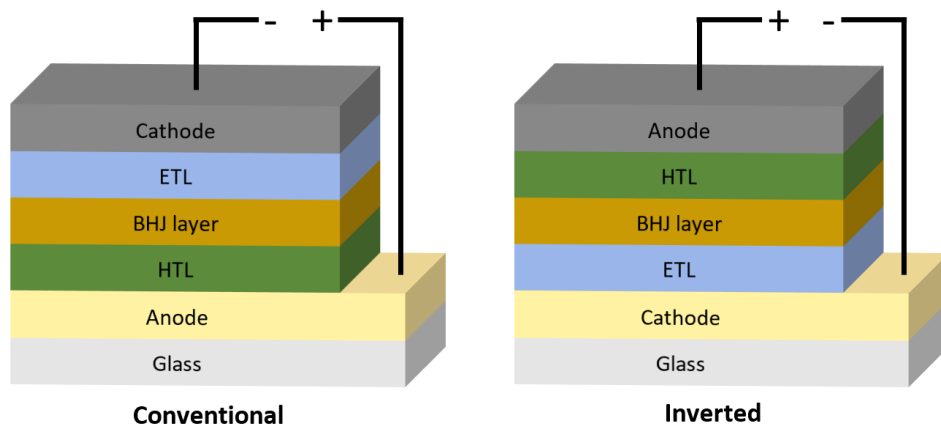


Figure 2.3: Schematic of conventional (left) and inverted (right) devices.

2.4.1. Conventional device structure

In conventional OPV devices, the Indium Tin Oxide (ITO) is used as the anode, allowing for the collection of holes, and for light to pass through to reach the active layer. Poly(3,4-ethylenedioxythiophene):poly(4-styrenesulfonate) (PEDOT:PSS) is commonly applied between the anode and the active layer [39-41]. It serves to modify the work function of the anode, act as a hole-transport layer (HTL) and smooths the anode [42-44]. It can also act as a barrier between the anode and active layer to limit diffusion of ITO into the BHJ [45], which would otherwise reduce the device efficiency [45]. Post-annealing of the PEDOT:PSS allows for the removal of moisture from the film, while the annealing improves the conductivity and thus, performance of devices [46].

Layered over the active layer, either Lithium Fluoride (LiF) [47] or Calcium (Ca) [48] is commonly used as a cathode buffer layer to improve devices. These materials are generally processed via thermal evaporation and thus, are not large-scale process friendly, resulting in an increase in fabrication cost [49]. There are, however, materials that can be deposited via non-vacuum processes, including but not limited Zinc Oxide (ZnO) [50, 51], Titanium Oxide (TiO_x) [52, 53], Tin Oxide (SnO_2) [54, 55], Polyethyleneimine (PEI) [56] and Polyethyleneimine Ethoxylated (PEIE) [57]. For printed/coated devices, Zinc Oxide nanoparticles (ZnO NPs) can be used as popular alternative as they are solution processable, allowing for ease of deposition as a ETL without requiring high temperature post-annealing of the film [58]. Lastly, Aluminium (Al) is commonly positioned on top to allow for the collection of electrons [40]. The top electrode has been demonstrated to deposit via solution-processes, however, for OPV fabrication, it has been dominated by the deposition of silver paste.

2.4.2. Inverted device structure

In inverted OPV devices, the ITO is used as the cathode, allowing for the collection of electrons. ZnO is commonly used as the cathode buffer layer / electron transport layer, allowing for the lower work function of the ITO, thus improving the anode alignment with the LUMO energy level of the acceptor material [59-61]. Above the active layer, Molybdenum Oxide (MoO_x) is used to increase the work-function of the anode as well as act as a HTL [62, 63].

Though it can improve the efficiency of small-scale devices, it is not desired for large-scale roll-to-roll fabrication due to having to involve sputtering techniques for MoO_x deposition [49]. To resolve this, there has been work towards solution-processable MoO_x [64-66], which has been demonstrated by depositing via blade-coating [66]. PEDOT:PSS has been used as an alternative as it can be coated/printed over the active layer [59]. Though popular as an HTL, literature has also demonstrated other materials as effective alternatives, including but not limited to Vanadium Oxide (V_2O_5) [67, 68], Graphene Oxide [69, 70] and Nickel Oxide (NiO_x) [71, 72]. Lastly, either aluminium or silver is used as the anode for inverted devices [73].

Inverted devices are normally more stable than conventional OPVs [74-76]. As mentioned in *Section 2.6.1*, the top electrode can be deposited via solution-process coating techniques, however, it is usually done with silver paste.

2.5. Morphology

With most OPV devices implementing a BHJ design for the active layer, the morphology of this thin film plays a crucial role in performance. Ideally, the layer consists of a tightly intermixed donor-acceptor domain that is no larger than the exciton diffusion length (1-10 nm) [77]; allowing for maximum probability of diffusion [16].

These domains should also provide a continuous network to allow for efficient charge transportation throughout the active layer. This prevents a build-up of charge which would otherwise reduce the device performance. Lastly, the material purity of domains affects the electric field strength at the donor-acceptor interface. Having high-purity domains results in the presence of a high electric field, allowing for efficient charge-pair separation. On the opposite end, a homogeneous active layer blend results in a lack of such field resulting in charge carrier recombination.

There are several strategies for the optimisation of the active layer morphology, including, however not limited to: i) adjustment of base solvent, ii) use of additional high boiling solvents additives, iii) addition of nucleating agents, iv) thermal annealing and v) solvent annealing. There are several properties that are taken into consideration for deciding on solvent used in the formation of the active layer. These include adequate viscosity of film formation and high solubility of active materials used [78].

For spin-coating fabrication, the drying rate is relatively quick, allowing for the morphology to be frozen in. This can allow for the formation of optimised nanostructure resulting in performance devices. The issue is that the morphology is generally not thermodynamically stable, resulting in the morphology changing over-time to a more thermally stable structuring [79].

2.6. OPV performance characterisation and key parameters

To evaluate the performance of OPVs, lab-scale devices are tested under a solar simulator lamp with a standardised air-mass coefficient (AM) of 1.5 solar irradiance spectrum, which corresponded to a power density of 100 mW cm^{-2} [80], allowing for the simulation of 1 sun of irradiance. A series of voltages is then applied across the device while a current measurement recorded, resulting in a current density-voltage (JV) curve being produced (as seen in *Figure 2.4*). There are four parameters that are important for determining the performance of solar cells, Short-circuit Current-density (J_{sc}), open-circuit voltage (V_{oc}), Fill-factor (FF) and power conversion efficiency (PCE).

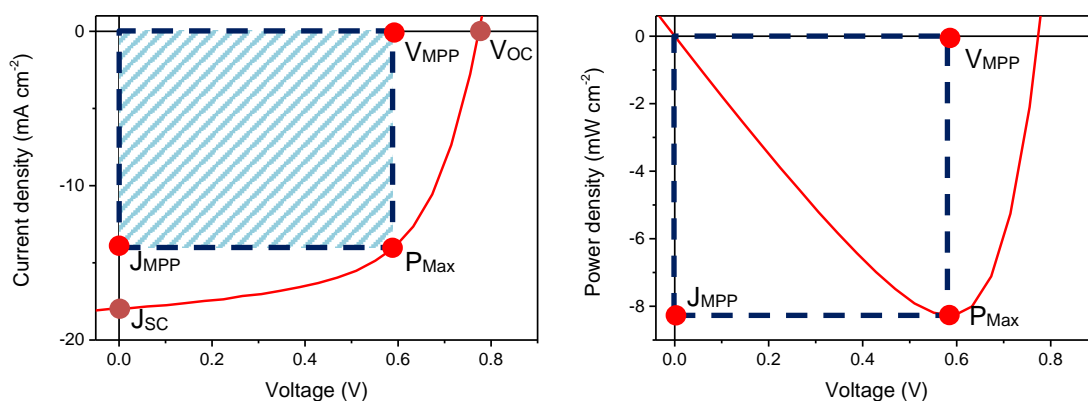


Figure 2.4: JV-curve (left) and PV curve (right), including markings of Short-circuit Current-density (J_{SC}), open-circuit voltage (V_{OC}), maximum power, as well as voltage and current density position of maximum power point (V_{MPP} & J_{MPP}), respectively.

2.6.1. Open-circuit voltage

The open-circuit voltage is the maximum potential generated by the device, with the current density reaching a value of 0 mA cm⁻². The maximum V_{OC} that can be achieved by the OPV has been found to be linearly dependant on the charge transfer state (CTS) energy. This is associated with the offset between the HOMO of the donor polymer ($HOMO_{donor}$) and the LUMO level of the acceptor material ($LUMO_{acceptor}$) [13, 81]. Improving the bandgap alignment of the donor and acceptor materials can yield an improved V_{OC} , yet, there still needs to be a LUMO-LUMO difference (at least 0.2-0.5 eV [82]) to allow for the dissociation of the exciton at the donor-acceptor interface [83]. There are also several other factors that can influence the V_{OC} , including non-radiative recombination at the donor/acceptor interface, as the built-in field associated with the work functions of the electrodes and interface layers [84].

2.6.2. Short-circuit current density

The short-circuit current density (J_{SC}) is the current-density recorded when no external potential is applied to the solar cell. From the JV-curve, this is the J-intercept found when voltage is 0 V. The J_{SC} can be improved by increasing the amount of photons being absorbed by either adjusting the bandgap of the active materials and/or the thickness of the active layer [83, 85]. A relatively simple method of increased light absorbance can occur by increasing the thickness the active layer, however, there is a limit to how large thickness can be before there is a reduction in efficiency due to increased probability of recharge-recombination for thicker films.

Another way to increase the J_{SC} is to decrease the bandgap, allowing for lower energy photons to be absorbed by the active layer and thus, an increase in current [86, 87]. The side-effect of band lowering can lead to a decrease in V_{OC} due to the reduction in the $HOMO_{donor}$ - $LUMO_{acceptor}$ energy gap, thus reducing the PCE. Lastly, achieving a good control over the film morphology can increase the J_{SC} as it reduces the presence of exciton recombination [88].

2.6.3. Fill-factor

The Fill-factor is determined from the ratio of maximum produced power to the product of J_{SC} and V_{OC} as seen in the following equation (*Equation 2.1*):

$$FF = \frac{V_{MPP} \times J_{MPP}}{V_{OC} \times J_{SC}} = \frac{P_{Max}}{V_{OC} \times J_{SC}} \quad (2.1)$$

where P_{Max} , J_{MPP} & V_{MPP} are the power, current density and voltage points where maximum power is produced.

There are a few factors that can influence the fill-factor, primarily, ones such being the series resistance and parallel resistance. Parallel resistance is related to the shunt resistance of the OPV, where a leakage current opposes the photogenerated current. If the shunt resistance is non-negligible, it can result in reduction in both the FF and PCE, while the V_{OC} increases as light intensity increases [89]. Series resistance is strongly related to the resistance within the film. One source of this resistance is influenced by the sheet resistance (R_{Sh}) of the bottom transparent electrode (usually ITO) [90], with a reduction in R_{Sh} resulting in an increase in FF and PCE.

2.6.4. Power conversion efficiency

Power Conversion Efficiency is the percentage of the maximum power produced by the devices against the power of irradiance from the solar simulator (100 mW cm^{-2}) (seen in *Equation 2.2*).

$$PCE = \frac{P_{Max}}{P_{in}} = \frac{FF \times V_{OC} \times J_{SC}}{P_{in}} \quad (2.2)$$

It is noted that FF, V_{OC} and J_{SC} strongly influence the efficiency of solar cells, with the adjustment and optimisation of these factors to allowing for the production of high-performance OPVs.

2.7. Stability

With interest towards commercialisation of devices, performance is not the only aspect of OPV that require improving. As seen in the diagram below (*Figure 2.5*), OPVs also need to be cost effective to be commercially comparable with silicon solar cells.

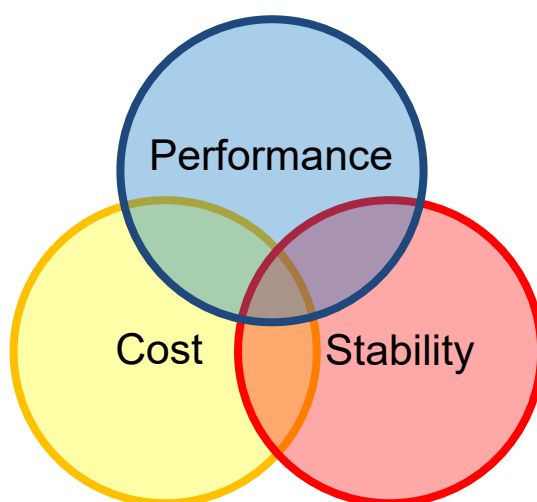


Figure 2.5: Key areas of importance for OPV fabrication.

The other aspect of OPV is the stability, or the lifetime of the devices. For PVs, the lifetime is the time it takes for the performance of the solar cell to reach 80% of its initial efficiency. There are several factors that can lead to the degradation of OPVs and there has been extensive research towards methods and strategies for reducing the effect of said degradation mechanisms. Initially, there is a large performance loss which occurs in a relatively short duration, known as a burn-in process [91]. After the initial burn-in loss, the relatively small degradation occurs with a general linear trend [92].

2.7.1. UV irradiance

Exposure of the OPV to sunlight has been observed to photochemical degradation and photophysical degradation in the active layer, transport layer and active layer/electrode interface. The photochemical degradation occurs due to photo-oxidation of the acceptor and donor materials [93-95].

To reduce the impact from UV irradiance degradation, there are two general strategies: prevention and durability. For prevention, a barrier film can be applied to substrate-side of the solar cells to block UV-radiation from reacting the active layer. With a barrier that is used to “block” UV radiation from reaching the active layer improved photo-degradation. Encapsulation also helped with improving stability of PBDB-T:ITIC organic solar cells [96, 97]

As for durability, photostability of the donor and acceptor materials, the end-groups and sidechains can be modified. Du *et al.* demonstrated that for PBDB-T:ITIC-2F devices, a lifetime of 10 years was achieved with the devices being exposed to 1 sun of irradiance [98]. This was longer compared to devices that had used PCBM and ITIC as an acceptor material.

2.7.2. Oxygen and water

Oxygen has multiple modes of causing device degradation. Firstly, with the combination of UV radiation, the material can undergo photo-oxidation of the active material. With the presence of UV-radiation, the oxygen undergoes the formation of superoxide oxygen anion [93, 99, 100]. These oxygen anions then react with the polymer, with a hydroperoxide formation at the benzylic position [101, 102]. This results in the removal of side chains from the polymer results in the change in photon absorption, energy levels and charge mobility. Lastly, the presence of oxygen in the layer can enhance the hole concentration, resulting in the increase of the density of deeper electron traps, resulting in a decrease in fill-factor and V_{oc} [103, 104].

With the combination of moisture and oxygen, oxidation of low work function metals such as aluminium and calcium metal can lead to a reduction in efficiency [105]. Generally, the reaction of water and oxygen leads to the formation of metal oxide in the metal, creating transport barriers and eventually induces an S-shaped JV-curve and degrades the performance of the device [106].

To prevent oxygen and moisture from interacting with the OPV devices, a common solution is to encapsulate the cell. There are several techniques that can be used for blocking the oxygen and water effectively, with either organic, inorganic or a inorganic-organic hybrid [107]. Another comparison is the stability of OPVs with different acceptor materials. For all-polymer solar cells, they appear to be more stable to moisture when compared with polymer:fullerene devices [108].

Lastly, there is the stability comparison between conventional and inverted devices. Krebs *et al.* observed the difference in oxygen and moisture stability of P3HT:PCBM devices with normal and inverted geometry, implementing aluminium and silver respectively [109]. It was observed that the normal geometry devices were stable under dry oxygen but in-stable under humidity, whereas inverted devices were stable under humidity but not in the presence of oxygen.

2.7.3. Mechanical

With interest towards large-scale R2R fabrication, flexibility (and some stretchability) of OPV is crucial for device fabrication, as such, mechanical straining, including bending and stretching of the device, can result in several areas of defects. Firstly, fracturing can occur at the active layer, interface layer and active layer/transport layer interface [110]. Straining can also occur of the active materials [111]. If fracturing doesn't occur, decohesion process can progress instead, leading to degradation of the active layer and buffer layer [112].

One of the largest sources of mechanical degradation results in the bottom electrode, ITO, a transparent electrode that is known to be expensive to manufacture [113]. As ITO is exposed to mechanical strain, there is an increase in sheet resistance resulting in a decrease in fill-factor and thus, a reduction in efficiency [114].

A replacement material with similar optical transmittance and sheet resistance in achieving similar or improved initial performance for the flexible OPVs is needed. An alternative electrode is the use of PEDOT:PSS, however, it is not quite comparable, resulting in a reduction in performance when compared with devices with flexible ITO [39, 115]. A solution to this is to embed silver nanowires (NW) to improve sheet resistance and mechanical stability [116, 117].

It has been found that using NW for the bottom electrode can pierce through the active layer, resulting in either a decrease in shunt resistance or shorting of the device, massively reducing the OPV performance. Using high transparency planarizing materials over the NW, including ZnO [62], PEDOT:PSS [118] or polyimide [119] can result in the smoothing of the electrode, allowing for the preventing of the NWs from reaching the active material.

2.7.4. Thermal and storage

When operating in real-life conditions, the continuous illumination of the sun results in an increase in working temperature of the OPV. It has been shown that polymers show mobility to some extent, especially if the environmental temperature is greater than their glass transition temperature [120, 121]. The glass transition is when the material goes from a glassy state where the material is frozen in, to a rubbery state, allowing for motion to occur. The heating can also assist towards the aggregation and crystallization of fullerene, which can lead towards thermal degradation [122, 123].

Large crystallisation/aggregation can lead to a reduction in performance as inefficient exciton dissociation can occur and charge transfer decreases as donor/acceptor interface decreases. Lastly, heating of the OPV can also lead to degradation at the active layer/electrode interface [124] and the buffer layer [125] as material diffusion and de-wetting could occur [126, 127].

There are many strategies that have been investigated and implemented for improving the thermal stability of OPV. One method is to increase the glassing temperature, allowing for the active layer to withstand higher temperatures. Increasing glassing transition can occur by modifying chemical structure [128], polymer molecular weight [129], and the thermal treatment of the OPV [130].

It is possible to reduce the effect of fullerene crystallization by using nucleating reagents can improve thermal stability by limiting size of crystals in the active layer [128, 131]. Lindqvist *et al.* demonstrated that the addition of neat fullerene, C₆₀, was able to improve the thermal stability of TQ1:PCBM BHJ, even when heated up to 130 °C, above the glassing transition of the BHJ [132].

For all-polymer devices, photocross-linking to improve morphology and thermal stability is used. The purpose is to bond the polymers together with cross-linkers after obtaining prefer morphology. Feng *et al.* showed for PBDT-TPD-8:PNDI-T-5 with crosslinking lead to the OPVs retaining 86% PCE of it highest efficiency without obvious burn-in loss under 24 hrs at 150 °C [133]. It has also been shown to improve the performance by increasing the fill-factor [134].

Another method proposed is replacing the BHJ active layer with a double-cable conjugated polymer, containing donor and acceptor blocks in one molecule, resulting in the formation of a single-component organic solar cells (SCOSCs). This removes the disadvantages associated with BHJ, allowing for improved photostability and thermal stability [135].

Lastly, the addition of a ternary component to the BHJ has led to an improvement in the thermal stability of the active layer. Pan *et al.* demonstrated that the addition of PC₇₁BM improved the efficiency of PM6:Y6 as it increases the current and allows for optimal morphology [136]. The Addition of N2200 polymer has also shown to increase the thermal stability of PTzBI-2FP:ITIC-4F [137]. The use of an appropriate ternary compound can allow for improved efficiency with an increase in J_{SC}, and improved thermal stability [138].

2.8. Coating and printing techniques for OPV

Another area of importance for the commercialisation of OPV is related towards the development of scalable, and upscaled, coating and printing techniques. Since 2008, several scalable coating and printing techniques have been investigated, focusing on either reducing the performance gap between lab-based cells, large-area cells and even modules, while other groups look towards reducing the complexity and environmental impact of OPV fabrication.

2.8.1. Vacuum and non-vacuum deposition

When discussing coating and printing techniques, they are be broken up into two areas, vacuum-based and non-vacuum-based techniques. As the name suggests, vacuum processes involve techniques that require a high vacuum to perform material deposition. Depending on the material, either thermal evaporation or sputter coating is employed. Materials that are commonly deposited via vacuum deposition include metal oxides (MoO_x [3, 55, 139], LiF [140, 141]) and metal electrodes (Ag [142, 143], Al [144, 145]). These techniques are useful for the deposition of thin film materials (< 50 nm) without exposing the layer to oxygen/moisture which would otherwise result in device degradation. There has also been interest towards the development of vacuum-processed active layers, a method that deposits photoactive organic molecules to form the active layer of the OPV [146-149], yet, with limited success compared to either solution-processed counterparts.

The major issue associated with vacuum-processing is associated with their capital and running cost, requiring complex machinery which leads to high initial costs, as well as high electricity costs due to the amount of energy required to form the vacuum and deposit the materials. In saying that, the high precision and control of deposition thickness cannot be understated when compared with some non-vacuum methods.

Non-vacuum processed (also known as solution-processed) techniques are generally less complex and cost-effective compared to vacuum-processed techniques. To control the thickness of the layers, the concentration, as well as printing/coating conditions can be optimised. Depending on the method, however, some issues with non-vacuum deposition can include the layers being exposed to oxygen/moisture, lack of precise control of layer thickness, material wastage, as well as lack of pattern control. These issues are heavily dependent on printing/coating techniques (as discussed in *Chapter 2, Section 10.4.*), with it being shown that some of these issues can be resolved with post-processing techniques.

In general, majority of small-scale, scalable, and large-scale OPV fabrication incorporate a combination of non-vacuum techniques to deposited layers, depending on layer composition and thickness control. Some literatures have focused towards depositing these materials using non-vacuum processes, with silver paste printing being the most used in these attempts [139, 150, 151]. As for metal oxides, there have been attempts to transfer previously vacuum-processed materials to solution-processed, such as MoO_x [152], to alternative materials, such as SnO_2 [55], V_2O_5 [153, 154] and PEDOT:PSS [151, 155]. It is worth noting that, some literatures have demonstrated the increased scalability of vacuum-based processes that are large-scale roll-to-roll compatible [40, 149, 156].

2.8.2. OPV fabrication scalability via alternative printing and coating techniques

Most papers also compare the scalability of fabrication methods based on the idea that printing/coating techniques can be performed via roll-to-roll fabrication. However, some methods such as sheet-to-sheet, sheets-on-shuttle & and roll-to-sheet, can still yield large scale OPV fabrication, rather than requiring a continuous roll fabrication [157]. Overall, roll-to-roll is ideal for the fabrication of flexible OPV devices, while flat-bed processing is more ideal for rigid OPV devices (such as for windows).

Another important aspect is associated with the scalability of the active area, and the definition of cell vs molecules. Firstly, an active area is defined as the area of the device that is being exposed to the light, resulting in exciton generation. It is common to use small active areas ($\sim 0.1 \text{ cm}^2$) to yield higher performance as it minimises the impact of film defects that would otherwise result in a PCE reduction. For demonstrating scalability, larger active areas ranging from $\sim 1 \text{ cm}^2$, $\sim 10 \text{ cm}^2$ and even above $\sim 100 \text{ cm}^2$ have been employed.

Secondly, a cell is defined by a single OPV device that, when under operating conditions, is not connected to any other PV device (neither in series nor parallel). These cells can range from having an active area of 0.4 cm² [158, 159] to 18 cm² [160], and are commonly used individually to maximise device performance. Lastly, when wanting to demonstrate the efficiency of large-area OPV is with the fabrication of modules, consisting of cells that are connected either in parallel or series (depending on the groups conducting the research). For OPVs, the active area of these modules found in literature can range from 2 cm² [161] to 360 cm² [151].

When discussing literature that is focused on alternative printing and coating methods, it is common to find papers incorporating either “printed” or “fully printed.” For literature with the word “printed” in the title, it has been observed that the term is used from a range from devices that contain one printed layer using an alternative method to spin-coating, to two or three layers having been printed [162]. Also, the printed layer in question is usually the active layer, however, this can also refer to the interface and/or the electrode layer.

As for “fully printed” devices, both the active layer and interface materials are deposited using a non-spin-coating method, however, this can also include OPVs containing an ITO covered substrate and/or an electrode that has been deposited via vacuum deposition [160]. It is also worth noting that the active area does not affect the definition of devices being “printed,” rather, assumed based on coating method implemented. Lastly, some literature that implement coating techniques such as blade and slot-die coating will title their papers as “printed,” even though the techniques themselves are not defined as a printing technique.

2.8.3. Roll-to-roll fabrication

Whenever discussing the upscaling of OPV fabrication, it is important to mention roll-to-roll processing. Usually involving a transparent-flexible substrate, the substrate is fed from one roll to another, with a series of coating processes and pre/post processes interacting with said substrate. For roll-to-roll, it can be defined into two parts, modular and inline (as seen in *Figure 2.7*).

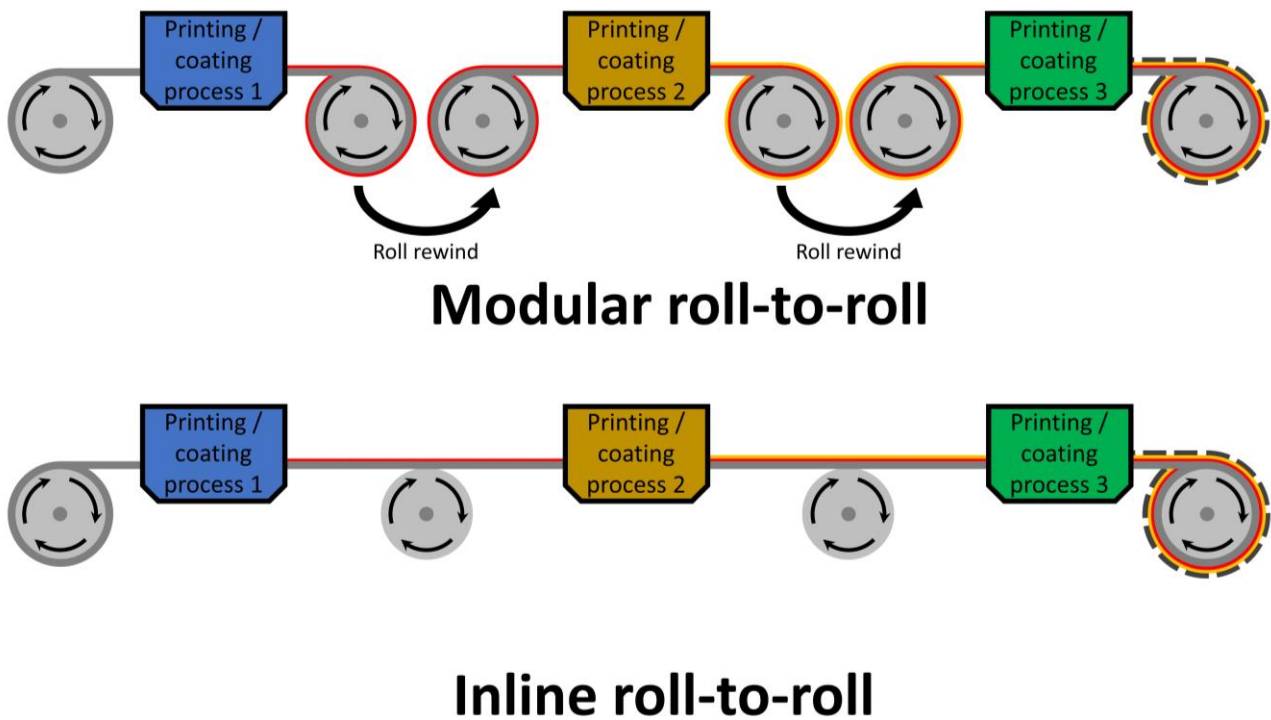


Figure 2.6: Basic schematics of the type of roll-to-roll fabrication procedures.

For modular, a single printing/coating process is conducted during the re-winding of the substrate, resulting in a single thin layer being deposited prior to the rewind of the roll. The advantage of this method is that it is incorporated in small-scale OPV fabrication, while only requiring a medium amount of lab space. This method also allows for optimised coating conditions to be implemented during each layer deposition. The only noted issue with the technique is that the fabrication time is greatly increased, due to the time taken to setup for the next deposition process. A few groups have employed this method of roll-to-roll [96, 151], being more suitable for laboratory conditions.

As for Inline roll-to-roll fabrication, multiple coating processes are conducted on a single wind of the substrate (seen in *Figure 2.6*), allowing for the reduction of overall fabrication time, thus, making favourable for commercial conditions. One setback is that the winding speed is required to be the same for all coating processes, which may be an issue if the optimal coating is not the same for all material depositions. This technique has been performed by a few research groups during the past decade [163, 164].

2.8.4. Types of printing and coating methods

In the past 15 years, there has been a significant increase in effort towards the development and implementation for printing and coating techniques that not only allow for the fabrication of high performance OPVs, but also devices with large active areas, minimal film defects and reduced manufacturing costs. As such, there are several methods that have been shown to be key towards solving this goal, each with their own benefits and challenges.

In this section, several types of solution-processed printing and coating technique will be investigated, highlighting past and current developments, and their popularity in the OPV field. When discussing the pattern control of printing and coating conditions, coating methods are only able to adjust the film thickness (zero-dimensional) or both strip width and thickness (one-dimensional), whereas printing can form patterns along the XY-plane, as well as thickness (two-dimensional).

2.8.4.1. Spin-coating

Spin-coating is a zero-dimensional, non-roll-to-roll compatible coating method that requires spinning a substrate at high speeds (1000 to 5000 rpm) to allow for the formation of thin films (seen in *Figure 2.7*). The ink can be placed on the spinning substrate either before or during the spinning process. The thickness of the film can be controlled by adjusting spin speed, acceleration, coating time and solution concentration. Due to the simplicity of the method for producing small-scale devices, it is one of the most common methods employed in labs to fabricate OPVs. This method has also yielded the highest efficiency OPVs when compared to other coating methods [1, 165-167]. The major issue is that with this method the ability to be upscaled is limited, due to the reduction in layer thickness as you move away from the centre of the substrate [163, 168]. Due to the efficiencies achieved by this process, it is used a scale comparison for other printing/coating methods.

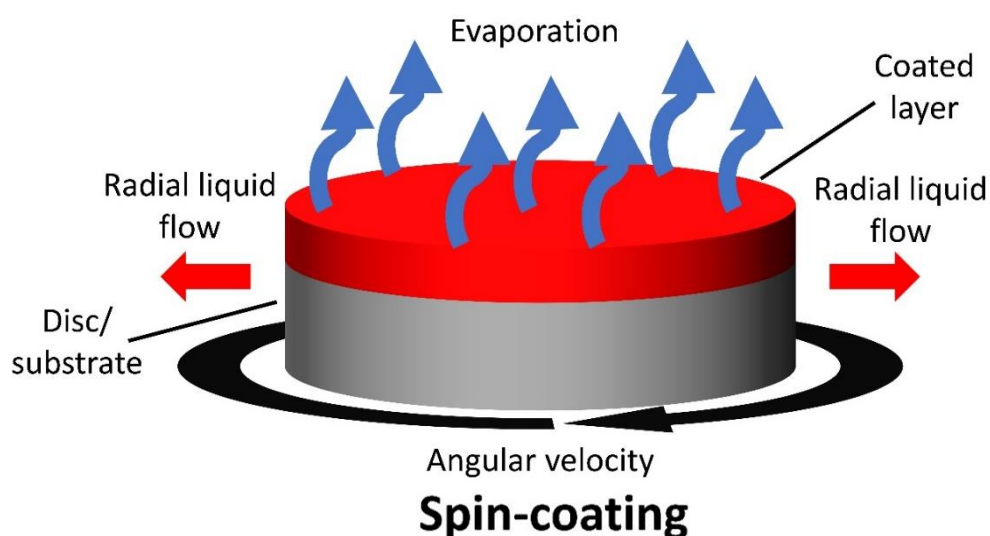


Figure 2.7: Basic schematic of spin-coating. Adapted from Krebs, 2009 [168].

Owing from its simplicity as a coating method, and ability to fabricate high performing devices reproducibility, a wide range of materials have been processed using this technique, several active layer blend combinations (i.e., P3HT:PCBM [169-171], PBDB-T:ITIC [172-174], PM6:Y6 [24, 175, 176]), electron transport layer (i.e., ZnO [177, 178], AZO [179-181]), and hole transport layer (i.e. PEDOT:PSS [182, 183], V₂O₅ [68]). To date, the highest efficiency for a single junction OPV that has been achieved was $19.3 \pm 0.1\%$, with the device using PM6:D18:L8-BO as the photoactive materials [1].

Overall, spin-coating is one of the most common coating methods used in OPV research due to its reproducibility and ability to achieve high device performances. Despite the lack of scalability, spin-coated devices are still useful for comparing with scalable and large scale OPVs, as well as in the research of novel materials, processing, and ink preparation.

2.8.4.2. Rod coating

Rod coating is a zero-dimensional, contactless coating method, which works by forming a meniscus between the rod and substrate from the coating ink (seen in *Figure 2.8*). The coating occurs as either the rod or substrate moves, resulting in ink removing from the meniscus. From an extensive exploration of literature, it was found at least one attempt had been made using rod-coating for active layer deposition, with P3HT:PCBM being the active layer blend yielding an efficiency of $1.9 \pm 0.4\%$. All other applications of the technique have been used for silver nanowires (AgNW) [184], with the application aiming towards ITO-free substrates.

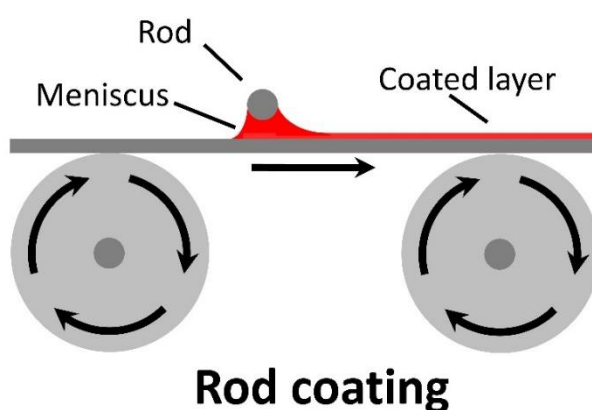


Figure 2.8: Basic schematic of Rod coating. Adapted from Søndergaard *et al.*, 2012 [185].

Although this technique is relatively simple to operate and automate, rod coating has seen little interest as a meniscus-based coating method, especially when compared to blade-coating and slot-die coating (to be discussed later).

2.8.4.3. Blade coating / Knife-over-edge coating / Doctor blading

Blade coating is a zero-dimensional, contactless coating method that has minimal ink wastage and roll-to-roll compatible. A build-up of ink on one side of the blade allows for the formation of a meniscus, where the thickness can be adjusted by controlling substrate speed and blade-substrate gap (seen in *Figure 2.9*).

For the final dry thickness of the blade-coated film (d), it can be calculated from the following equation (*Equation 2.3*):

$$d = \frac{1}{2} \left(g \frac{c}{\rho} \right) \quad (2.3)$$

Where g is the gap distance between the blade and substrate, c is the concentration of the solid material in the ink (g cm^{-3}), and ρ is the material density in the final film (g cm^{-3}).

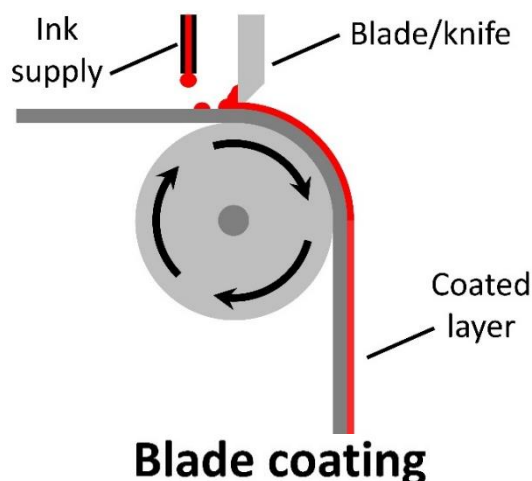


Figure 2.9: Basic schematic of blade coater. Adapted from Søndergaard *et al.*, 2012 [185].

Blade coating is one of the simplest methods for scalable and large-scale coating, only requiring a method for moving a substrate, a blade, and a method introducing ink between the blade and substrate. Due to its simplicity and ease-of use, it has gained interest towards large-scale fabrication, with many groups interested in the method.

Due to the simplicity, low installation, and operational cost, as well as ranging in varied sizes, blade coating is one of the most employed methods for scalable OPV fabrication. The disadvantage of this method is, besides controlling thickness, patterns are unable to be formed without employing an etching method (manual [141, 186], chemical [60, 187], laser etching [3, 188, 189]). This makes blade coating not ideal for electrode coating, however, there is literature where they have coated electrodes at a small scale [190]. The other downside is this technique is more suitable towards flat-bed processing, resulting in majority of research using rigid substrates [66, 142, 186, 189-198], yet, it has been demonstrated that flat-deposition on flexible substrates is possible [139, 188, 199].

Despite these limitations, there has been extensive research towards reducing the performance gap between blade coating and spin-coating [142, 196, 197, 199], as well as device fabrication to higher active areas. To improve coating quality, uniformity, and morphological control of the active layer, there have been several examples of the implementation of in-situ annealing [141, 186, 189, 190, 194, 200-202], as well as the use of hot air upon deposition of the film [141, 186]. These methods have allowed for the fabrication of OPVs to extend not just past 1 cm² [188, 198], nor past 10 cm² [3, 189, 197], but beyond 100 cm² [3, 141, 186]. Though some blade-coated OPVs are prepared under nitrogen [192, 194-196] and argon [142] conditions to allow for the best performance possible, a vast majority fabricate the devices under ambient conditions [188-190, 192, 193, 198, 199, 202].

In terms of number of layers printed or coated using alternative techniques, the majority of literature focus on only one layer, usually the active layer, with the remaining having either been spin-coated or deposited via vacuum-based processes [142, 189, 194-198, 201].

Though, there have been successful demonstrations of multiple layers being blade coated, specifically the coating of 2 [189, 197, 203] or 3 layers [139, 186, 188], and even all-printed devices [190].

With the versatility that has been shown with blade coating, there have been an array of active layer materials that have been coated with this method, including, but not limited to, P3HT:PCBM [158, 159], PCDTBT:PC₇₁BM [199, 204], PBDB-T:ITIC [172] & PTB7-Th:PC₇₁BM [66]. This has allowed for performances to reach as high as 15.7% using “PV-X Plus”, with an active layer of 0.04 cm² [189]. There has also been interest toward fabricating large-scale device using blade coating, reaching an efficiency of 12.6 % with an active area of 194.8 cm², when using active materials of PM6:Y6:PC₆₁BM. This performance is much lower than the 16.2% reached when using spin-coating of the same materials [205].

These higher performances can be contributed towards the use of more suitable solvents [142, 158, 195, 196, 198, 200, 206], solvent additives [142, 172, 194, 202, 206], ink preparation strategies [193, 201, 203] and ternary blend combinations [199]. There has also been interest towards implementing active materials that are more suitable towards blade coating, rather than those that perform better for spin-casting, with more such materials like PBDB-T:ITIC appearing to achieve better performance when blade coated, when compared their spin-coated counterparts [172, 198].

Other layers that have been demonstrated to be coated include hole transport layer (i.e. PEDOT:PSS [190]), electron transport layer (i.e. ZnO NPs [190, 193]) and electrodes (i.e. Silver [207], Silver nanotubes [190, 193]). Other work that has been conducted by blade-coated OPVs include methods for improving stability [172, 188, 189, 197], the development of OPV for indoor applications (a.k.a. light recycling) [188], ink preparation via halogen-free/environmentally friendly processing [198], and coating of active layer nanoparticles [192].

Overall, there are some groups that use blade coating to demonstrate the upscale printing, while other groups use blade coating as a step towards upscale roll-to-roll, usually then performing either roll-to-roll or MRC slot-die coating [188]. While others are using blade coating as the first step away from relying on spin-coating as a fabrication process. Blade coating is also a viable coating method for scalable OPV fabrication for rigid substrates via flat bed. This technique seems to struggle for roll-to-roll fabrication methods.

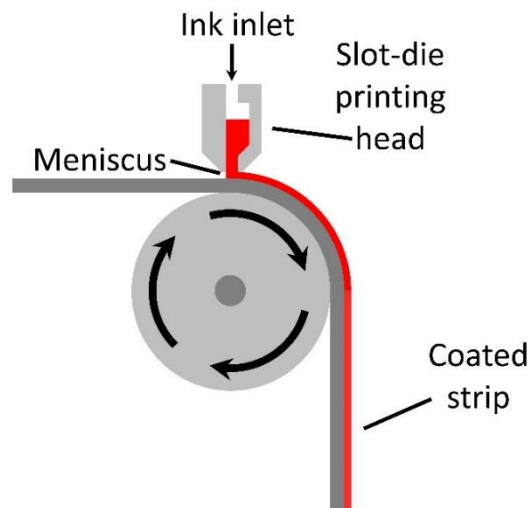
2.8.4.4. Slot-die coating

Slot-die coating is a one-dimensional, contactless coating method, which works by constantly supplying inking into a meniscus formed between the slot-die and substrate. Unlike with blade coating which coats the entire surface, the slot-die can control the meniscus width, allowing for the coating of strips with a defined width.

The slot-die itself is relatively simple in design, with the ink being fed into a reservoir, before flowing down to the meniscus (seen in *Figure 2.10*). As the input of ink is controlled, there is a minimal wastage of ink. Unlike blade coating, where post-processing is required to form strips, the slot-die can control the meniscus width, allowing for the in-situ formation of strips throughout the printing process. For a given web, ink flow rate, coating width and solid concentration the final dry film thickness (d) can be estimated as follows (*Equation 2.4*):

$$d = \frac{f \cdot c}{S \cdot w \cdot \rho} \quad (2.4)$$

where d is the thickness in cm, f is the flow rate in $\text{cm}^3 \text{min}^{-1}$, S is the web speed in cm min^{-1} , w is the coated width in cm, c is the solid content in the ink in g cm^{-3} and, ρ is the density of the dried ink material in g cm^{-3} .



Slot-die coating

Figure 2.10: Basic schematic of slot-die coating. Adapted from Søndergaard *et al.*, 2012 [185].

With a similar case to blade coating, slot-die coating is a relatively simple method that is easily scalable, from rigid devices on a flat-bed [55, 59, 96, 161, 191, 208-212], to scalable devices coated from a mini-roll coater (MRC) [145, 161, 210, 211, 213-215], and even up to scalable and large-scale roll-to-roll fabrication [59, 60, 96, 109, 143, 151, 155, 162, 163, 188, 216, 217]. With the variety of web-movement methods (flat-bed, MRC, roll-to-roll), it allows more easier transition between scales; from the fabrication of small-scale to scalable [61], as well as scalable to upscaled [213] OPV devices. This variability of scale has allowed for the fabrication and testing of OPV devices with increasing active areas, some reaching above 1 cm^2 [143, 188, 209, 213-215, 218], 10 cm^2 [144, 151, 155, 161, 163, 211] and even above 100 cm^2 [109, 151].

With the increased interest towards slot-die coating, primarily of the active layer, there has been investigations into ways to improve the OPV devices performances, from the selection of appropriate solvents and solvent additives [143], solvent post-annealing [162], as well as the implementation of materials more suitable for slot-die coating [61]. There is also interest towards using more environmentally friendly solvents with minimal loss to device performance [161].

One method that has seen increased interest for this technique is hot-deposition, a method for controlling morphology and printing quality by heating up the slot-die and/or substrate during deposition. Though a common method for MRCs, it has been demonstrated to allow for coating without the use of high-boiling point / low vapour pressure solvents, while also shown to be R2R compatible via a bench-sized R2R coater [59].

The highest efficiency achieved using this process of constructing the active layer was 13.5% with an active area of 0.1 cm², using PTB7-Th:PC₇₁BM:CO98DFIC [144], while the largest area attempted was 360 cm² with an efficiency of 1.18% using P3HT:PC₆₁BM [151]. The majority of literature focuses on the slot-die coating of the active layer [61, 63, 217], while some literature also uses slot-die coating of the bottom and top interface layer [143, 213, 216]. A minor amount of literature has demonstrated coating of the bottom and top electrodes by utilising this technique. Recently, there has been a shift towards high performance active materials, such as PM6:Y6 and their derivatives [55, 161, 210].

It is worth noting that a vast majority of devices that have been investigated are fabricated over a flexible substrate [59, 60, 161, 162, 211, 212, 215, 217, 218], with a small percentage over a rigid substrate [55, 59, 161, 191, 208-210]. This can be contributed to the higher complexity when compared to blade coating, even with the ability to form controlled widths without post-processing, blade coating has demonstrated the ease these processes are to conduct on flat-bed devices. Also, several groups have demonstrated the ability to use slot-die coating under ambient conditions, both on rigid [208, 210] and flexible substrates [60, 145, 214].

Other areas of interest for slot-die coated devices include methods for improving stability [59, 145, 155, 161, 208], fabrication of indoor-based OPVs [60, 63], using ITO-free substrates [96, 212, 214, 215], the formation of a ternary active layer [209], device encapsulation [155], and alternative coating methods, from sequential deposition of the active layer [209], to the use of differentially pumped slot-die coating [216].

In summary, slot-die coating has been demonstrating as a viable method of active layer and interface layer coating, with the aim towards the fabrication of flexible OPV cells and modules, especially when implemented to roll-to-roll fabrication.

2.8.4.5. Spray coating

Spray coating is a contactless, zero-dimensional coating method where a continuous spray of ink is atomised into spray that is directed towards the substrate's surface. By pushing the ink through a nozzle with the use of a nitrogen/argon/oxygen gas, ink is ejected to free space and to the substrate (seen in *Figure 2.11*). The thickness can be adjusted by increasing spray amount or reapplying layers.

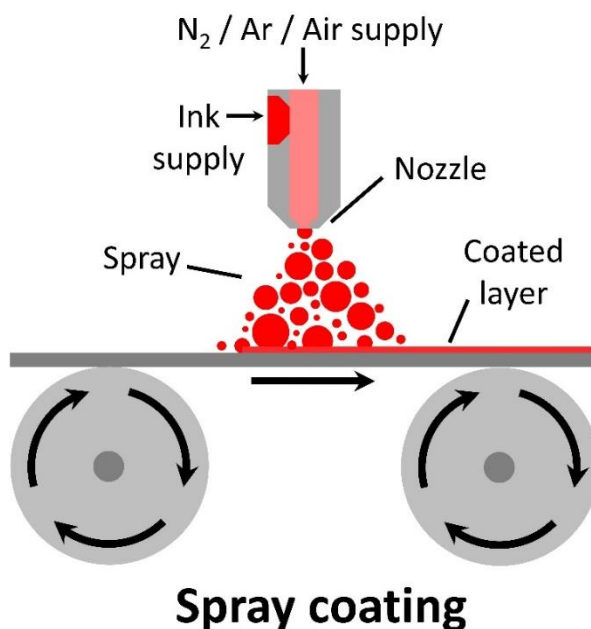


Figure 2.11: Basic schematic of spray coating. Adapted from Søndergaard *et al.*, 2012 [185].

To allow for a uniform coating during deposition, several papers have incorporated ultrasonic nozzles [219, 220], allowing for a reduced droplet size without reducing the high pressure gas that would allow for large area deposition [221]. Another method that has been demonstrated in acoustic vibration of the substrate during deposition [219], is in-situ annealing [220, 222, 223]. Spray coating has been used to process several active layer blend combinations (i.e., P3HT:PCBM [224-227]), electron transport layer (i.e., ZnO [225, 228], PEIE [154]), hole transport layer (i.e., PEDOT:PSS [225, 229], V2O5 [154]) and even AgNWs used as an electrode [228].

From 2010 to 2015, there was a lot of interest in this coating technique, especially towards improving the spray quality to allow for a uniform thin film. Since 2015, however, there has been less interest while other coating techniques gained popularity. As of 2017, the highest efficiency achieved using this process of the active layer 7.3%, p-DTS(FBTTh₂)₂:PC₇₁BM [229], while the large active layer attempted was in 2018 with P3HT:PCBM, having achieved 2.4% with an area of 4 cm². Even though there have been devices that have been made with an active area larger than 1 cm² [225, 226], there has been very little research done to fabricate devices utilising a larger active area.

From the assessment of literature, the majority of device fabricated OPV via spray coating only focus using the technique to deposit the active layer only [219, 220, 222, 224, 226, 227, 230, 231], with the rest of the layers either being spin-coated or deposited via vacuum-based processes. Only a few papers have implemented spray coating for the film formation of 2 [229, 232] or 3 layers [154]. It is also worth noting that the majority of devices using this technique were fabricated on a rigid substrate [220, 223, 226, 229], with only one paper, to date, demonstrating the deposition over a flexible substrate [226].

For spray coating, the areas that have been focused on, outside of the influence of the active layer, includes ITO-free device fabrication [154, 228, 232], improving light degradation [229], producing all spray coated devices [225, 228] and printing on uneven surfaces such as textiles [228]. Other areas also include the formation of bilayers in the active layer region by the implantation of “dry spray-coating” [233], and the use of s-MoO₃ nanoparticle ink [66].

Even though there are a variety of implementations for spray coatings in OPV fabrication, it has not reached the same success as other non-contact coating methods, such as blade or slot-die coating. This can be contributed to the large amount of material wastage, resulting in groups using cheaper yet lower performing materials to produce devices. Despite this, there is continued interest in this technique due to its versatility and ability to coat thin films on uneven surfaces.

2.8.4.6. Inkjet printing

Inkjet printing is a 2-dimensional printing method that can easily control the thickness and can be adjusted by either re-coating over the same area or increasing the rate of ink deposition during printing. Unlike spray coating that covers a large area simultaneously, the ink produces ink droplets that follow a relatively linear path towards the substrate (seen in *Figure 2.12*), allowing for fine control of area being coated, as well as reducing the amount of ink wastage being produced.

There are two main types of inkjets that have been employed for OPV fabrication: piezoelectric (a.k.a. Droplet on demand, DOD) and continuous inkjet. For DOD inkjet printing, a piezoelectric pump is used to produce droplets when over a position that requires ink deposition, whereas the continuous inkjet has a continuous flow of ink drops, where the deposition is controlled with deflector plates, allowing the illusion of the inkjet stopping and starting [202].

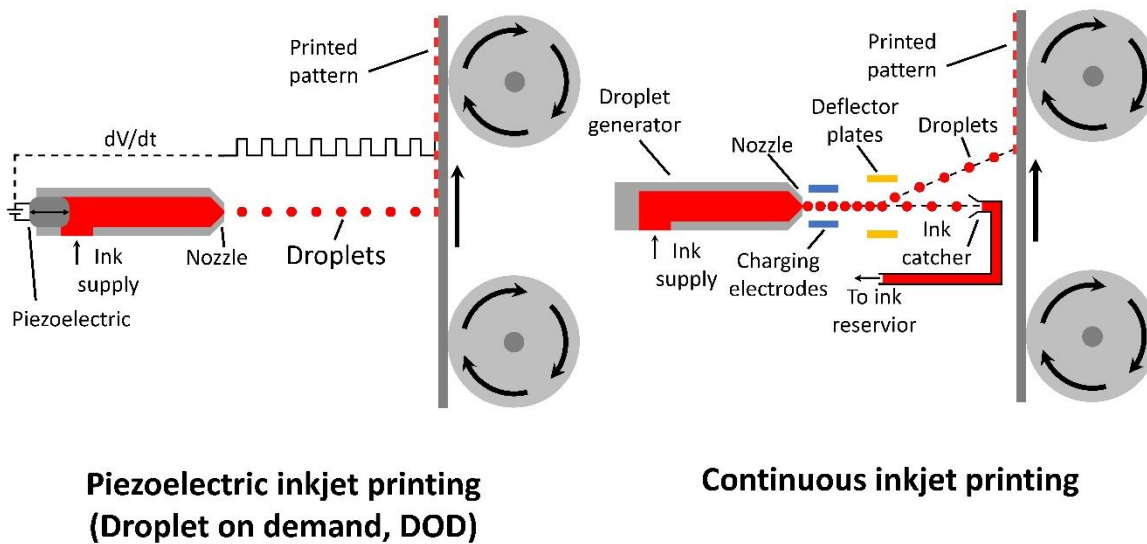


Figure 2.12: Basic schematic of two types of inkjet printing, Piezoelectric (LEFT) and continuous (RIGHT) [185].

The final dry thickness of the inkjet-printed films (d) can be determined based on the number of droplets (N_d) delivered per area (cm^{-2}), the individual droplet volume (V_d), as well as the concentration (C) and density (ρ) of the solid material ink the ink, with the equation as follows (Equation 2.5):

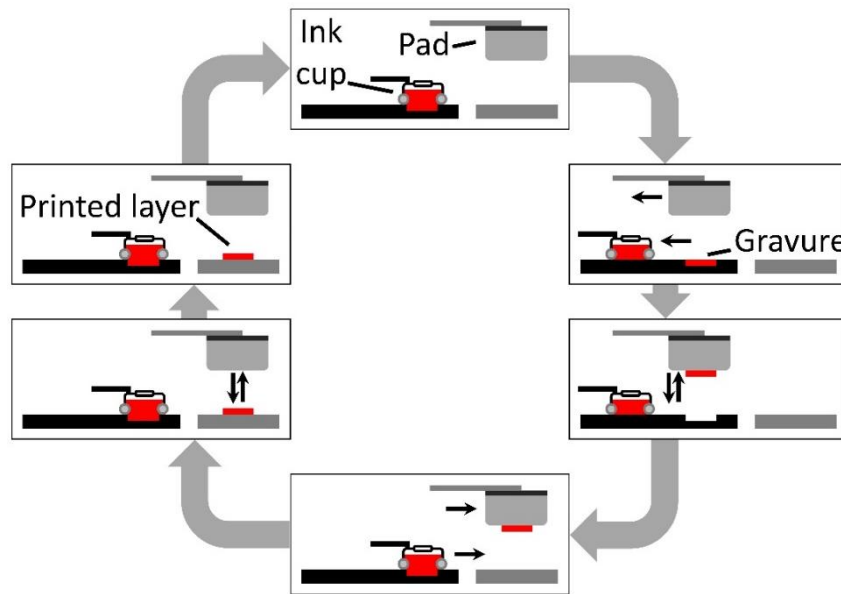
$$d = N_d V_d \frac{c}{\rho} \quad (2.5)$$

Though there has been some interest towards employing inkjet printing towards high performance OPVs, reaching up to 7.3% PCE using p-DTS(FBTTh₂)₂:PC₇₁BM [234], P3HT:PCBM blend devices still take up a good amount of devices fabricated with this method [235-237]. The highest efficiency with an upscaled active area of 1 cm² was reached up to 4.7% using “Activlink PV2000”. Due to the ability to form patterns using printing, there is a relatively even distribution by way of using inkjet printing of the active layer, interface, and electrode deposition. Other materials that have been deposited by inkjet printing include transport/interface materials, such as PEDOT:PSS [192, 238] and ZnO [192, 236], as well as electrodes, including Ag [239, 240] and Ag NWs [241].

Due to the printing web speed, it will be difficult for the technique to compete with faster printing and coating methods, especially when coating the active layer, however, there is still interest towards high-resolution printing, especially for sheet-to-sheet device fabrication, as well as small-scaled printing where minimal wastage is a necessary required for reducing manufacturing cost.

2.8.4.7. Pad printing

Pad printing is a two-dimensional, contact-based printing method that implements a pad to collect ink from a gravure and transfers it to a substrate. As seen in Figure 2.13, a gravure is filled from the ink cup with ink, prior to a pad picking up the ink and transferring it to a substrate.



Pad printing

Figure 2.13: Basic schematic of pad printing. Adapted from Krebs *et al.*, 2009 [242].

The final dry thickness of the deposited film can be calculated based on the volume of ink contained in the gravure per unit area (V_g) ($\text{cm}^3 \text{m}^{-2}$), the concentration of solid material in the printing ink (c) and the material density of the dry film (ρ) (seen in *Equation 2.6*):

$$d = V_g k_p \frac{c}{\rho} \quad (2.6)$$

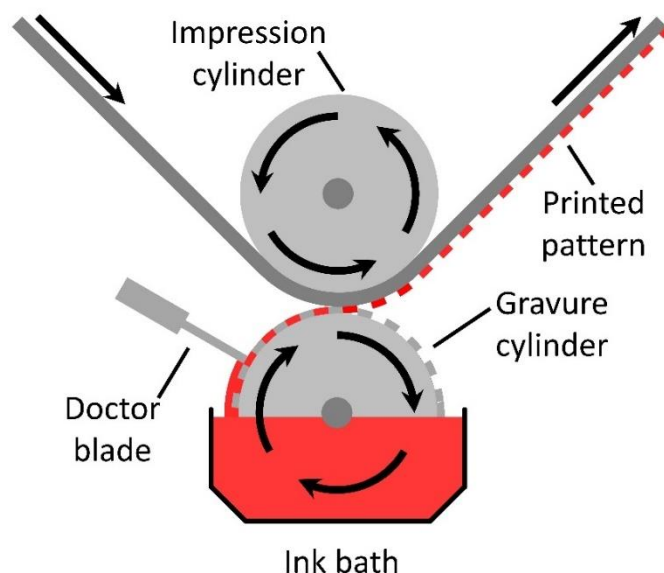
It is worth noting that the pickup and deposition of the ink from the pad is not always complete, resulting in a reduction in the expected dry film thickness. As such, a constant (k_p) is associated with the thickness equation.

So far, there has only been one pad to demonstrate pad printing for the fabrication of OPV devices, with the results having been published by Krebs *et al.* 2008, with the printing of the P3MHOCT + Zinc resulting in an efficiency of 0.07% [242]. Due to the complexity of the printing method instrumentation, the pad coating method has seen little interest for both small-scale and large-scale OPV fabrication, especially with the existence of better printing and coating systems that are available on the market.

2.8.4.8. Gravure printing

Gravure is a contact-based, two-dimensional coating method, with the pattern forming from the ink within the cavities of the engravings. The basic version of printing method has the ink being withdrawn from an ink bath, with any excess ink being removed via a blade. A substrate is then fed between impression cylinder and the ink-covered gravure roll to imprint a patterned coating (seen in *Figure 2.14*). As such, this technique relies on the surface energy of the substrate to remove the ink from the cavities as the web is brought into contact with the cylinder.

Both the thickness and shape of the printed layer is dependent on the engraved pattern and depth of the cavities of the cylinder, making it difficult and costly to optimise the coating thickness, however, some papers have shown that with adjustment of the blade against the gravure cylinder can influence amount of ink deposited [243-246]. The quality of printing is dependent on the ink rheology, web/substrate speed, as well as the pressure between the impression cylinder and gravure cylinder against the cylinder.



Gravure printing

Figure 2.14: Basic schematic of Gravure printing. Adapted from Søndergaard *et al.*, 2012 [185].

For the past 10 years, gravure printing has been demonstrated to be compatible for roll-to-roll printing of OPVs [245-247], having printing transport layers such as ZnO, ZnO NP or ZnO:PEI [244, 247], PEDOT:PSS [200, 245, 246], as well as active layer printing. Initial work was based on P3HT:PCBM devices [243], however, has expanded to more moderate performing materials, such as PTB7-Th:PC₇₁BM devices [247].

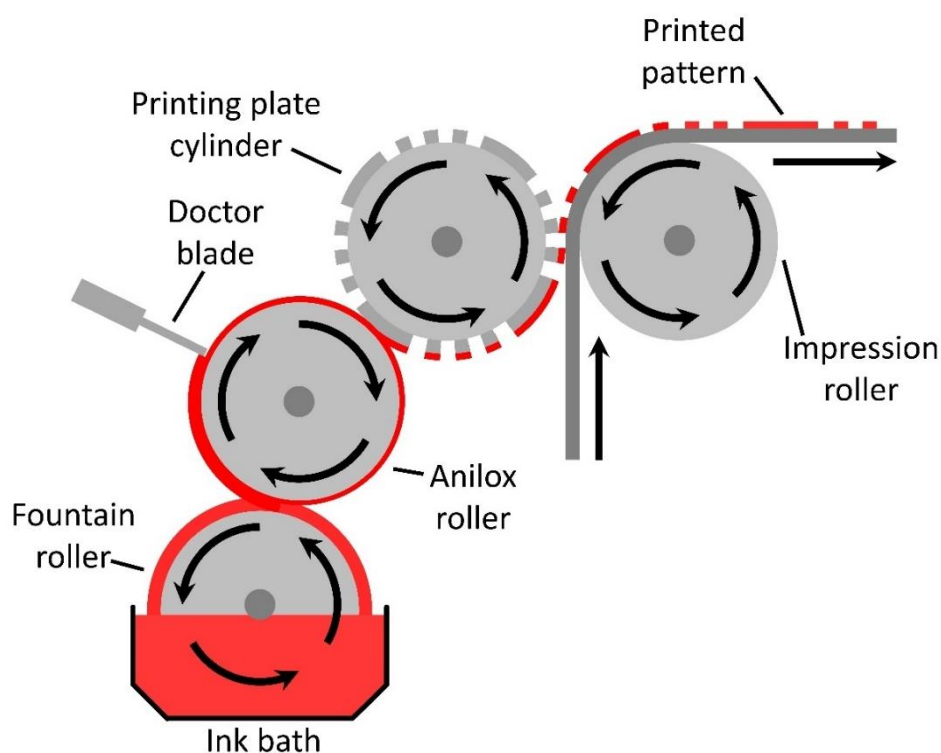
Though there was a lot of interest in the 2010's, there has been less literature focused on improving the method, generally due to the amount of material used in the method. As such, devices mostly used P3HT:PCBM active material for the OPVs.

Despite this method being roll-to-roll compatible, the technique is difficult to down scale, and there is a large amount of material waste, making it less desirable for lab-scale device fabrication. It is also worth noting that the method has seen more devices made with flexible substrates [200, 243-245], with very few performed (if any) on rigid substrates. Some work that has been focused on gravure printed devices include optimising the plate and grid sizing, improving mechanical stability [244, 245], and optimising conditions to reduce the gap between gravure and spin-coated devices [245, 247].

Based on the number of papers, gravure had peaked in interest towards printing of the active layer around 2017 [247, 248], however, we have seen that interest decay as of late. Several factors including difficulty to use in small-scale fabrication, potential material wastage, and more focus on blade and slot-die coated active layer research, has made this method less desirable for OPV research of high-performance devices. Despite this, there has still been interest towards gravure-printing of the ZnO:PEI and ZnO as the bottom interface for inverted OPVs [243, 244, 249].

2.8.4.9. Flexographic printing

Flexographic is another two-dimensional, contact-based printing method that has direct contact with the substrate. Unlike gravure printing that relies on filling engravings with ink, flexographic printing has the ink being deposited from patterned plates from the cylinder. To achieve this via roll-to-roll fabrication, a foundation collects ink from an ink bath and deposited it onto an anilox roll. To control the wet thickness, a doctor blade can be used. The ink is then transferred onto the printing plate cylinder before being deposited onto a substrate that is pressed against the printing plate and impression roll (seen in *Figure 2.15*). This method can be down scaled for the implementation on a mini-roll coater, with the mini-roll acting as the impression roll, while the deposition of the ink onto the printing plate cylinder occurring manually [214, 250].



Flexographic printing

Figure 2.15: Basic schematic of flexographic printing. Adapted from Søndergaard et al., 2012 [185].

Based on the properties flexographic printing relies on, this method allows for the printing of inks that have higher viscosity, unlike gravure that relies on low viscous inks. This has allowed this printing method to be commonly used for the printing of electrodes of ITO-free OPVs [139], with the most common material being silver-based paints [163, 214, 215, 251, 252]. This Technique has also been used for the printing of the electron transport layer (ZnO) and active layer containing PCDTBT:PC₇₁BM [139].

Other research that has been conducted for this technique include improving printing by improving pre-wetting techniques [163], patterning optimisation to improve resolution [253, 254] and adjusting ink preparation and printing temperature [255]. Though, a significant amount of research is aimed at flexible electronic devices, rather than focusing on OPV device fabrication.

Like gravure printing, due to the large amount of ink wastage, complexity and the difficult to performance small-scale fabrication, there has been minimal amount of interest from the OPV community to investigate this technique. Despite this, the method is still used for scalable ITO-free OPV device fabrication.

2.8.4.10. Screen printing

Screen printing is a contact-based, two-dimensional printing method where ink is forced through a patterned screen with the use of a squeegee, resulting in the ink deposited onto the waiting substrate below (seen in Figure 2.16). Unlike flexographic and gravure printing, screen printing allows for the formation of thicker films, making it ideal for printing of electrodes. As to date, there are two major methods of screen printing implemented in OPV fabrication, flat bed (small-scale) and rotary (large-scale). For the flat-bed, ink is based over a flat, patterned screen, allowing for the sheet-to-sheet patterning of flat substrates [123, 256, 257]. As for rotary, the patterned screen is shaped into a roll, with the squeegee and ink positioned inside, making it ideal for roll-to-roll device fabrication [163, 258].

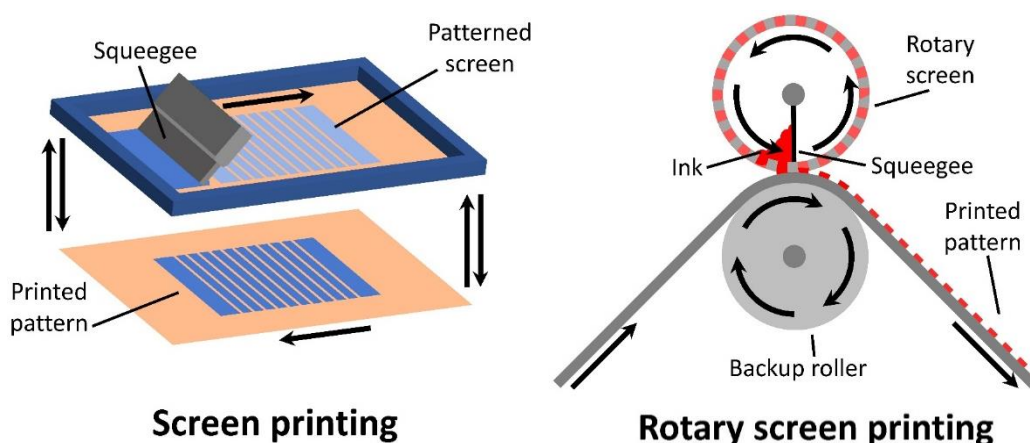


Figure 2.16: Basic schematic of screen printing, specifically flatbed and rotary. Adapted from Søndergaard *et al.*, 2012 [185].

The final dry thickness of the film (d) can be determined based on the assumed amount being partially by the screen (V_{Screen}), the pick-out ratio (k_p), the concentration of the solid material in the ink (c), and the dry film density (ρ) (seen in Equation 2.7):

$$d = V_{Screen} k_p \frac{c}{\rho} \quad (2.7)$$

There is not much literature that primarily focuses the application of screen printing, with those that do having printed PEDOT:PSS over the active layer [256], the active layer only [259], or the Ag grid on top of ITO and the active layer [123]. For devices with an active layer deposited via screen printing, the highest efficiency achieved was of 2.4% with an active area of 3 cm², having an active material of P3HT:PCBM [259]. Little investigation has been done into screen printing as a method for active layer coating, however, it has become one of the most common methods for scalable and upscale deposition of electrode, for both top [163] and bottom [123, 258, 260], as well as the transport layers [212, 256, 258]. Screen printing is also commonly depositing an etching solution over ITO-covered PET, allowing for the patterning of the substrate prior to device fabrication [139, 163, 199, 203].

With the existence of both flatbed and rotary screen printing techniques, it has allowed for screen printing to be demonstrated to deposit films over rigid [258, 259] and flexible substrate [123, 257]. Despite the lack of interest towards active layer deposition using screen printing, the technique has still found use for patterned electrode printing, for both flatbed and rotatory screen. This has allowed for the technique to be a significant technique, especially for device fabrication that is moving away from vacuum-based processes.

2.8.5. Printing and coating method comparison

As seen so far in this chapter, there is quite an extensive array of printing and coating techniques that have been shown to work successfully towards the fabrication of OPVs, however, some techniques have seen more success in publication numbers than others due to a multitude of factors. For an in-depth comparison of the printing and coatings techniques, *Table 2.1* was prepared, comparing device architecture, printing/coating methods implemented, active area and device performance. This section will also relate the summary of literature with the technical comparison of printing and coating techniques (seen in *Table 2.2*), adapted from Krebs *et al.* 2009 [168].

Table 2.1: List of literature summary, including device architecture, which layers are printed, device area and device performance.

Method	Year	Device structure	Printed layers	Area (cm ²)	Performance (%)	Cell or module	Author
Blade	2009	Glass/ITO/PEDOT:PSS/P3HT:PCBM/Ca/Al	P3HT:PCBM (Blade)	0.04	3.8	Cell	[158]
	2011	Glass/ITO/PEDOT:PSS/P3HT:PCBM/LiF/Al	P3HT:PCBM (Blade)	0.167	1.9	Cell	[206]
	2012	Glass/ITO/PEDOT:PSS/POD2T-DTBT:PC71BM/Al	POD2T-DTBT:PC71BM (Blade)	0.04	6.49	Cell	[159]
	2014	Glass/ITO/PEDOT:PSS/pDPP5T-2:PC61BM/ZnO-NP/Ag	PEDOT:PSS, pDPP5T-2:PC61BM & ZnO-NP (Blade)	0.104	3.96	Cell	[190]
	2014	Glass/AgNW/PEDOT:PSS/pDPP5T-2:PC61BM/ZnO-NP/AgNW	AgNW, PEDOT:PSS, pDPP5T-2:PC61BM & ZnO-NP, AgNW (Blade)	0.104	2.89	Cell	[190]
	2014	Glass/ITO/PEDOT:PSS/PTB7:PC61BM/Ca/Al	PTB7:PC61BM (Blade)	-	3.61	Cell	[200]
	2015	Glass/ITO/ZnO/pDPP5T-2:PC71BM/MoO ₃ /Ag	pDPP5T-2:PC71BM (Blade)	-	6.3	Cell	[195]
	2015	Glass/ITO/PEDOT:PSS/POD2T-DTBT:PC71BM/LiF/Al	PEDOT:PSS, POD2T-DTBT:PC71BM (Blade)	108	3.45	Module	[141]
	2016	Glass/ITO/ZnO/PBDT-TSR:PPDIODT/MoO ₃ /Al	PBDT-TSR:PPDIODT (Blade)	0.069	5.07	Cell	[194]
	2016	Glass/ITO/ZnO/PBDT-TSR:PC71BM/MoO ₃ /Al	PBDT-TSR:PC71BM (Blade)	0.069	8.02	Cell	[194]
	2016	Glass/ITO/ZnO/P3HT:IC60BA/PEDOT:PSS/Ag	ZnO, P3HT:IC60BA & PEDOT:PSS (Blade)	0.1	3.9	Cell	[192]
	2016	Glass/ITO/ZnO/P3HT:IC60BA/PEDOT:PSS/Ag	ZnO, P3HT:IC60BA & PEDOT:PSS (Blade)	1.1	3.4	Cell	[192]
	2017	Glass/ITO/ZnO/P(T3-TPD):PC71BM/MoO ₃ /Ag	P(T3-TPD):PC71BM (Blade)	0.07	5.40	Cell	[142]
	2018	PET/ITO/ZnO/PCDTBT:PC71BM/MoO ₃ /Ag	ZnO & PCDTBT:PC71BM (Blade)	1	4.3	Cell	[139]
	2018	PET/ITO/ZnO/PCDTBT:PC71BM/MoO ₃ /Ag	ZnO, PCDTBT:PC71BM & VO _x (Blade). Ag (Flexography)	1	1.9	Cell	[139]
	2018	ITO/ZnO/PBDB-T:ITIC/MoO ₃ /Al	PBDB-T:ITIC (Blade)	-	10.03	Cell	[172]
	2018	Glass/ZnO NP/P3HT:IDTBR/PEDOT:PSS/Ag NWs	ZnO NP, P3HT:IDTBR, PEDOT:PSS & Ag NWs (Blade)	0.1 04	5.25	Cell	[193]
	2018	Glass/ITO/ZnO/PBTA-TF:IT-M/MoO ₃ /Al	PBTA-TF:IT-M (Blade)	0.04	11.4	Cell	[198]
	2019	Glass/ITO/ZnO/PBDB-T:iIEICO-4F/MoO ₃ /Al	PBDB-T:iIEICO-4F (Blade)	-	11.5	Cell	[61]
	2019	Glass/PEDOT:PSS/PBDB-TF:BTP-4Cl-12/PDINO/Al	PBDB-TF:BTP-4Cl-12 (Blade)	0.81	15.5	Cell	[201]
	2019	Glass/ITO/PEDOT:PSS/PBDB-TF-T1:BTP-4F-8/PFN-Br/Al	PBDB-TF-T1:BTP-4F-8 (Blade)	1.07	14.4	Cell	[196]
	2020	PET/ITO/ZnO/PDTSTPD:PC71BM/MoO ₃ /Ag	ZnO & PDTSTPD:PC71BM (Blade)	1	4.2	Cell	[203]
	2020	Glass/ITO/ZnO/PCDTBT:PC71BM/MoO ₃ /Ag	PCDTBT:PC71BM & ZnO (Blade)	0.04	12.3	Cell	[204]
	2020	glass/ITO/ZnO/TPD-3F:IT-4F/MoO ₃ /Ag	TPD-3F:IT-4F (Blade)	20.4	10.08	Module	[197]
	2020	glass/ITO/ZnO/TPD-3F:IT-4F/m-PEDOT:PSS/Ag	PEDOT:PSS & TPD-3F:IT-4F (Blade)	20.4	6.77	Module	[197]
	2020	Glass/ITO/PEDOT:PSS/NF3000-P:NF3000-N/TASiW-12/Al	PEDOT:PSS,NF3000-P:NF3000-N & TASiW-12 (Blade)	0.04	12.3	Cell	[186]

Blade	2020	Glass/ITO/PEDOT:PSS/NF3000-P:NF3000-N/ TASiW-12/Al	PEDOT:PSS,NF3000-P:NF3000-N & TASiW-12 (Blade)	216	9.5	Module	[186]
	2021	Glass/ITO/PM6:Y6:PC61BM/MoOx/Ag	ZnO & PM6:Y6:PC61BM (Blade)	25	13.27	Module	[3]
	2021	Glass/ITO/PM6:Y6:PC61BM/MoOx/Ag	ZnO & PM6:Y6:PC61BM (Blade)	194.8	12.63	Module	[3]
	2021	PET/ITO/ZnO NP + PEIE/P3HT:PC61BM/PEDOT:PSS/Ag	Ag top (Blade)	0.21	0.95	Cell	[207]
	2021	PET/ITO/Ag/ITO/PEI/RaynergyTek:PC61BM/ PEDOT:PSS/Ag	PEI, RaynergyTek:PC61BM & PEDOT:PSS (Blade)	0.55	6.5	Cell	[188]
	2021	PET/ITO/silver/ITO/PEI/C1:PC61BM/PEDOT:PSS/Ag	C1:PC61BM, PEI, PEDOT:PSS (Blade)	0.55	6.5	Cell	[188]
	2021	PET/ITO/ZnO NP/PCDTBT:PC71BM/MoO3/Ag	Pattern ITO(Screen), ZnO NPs & PCDTBT:PC71BM (Blade)	1	5.3	Cell	[199]
	2021	Glass/ITO/ZnO/PTB7-Th:P(NDI2OD-2T)/MoO3/Ag	PTB7-Th:P(NDI2OD-2T) (Blade)	-	4.5	Cell	[199]
	2021	Glass/ITO/ZnO/PV-X Plus/MoO3/Ag	PV-X Plus (Blade)	0.04	15.7	Cell	[189]
	2021	Glass/ITO/ZnO/PV-X Plus/MoO3/Ag	ZnO, PV-X Plus (Blade)	32.64	10.3	Module	[189]
	2021	Glass/ITO/ZnO/PTB7-Th:PC71BM/MoO3/Al	ZnO & PTB7-Th:PC71BM (Blade)	-	7.58	Cell	[66]
	2021	Glass/ITO/ZnO/PTB7-Th:PC71BM/MoO3/Ag NWs	ZnO & PTB7-Th:PC71BM (Blade), MoO3 & Ag NWs (Spray)	-	4.19	Cell	[66]
Flexography	2012	PET/Ag-grid/PEDOT:PSS/ZnO/P3HT:PCBM/ PEDOT:PSS/Ag	Bottom Ag-grid (Flexography)	-	1.82	Cell	[252]
	2016	PET/Ag grids or (Ag grid/CNT hybrid coating)/PEDOT:PSS/P3HT:PC60BM/Ca/Al	Ag-grid (Flexography)	0.09	0.61	Cell	[251]
	2018	PET/ITO/ZnO/PCDTBT:PC71BM/MoOx/Ag	ZnO & Active layer (Flexography)	1	3.4	Cell	[139]
Gravure	2011	PET/PEDOT:PSS/P3HT:PC61BM/Ca/Al	PEDOT:PSS (Gravure)	0.0466	2	Cell	[245]
	2013	PET/ITO/PEDOT:PSS/P3HT:PCBM/ZnO/Al	PEDOT:PSS, P3HT:PCBM & ZnO (Gravure)	75	0.86	Module	[246]
	2014	Glass/ITO/PEDOT:PSS/PTB7:PC61BM/Ca/Al	PEDOT:PSS & PTB7:PC61BM (Gravure)	-	1.61	Cell	[200]
	2014	PET/ITO/PEDOT:PSS/P3HT:PC61BM/LiF/Al	PEDOT:PSS & P3HT:PC61BM (Gravure)	15	1.72	Cell	[261]
	2015	PET/ITO/ZnO NP/P3HT:PC61BM/PEDOT:PSS/Silver	ZnO NP & P3HT:PC61BM (Gravure), Silver (Flexography)	0.32	1.26	Cell	[150]
	2015	PET/ITO/ZnO/P3HT:PC61BM/PEDOT:PSS/Ag	ZnO & P3HT:PC61BM (Gravure), PEDOT:PSS & Ag (Rotary Screen)	96.5	1.8	Module	[187]
	2015	PET/ITO/ZnO/P3HT:PC61BM/PEDOT:PSS/Ag	ITO pattern, PEDOT:PSS, & Ag (Rotary screen), ZnO & P3HT:PC61BM (Gravure)	96.5	1.97	Module	[187]
	2016	PET/ITO/ZnO NP/P3HT:PC61BM/PEDOT:PSS/Silver	ZnO NP, P3HT:PC61BM, PEDOT:PSS & Ag (Gravure)	18	2.22	Cell	[160]
	2017	PET/ITO/ZnO/PTB7-Th:PC71BM/MoOx/Al	ZnO & PTB7-Th:PC71BM (Gravure)	0.09	6.61	Cell	[247]
	2017	PET/ITO/PEDOT:PSS/P3HT:PCBM/Li/Al	PEDOT:PSS & P3HT:PCBM (Gravure)	21.8	2	Module	[248]
	2018	Glass/ITO/ZnO/PTB7-Th:PC71BM/MoO3/Al	ZnO (micro-gravure)	-	6.83	Cell	[249]
	2019	PET/ITO/ZnO:PEI/P3HT:PCBM/MoO3/Ag	ZnO:PEI & P3HT:PCBM (Micro-gravure)	0.09	2.43	Cell	[243]

Gravure	2019	PETs/ITO/ZnO:PEI/PTB7-Th/MoOx/Al	ZnO:PEI (Micro-gravure)	0.09	6.9	Cell	[244]
Inkjet	2007	Glass/TO/ PEDOT:PSS/P3HT:PCBM/ZnO/Ag	Ag (Inkjet)	-	0.209	Cell	[239]
	2010	Glass/ITO/ PEDOT:PSS/P3HT:PC61BM/LiF/Ag	PEDOT:PSS & P3HT:PC61BM (Inkjet)	-	3.71	Cell	[237]
	2012	PET/Ag/PEDOT:PSS/ZnO/P3HT:PCBM/PEDOT:PSS/Ag	Bottom Ag (Inkjet)	-	0.75	Cell	[252]
	2015	Glass/Ag/PEDOT:PSS/ZnO NP/Activlink PV2000/PEDOT/Ag	PEDOT:PSS, Activlink PV2000, ZnO NP (Inkjet)	1	4.7	Cell	[238]
	2015	Glass/ITO/ZnO/P3HT:PCBM/MoOx/Ag	ZnO & P3HT:PCBM (inkjet)	1	2.83	Cell	[236]
	2015	Glass/Mo/Al/Mo/PEDOT:PSS/ZnO/P3HT:PCBM/ MoOx/Ag	PEDOT:PSS, ZnO & P3HT:PCBM (inkjet)	1	2.18	Cell	[236]
	2015	Glass/ITO/ZnO/P3HT:PC61BM/ PEDOT:PSS:MoO3/Ag NW	Ag (Inkjet)	-	2.71	Cell	[240]
	2016	Glass/ITO/ZnO/P3HT:IC60BA/WoO3/PEDOT:PSS/Ag	ZnO, P3HT:IC60BA, WoO3, PEDOT:PSS & Ag (inkjet)	0.1	2.9	Cell	[192]
	2016	Glass/ITO/ZnO/P3HT:IC60BA/PEDOT:PSS/Ag	P3HT:IC60BA (Inkjet)	0.1	1.6	Cell	[192]
	2016	Glass/Ag NP/Ag NW/PV2000:PC70BM/ PEDOT:PSS/Ag NW	Ag NP, Ag NW, PV2000:PC70BM, PEDOT:PSS & Ag NW (Inkjet)	1	4.3	Cell	[241]
	2018	Glass/ITO/ZnO np/P3HT:PC61BM/PEDOT:PSS/Ag	PEDOT:PSS (Inkjet)	-	1.9	Cell	[262]
	2018	PEN/Ag/ZnO/P3HT:PCBM/PEDOT:PSS	Ag, ZnO, P3HT:PCBM & PEDOT:PSS (Inkjet)	0.02	0.18	Cell	[235]
	2019	Glass/ITO/ZnO/P3HT:ICBA/MoO3/Ag	ZnO, P3HT:ICBA (inkjet)	0.045	4.7	Cell	[263]
	2020	Glass/ITO/ZnO/P3HT:O-IDTBR/MoOx/Ag	P3HT:O-IDTBR (Inkjet)	0.1	6.47	Cell	[264]
	2020	Glass/PEDOT:PSS/P3HT:O-IDTBR/ZnO/PEDOT:PSS	PEDOT:PSS, P3HT:O-IDTBR & ZnO (Inkjet)	0.1	4.73	Cell	[264]
2021	glass/ITO/PEDOT:PSS/p-DTS(FBTTh2)2:PC70BM/Ca/Al	p-DTS(FBTTh2)2:PC70BM (inkjet)	-	7.3	Cell	[234]	
2022	Glass/ITO/PEDOT:PSS:Graphene/PTB7:PCBM/LiF/Al	PEDOT:PSS:Graphene & PTB7:PCBM (Inkjet)	0.7	1.12	Cell	[265]	
Pad	2008	Glass/ITO/ ZnO/P3MHOCT + Zinc/PEDOT:PSS/Silver	P3MHOCT + Zinc (Pad)	-	0.07	Cell	[242]
Rod	2011	Glass/AgNWs-TiO ₂ /PEDOT:PSS/P3HT:PC ₆₁ BM/Ca/Al	AgNW film (Rod)	-	3.4	Cell	[184]
	2017	Glass/ITO/PEDOT:PSS/P3HT:PCBM/LiF/Al	PEDOT:PSS & P3HT:PCBM (Rod)	0.1	1.9 ± 0.4	Cell	[266]
Screen	2004	PET/ITO/Ag/MEH-PPV/Al	Ag and Active (Screen)	0.12	0.046	Cell	[123]
	2009	Glass/ITO/PEDOT:PSS/P3HT:PCBM/Al	Active layer (Screen)	3	2.3845	Cell	[259]
	2018	Steel/Insulator/Al/ZnO/P3HT:PC61BM/PEDOT:PSS/Al	PEDOT:PSS (Screen)	0.09	0.67	Cell	[256]
Slot-die	2009	PET/ITO/ZnO/P3HT/PEDOT:PSS/Ag	ZnO, P3HT, PEDOT:PSS & Ag (Slot-die)	120	0.84	Module	[267]
	2010	PET/ITO/ZnO NP/P3HT:PCBM/PEDOT:PSS/Nickel	ZnO NP, P3HT:PCBM & PEDOT:PSS (Slot-die), n-octanol (flexographic), Nickel (Rotary screen)	15	2.75	Cell	[163]
	2010	PET/ITO/ZnO/P3HT:PC61BM/PEDOT:PSS/Al	ZnO, P3HT:PC61BM & PEDOT:PSS (Slot-die). Silver (Rotary screen)	360	1.18 ± 0.13	Module	[151]
	2010	PET/ITO/ZnO/P3HT:PC61BM/PEDOT:PSS/Al	ZnO, P3HT:PC61BM & PEDOT:PSS (Slot-die). Silver (Rotary screen)	160	1.22 ± 0.11	Module	[151]

Slot-die	2010	PET/ITO/ZnO/P3HT:PC61BM/PEDOT:PSS/AI	ZnO, P3HT:PC61BM & PEDOT:PSS (Slot-die). Silver (Rotary screen)	96	1.79 ± 0.09	Module	[151]
	2011	PET/Cr/AI/Cr/P3HT:PCBM/PEDOT:PSS/Au	P3HT:PC61BM & PEDOT:PSS (Slot-die)	20.6	1.40%	Module	[211]
	2012	PET/Silver/PEDOT:PSS/ZnO NP/P3HT:PC61BM/PEDOT:PSS/ Silver	PEDOT:PSS, P3HT:PC61BM & ZnO NP (Slot-die)	1	1.5	Cell	[213]
	2013	ITO/ZnO/PSBTBT:PDI-DTT/PEDOT:PSS/Ag	PSBTBT:PDI-DTT (Slot-die)	4.2	0.204	Cell	[217]
	2013	Ag grid/PEDOT:PSS/ZnO/P3HT:PCBM/PEDOT:PSS/Ag grid (TOP)	Bottom Ag (Flexography), PEDOT:PSS (Rotary Screen), ZnO & Active (Slot-die), Top Ag (Flatbed screen)	24	2.09	Cell	[258]
	2013	Ag grid/PEDOT:PSS/ZnO/P3HT:PCBM/PEDOT:PSS/Ag grid (TOP)	Bottom Ag (Flexography), PEDOT:PSS (Rotary Screen), ZnO & Active (Slot-die), Top Ag (Rotary screen)	24	1.84	Cell	[258]
	2013	Ag grid/PEDOT:PSS/ZnO/P3HT:PCBM/PEDOT:PSS/Ag grid (TOP)	Bottom Ag (Flexography), PEDOT:PSS (Rotary Screen), ZnO & Active (Slot-die), Top Ag (Inkjet)	24	0.54	Cell	[258]
	2013	Ag grid/PEDOT:PSS/ZnO/P3HT:PCBM/PEDOT:PSS/Ag grid (TOP)	Bottom Ag (Flexography), PEDOT:PSS (Rotary Screen), ZnO & Active (Slot-die), PEDOT:PSS (Rotary Scree), Top Ag (Flexography)	24	0.12	Cell	[258]
	2014	PET/ITO/Ag/ITO/AZO/P3HT:PCBM/PEDOT:PSS/Ag	AZO & PEDOT:PSS (Blade), P3HT:PCBM (Slot-die)	2.5	3.03±0.06	Cell	[218]
	2015	PET/AgNW/ZnO/PBDPTTz-4:PC61BM/PEDOT:PSS/Ag	AgNW, PEDOT:PSS & PBDPTTz-4:PC61BM (Slot-die). Ag (Flexography)	1	3.3	Cell	[214]
	2017	PET/ITO/AZO:PEIE/P3HT:PC71BM/MoO ₃ /Ag	AZO & P3HT:PC71BM (Slot-die)	2	5.7	Cell	[143]
	2017	PET/ITO/AZO/PTB7:PC71BM/MoO _x /Ag	AZO & PTB7:PC71BM (Slot-die)	0.3	7.32	Cell	[143]
	2018	PET/Ag grid/PEDOT:PSS/ZnO/PI-4 ink/HTL/ Ag Vacuum	PI-4 ink & HTL (Slot-die)	-	0.669	Cell	[212]
	2018	PET/ZnO NPs/PPDT2FBT:PC71BM/MoO _x /AI	ZnO NPs & PPDT2FBT:PC71BM (Slot-die)	0.1	7.1	Cell	[59]
	2019	glass+C14:G14s/ITO/ZnO/PEIE/PPDT2FBT:PC61BM/ MoOX/Ag	PPDT2FBT:PC61BM (Slot-die)	0.09	8.48	Cell	[63]
	2019	glass/ITO/ZnO/PEIE/PPDT2FBT:ITIC-F/MoOX/Ag	PPDT2FBT:ITIC-F (Slot-die)	0.09	8.48	Cell	[63]
	2019	PET/Ag/ZnO/PBDB-T:ITIC/HTL solar/ CPP PEDOT:PSS	ZnO, PBDB-T:ITIC, HTL & PEDOT:PSS (Slot-die)	0.054	5.07±0.09	Cell	[96]
	2019	PET/Ag/PEDOT:PSS/P3HT:ICx/A/ZnO/AI	Ag (Flexography), PEDOT:PSS, P3HT:ICx & ZnO (Slot-die)	4	0.33 ± 0.09	Cell	[162]
	2019	PET/ITO/ZnO/PTB7-Th+p- DTS(FBTTH2)2:PC71BM/MoO _x /Ag	ZnO, PTB7-Th+p-DTS(FBTTH2)2:PC71BM	0.75	7.32 ± 0.431	Cell	[209]
	2019	PET/ITO/ZnO/PTB7-Th+p- DTS(FBTTH2)2:PC71BM/MoO _x /Ag	ZnO, PTB7-Th+p-DTS(FBTTH2)2:PC71BM	1	7.11 ± 0.263	Cell	[209]
	2019	PET/ITO/ZnO/PTB7-Th+p- DTS(FBTTH2)2:PC71BM/MoO _x /Ag	ZnO, PTB7-Th+p-DTS(FBTTH2)2:PC71BM	2	6.79±0.212	Cell	[209]
	2019	Glass/ITO/ZnO/PBDB-T:iIEICO-4F/MoO ₃ /AI	PBDB-T:iIEICO-4F (Slot-die)	-	12.2 ± 0.17	Cell	[61]
	2019	Glass/ITO/ZnO/PTB7-Th:PC71BM:Co ₈ DFIC/MoO ₃ /AI	PTB7-Th:PC71BM:Co ₈ DFIC (Slot-die)	0.1	13.5	Cell	[144]

	2019	Glass/ITO/ZnO/PTB7-Th:PC71BM:Coi8DFIC/MoO3/Al	PTB7-Th:PC71BM:Coi8DFIC & ZnO (Slot-die)	30	8.6	Module	[144]
	2019	PET/TCO/ZnO/PTB7-Th:PC71BM:Coi8DFIC/MoO3/Al	PTB7-Th:PC71BM:Coi8DFIC & ZnO (Slot-die)	0.14	9.57	Cell	[144]
	2020	flextrode/P3HT:O-IDTBR/PEDOT:PSS/Ag	Active layer & PEDOT:PSS (Slot-die). Ag (Flexography)	1	3.26 ± 0.14	Cell	[215]
	2020	PET/ZnO/PV2001:PC61BM/PEDOT:PSS/Ag	ITO patterning (Rotary screen), ZnO & PV2001:PC61BM (Slot-die), PEDOT:PSS and Silver (Flatbed screen)	-	4.6	Module	[60]
	2021	PET/ITO/Ag/ITO/PEI/RaynergyTek:PC61BM/PEDOT:PSS/Ag	PEI, RaynergyTek:PC61BM & PEDOT:PSS (Slot-die)	7.2	5.6 ± 0.6 (6.0)	Module	[188]
	2021	PET/TCE/ZnO NP/PM6:Y6:IT-4F/MoO3/Ag	ZnO NPs & PM6:Y6:IT-4F (Slot-die)	0.14	10.2	Cell	[216]
	2021	Glass/ITO/ZnO/PTB7-Th:IEICO-4F/ PEDOT:PSS&MoO3/Ag	PEDOT:PSS, ZnO, PTB7-Th:IEICO-4F (Slot-die)	0.1	11	Cell	[208]
	2021	PET/ITO/silver/ITO/PEI/M3:PC60BM/PEDOT:PSS/Ag	PEI, M3:PC60BM & PEDOT:PSS (Slot-die)	7.2	5.6± 0.6	Module	[188]
	2021	ITO/PEDOT:PSS/PTB7-Th:IEICO-4F/AZO/Ag	PEDOT:PSS, PTB7-Th:IEICO-4F & AZO (Slot-die)	1	9.6	Cell	[208]
	2021	ITO/PEDOT:PSS/PTB7-Th:IEICO-4F/AZO/Ag NWs	PEDOT:PSS, PTB7-Th:IEICO-4F & AZO (Slot-die), Ag NWs (blade)	0.2	8.8	Cell	[208]
	2021	PET/ITO/ZnO/PV2000:PC71BM/PEDOT:PSS/Ag	ZnO, PV2000:PC71BM & PEDOT:PSS (Slot-die)	48	2.2	Module	[155]
	2022	Glass/ITO/PEDOT:PSS/PM6:Y6C12/PFNBr/Ag	PEDOT:PSS, PM6:Y6C12 & PFNBr (Slot-die)	0.14	10.1 ± 0.6	Cell	[210]
	2022	Glass/ITO/SnO2/PDIN-H/PTQ10:Y6-C12/MoOx/Ag	SnO2, PDIN-H, PTQ10:Y6-C12 & PEDOT:PSS (Slot-die)	0.12	11.26 ± 0.49	Cell	[55]
	2022	Glass/ITO/SnO2/PDIN-H/PTQ10:Y6-C12/PEDOT:PSS/Ag	SnO2, PDIN-H, PTQ10:Y6-C12 & PEDOT:PSS (Slot-die)	0.12	9.38 ± 0.2	Cell	[55]
	2022	Glass/ITO/PEDOT:PSS/PM6:Y6C12/PDIN-EH/Ag	PEDOT:PSS, PM6:Y6C12 & PDIN-EH (Slot-die)	0.12	11.9 ± 0.2	Cell	[161]
	2022	Glass/ITO/PEDOT:PSS/PM6:Y6C12/PDIN-EH/Ag	PEDOT:PSS, PM6:Y6C12 & PDIN-EH (Slot-die)	2	7.5	Module	[161]
	2022	PET/ITO/PEDOT:PSS/PM6:Y6C12/PDIN-EH/Ag	PEDOT:PSS, PM6:Y6C12 & PDIN-EH (Slot-die)	16	2.4	Module	[161]
	2022	PET/ITO/ZnO NPs/ PPDT2FBT:PC61BM/MoOx/Al	ZnO NPs, PPDT2FBT:PC61BM (Slot-die)	0.1	8.49 ± 0.07	Cell	[145]
Spray	2013	Glass/ITO/PEDOT:PSS/CuPc:C60/Al	CuPc/C60 (Spray)	-	1.08	Cell	[232]
	2013	Glass/ITO/PEDOT:PSS/P2:PC71BM/Ca/Al	P2:PC71BM (Spray)	0.045	5	Cell	[220]
	2013	Glass/ITO/PEDOT:PSS/P3HT:PCBM/Bphen/Ag	P3HT:PC61BM (Spray)	-	2.91	Cell	[222]
	2013	Glass/ITO/PEDOT:PSS/P3HT:PCBM/Ca/Ag	P3HT:PCBM (Spray)	-	3.9 ± 0.2	Cell	[224]
	2013	Glass/ITO/PEDOT:PSS/P3HT:PC61BM/LiF/Al	P3HT:PCBM (Spray)	0.25	2.59	Cell	[233]
	2015	Glass/ITO/PEDOT:PSS/P3HT:PC61BM/Ca/Al	Active layer (Spray)	0.1	3.33 ± 0.16	Cell	[231]
	2017	Glass/ITO/PEDOT:PSS/PTB7:PC71BM/LiF/Al	PTB7:PC71BM (Electrospray)	-	5.6	Cell	[140]
	2018	Glass/ITO/ZnO/P3HT:PC61BM/PEDOT:PSS	ZnO, P3HT:PCBM & PEDOT:PSS (Spray)	4	2.44	Cell	[225]
	2018	Textile/Ag/ZnO/P3HT:ICBA/PEDOT:PSS/AgNW	ZnO, P3HT:ICBA, PEDOT:PSS, AgNW (Spray)	0.03	1.23	Cell	[228]
	2018	Glass/ITO/PEDOT:PSS/P3HT:PC71BM/Al	P3HT:PC71BM (Spray)	-	2.17	Cell	[230]
	2018	Glass/ITO/PEDOT:PSS/PffBT4T2OD:PC71BM/PEIE/ V2O5/Ag	PffBT4T2OD:PC71BM, PEIE & V2O5 (Spray)	-	3.56 ± 0.25	Cell	[154]

Spray	2018	Glass/Graphene/PEDOT:PSS/PffBT4T2OD:PC71BM/ PEIE/V2O5/Ag	PffBT4T2OD:PC71BM, PEIE & V2O5 (Spray)	-	2.82 ± 0.15	Cell	[154]
	2019	PEN/Graphene/MoOx/PEDOT:PSS/P3HT:PC61BM/Ca/ Ag	P3HT:PC61BM (Spray)	2	1.5	Cell	[226]
	2019	Glass/ITO/PEDOT:PSS/PBDTTT-EFT:PC71BM/Ca/Al	PEDOT:PSS & PBDTTT-EFT:PC71BM (Spray)	-	7.5	Cell	[229]
	2020	Glass/ITO/PEDOT:PSS/P3HT:PC71BM/LiF/Al	P3HT:PC71BM (Spray)	-	3.48	Cell	[219]
	2020	ITO/PEDOT:PSS/P3HT:60PCBM/LiF/Al	P3HT:PC71BM (Spray)	-	1.97	Cell	[227]

As seen in *Table 2.1*, it can be observed that some techniques, such as blade and slot-die coating have seen extensive use for active layer deposition, while gravure inkjet printing, as well as spray coating moderate interest. As for rod coating and rod printing, they have seen minimal interest towards OPV fabrication. Lastly, though flexography and screen printing have seen little interest towards active layer deposition, they have extensively been implementation towards PEDOT:PSS and Ag electrode printing. This observation can be partially explained by the technical details (seen in *Table 2.2*) in relation to the printing and coating techniques.

Table 2.2: Technical comparison of different printing/coating techniques. Table was adapted from Krebs 2009 [1].

Conditions	R2R compatible	Pattern	Ink preparation	Wastage	Web speed	Wet thickness (l)	Ink viscosity
Spin	N	0	1	5	-	0-100	1
Blade	Y	0	2	2	2-4	0-100	1
Slot-die	Y	1	2	1	3-5	10-250	2-5
Spray	Y	0	2	3	1-4	1-500	2-3
Inkjet	Y	2	3	1	1	1-500	1
Pad	Y	2	5	1	1-2	5-250	1
Gravure	Y	2	4	1	1-3	5-80	1-3
Flexography	Y	2	4	1	1-3	5-200	1-3
Screen	Y	2	4	1	1-4	10-500	3-5

Pattern: 0 (0-dimensional), 1 (1-dimensional), 2 (2-dimensional). **Ink preparation:** 1 (simple), 2 (moderate), 3 (demanding), 4 (difficult), 5 (critical). **Ink waste:** 1 (none), 2 (little), 3 (some), 4 (considerable), 5 (significant). **Web Speed:** 1 (very slow), 2 (slow < 1 m min⁻¹), 3 (medium 1–10 m min⁻¹), 4 (fast 10–100 m min⁻¹), 5 (very fast 100–1000 m min⁻¹). **Ink viscosity:** 1 (very low < 10 cP) 2 (low 10–100 cP), 3 (medium 100–1000 cP), 4 (high 1000–10,000 cP), 5 (very high 10,000–100,000 cP).

When observing the ink preparation for given deposition techniques, it is relatively simple to prepare the ink for spin, blade, slot-die, and spray coating, with the focus towards influencing the physical properties of thin film. Whereas for pad, gravure, flexography, and screen printing requires the ink preparation to also consider the printability using this specified deposition method, thus, limiting to what inks and materials can be deposited. This can be an issue for active layer deposition as several factors can influence the morphology of the BHJ, including ink preparation [230, 268-270].

With a significant focus towards improving the performance of OPVs, and how the active layer has a substantial impact on said performance, thus with simple ink preparation, fast web speeds and low ink wastage, such as blade and slot-die coating has gained majority interest towards scalable and large scale OPV fabrication. These techniques are also very versatile, having been demonstrated to deposit at a small-scale in a glovebox, to be used in roll-to-roll fabrication. These methods also allow for minimal material wastage, allowing for research using more expensive high-performing materials.

Other printing methods have received less attention in the past few years due to their moderately high material wastage, relatively large space required for installation (unable to be installed in a glovebox), and difficulty to be used for small-scale fabrication without large amount of substrate wasted. Despite these flaws, they have advantages that make them applicable for upscaled OPV device fabrications, including the use of flexography for electrode printing and rotary screen printing for etching and pre-wetting of films.

Another interesting observation associated with printing and coating techniques is associated with the goal of the research. For the past ten years, there has been a massive focus on determining methods for improving performance and scalable and large-scale devices. Yet, there has been minimal interest towards improving stability, despite the research seen in spin-coated OPVs.

Lastly, many papers investigating the performance of printed and/or coated OPVs primarily aim at developing improved photoactive or interfacial materials. There have been few papers that aim at improving the printing technique themselves, either during or post deposition. Such techniques including heading of the substrate/printing head [59, 141], use of air/nitrogen to improve coating uniformity [186], influencing printing quality by the choice of solvent, combination and additives all have an impact on influencing printing quality [31, 269].

Overall, each printing condition has its advantages and disadvantages. With the rise of scalable and upscaling coating, a majority have been based around blade and slot-die coating, with a constant stream of spray-based coatings. Since 2019, there has been a spike in papers around working module devices, usually consisting of several cells on one substrate tested altogether.

With the methods having advantages and disadvantages, it is unlikely that a single printing/coating method can be used to produce high performance OPVs, instead a combination of coating methods. There have also been examples of roll-to-roll setups that implement several different coating instruments to a single fabrication line. Also, though scalability has seen an increased interest for both slot-die and blade coated OPV modules, there appears to be a lack of interest towards device lifespan. As stability is one of the important aspects that impact the commerciality of OPV, more work needs to be conducted on investigating strategies for reducing the impact of degradation pathway of which can be upscaled to R2R and S2S module fabrication.

2.9. Outlook

Overall, there has been considerable progress towards the improvement of OPV performance, reducing the gap between OPV and silicon-based PVs. Despite this, there are still challenges that are needed to be overcome, including stability, cost, and scalability of fabrication. In relation to stability, there has been an increased amount of interest towards developing materials and techniques for reducing this degradation, however, it is still heavily focused towards small-scale fabrication, with minimal interest to support the scalability.

When investigating the research that has been conducted for scalable and large scale OPVs, the majority of the focus is on reducing the performance gap between small-scale spin-coated devices, and alternatively printed/coated OPVs. As such, only a small amount of literature has focused on determining scalable methods for improving the lifespan of said devices. On the positive side, in the past 5 years, there has been a shift in some small-area printing and coating under nitrogen conditions, towards more scalable fabrication under ambient conditions, allowing for the research to more closely follow deposition procedures used in upscaled manufacturing.

For OPV scalable fabrication to be more competitive in the PV field, there needs to be more focus towards scalable fabrication methods that bridge between lab-scale and large-scale fabrication processes and investigating strategies for improving stability of scalable and large-scale devices. This focus on research in scalable OPV fabrication would allow for better connection between small and large-scale research, accelerating the field towards commercialisation.

In terms of the thesis, there has been a lack of interest for investigating the scalability of methods for reducing the impact of thermal degradation, with majority of literature focusing on spin-coated devices fabricated under nitrogen conditions. As such, it was determined that the focus of the research project would be to investigate the thermal degradation pathway associated with OPV manufactured using scalable coating techniques, and determine which methods can not only improve stability, but can be translated to upscaled devices. Slot-die coating was chosen for the project as it has been utilised effectively for active layer coating, as well as been demonstrated to be used for upscale R2R OPV fabrication.

2.10. Reference

1. Zhu, L., Zhang, M., Xu, J., Li, C., Yan, J., Zhou, G., Zhong, W., Hao, T., Song, J., Xue, X., Zhou, Z., Zeng, R., Zhu, H., Chen, C.-C., MacKenzie, R. C. I., Zou, Y., Nelson, J., Zhang, Y., Sun, Y., and Liu, F., Single-junction organic solar cells with over 19% efficiency enabled by a refined double-fibril network morphology. *Nature Materials*, **2022**. 21 (6), 656-663.
2. Wei, Y., Chen, Z., Lu, G., Yu, N., Li, C., Gao, J., Gu, X., Hao, X., Lu, G., Tang, Z., Zhang, J., Wei, Z., Zhang, X., and Huang, H., Binary Organic Solar Cells Breaking 19% via Manipulating the Vertical Component Distribution. *Advanced Materials*, **2022**. 34 (33), 2204718.
3. Distler, A., Brabec, C. J., and Egelhaaf, H.-J., Organic photovoltaic modules with new world record efficiencies. *Progress in Photovoltaics: Research and Applications*, **2021**. 29 (1), 24-31.
4. JR, M. and T, J., Device architectures in organic photovoltaics. *Turkish Journal of Physics*, **2014**. 38 (3), 516-525.
5. Pierini, F., Lanzi, M., Nakielski, P., Pawłowska, S., Urbanek, O., Zembrzycki, K., and Kowalewski, T. A., Single-material organic solar cells based on electrospun fullerene-grafted polythiophene nanofibers. *Macromolecules*, **2017**. 50 (13), 4972-4981.
6. Wu, Y., Guo, J., Wang, W., Chen, Z., Chen, Z., Sun, R., Wu, Q., Wang, T., Hao, X., and Zhu, H., A conjugated donor-acceptor block copolymer enables over 11% efficiency for single-component polymer solar cells. *Joule*, **2021**. 5 (7), 1800-1815.
7. Guo, J., Wu, Y., Wang, W., Wang, T., and Min, J., Achieving 12.6% Efficiency in Single-Component Organic Solar Cells Processed from Nonhalogenated Solvents. *Solar RRL*, **2022**. 6 (6), 2101024.
8. Liang, S., Xiao, C., Xie, C., Liu, B., Fang, H., and Li, W., 13% Single-Component Organic Solar Cells based on Double-Cable Conjugated Polymers with Pendent Y-Series Acceptors. *Advanced Materials*, **2023**. 35 (18), 2300629.
9. Chiang, C. K., Fincher, C. R., Park, Y. W., Heeger, A. J., Shirakawa, H., Louis, E. J., Gau, S. C., and MacDiarmid, A. G., Electrical Conductivity in Doped Polyacetylene. *Physical Review Letters*, **1977**. 39 (17), 1098-1101.
10. Dou, L., Liu, Y., Hong, Z., Li, G., and Yang, Y., Low-bandgap near-IR conjugated polymers/molecules for organic electronics. *Chemical reviews*, **2015**. 115 (23), 12633-12665.
11. Yiu, A. T., Beaujuge, P. M., Lee, O. P., Woo, C. H., Toney, M. F., and Frechet, J. M., Side-chain tunability of furan-containing low-band-gap polymers provides control of structural order in efficient solar cells. *Journal of the American Chemical Society*, **2012**. 134 (4), 2180-2185.
12. Sariciftci, N. S., Braun, D., Zhang, C., Srdanov, V. I., Heeger, A. J., Stucky, G., and Wudl, F., Semiconducting polymer-buckminsterfullerene heterojunctions: Diodes, photodiodes, and photovoltaic cells. *Applied Physics Letters*, **1993**. 62 (6), 585-587.
13. Brabec, C. J., Sariciftci, N. S., and Hummelen, J. C., Plastic solar cells. *Advanced functional materials*, **2001**. 11 (1), 15-26.
14. Kroto, H. W. and Heath, J. R., O, Brien, SC; Curl, RF; Smalley, RE. *Nature*, **1985**. 318 (162), 22-11.
15. Sariciftci, N. S., Smilowitz, L., Heeger, A. J., and Wudl, F., Photoinduced Electron Transfer from a Conducting Polymer to Buckminsterfullerene. *Science*, **1992**. 258 (5087), 1474.
16. Yu, G., Gao, J., Hummelen, J. C., Wudl, F., and Heeger, A. J. J. S., Polymer photovoltaic cells: enhanced efficiencies via a network of internal donor-acceptor heterojunctions. **1995**. 270 (5243), 1789-1791.
17. Wienk, M. M., Kroon, J. M., Verhees, W. J. H., Knol, J., Hummelen, J. C., van Hal, P. A., and Janssen, R. A. J., Efficient Methano[70]fullerene/MDMO-PPV Bulk Heterojunction Photovoltaic Cells. *Angewandte Chemie International Edition*, **2003**. 42 (29), 3371-3375.
18. Ding, G., Chen, T., Wang, M., Xia, X., He, C., Zheng, X., Li, Y., Zhou, D., Lu, X., Zuo, L., Xu, Z., and Chen, H., Solid Additive-Assisted Layer-by-Layer Processing for 19% Efficiency Binary Organic Solar Cells. *Nano-Micro Letters*, **2023**. 15 (1), 92.

19. Cheng, P., Bai, H., Zawacka, N. K., Andersen, T. R., Liu, W., Bundgaard, E., Jørgensen, M., Chen, H., Krebs, F. C., and Zhan, X., Roll-Coated Fabrication of Fullerene-Free Organic Solar Cells with Improved Stability. *Advanced Science*, **2015**. 2 (6), 1500096.
20. Gurney, R. S., Li, W., Yan, Y., Liu, D., Pearson, A. J., and Wang, T., Morphology and efficiency enhancements of PTB7-Th: ITIC nonfullerene organic solar cells processed via solvent vapor annealing. *Journal of Energy Chemistry*, **2019**. 37, 148-156.
21. Lin, Y., Zhao, F., He, Q., Huo, L., Wu, Y., Parker, T. C., Ma, W., Sun, Y., Wang, C., and Zhu, D., High-performance electron acceptor with thienyl side chains for organic photovoltaics. *Journal of the American Chemical Society*, **2016**. 138 (14), 4955-4961.
22. Lin, Y. and Zhan, X., Oligomer molecules for efficient organic photovoltaics. *Accounts of chemical research*, **2016**. 49 (2), 175-183.
23. Jiang, B.-H., Chen, C.-P., Liang, H.-T., Jeng, R.-J., Chien, W.-C., and Yu, Y.-Y., The role of Y6 as the third component in fullerene-free ternary organic photovoltaics. *Dyes and Pigments*, **2020**. 181, 108613.
24. Wang, R., Zhang, C., Li, Q., Zhang, Z., Wang, X., and Xiao, M., Charge separation from an intra-moiety intermediate state in the high-performance PM6: Y6 organic photovoltaic blend. *Journal of the American Chemical Society*, **2020**. 142 (29), 12751-12759.
25. Lv, J., Tang, H., Huang, J., Yan, C., Liu, K., Yang, Q., Hu, D., Singh, R., Lee, J., and Lu, S., Additive-induced miscibility regulation and hierarchical morphology enable 17.5% binary organic solar cells. *Energy & Environmental Science*, **2021**. 14 (5), 3044-3052.
26. Kim, T., Kim, J.-H., Kang, T. E., Lee, C., Kang, H., Shin, M., Wang, C., Ma, B., Jeong, U., and Kim, T.-S., Flexible, highly efficient all-polymer solar cells. *Nature communications*, **2015**. 6 (1), 1-7.
27. Peng, F., An, K., Zhong, W., Li, Z., Ying, L., Li, N., Huang, Z., Zhu, C., Fan, B., Huang, F., and Cao, Y., A Universal Fluorinated Polymer Acceptor Enables All-Polymer Solar Cells with >15% Efficiency. *ACS Energy Letters*, **2020**, 3702-3707.
28. Park, S. Y., Labanti, C., Luke, J., Chin, Y.-C., and Kim, J.-S., Organic Bilayer Photovoltaics for Efficient Indoor Light Harvesting. *Advanced Energy Materials*, **2022**. 12 (3), 2103237.
29. Lee, K. H., Schwenn, P. E., Smith, A. R. G., Cavaye, H., Shaw, P. E., James, M., Krueger, K. B., Gentle, I. R., Meredith, P., and Burn, P. L., Morphology of All-Solution-Processed "Bilayer" Organic Solar Cells. *Advanced Materials*, **2011**. 23 (6), 766-770.
30. Seok, J., Shin, T. J., Park, S., Cho, C., Lee, J.-Y., Yeol Ryu, D., Kim, M. H., and Kim, K., Efficient Organic Photovoltaics Utilizing Nanoscale Heterojunctions in Sequentially Deposited Polymer/fullerene Bilayer. *Scientific Reports*, **2015**. 5 (1), 8373.
31. Hong, M., Youn, J., Ryu, K. Y., Shafian, S., and Kim, K., Improving the Stability of Non-fullerene-Based Organic Photovoltaics through Sequential Deposition and Utilization of a Quasi-orthogonal Solvent. *ACS Applied Materials & Interfaces*, **2023**. 15 (16), 20151-20158.
32. Sun, R., Wang, T., Yang, X., Wu, Y., Wang, Y., Wu, Q., Zhang, M., Brabec, C. J., Li, Y., and Min, J., High-speed sequential deposition of photoactive layers for organic solar cell manufacturing. *Nature Energy*, **2022**. 7 (11), 1087-1099.
33. Halls, J., Walsh, C., Greenham, N. C., Marseglia, E., Friend, R. H., Moratti, S., and Holmes, A., Efficient photodiodes from interpenetrating polymer networks. *Nature*, **1995**. 376 (6540), 498.
34. Fontana, M., Kang, H., Yee, P. Y., Fan, Z., Hawks, S. A., Schelhas, L. T., Subramaniyan, S., Hwang, Y.-J., Jenekhe, S. A., and Tolbert, S. H., Low-Vapor-Pressure Solvent Additives Function as Polymer Swelling Agents in Bulk Heterojunction Organic Photovoltaics. *The Journal of Physical Chemistry C*, **2018**.
35. Brédas, J. L., Cornil, J., and Heeger, A. J., The exciton binding energy in luminescent conjugated polymers. *Advanced Materials*, **1996**. 8 (5), 447-452.
36. Bittner, E. R., Ramon, J. G. S., and Karabunarliev, S., Exciton dissociation dynamics in model donor-acceptor polymer heterojunctions. i. energetics and spectra. *The Journal of chemical physics*, **2005**. 122 (21), 214719.
37. Yao, H., Qian, D., Zhang, H., Qin, Y., Xu, B., Cui, Y., Yu, R., Gao, F., and Hou, J., Critical Role of Molecular Electrostatic Potential on Charge Generation in Organic Solar Cells. *Chinese Journal of Chemistry*, **2018**. 36 (6), 491-494.

38. Xian, K., Cui, Y., Xu, Y., Zhang, T., Hong, L., Yao, H., An, C., and Hou, J., Efficient Exciton Dissociation Enabled by the End Group Modification in Non-Fullerene Acceptors. *The Journal of Physical Chemistry C*, **2020**. 124 (14), 7691-7698.
39. Zhang, W., Zhao, B., He, Z., Zhao, X., Wang, H., Yang, S., Wu, H., Cao, Y. J. E., and Science, E., High-efficiency ITO-free polymer solar cells using highly conductive PEDOT: PSS/surfactant bilayer transparent anodes. **2013**. 6 (6), 1956-1964.
40. Andersen, T. R., Cooling, N. A., Almyahi, F., Hart, A. S., Nicolaidis, N. C., Feron, K., Noori, M., Vaughan, B., Griffith, M. J., Belcher, W. J., and Dastoor, P. C., Fully roll-to-roll prepared organic solar cells in normal geometry with a sputter-coated aluminium top-electrode. *Solar Energy Materials and Solar Cells*, **2016**. 149, 103-109.
41. Hu, Z., Zhang, J., Hao, Z., and Zhao, Y., Influence of doped PEDOT: PSS on the performance of polymer solar cells. *Solar Energy Materials and Solar Cells*, **2011**. 95 (10), 2763-2767.
42. Khodabakhsh, S., Sanderson, B. M., Nelson, J., and Jones, T. S., Using self-assembling dipole molecules to improve charge collection in molecular solar cells. *Advanced Functional Materials*, **2006**. 16 (1), 95-100.
43. Jonda, C., Mayer, A., Stolz, U., Elschner, A., and Karbach, A., Surface roughness effects and their influence on the degradation of organic light emitting devices. *Journal of Materials Science*, **2000**. 35, 5645-5651.
44. Malliaras, G., Salem, J., Brock, P., and Scott, J., Photovoltaic measurement of the built-in potential in organic light emitting diodes and photodiodes. *Journal of Applied Physics*, **1998**. 84 (3), 1583-1587.
45. Benanti, T. L. and Venkataraman, D., Organic solar cells: An overview focusing on active layer morphology. *Photosynthesis research*, **2006**. 87 (1), 73-81.
46. Kim, Y., Ballantyne, A. M., Nelson, J., and Bradley, D. D., Effects of thickness and thermal annealing of the PEDOT: PSS layer on the performance of polymer solar cells. *Organic Electronics*, **2009**. 10 (1), 205-209.
47. Chen, X., Zhao, C., Rothberg, L., and Ng, M.-K., Plasmon enhancement of bulk heterojunction organic photovoltaic devices by electrode modification. *Applied Physics Letters*, **2008**. 93 (12), 344.
48. Jørgensen, M., Norrman, K., Gevorgyan, S. A., Tromholt, T., Andreasen, B., and Krebs, F. C., Stability of Polymer Solar Cells. *Advanced Materials*, **2012**. 24 (5), 580-612.
49. Po, R., Bernardi, A., Calabrese, A., Carbonera, C., Corso, G., and Pellegrino, A., From lab to fab: how must the polymer solar cell materials design change? – an industrial perspective. *Energy & Environmental Science*, **2014**. 7 (3), 925-943.
50. Huang, J., Yin, Z., and Zheng, Q., Applications of ZnO in organic and hybrid solar cells. *Energy & Environmental Science*, **2011**. 4 (10), 3861-3877.
51. White, M.-S., Olson, D., Shaheen, S., Kopidakis, N., and Ginley, D. S., Inverted bulk-heterojunction organic photovoltaic device using a solution-derived ZnO underlayer. *Applied Physics Letters*, **2006**. 89 (14), 143517.
52. Park, S. H., Roy, A., Beaupré, S., Cho, S., Coates, N., Moon, J. S., Moses, D., Leclerc, M., Lee, K., and Heeger, A. J., Bulk heterojunction solar cells with internal quantum efficiency approaching 100%. *Nature photonics*, **2009**. 3 (5), 297-302.
53. Xiong, J., Yang, B., Zhou, C., Yang, J., Duan, H., Huang, W., Zhang, X., Xia, X., Zhang, L., and Huang, H., Enhanced efficiency and stability of polymer solar cells with TiO₂ nanoparticles buffer layer. *Organic Electronics*, **2014**. 15 (4), 835-843.
54. Bob, B., Song, T.-B., Chen, C.-C., Xu, Z., and Yang, Y., Nanoscale dispersions of gelled SnO₂: material properties and device applications. *Chemistry of Materials*, **2013**. 25 (23), 4725-4730.
55. Niazi, M. R., Munir, R., D'Souza, R. M., Kelly, T. L., and Welch, G. C., Scalable Non-Halogenated Co-solvent System for Large-Area, Four-Layer Slot-Die-Coated Organic Photovoltaics. *ACS Applied Materials & Interfaces*, **2022**. 14 (51), 57055-57063.
56. Chang, Y.-M., Liao, C.-Y., Lee, C.-C., Lin, S.-Y., Teng, N.-W., and Huei-Shuan Tan, P., All solution and ambient processable organic photovoltaic modules fabricated by slot-die coating and achieved a certified 7.56% power conversion efficiency. *Solar Energy Materials and Solar Cells*, **2019**. 202, 110064.

57. Wang, J., Xu, L., Zhang, B., Lee, Y. J., and Hsu, J. W., n-Type doping induced by electron transport layer in organic photovoltaic devices. *Advanced Electronic Materials*, **2017**. 3 (2), 1600458.
58. Andersen, T. R., Almyahi, F., Cooling, N. A., Elkington, D., Wiggins, L., Fahy, A., Feron, K., Vaughan, B., Griffith, M. J., and Mozer, A. J., Comparison of inorganic electron transport layers in fully roll-to-roll coated/printed organic photovoltaics in normal geometry. *Journal of Materials Chemistry A*, **2016**. 4 (41), 15986-15996.
59. Song, S., Lee, K. T., Koh, C. W., Shin, H., Gao, M., Woo, H. Y., Vak, D., and Kim, J. Y., Hot slot die coating for additive-free fabrication of high performance roll-to-roll processed polymer solar cells. *Energy & Environmental Science*, **2018**. 11 (11), 3248-3255.
60. Ylikunnari, M., Välimäki, M., Väisänen, K.-L., Kraft, T. M., Sliz, R., Corso, G., Po, R., Barbieri, R., Carbonera, C., Gorni, G., and Vilkmann, M., Flexible OPV modules for highly efficient indoor applications. *Flexible and Printed Electronics*, **2020**. 5 (1), 014008.
61. Zhao, H., Zhang, L., Naveed, H. B., Lin, B., Zhao, B., Zhou, K., Gao, C., Zhang, C., Wang, C., and Ma, W., Processing-Friendly Slot-Die-Cast Nonfullerene Organic Solar Cells with Optimized Morphology. *ACS Applied Materials & Interfaces*, **2019**. 11 (45), 42392-42402.
62. Zhang, Y.-X., Fang, J., Li, W., Shen, Y., Chen, J.-D., Li, Y., Gu, H., Pelivani, S., Zhang, M., Li, Y., and Tang, J.-X., Synergetic Transparent Electrode Architecture for Efficient Non-Fullerene Flexible Organic Solar Cells with >12% Efficiency. *ACS Nano*, **2019**. 13 (4), 4686-4694.
63. Dayneko, S. V., Pahlevani, M., and Welch, G. C., Indoor Photovoltaics: Photoactive Material Selection, Greener Ink Formulations, and Slot-Die Coated Active Layers. *ACS Applied Materials & Interfaces*, **2019**. 11 (49), 46017-46025.
64. Jasieniak, J. J., Seifert, J., Jo, J., Mates, T., and Heeger, A. J., A Solution-Processed MoO_x Anode Interlayer for Use within Organic Photovoltaic Devices. *Advanced Functional Materials*, **2012**. 22 (12), 2594-2605.
65. Ki, T., Lee, C., Kim, J., Hwang, I.-W., Oh, C.-M., Park, K., Lee, S., Kim, J.-H., Balamurugan, C., Kong, J., Jeong, H.-S., Kwon, S., and Lee, K., Anion-Induced Catalytic Reaction in a Solution-Processed Molybdenum Oxide for Efficient Inverted Ternary Organic Photovoltaics. *Advanced Functional Materials*, **2022**. 32 (35), 2204493.
66. Yang, H.-C., Zha, W., Weng, C.-N., Chen, C.-H., Zan, H.-W., Su, K.-W., Luo, Q., Ma, C.-Q., Chao, Y.-C., and Meng, H.-F., Vacuum-free fabrication of organic solar cell on assembled glass substrates. *Optical Materials*, **2021**. 112, 110683.
67. Chiang, W.-T., Su, S.-H., Lin, Y.-F., and Yokoyama, M., Increasing the fill factor and power conversion efficiency of polymer photovoltaic cell using V₂O₅/CuPc as a buffer layer. *Japanese Journal of Applied Physics*, **2010**. 49 (4S), 04DK14.
68. Wang, H.-Q., Li, N., Guldal, N. S., and Brabec, C. J., Nanocrystal V₂O₅ thin film as hole-extraction layer in normal architecture organic solar cells. *Organic Electronics*, **2012**. 13 (12), 3014-3021.
69. Li, S.-S., Tu, K.-H., Lin, C.-C., Chen, C.-W., and Chhowalla, M., Solution-processable graphene oxide as an efficient hole transport layer in polymer solar cells. *ACS nano*, **2010**. 4 (6), 3169-3174.
70. Murray, I. P., Lou, S. J., Cote, L. J., Loser, S., Kadleck, C. J., Xu, T., Szarko, J. M., Rolczynski, B. S., Johns, J. E., and Huang, J., Graphene oxide interlayers for robust, high-efficiency organic photovoltaics. *The Journal of Physical Chemistry Letters*, **2011**. 2 (24), 3006-3012.
71. Widjonarko, N. E., Ratcliff, E. L., Perkins, C. L., Sigdel, A. K., Zakutayev, A., Ndione, P. F., Gillaspie, D. T., Ginley, D. S., Olson, D. C., and Berry, J. J., Sputtered nickel oxide thin film for efficient hole transport layer in polymer–fullerene bulk-heterojunction organic solar cell. *Thin solid films*, **2012**. 520 (10), 3813-3818.
72. Steirer, K. X., Ndione, P. F., Widjonarko, N. E., Lloyd, M. T., Meyer, J., Ratcliff, E. L., Kahn, A., Armstrong, N. R., Curtis, C. J., and Ginley, D. S., Enhanced efficiency in plastic solar cells via energy matched solution processed NiO_x interlayers. *Advanced Energy Materials*, **2011**. 1 (5), 813-820.
73. Li, M., Zhang, W., Wang, H., Chen, L., Zheng, C., and Chen, R., Effect of organic cathode interfacial layers on efficiency and stability improvement of polymer solar cells. *RSC advances*, **2017**. 7 (50), 31158-31163.

74. Kundu, S., Gollu, S. R., Sharma, R., Srinivas, G., Ashok, A., Kulkarni, A., and Gupta, D., Device stability of inverted and conventional bulk heterojunction solar cells with MoO₃ and ZnO nanoparticles as charge transport layers. *Organic Electronics*, **2013**. 14 (11), 3083-3088.
75. Hau, S. K., Yip, H.-L., Baek, N. S., Zou, J., O'Malley, K., and Jen, A. K.-Y., Air-stable inverted flexible polymer solar cells using zinc oxide nanoparticles as an electron selective layer. *Applied Physics Letters*, **2008**. 92 (25), 253301.
76. Lloyd, M. T., Olson, D. C., Lu, P., Fang, E., Moore, D. L., White, M. S., Reese, M. O., Ginley, D. S., and Hsu, J. W., Impact of contact evolution on the shelf life of organic solar cells. *Journal of Materials Chemistry*, **2009**. 19 (41), 7638-7642.
77. Blom, P. W., Mihailetschi, V. D., Koster, L. J. A., and Markov, D. E., Device physics of polymer: fullerene bulk heterojunction solar cells. *Advanced Materials*, **2007**. 19 (12), 1551-1566.
78. Chueh, C.-C., Yao, K., Yip, H.-L., Chang, C.-Y., Xu, Y.-X., Chen, K.-S., Li, C.-Z., Liu, P., Huang, F., Chen, Y. J. E., and Science, E., Non-halogenated solvents for environmentally friendly processing of high-performance bulk-heterojunction polymer solar cells. **2013**. 6 (11), 3241-3248.
79. Ghasemi, M., Hu, H., Peng, Z., Rech, J. J., Angunawela, I., Carpenter, J. H., Stuard, S. J., Wadsworth, A., McCulloch, I., and You, W., Delineation of thermodynamic and kinetic factors that control stability in non-fullerene organic solar cells. *Joule*, **2019**. 3 (5), 1328-1348.
80. Gueymard, C. A., Myers, D., and Emery, K., Proposed reference irradiance spectra for solar energy systems testing. *Solar energy*, **2002**. 73 (6), 443-467.
81. Mühlbacher, D., Scharber, M., Morana, M., Zhu, Z., Waller, D., Gaudiana, R., and Brabec, C., High photovoltaic performance of a low-bandgap polymer. *Advanced Materials*, **2006**. 18 (21), 2884-2889.
82. Bertrandie, J., Han, J., De Castro, C. S. P., Yengel, E., Gorenflot, J., Anthopoulos, T., Laquai, F., Sharma, A., and Baran, D., The Energy Level Conundrum of Organic Semiconductors in Solar Cells. *Advanced Materials*, **2022**. 34 (35), 2202575.
83. Kroon, R., Lenes, M., Hummelen, J. C., Blom, P. W., and De Boer, B., Small bandgap polymers for organic solar cells (polymer material development in the last 5 years). *Polymer Reviews*, **2008**. 48 (3), 531-582.
84. Li, G., Zhu, R., and Yang, Y., Polymer solar cells. *Nature photonics*, **2012**. 6 (3), 153-161.
85. Kroon, R., Diaz de Zerio Mendaza, A., Himmelberger, S., Bergqvist, J., Bäcke, O., Faria, G. r. C., Gao, F., Obaid, A., Zhuang, W., and Gedefaw, D., A new tetracyclic lactam building block for thick, broad-bandgap photovoltaics. *Journal of the American Chemical Society*, **2014**. 136 (33), 11578-11581.
86. Winder, C. and Sariciftci, N. S., Low bandgap polymers for photon harvesting in bulk heterojunction solar cells. *Journal of Materials Chemistry*, **2004**. 14 (7), 1077-1086.
87. Dou, L., You, J., Yang, J., Chen, C.-C., He, Y., Murase, S., Moriarty, T., Emery, K., Li, G., and Yang, Y., Tandem polymer solar cells featuring a spectrally matched low-bandgap polymer. *Nature Photonics*, **2012**. 6 (3), 180-185.
88. Zhao, F., Wang, C., and Zhan, X., Morphology control in organic solar cells. *Advanced Energy Materials*, **2018**. 8 (28), 1703147.
89. Proctor, C. M. and Nguyen, T.-Q., Effect of leakage current and shunt resistance on the light intensity dependence of organic solar cells. *Applied Physics Letters*, **2015**. 106 (8), 083301.
90. Kang, J.-W., Lee, S.-P., Kim, D.-G., Lee, S., Lee, G.-H., Kim, J.-K., Park, S.-Y., Kim, J. H., Kim, H.-K., and Jeong, Y.-S., Reduction of series resistance in organic photovoltaic using low sheet resistance of ITO electrode. *Electrochemical and Solid State Letters*, **2008**. 12 (3), H64.
91. Kong, J., Song, S., Yoo, M., Lee, G. Y., Kwon, O., Park, J. K., Back, H., Kim, G., Lee, S. H., and Suh, H., Long-term stable polymer solar cells with significantly reduced burn-in loss. *Nature communications*, **2014**. 5 (1), 1-8.
92. Tipnis, R., Bernkopf, J., Jia, S., Krieg, J., Li, S., Storch, M., and Laird, D., Large-area organic photovoltaic module—fabrication and performance. *Solar Energy Materials and Solar Cells*, **2009**. 93 (4), 442-446.

93. Chambon, S., Rivaton, A., Gardette, J.-L., and Firon, M., Photo-and thermo-oxidation of poly (p-phenylene-vinylene) and phenylene-vinylene oligomer. *Polymer degradation and Stability*, **2011**. 96 (6), 1149-1158.
94. Manceau, M., Rivaton, A., Gardette, J.-L., Guillerez, S., and Lemaître, N., The mechanism of photo-and thermooxidation of poly (3-hexylthiophene)(P3HT) reconsidered. *Polymer Degradation and Stability*, **2009**. 94 (6), 898-907.
95. Tournebize, A., Bussi re, P. O., Wong-Wah-Chung, P., Th rias, S., Rivaton, A., Gardette, J. L., Beaupr , S., and Leclerc, M., Impact of UV-visible light on the morphological and photochemical behavior of a low-bandgap poly (2, 7-Carbazole) derivative for use in high-performance solar cells. *Advanced Energy Materials*, **2013**. 3 (4), 478-487.
96. Destouesse, E., Top, M., Lamminaho, J., Rubahn, H. G., Fahlteich, J., and Madsen, M., Slot-die processing and encapsulation of non-fullerene based ITO-free organic solar cells and modules. *Flexible and Printed Electronics*, **2019**. 4 (4), 045004.
97. Weng, C.-N., Yang, H.-C., Tsai, C.-Y., Chen, S.-H., Chen, Y.-S., Chen, C.-H., Huang, K.-M., Meng, H.-F., Chao, Y.-C., and Chang, C.-Y., The influence of UV filter and Al/Ag moisture barrier layer on the outdoor stability of polymer solar cells. *Solar Energy*, **2020**. 199, 308-316.
98. Du, X., Heumueller, T., Gruber, W., Classen, A., Unruh, T., Li, N., and Brabec, C. J., Efficient Polymer Solar Cells Based on Non-fullerene Acceptors with Potential Device Lifetime Approaching 10 Years. *Joule*, **2019**. 3 (1), 215-226.
99. Chochos, C. L., Leclerc, N., Gasparini, N., Zimmerman, N., Tatsi, E., Katsouras, A., Moschovas, D., Serpetzoglou, E., Konidakis, I., and Fall, S., The role of chemical structure in indacenodithienothiophene-alt-benzothiadiazole copolymers for high performance organic solar cells with improved photo-stability through minimization of burn-in loss. *Journal of Materials Chemistry A*, **2017**. 5 (47), 25064-25076.
100. Rivaton, A., Chambon, S., Manceau, M., Gardette, J.-L., Lemaître, N., and Guillerez, S., Light-induced degradation of the active layer of polymer-based solar cells. *Polymer Degradation and Stability*, **2010**. 95 (3), 278-284.
101. Manceau, M., Chambon, S., Rivaton, A., Gardette, J.-L., Guillerez, S., and Lemaître, N., Effects of long-term UV-visible light irradiation in the absence of oxygen on P3HT and P3HT: PCBM blend. *Solar Energy Materials and Solar Cells*, **2010**. 94 (10), 1572-1577.
102. Hintz, H., Egelhaaf, H.-J., Peisert, H., and Chass , T., Photo-oxidation and ozonization of poly (3-hexylthiophene) thin films as studied by UV/VIS and photoelectron spectroscopy. *Polymer Degradation and Stability*, **2010**. 95 (5), 818-825.
103. Schafferhans, J., Baumann, A., Wagenpfahl, A., Deibel, C., and Dyakonov, V., Oxygen doping of P3HT: PCBM blends: Influence on trap states, charge carrier mobility and solar cell performance. *Organic Electronics*, **2010**. 11 (10), 1693-1700.
104. Seemann, A., Sauermann, T., Lungenschmied, C., Armbruster, O., Bauer, S., Egelhaaf, H.-J., and Hauch, J., Reversible and irreversible degradation of organic solar cell performance by oxygen. *Solar Energy*, **2011**. 85 (6), 1238-1249.
105. Adams, J., Salvador, M., Lucera, L., Langner, S., Spyropoulos, G. D., Fecher, F. W., Voigt, M. M., Dowland, S. A., Osvet, A., and Egelhaaf, H. J., Water ingress in encapsulated inverted organic solar cells: Correlating infrared imaging and photovoltaic performance. *Advanced Energy Materials*, **2015**. 5 (20), 1501065.
106. Glatthaar, M., Riede, M., Keegan, N., Sylvester-Hvid, K., Zimmermann, B., Niggemann, M., Hinsch, A., and Gombert, A., Efficiency limiting factors of organic bulk heterojunction solar cells identified by electrical impedance spectroscopy. *Solar energy materials and solar cells*, **2007**. 91 (5), 390-393.
107. Ahmad, J., Bazaka, K., Anderson, L. J., White, R. D., and Jacob, M. V., Materials and methods for encapsulation of OPV: A review. *Renewable and Sustainable Energy Reviews*, **2013**. 27, 104-117.
108. Xu, Y., Yuan, J., Zhou, S., Seifrid, M., Ying, L., Li, B., Huang, F., Bazan, G. C., and Ma, W., Ambient Processable and Stable All-Polymer Organic Solar Cells. *Advanced Functional Materials*, **2019**. 29 (8), 1806747.
109. Krebs, F. C., Gevorgyan, S. A., and Alstrup, J., A roll-to-roll process to flexible polymer solar cells: model studies, manufacture and operational stability studies. *Journal of Materials Chemistry*, **2009**. 19 (30), 5442-5451.

110. Dupont, S. R., Voroshazi, E., Heremans, P., and Dauskardt, R. H., Adhesion properties of inverted polymer solar cells: Processing and film structure parameters. *Organic Electronics*, **2013**. *14* (5), 1262-1270.
111. Dupont, S. R., Novoa, F., Voroshazi, E., and Dauskardt, R. H., Decohesion kinetics of PEDOT: PSS conducting polymer films. *Advanced functional materials*, **2014**. *24* (9), 1325-1332.
112. Bruner, C., Novoa, F., Dupont, S., and Dauskardt, R., Decohesion kinetics in polymer organic solar cells. *ACS applied materials & interfaces*, **2014**. *6* (23), 21474-21483.
113. Liu, J., Buchholz, D. B., Chang, R. P. H., Facchetti, A., and Marks, T. J., High-Performance Flexible Transparent Thin-Film Transistors Using a Hybrid Gate Dielectric and an Amorphous Zinc Indium Tin Oxide Channel. *Advanced Materials*, **2010**. *22* (21), 2333-2337.
114. Cairns, D. R., Witte, R. P., Sparacin, D. K., Sachsman, S. M., Paine, D. C., Crawford, G. P., and Newton, R. R., Strain-dependent electrical resistance of tin-doped indium oxide on polymer substrates. *Applied Physics Letters*, **2000**. *76* (11), 1425-1427.
115. Yan, T., Song, W., Huang, J., Peng, R., Huang, L., and Ge, Z., 16.67% Rigid and 14.06% Flexible Organic Solar Cells Enabled by Ternary Heterojunction Strategy. **2019**. *31* (39), 1902210.
116. Kim, Y.-S., Chang, M.-H., Lee, E.-J., Ihm, D.-W., and Kim, J.-Y., Improved electrical conductivity of PEDOT-based electrode films hybridized with silver nanowires. *Synthetic Metals*, **2014**. *195*, 69-74.
117. Lei, T., Peng, R., Song, W., Hong, L., Huang, J., Fei, N., and Ge, Z., Bendable and foldable flexible organic solar cells based on Ag nanowire films with 10.30% efficiency. *Journal of Materials Chemistry A*, **2019**. *7* (8), 3737-3744.
118. Sears, K. K., Fievez, M., Gao, M., Weerasinghe, H. C., Easton, C. D., and Vak, D., ITO-Free Flexible Perovskite Solar Cells Based on Roll-to-Roll, Slot-Die Coated Silver Nanowire Electrodes. **2017**. *1* (8), 1700059.
119. Dong, X., Shi, P., Sun, L., Li, J., Qin, F., Xiong, S., Liu, T., Jiang, X., and Zhou, Y., Flexible nonfullerene organic solar cells based on embedded silver nanowires with an efficiency up to 11.6%. *Journal of Materials Chemistry A*, **2019**. *7* (5), 1989-1995.
120. Paci, B., Generosi, A., Rossi Albertini, V., Perfetti, P., de Bettignies, R., Leroy, J., Firon, M., and Sentein, C., Controlling photoinduced degradation in plastic photovoltaic cells: A time-resolved energy dispersive x-ray reflectometry study. *Applied physics letters*, **2006**. *89* (4), 043507.
121. Andreasen, J. W., Gevorgyan, S. A., Schlepütz, C. M., and Krebs, F. C., Applicability of X-ray reflectometry to studies of polymer solar cell degradation. *Solar energy materials and solar cells*, **2008**. *92* (7), 793-798.
122. Yang, X., Loos, J., Veenstra, S. C., Verhees, W. J., Wienk, M. M., Kroon, J. M., Michels, M. A., and Janssen, R. A., Nanoscale morphology of high-performance polymer solar cells. *Nano letters*, **2005**. *5* (4), 579-583.
123. Krebs, F. C., Alstrup, J., Spanggaard, H., Larsen, K., and Kold, E., Production of large-area polymer solar cells by industrial silk screen printing, lifetime considerations and lamination with polyethyleneterephthalate. *Solar Energy Materials and Solar Cells*, **2004**. *83* (2), 293-300.
124. Krebs, F. C., Biancardo, M., Winther-Jensen, B., Spanggaard, H., and Alstrup, J., Strategies for incorporation of polymer photovoltaics into garments and textiles. *Solar Energy Materials and Solar Cells*, **2006**. *90* (7-8), 1058-1067.
125. Winther-Jensen, B. and Krebs, F. C., High-conductivity large-area semi-transparent electrodes for polymer photovoltaics by silk screen printing and vapour-phase deposition. *Solar Energy Materials and Solar Cells*, **2006**. *90* (2), 123-132.
126. Greenbank, W., Hirsch, L., Wantz, G., and Chambon, S., Interfacial thermal degradation in inverted organic solar cells. *Applied Physics Letters*, **2015**. *107* (26), 263301.
127. Greenbank, W., Rolston, N., Destouesse, E., Wantz, G., Hirsch, L., Dauskardt, R., and Chambon, S., Improved mechanical adhesion and electronic stability of organic solar cells with thermal ageing: the role of diffusion at the hole extraction interface. *Journal of Materials Chemistry A*, **2017**. *5* (6), 2911-2919.

128. Lindqvist, C., Stability of Bulk-heterojunction Blends for Solar Cell Applications. 2014: Chalmers University of Technology.
129. Cowie, J. M. G. and Arrighi, V., Polymers: chemistry and physics of modern materials. 2007: CRC press.
130. Fillon, B., Thierry, A., Lotz, B., and Wittmann, J., Efficiency scale for polymer nucleating agents. *Journal of thermal analysis*, **1994**. 42 (4), 721-731.
131. Lindqvist, C., Sanz-Velasco, A., Wang, E., Bäcke, O., Gustafsson, S., Olsson, E., Andersson, M. R., and Müller, C., Nucleation-limited fullerene crystallisation in a polymer–fullerene bulk-heterojunction blend. *Journal of Materials Chemistry A*, **2013**. 1 (24), 7174-7180.
132. Lindqvist, C., Bergqvist, J., Feng, C. C., Gustafsson, S., Bäcke, O., Treat, N. D., Bounioux, C., Henriksson, P., Kroon, R., Wang, E., Sanz-Velasco, A., Kristiansen, P. M., Stingelin, N., Olsson, E., Inganäs, O., Andersson, M. R., and Müller, C., Fullerene nucleating agents: a route towards thermally stable photovoltaic blends. *Advanced Energy Materials*, **2014**. 4 (9), 1301437.
133. Feng, W., Lin, Z., Cui, J., Lv, W., Wang, W., and Ling, Q., Photoactive layer crosslinking in all-polymer solar cells: Stabilized morphology and enhanced thermal-stability. *Solar Energy Materials and Solar Cells*, **2019**. 200, 109982.
134. Yang, F., Zhao, W., Zhu, Q., Li, C., Ma, W., Hou, J., and Li, W., Boosting the Performance of Non-Fullerene Organic Solar Cells via Cross-Linked Donor Polymers Design. *Macromolecules*, **2019**. 52 (5), 2214-2221.
135. He, Y., Heumüller, T., Lai, W., Feng, G., Classen, A., Du, X., Liu, C., Li, W., Li, N., and Brabec, C. J., Evidencing Excellent Thermal- and Photostability for Single-Component Organic Solar Cells with Inherently Built-In Microstructure. *Advanced Energy Materials*, **2019**. 9 (21), 1900409.
136. Pan, M.-A., Lau, T.-K., Tang, Y., Wu, Y.-C., Liu, T., Li, K., Chen, M.-C., Lu, X., Ma, W., and Zhan, C., 16.7%-efficiency ternary blended organic photovoltaic cells with PCBM as the acceptor additive to increase the open-circuit voltage and phase purity. *Journal of Materials Chemistry A*, **2019**. 7 (36), 20713-20722.
137. Zheng, N., Mahmood, K., Zhong, W., Liu, F., Zhu, P., Wang, Z., Xie, B., Chen, Z., Zhang, K., Ying, L., Huang, F., and Cao, Y., Improving the efficiency and stability of non-fullerene polymer solar cells by using N2200 as the Additive. *Nano Energy*, **2019**. 58, 724-731.
138. Wang, Z., Nian, Y., Jiang, H., Pan, F., Hu, Z., Zhang, L., Cao, Y., and Chen, J., High Voc ternary nonfullerene polymer solar cells with improved efficiency and good thermal stability. *Organic Electronics*, **2019**. 69, 174-180.
139. Alem, S., Graddage, N., Lu, J., Kololuoma, T., Movileanu, R., and Tao, Y., Flexographic printing of polycarbazole-based inverted solar cells. *Organic Electronics*, **2018**. 52, 146-152.
140. Takahira, K., Toda, A., Suzuki, K., and Fukuda, T., Highly efficient organic photovoltaic cells fabricated by electrospray deposition using a non-halogenated solution. *physica status solidi (a)*, **2017**. 214 (3), 1600536.
141. Tsai, P.-T., Yu, K.-C., Chang, C.-J., Horng, S.-F., and Meng, H.-F., Large-area organic solar cells by accelerated blade coating. *Organic Electronics*, **2015**. 22, 166-172.
142. Hernandez, Jeff L., Deb, N., Wolfe, R. M. W., Lo, C. K., Engmann, S., Richter, L. J., and Reynolds, J. R., Simple transfer from spin coating to blade coating through processing aggregated solutions. *Journal of Materials Chemistry A*, **2017**. 5 (39), 20687-20695.
143. Huang, Y.-C., Cha, H.-C., Chen, C.-Y., and Tsao, C.-S., A universal roll-to-roll slot-die coating approach towards high-efficiency organic photovoltaics. *Progress in Photovoltaics: Research and Applications*, **2017**. 25 (11), 928-935.
144. Lee, J., Seo, Y.-H., Kwon, S.-N., Kim, D.-H., Jang, S., Jung, H., Lee, Y., Weerasinghe, H., Kim, T., Kim, J. Y., Vak, D., and Na, S.-I., Slot-Die and Roll-to-Roll Processed Single Junction Organic Photovoltaic Cells with the Highest Efficiency. **2019**. 9 (36), 1901805.
145. Kirk, B., Pan, X., Jevric, M., Andersson, G., and Andersson, M. R., Introducing neat fullerenes to improve the thermal stability of slot-die coated organic solar cells. *Materials Advances*, **2022**.

146. Camarada, M. B., Saldías, C., Castro-Castillo, C., and Angel, F. A., Evaluation of electro-synthesized oligothiophenes as donor materials in vacuum-processed organic photovoltaic devices. *Materials Letters*, **2023**. 339, 134114.
147. Xi, X., Li, W., Wu, J., Ji, J., Shi, Z., and Li, G., A comparative study on the performances of small molecule organic solar cells based on CuPc/C60 and CuPc/C70. *Solar Energy Materials and Solar Cells*, **2010**. 94 (12), 2435-2441.
148. Yagui, J. and Angel, F. A., Benzodithiophene-based small molecules for vacuum-processed organic photovoltaic devices. *Optical Materials*, **2020**. 109, 110354.
149. Chen, C.-H., Ting, H.-C., Li, Y.-Z., Lo, Y.-C., Sher, P.-H., Wang, J.-K., Chiu, T.-L., Lin, C.-F., Hsu, I. S., Lee, J.-H., Liu, S.-W., and Wong, K.-T., New D–A–A-Configured Small-Molecule Donors for High-Efficiency Vacuum-Processed Organic Photovoltaics under Ambient Light. *ACS Applied Materials & Interfaces*, **2019**. 11 (8), 8337-8349.
150. Iannaccone, G., Välimäki, M., Jansson, E., Sunnari, A., Corso, G., Bernardi, A., Levi, M., Turri, S., Hast, J., and Griffini, G., Roll-to-roll compatible flexible polymer solar cells incorporating a water-based solution-processable silver back electrode with low annealing temperature. *Solar Energy Materials and Solar Cells*, **2015**. 143, 227-235.
151. Krebs, F. C., Tromholt, T., and Jørgensen, M., Upscaling of polymer solar cell fabrication using full roll-to-roll processing. *Nanoscale*, **2010**. 2 (6), 873-886.
152. Garg, A., Gupta, S. K., Jasieniak, J. J., Singh, T. B., and Watkins, S. E., Improved lifetimes of organic solar cells with solution-processed molybdenum oxide anode-modifying layers. *Progress in Photovoltaics: Research and Applications*, **2015**. 23 (8), 989-996.
153. Lima, F. A. S., Beliatas, M. J., Roth, B., Andersen, T. R., Bortoti, A., Reyna, Y., Castro, E., Vasconcelos, I. F., Gevorgyan, S. A., Krebs, F. C., and Lira-Cantu, M., Flexible ITO-free organic solar cells applying aqueous solution-processed V2O5 hole transport layer: An outdoor stability study. *APL Materials*, **2016**. 4 (2), 026104.
154. La Notte, L., Bianco, G. V., Palma, A. L., Di Carlo, A., Bruno, G., and Reale, A., Sprayed organic photovoltaic cells and mini-modules based on chemical vapor deposited graphene as transparent conductive electrode. *Carbon*, **2018**. 129, 878-883.
155. Lee, C.-Y., Tsao, C.-S., Lin, H.-K., Cha, H.-C., Chung, T.-Y., Sung, Y.-M., and Huang, Y.-C., Encapsulation improvement and stability of ambient roll-to-roll slot-die-coated organic photovoltaic modules. *Solar Energy*, **2021**. 213, 136-144.
156. Griffith, M. J., Cooling, N. A., Vaughan, B., O'Donnell, K. M., Al-Mudhaffer, M. F., Al-Ahmad, A., Noori, M., Almyahi, F., Belcher, W. J., and Dastoor, P. C., Roll-to-Roll Sputter Coating of Aluminum Cathodes for Large-Scale Fabrication of Organic Photovoltaic Devices. **2015**. 3 (4), 428-436.
157. Willmann, J., Stocker, D., and Dörsam, E., Characteristics and evaluation criteria of substrate-based manufacturing. Is roll-to-roll the best solution for printed electronics? *Organic Electronics*, **2014**. 15 (7), 1631-1640.
158. Chang, Y.-H., Tseng, S.-R., Chen, C.-Y., Meng, H.-F., Chen, E.-C., Horng, S.-F., and Hsu, C.-S., Polymer solar cell by blade coating. *Organic Electronics*, **2009**. 10 (5), 741-746.
159. Lim, F. J., Ananthanarayanan, K., Luther, J., and Ho, G. W., Influence of a novel fluorosurfactant modified PEDOT:PSS hole transport layer on the performance of inverted organic solar cells. *Journal of Materials Chemistry*, **2012**. 22 (48), 25057-25064.
160. Kapnopoulos, C., Mekeridis, E. D., Tzounis, L., Polyzoidis, C., Zachariadis, A., Tsimikli, S., Gravalidis, C., Laskarakis, A., Vouroutzis, N., and Logothetidis, S., Fully gravure printed organic photovoltaic modules: A straightforward process with a high potential for large scale production. *Solar Energy Materials and Solar Cells*, **2016**. 144, 724-731.
161. Hoff, A., Gasonoo, A., Pahlevani, M., and Welch, G. C., An Alcohol-Soluble N-Annulated Perylene Diimide Cathode Interlayer for Air-Processed, Slot-Die Coated Organic Photovoltaic Devices and Large-Area Modules. *Solar RRL*, **2022**. 6 (11), 2200691.
162. Hart, A. S., Andersen, T. R., Griffith, M. J., Fahy, A., Vaughan, B., Belcher, W. J., and Dastoor, P. C., Roll-to-roll solvent annealing of printed P3HT : ICXA devices. *RSC Advances*, **2019**. 9 (72), 42294-42305.
163. Krebs, F. C., Fyenbo, J., and Jørgensen, M., Product integration of compact roll-to-roll processed polymer solar cell modules: methods and manufacture using flexographic printing, slot-die coating and rotary screen printing. *Journal of Materials Chemistry*, **2010**. 20 (41), 8994-9001.

164. Hösel, M., Søndergaard, R. R., Jørgensen, M., and Krebs, F. C., Fast Inline Roll-to-Roll Printing for Indium-Tin-Oxide-Free Polymer Solar Cells Using Automatic Registration. *Energy Technology*, **2013**. 1 (1), 102-107.
165. Bao, S., Yang, H., Fan, H., Zhang, J., Wei, Z., Cui, C., and Li, Y., Volatilizable Solid Additive-Assisted Treatment Enables Organic Solar Cells with Efficiency over 18.8% and Fill Factor Exceeding 80%. *Advanced Materials*, **2021**. 33 (48), 2105301.
166. An, Q., Wang, J., Gao, W., Ma, X., Hu, Z., Gao, J., Xu, C., Hao, M., Zhang, X., Yang, C., and Zhang, F., Alloy-like ternary polymer solar cells with over 17.2% efficiency. *Science Bulletin*, **2020**. 65 (7), 538-545.
167. Liu, Q., Jiang, Y., Jin, K., Qin, J., Xu, J., Li, W., Xiong, J., Liu, J., Xiao, Z., and Sun, K., 18% Efficiency organic solar cells. *Science Bulletin*, **2020**. 65 (4), 272-275.
168. Krebs, F. C., Fabrication and processing of polymer solar cells: a review of printing and coating techniques. *Solar energy materials and solar cells*, **2009**. 93 (4), 394-412.
169. Chen, D., Nakahara, A., Wei, D., Nordlund, D., and Russell, T. P., P3HT/PCBM bulk heterojunction organic photovoltaics: correlating efficiency and morphology. *Nano letters*, **2011**. 11 (2), 561-567.
170. Vanlaeke, P., Swinnen, A., Haeldermans, I., Vanhoyland, G., Aernouts, T., Cheyns, D., Deibel, C., D'Haen, J., Heremans, P., and Poortmans, J., P3HT/PCBM bulk heterojunction solar cells: Relation between morphology and electro-optical characteristics. *Solar energy materials and solar cells*, **2006**. 90 (14), 2150-2158.
171. Zhao, J., Swinnen, A., Van Assche, G., Manca, J., Vanderzande, D., and Mele, B. V., Phase diagram of P3HT/PCBM blends and its implication for the stability of morphology. *The Journal of Physical Chemistry B*, **2009**. 113 (6), 1587-1591.
172. Zhang, L., Lin, B., Hu, B., Xu, X., and Ma, W., Blade-Cast Nonfullerene Organic Solar Cells in Air with Excellent Morphology, Efficiency, and Stability. *Advanced Materials*, **2018**. 30 (22), 1800343.
173. Zhao, W., Qian, D., Zhang, S., Li, S., Inganäs, O., Gao, F., and Hou, J., Fullerene-free polymer solar cells with over 11% efficiency and excellent thermal stability. *Advanced materials*, **2016**. 28 (23), 4734-4739.
174. Liang, Q., Han, J., Song, C., Yu, X., Smilgies, D.-M., Zhao, K., Liu, J., and Han, Y., Reducing the confinement of PBDB-T to ITIC to improve the crystallinity of PBDB-T/ITIC blends. *Journal of Materials Chemistry A*, **2018**. 6 (32), 15610-15620.
175. Perdigón-Toro, L., Zhang, H., Markina, A., Yuan, J., Hosseini, S. M., Wolff, C. M., Zuo, G., Stolterfoht, M., Zou, Y., and Gao, F., Barrierless free charge generation in the high-performance PM6: Y6 bulk heterojunction non-fullerene solar cell. *Advanced Materials*, **2020**. 32 (9), 1906763.
176. Lin, Y., Adilbekova, B., Firdaus, Y., Yengel, E., Faber, H., Sajjad, M., Zheng, X., Yarali, E., Seitkhan, A., and Bakr, O. M., 17% efficient organic solar cells based on liquid exfoliated WS₂ as a replacement for PEDOT: PSS. *Advanced materials*, **2019**. 31 (46), 1902965.
177. Barrera, D., Lee, Y.-J., and Hsu, J. W., Influence of ZnO sol-gel electron transport layer processing on BHJ active layer morphology and OPV performance. *Solar energy materials and solar cells*, **2014**. 125, 27-32.
178. Zhang, C., You, H., Lin, Z., and Hao, Y., Inverted organic photovoltaic cells with solution-processed zinc oxide as electron collecting layer. *Japanese Journal of Applied Physics*, **2011**. 50 (8R), 082302.
179. Jagadamma, L. K., Al-Senani, M., El-Labban, A., Gereige, I., Ngongang Ndjawa, G. O., Faria, J. C., Kim, T., Zhao, K., Cruciani, F., and Anjum, D. H., Polymer solar cells with efficiency > 10% enabled via a facile solution-processed Al-doped ZnO electron transporting layer. *Advanced Energy Materials*, **2015**. 5 (12), 1500204.
180. Jiang, Z., Soltanian, S., Gholamkhash, B., Aljaafari, A., and Servati, P., Light-soaking free organic photovoltaic devices with sol-gel deposited ZnO and AZO electron transport layers. *RSC advances*, **2018**. 8 (64), 36542-36548.
181. Murdoch, G., Hinds, S., Sargent, E., Tsang, S., Mordoukhovski, L., and Lu, Z., Aluminum doped zinc oxide for organic photovoltaics. *Applied physics letters*, **2009**. 94 (21), 138.
182. Cameron, J. and Skabara, P. J., The damaging effects of the acidity in PEDOT: PSS on semiconductor device performance and solutions based on non-acidic alternatives. *Materials Horizons*, **2020**. 7 (7), 1759-1772.

183. Park, H., Shi, Y., and Kong, J., Application of solvent modified PEDOT: PSS to graphene electrodes in organic solar cells. *Nanoscale*, **2013**. 5 (19), 8934-8939.
184. Zhu, R., Chung, C.-H., Cha, K. C., Yang, W., Zheng, Y. B., Zhou, H., Song, T.-B., Chen, C.-C., Weiss, P. S., Li, G., and Yang, Y., Fused Silver Nanowires with Metal Oxide Nanoparticles and Organic Polymers for Highly Transparent Conductors. *ACS Nano*, **2011**. 5 (12), 9877-9882.
185. Søndergaard, R., Hösel, M., Angmo, D., Larsen-Olsen, T. T., and Krebs, F. C., Roll-to-roll fabrication of polymer solar cells. *Materials today*, **2012**. 15 (1-2), 36-49.
186. Tsai, C.-Y., Lin, Y.-H., Chang, Y.-M., Kao, J.-C., Liang, Y.-C., Liu, C.-C., Qiu, J., Wu, L., Liao, C.-Y., Tan, H.-S., Chao, Y.-C., Horng, S.-F., Zan, H.-W., Meng, H.-F., and Li, F., Large area organic photovoltaic modules fabricated on a 30 cm by 20 cm substrate with a power conversion efficiency of 9.5%. *Solar Energy Materials and Solar Cells*, **2020**. 218, 110762.
187. Välimäki, M., Apilo, P., Po, R., Jansson, E., Bernardi, A., Ylikunnari, M., Vilkmann, M., Corso, G., Puustinen, J., Tuominen, J., and Hast, J., R2R-printed inverted OPV modules – towards arbitrary patterned designs. *Nanoscale*, **2015**. 7 (21), 9570-9580.
188. Miranda, B. H., Corrêa, L. d. Q., Soares, G. A., Martins, J. L., Lopes, P. L., Vilela, M. L., Rodrigues, J. F., Cunha, T. G., Vilaça, R. d. Q., and Castro-Hermosa, S., Efficient fully roll-to-roll coated encapsulated organic solar module for indoor applications. *Solar Energy*, **2021**. 220, 343-353.
189. Liao, C.-Y., Hsiao, Y.-T., Tsai, K.-W., Teng, N.-W., Li, W.-L., Wu, J.-L., Kao, J.-C., Lee, C.-C., Yang, C.-M., Tan, H.-S., Chung, K.-H., and Chang, Y.-M., Photoactive Material for Highly Efficient and All Solution-Processed Organic Photovoltaic Modules: Study on the Efficiency, Stability, and Synthetic Complexity. *Solar RRL*, **2021**. 5 (3), 2000749.
190. Guo, F., Kubis, P., Stubhan, T., Li, N., Baran, D., Przybilla, T., Spiecker, E., Forberich, K., and Brabec, C. J., Fully Solution-Processing Route toward Highly Transparent Polymer Solar Cells. *ACS Applied Materials & Interfaces*, **2014**. 6 (20), 18251-18257.
191. Pérez-Gutiérrez, E., Lozano, J., Gaspar-Tánori, J., Maldonado, J.-L., Gómez, B., López, L., Amores-Tapia, L.-F., Barbosa-García, O., and Percino, M.-J., Organic solar cells all made by blade and slot–die coating techniques. *Solar Energy*, **2017**. 146, 79-84.
192. Sankaran, S., Glaser, K., Gärtner, S., Rödlmeier, T., Sudau, K., Hernandez-Sosa, G., and Colmann, A., Fabrication of polymer solar cells from organic nanoparticle dispersions by doctor blading or ink-jet printing. *Organic Electronics*, **2016**. 28, 118-122.
193. Strohm, S., Machui, F., Langner, S., Kubis, P., Gasparini, N., Salvador, M., McCulloch, I., Egelhaaf, H. J., and Brabec, C. J., P3HT: non-fullerene acceptor based large area, semi-transparent PV modules with power conversion efficiencies of 5%, processed by industrially scalable methods. *Energy & Environmental Science*, **2018**. 11 (8), 2225-2234.
194. Ye, L., Xiong, Y., Yao, H., Gadisa, A., Zhang, H., Li, S., Ghasemi, M., Balar, N., Hunt, A., O'Connor, B. T., Hou, J., and Ade, H., High Performance Organic Solar Cells Processed by Blade Coating in Air from a Benign Food Additive Solution. *Chemistry of Materials*, **2016**. 28 (20), 7451-7458.
195. Tait, J. G., Merckx, T., Li, W., Wong, C., Gehlhaar, R., Cheyns, D., Turbiez, M., and Heremans, P., Determination of Solvent Systems for Blade Coating Thin Film Photovoltaics. *Advanced Functional Materials*, **2015**. 25 (22), 3393-3398.
196. Hong, L., Yao, H., Wu, Z., Cui, Y., Zhang, T., Xu, Y., Yu, R., Liao, Q., Gao, B., Xian, K., Woo, H. Y., Ge, Z., and Hou, J., Eco-Compatible Solvent-Processed Organic Photovoltaic Cells with Over 16% Efficiency. *Advanced Materials*, **2019**. 31 (39), 1903441.
197. Liao, C.-Y., Chen, Y., Lee, C.-C., Wang, G., Teng, N.-W., Lee, C.-H., Li, W.-L., Chen, Y.-K., Li, C.-H., Ho, H.-L., Tan, P. H.-S., Wang, B., Huang, Y.-C., Young, R. M., Wasielewski, M. R., Marks, T. J., Chang, Y.-M., and Facchetti, A., Processing Strategies for an Organic Photovoltaic Module with over 10% Efficiency. *Joule*, **2020**. 4 (1), 189-206.
198. Zhao, W., Zhang, S., Zhang, Y., Li, S., Liu, X., He, C., Zheng, Z., and Hou, J., Environmentally Friendly Solvent-Processed Organic Solar Cells that are Highly Efficient and Adaptable for the Blade-Coating Method. *Advanced Materials*, **2018**. 30 (4), 1704837.
199. Sundaresan, C., Alem, S., Radford, C. L., Grant, T. M., Kelly, T. L., Lu, J., Tao, Y., and Lessard, B. H., Changes in Optimal Ternary Additive Loading when Processing Large Area

- Organic Photovoltaics by Spin- versus Blade-Coating Methods. *Solar RRL*, **2021**. 5 (10), 2100432.
200. Schneider, A., Traut, N., and Hamburger, M., Analysis and optimization of relevant parameters of blade coating and gravure printing processes for the fabrication of highly efficient organic solar cells. *Solar Energy Materials and Solar Cells*, **2014**. 126, 149-154.
 201. Cui, Y., Yao, H., Hong, L., Zhang, T., Tang, Y., Lin, B., Xian, K., Gao, B., An, C., Bi, P., Ma, W., and Hou, J., Organic photovoltaic cell with 17% efficiency and superior processability. *National Science Review*, **2019**. 7 (7), 1239-1246.
 202. Schneider, S. A., Gu, K. L., Yan, H., Abdelsamie, M., Bao, Z., and Toney, M. F., Controlling Polymer Morphology in Blade-Coated All-Polymer Solar Cells. *Chemistry of Materials*, **2021**. 33 (15), 5951-5961.
 203. Aïch, B. R., Lu, J., Moisa, S., Movileanu, R., Estwick, E., and Tao, Y., Ink formulation for organic photovoltaic active layers using non-halogenated main solvent for blade coating process. *Synthetic Metals*, **2020**. 269, 116513.
 204. Rodríguez-Martínez, X., Sevim, S., Xu, X., Franco, C., Pamies-Puig, P., Córcoles-Guija, L., Rodríguez-Trujillo, R., del Campo, F. J., Rodríguez San Miguel, D., deMello, A. J., Pané, S., Amabilino, D. B., Inganäs, O., Puigmartí-Luis, J., and Campoy-Quiles, M., Microfluidic-Assisted Blade Coating of Compositional Libraries for Combinatorial Applications: The Case of Organic Photovoltaics. *Advanced Energy Materials*, **2020**. 10 (33), 2001308.
 205. Yu, R., Yao, H., Cui, Y., Hong, L., He, C., and Hou, J., Improved Charge Transport and Reduced Nonradiative Energy Loss Enable Over 16% Efficiency in Ternary Polymer Solar Cells. *Advanced Materials*, **2019**. 31 (36), 1902302.
 206. Schmidt-Hansberg, B., Sanyal, M., Grossiord, N., Galagan, Y., Baunach, M., Klein, M. F. G., Colsmann, A., Scharfer, P., Lemmer, U., Dosch, H., Michels, J., Barrena, E., and Schabel, W., Investigation of non-halogenated solvent mixtures for high throughput fabrication of polymer–fullerene solar cells. *Solar Energy Materials and Solar Cells*, **2012**. 96, 195-201.
 207. Kadam, K. D., Kim, H., Rehman, S., Patil, H., Aziz, J., Dongale, T. D., Khan, M. F., and Kim, D.-k., Optimization of ZnO:PEIE as an Electron Transport Layer for Flexible Organic Solar Cells. *Energy & Fuels*, **2021**. 35 (15), 12416-12424.
 208. Chaturvedi, N., Gasparini, N., Corzo, D., Bertrandie, J., Wehbe, N., Troughton, J., and Baran, D., All Slot-Die Coated Non-Fullerene Organic Solar Cells with PCE 11%. *Advanced Functional Materials*, **2021**. n/a (n/a), 2009996.
 209. Zhao, Y., Wang, G., Wang, Y., Xiao, T., Adil, M. A., Lu, G., Zhang, J., and Wei, Z., A Sequential Slot-Die Coated Ternary System Enables Efficient Flexible Organic Solar Cells. *Solar RRL*, **2019**. 3 (3), 1800333.
 210. Tintori, F. and Welch, G. C., Ambient Condition, Three-Layer Slot-Die Coated Organic Photovoltaics with PCE of 10%. *Advanced Materials Interfaces*, **2022**. 9 (2), 2101418.
 211. Zimmermann, B., Schleiermacher, H.-F., Niggemann, M., Würfel, U., and Cells, S., ITO-free flexible inverted organic solar cell modules with high fill factor prepared by slot die coating. *Solar Energy Materials and Solar Cells*, **2011**. 95 (7), 1587-1589.
 212. Zhang, Y. M., Izquierdo, R., and Xiao, S. S. Printing of Flexible, Large-Area Organic Photovoltaic Cells. in *2018 International Flexible Electronics Technology Conference (IFETC)*. 2018.
 213. Carlé, J. E., Andreasen, B., Tromholt, T., Madsen, M. V., Norrman, K., Jørgensen, M., and Krebs, F. C., Comparative studies of photochemical cross-linking methods for stabilizing the bulk hetero-junction morphology in polymer solar cells. *Journal of Materials Chemistry*, **2012**. 22 (46), 24417-24423.
 214. Angmo, D., Andersen, T. R., Bentzen, J. J., Helgesen, M., Søndergaard, R. R., Jørgensen, M., Carlé, J. E., Bundgaard, E., and Krebs, F. C., Roll-to-Roll Printed Silver Nanowire Semitransparent Electrodes for Fully Ambient Solution-Processed Tandem Polymer Solar Cells. *Advanced Functional Materials*, **2015**. 25 (28), 4539-4547.
 215. Castro, M. F., Mazzolini, E., Søndergaard, R. R., Espindola-Rodríguez, M., and Andreasen, J. W., Flexible ITO-free roll-processed large-area nonfullerene organic solar cells based on P3HT: O-IDTBR. *Physical Review Applied*, **2020**. 14 (3), 034067.

216. An, N. G., Kim, J. Y., and Vak, D., Machine learning-assisted development of organic photovoltaics via high-throughput in situ formulation. *Energy & Environmental Science*, **2021**. 14 (6), 3438-3446.
217. Liu, Y., Larsen-Olsen, T. T., Zhao, X., Andreasen, B., Søndergaard, R. R., Helgesen, M., Norrman, K., Jørgensen, M., Krebs, F. C., and Zhan, X., All polymer photovoltaics: From small inverted devices to large roll-to-roll coated and printed solar cells. *Solar Energy Materials and Solar Cells*, **2013**. 112, 157-162.
218. Machui, F., Lucera, L., Spyropoulos, G. D., Cordero, J., Ali, A. S., Kubis, P., Ameri, T., Voigt, M. M., and Brabec, C. J., Large area slot-die coated organic solar cells on flexible substrates with non-halogenated solution formulations. *Solar Energy Materials and Solar Cells*, **2014**. 128, 441-446.
219. Waheed, S., Pareek, S., Sharma, P., and Karak, S., Performance improvement of ultrasonic spray deposited polymer solar cell through droplet boundary reduction assisted by acoustic substrate vibration. *Semiconductor Science and Technology*, **2020**.
220. Wang, T., Scarratt, N. W., Yi, H., Dunbar, A. D. F., Pearson, A. J., Watters, D. C., Glen, T. S., Brook, A. C., Kingsley, J., Buckley, A. R., Skoda, M. W. A., Donald, A. M., Jones, R. A. L., Iraqi, A., and Lidzey, D. G., Fabricating High Performance, Donor-Acceptor Copolymer Solar Cells by Spray-Coating in Air. *Advanced Energy Materials*, **2013**. 3 (4), 505-512.
221. Steirer, K. X., Reese, M. O., Rupert, B. L., Kopidakis, N., Olson, D. C., Collins, R. T., and Ginley, D. S., Ultrasonic spray deposition for production of organic solar cells. *Solar Energy Materials and Solar Cells*, **2009**. 93 (4), 447-453.
222. Zheng, Y., Wu, R., Shi, W., Guan, Z., and Yu, J., Effect of in situ annealing on the performance of spray coated polymer solar cells. *Solar Energy Materials and Solar Cells*, **2013**. 111, 200-205.
223. Waheed, S., Pareek, S., Singh, P., Sharma, P., Rana, A., and Karak, S., Effect of In Situ Annealing on Phase Segregation And Optoelectronic Properties of Ultrasonic-Spray Deposited Polymer Blend Films. *IEEE Journal of Photovoltaics*, **2020**. 10 (6), 1727-1734.
224. Tait, J. G., Rand, B. P., and Heremans, P., Concurrently pumped ultrasonic spray coating for donor:acceptor and thickness optimization of organic solar cells. *Organic Electronics*, **2013**. 14 (3), 1002-1008.
225. Huang, Y. C., Chou, C. W., Lu, D. H., Chen, C. Y., and Tsao, C. S., All-Spray-Coated Inverted Semitransparent Organic Solar Cells and Modules. *IEEE Journal of Photovoltaics*, **2018**. 8 (1), 144-150.
226. Jiang, Z., Rahmanian, R., Soltanian, S., Nouri, R., and Servati, P. Single-pass Spray-coated Flexible Organic Solar Cells Using Graphene Transparent Electrodes. in *2019 IEEE International Flexible Electronics Technology Conference (IFETC)*. 2019.
227. Aoki, Y. and Fujita, K., Characteristics of polymer semiconductor film prepared by evaporative spray deposition using ultra-dilute solution (ESDUS): application to polymer photovoltaic cells. *Molecular Crystals and Liquid Crystals*, **2020**. 704 (1), 35-40.
228. Arumugam, S., Li, Y., Glanc-Gostkiewicz, M., Torah, R. N., and Beeby, S. P., Solution Processed Organic Solar Cells on Textiles. *IEEE Journal of Photovoltaics*, **2018**. 8 (6), 1710-1715.
229. Zhang, Y., Griffin, J., Scarratt, N. W., Wang, T., and Lidzey, D. G., High efficiency arrays of polymer solar cells fabricated by spray-coating in air. *Progress in Photovoltaics: Research and Applications*, **2016**. 24 (3), 275-282.
230. Mori, T., Kobayashi, Y., Akenaga, H., Seike, Y., Miyachi, K., and Nishikawa, T., Development of Environmentally Controlled Desktop Spray Coater and Optimization of Deposition Conditions for Organic Thin-film Photovoltaic Cells. *Journal of Photopolymer Science and Technology*, **2018**. 31 (3), 335-341.
231. Vak, D., Embden, J. v., Wong, W. W. H., and Watkins, S., Optically monitored spray coating system for the controlled deposition of the photoactive layer in organic solar cells. *Applied Physics Letters*, **2015**. 106 (3), 033302.
232. Unsworth, N. K., Hancox, I., Dearden, C. A., Howells, T., Sullivan, P., Lilley, R. S., Sharp, J., and Jones, T. S., Highly conductive spray deposited poly(3, 4-ethylenedioxythiophene):poly(styrenesulfonate) electrodes for indium tin oxide-free small molecule organic photovoltaic devices. *Applied Physics Letters*, **2013**. 103 (17), 173304.

233. Colella, S., Mazzeo, M., Melcarne, G., Carallo, S., Ciccarella, G., and Gigli, G., Spray coating fabrication of organic solar cells bypassing the limit of orthogonal solvents. *Applied Physics Letters*, **2013**. 102 (20), 203307.
234. Lan, S., Zhong, J., and Wang, X., Impact of inkjet printing parameters on the morphology and device performance of organic photovoltaics. *Journal of Physics D: Applied Physics*, **2021**. 54 (46), 465105.
235. Mitra, K. Y., Alalawe, A., Voigt, S., Boeffel, C., and Baumann, R. R. Manufacturing of All Inkjet-Printed Organic Photovoltaic Cell Arrays and Evaluating Their Suitability for Flexible Electronics. *Micromachines*, **2018**. 9, DOI: 10.3390/mi9120642.
236. Eggenhuisen, T. M., Galagan, Y., Coenen, E. W. C., Voorthuizen, W. P., Slaats, M. W. L., Kommeren, S. A., Shanmugan, S., Coenen, M. J. J., Andriessen, R., and Groen, W. A., Digital fabrication of organic solar cells by Inkjet printing using non-halogenated solvents. *Solar Energy Materials and Solar Cells*, **2015**. 134, 364-372.
237. Eom, S. H., Park, H., Mujawar, S. H., Yoon, S. C., Kim, S.-S., Na, S.-I., Kang, S.-J., Khim, D., Kim, D.-Y., and Lee, S.-H., High efficiency polymer solar cells via sequential inkjet-printing of PEDOT:PSS and P3HT:PCBM inks with additives. *Organic Electronics*, **2010**. 11 (9), 1516-1522.
238. Eggenhuisen, T. M., Galagan, Y., Biezemans, A. F. K. V., Slaats, T. M. W. L., Voorthuizen, W. P., Kommeren, S., Shanmugam, S., Teunissen, J. P., Hadipour, A., Verhees, W. J. H., Veenstra, S. C., Coenen, M. J. J., Gilot, J., Andriessen, R., and Groen, W. A., High efficiency, fully inkjet printed organic solar cells with freedom of design. *Journal of Materials Chemistry A*, **2015**. 3 (14), 7255-7262.
239. Eom, S. H., Senthilarasu, S., Uthirakumar, P., Hong, C.-H., Lee, Y.-S., Lim, J., Yoon, S. C., Lee, C., and Lee, S.-H., Preparation and characterization of nano-scale ZnO as a buffer layer for inkjet printing of silver cathode in polymer solar cells. *Solar Energy Materials and Solar Cells*, **2008**. 92 (5), 564-570.
240. Lu, H., Lin, J., Wu, N., Nie, S., Luo, Q., Ma, C.-Q., and Cui, Z., Inkjet printed silver nanowire network as top electrode for semi-transparent organic photovoltaic devices. *Applied Physics Letters*, **2015**. 106 (9), 093302.
241. Maisch, P., Tam, K. C., Lucera, L., Egelhaaf, H.-J., Scheiber, H., Maier, E., and Brabec, C. J., Inkjet printed silver nanowire percolation networks as electrodes for highly efficient semitransparent organic solar cells. *Organic Electronics*, **2016**. 38, 139-143.
242. Krebs, F. C., Pad printing as a film forming technique for polymer solar cells. *Solar Energy Materials and Solar Cells*, **2009**. 93 (4), 484-490.
243. Li, H., Zhang, C., Wei, J., Huang, K., Guo, X., Yang, Y., So, S., Luo, Q., Ma, C.-Q., and Yang, J., Roll-to-roll micro-gravure printed P3HT:PCBM organic solar cells. *Flexible and Printed Electronics*, **2019**. 4 (4), 044007.
244. Wei, J., Zhang, C., Ji, G., Han, Y., Ismail, I., Li, H., Luo, Q., Yang, J., and Ma, C.-Q., Roll-to-roll printed stable and thickness-independent ZnO:PEI composite electron transport layer for inverted organic solar cells. *Solar Energy*, **2019**. 193, 102-110.
245. Cho, C.-K., Hwang, W.-J., Eun, K., Choa, S.-H., Na, S.-I., and Kim, H.-K., Mechanical flexibility of transparent PEDOT:PSS electrodes prepared by gravure printing for flexible organic solar cells. *Solar Energy Materials and Solar Cells*, **2011**. 95 (12), 3269-3275.
246. Yang, J., Vak, D., Clark, N., Subbiah, J., Wong, W. W. H., Jones, D. J., Watkins, S. E., and Wilson, G., Organic photovoltaic modules fabricated by an industrial gravure printing proofer. *Solar Energy Materials and Solar Cells*, **2013**. 109, 47-55.
247. Zhang, C., Luo, Q., Wu, H., Li, H., Lai, J., Ji, G., Yan, L., Wang, X., Zhang, D., Lin, J., Chen, L., Yang, J., and Ma, C., Roll-to-roll micro-gravure printed large-area zinc oxide thin film as the electron transport layer for solution-processed polymer solar cells. *Organic Electronics*, **2017**. 45, 190-197.
248. Välimäki, M., Jansson, E., Korhonen, P., Peltoniemi, A., and Rousu, S., Custom-Shaped Organic Photovoltaic Modules—Freedom of Design by Printing. *Nanoscale Research Letters*, **2017**. 12 (1), 117.
249. Wei, J., Ji, G., Zhang, C., Yan, L., Luo, Q., Wang, C., Chen, Q., Yang, J., Chen, L., and Ma, C.-Q., Silane-Capped ZnO Nanoparticles for Use as the Electron Transport Layer in Inverted Organic Solar Cells. *ACS Nano*, **2018**. 12 (6), 5518-5529.

250. Carlé, J. E., Andersen, T. R., Helgesen, M., Bundgaard, E., Jørgensen, M., and Krebs, F. C., A laboratory scale approach to polymer solar cells using one coating/printing machine, flexible substrates, no ITO, no vacuum and no spincoating. *Solar Energy Materials and Solar Cells*, **2013**. *108*, 126-128.
251. Mo, L., Ran, J., Yang, L., Fang, Y., Zhai, Q., and Li, L., Flexible transparent conductive films combining flexographic printed silver grids with CNT coating. *Nanotechnology*, **2016**. *27* (6), 065202.
252. Yu, J.-S., Kim, I., Kim, J.-S., Jo, J., Larsen-Olsen, T. T., Søndergaard, R. R., Hösel, M., Angmo, D., Jørgensen, M., and Krebs, F. C., Silver front electrode grids for ITO-free all printed polymer solar cells with embedded and raised topographies, prepared by thermal imprint, flexographic and inkjet roll-to-roll processes. *Nanoscale*, **2012**. *4* (19), 6032-6040.
253. Mariappan, D. D., Kim, S., Boutilier, M. S. H., Zhao, J., Zhao, H., Beroz, J., Muecke, U., Sojoudi, H., Gleason, K., Brun, P.-T., and Hart, A. J., Dynamics of Liquid Transfer from Nanoporous Stamps in High-Resolution Flexographic Printing. *Langmuir*, **2019**. *35* (24), 7659-7671.
254. Zhong, W., Hu, Q., Jiang, Y., Li, Y., Chen, T. L., Ying, L., Liu, F., Wang, C., Liu, Y., Huang, F., Cao, Y., and Russell, T. P., In Situ Structure Characterization in Slot-Die-Printed All-Polymer Solar Cells with Efficiency Over 9%. *Solar RRL*, **2019**. *3* (7), 1900032.
255. Sauer, H. M., Braig, F., and Dörsam, E., Leveling and Drying Dynamics of Printed Liquid Films of Organic Semiconductor Solutions in OLED/OPV Applications. *Advanced Materials Technologies*, **2021**. *6* (2), 2000160.
256. Pali, L. S., Jindal, R., and Garg, A., Screen printed PEDOT:PSS films as transparent electrode and its application in organic solar cells on opaque substrates. *Journal of Materials Science: Materials in Electronics*, **2018**. *29* (13), 11030-11038.
257. Kujala, M., Kololuoma, T., Keskinen, J., Lupo, D., Mäntysalo, M., and Kraft, T. M., Bending reliability of screen-printed vias for a flexible energy module. *npj Flexible Electronics*, **2020**. *4* (1), 24.
258. Hösel, M., Søndergaard, R. R., Angmo, D., and Krebs, F. C., Comparison of Fast Roll-to-Roll Flexographic, Inkjet, Flatbed, and Rotary Screen Printing of Metal Back Electrodes for Polymer Solar Cells. *Advanced Engineering Materials*, **2013**. *15* (10), 995-1001.
259. Zhang, B., Chae, H., and Cho, S. M., Screen-Printed Polymer:Fullerene Bulk-Heterojunction Solar Cells. *Japanese Journal of Applied Physics*, **2009**. *48* (2R), 020208.
260. He, P., Cao, J., Ding, H., Liu, C., Neilson, J., Li, Z., Kinloch, I. A., and Derby, B., Screen-Printing of a Highly Conductive Graphene Ink for Flexible Printed Electronics. *ACS Applied Materials & Interfaces*, **2019**. *11* (35), 32225-32234.
261. Apilo, P., Hiltunen, J., Välimäki, M., Heinilehto, S., Sliz, R., and Hast, J., Roll-to-roll gravure printing of organic photovoltaic modules—insulation of processing defects by an interfacial layer. *Progress in Photovoltaics: Research and Applications*, **2015**. *23* (7), 918-928.
262. Kommeren, S., Coenen, M. J. J., Eggenhuisen, T. M., Slaats, T. W. L., Gorter, H., and Groen, P., Combining solvents and surfactants for inkjet printing PEDOT:PSS on P3HT/PCBM in organic solar cells. *Organic Electronics*, **2018**. *61*, 282-288.
263. Ganesan, S., Gollu, S. R., Alam Khan, J., Kushwaha, A., and Gupta, D., Inkjet printing of zinc oxide and P3HT:ICBA in ambient conditions for inverted bulk heterojunction solar cells. *Optical Materials*, **2019**. *94*, 430-435.
264. Bihar, E., Corzo, D., Hidalgo, T. C., Rosas-Villalva, D., Salama, K. N., Inal, S., and Baran, D., Fully Inkjet-Printed, Ultrathin and Conformable Organic Photovoltaics as Power Source Based on Cross-Linked PEDOT:PSS Electrodes. *Advanced Materials Technologies*, **2020**. *5* (8), 2000226.
265. Chen, C.-T. and Yang, H.-H., Inkjet printing of composite hole transport layers and bulk heterojunction structure for organic solar cells. *Thin Solid Films*, **2022**. *751*, 139217.
266. Zhang, W., Nguyen, N. A., Murray, R., Xin, J., and Mackay, M. E., A comparative study on the morphology of P3HT:PCBM solar cells with the addition of Fe₃O₄ nanoparticles by spin and rod coating methods. *Journal of Nanoparticle Research*, **2017**. *19* (9), 315.
267. Krebs, F. C., Polymer solar cell modules prepared using roll-to-roll methods: knife-over-edge coating, slot-die coating and screen printing. *Solar Energy Materials and Solar Cells*, **2009**. *93* (4), 465-475.

268. Holmes, N. P., Munday, H., Barr, M. G., Thomsen, L., Marcus, M. A., Kilcoyne, A. L. D., Fahy, A., van Stam, J., Dastoor, P. C., and Moons, E., Unravelling donor–acceptor film morphology formation for environmentally-friendly OPV ink formulations. *Green Chemistry*, **2019**. 21 (18), 5090-5103.
269. Cha, H.-C., Huang, Y.-C., Li, C.-F., and Tsao, C.-S., Uniformity and process stability of the slot-die coated PTB7:PC71BM organic photovoltaic improved by solvent additives. *Materials Chemistry and Physics*, **2023**. 302, 127684.
270. Kwon, Y., Lee, C., Nam, M., and Ko, D.-H., Revealing conflicting effects of solvent additives on morphology and performance of non-fullerene organic photovoltaics under different illuminance conditions. *Dyes and Pigments*, **2022**. 207, 110754.

CHAPTER 3 – RESEARCH METHODOLOGY

3.1. Overview

This chapter contains a detailed discussion associated with the experimental methods and instrumentation that was conducted, including background information, how the method was conducted, as well as how crucial these methods are to the project. As such, the chapter is broken up into four components: materials and ink preparation (*Section 3.2.*), device fabrication (*Section 3.3.*), electronic property of organic photovoltaic (OPV) devices (*Section 3.4.*) and material analysis (*Section 3.5.*).

3.2. Materials and ink preparation

Throughout the project, several materials and inks were synthesised and prepared for the use in the fabrication of slot-die coated OPVs. As such, below is the method of material synthesis and ink preparation used.

3.2.1. Synthesis of PPDT2FBT

For the majority of the thesis work, poly[(2,5-bis(2hexyldecyloxy)phenylene)-alt-(5,6-difluoro-4,7-di(thiophen-2-yl)benzo[c][1,2,5]thiadiazole)] (PPDT2FBT) (structure seen *Figure 3.1*) was chosen as the main donor polymer of interest for the fabrication of slot-die coated OPV devices. This is due to its current use in scalable roll-to-roll fabrication by *Song et al.* [1], as well as it having a fairly robust thermal stability [2]. The synthesis has also been demonstrated to be in-expensive, as well as scalable, especially when compared to other higher performing donor polymers [3]. For comparison with literature, PPDT2FBT:PC₇₁BM devices that were fabricated via spin-coating and slot-die coating achieved an efficiency up to 9.39% [2] and 7.61% [1] respectively.

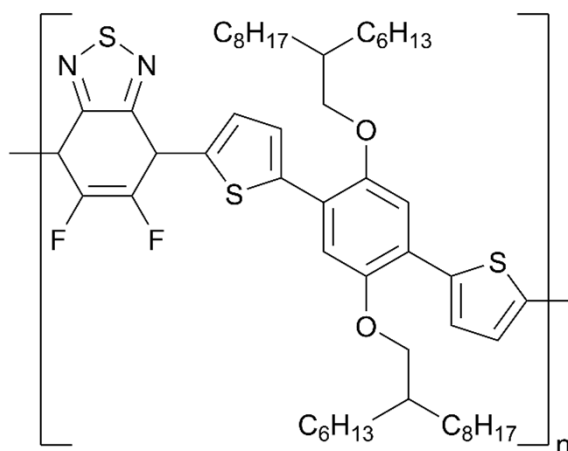


Figure 3.1: Molecular structure of PPDT2FBT donor polymer.

For the entirety of the thesis, the donor polymer PPDT2FBT was synthesised using a direct arylation polymerisation according to literature [4]. The molecular weight of PPDT2FBT was determined via Gel Permeation Chromatography (Agilent 1260 Infinity II High-Temperature GPC System) using trichlorobenzene at 150 °C. Two batches of PPDT2FBT were used throughout the thesis, the first batched (implemented in *Chapter 4*, was found to have an average molecular weight (M_n) of 50 of kg/mol with a PDI of 2.60 relative to polystyrene standards, while the remaining chapters (5-7) was found to have an average molecular weight (M_n) of 27 of kg/mol with a PDI of 3.5 relative to polystyrene standards. To prepare active layer ink, PPDT2FBT:PC₆₁BM was paired with PC₆₁BM with a w/w ratio of 1:2. Though different batches of PPDT2FBT polymers were used throughout the thesis, there appeared to be minimal difference in terms of OPV device performance (seen in *Table A1* in *Appendix A*).

3.2.2. Synthesis of TQ1

Another donor polymer of interest is poly[2,3-bis-(3-octyloxyphenyl)quinoxaline-5,8-diyl-alt-thiophene-2,5-diyl] (TQ1) (structure seen in *Figure 3.2*), a relatively easy polymer to synthesis [5], and been demonstrated to be used in either mini-roll coater (MRC) [6, 7] or roll-to-roll (R2R) coated devices [6]. To date, TQ1 has been demonstrated to achieved moderate performances when paired with either PC₆₁BM [5, 7], PC₇₁BM [7-9] or N2200 [10, 11], achieving a PCE of 4.9% [5], 7.08% [12], 3.15% [11], respectively. Unlike PPDT2FBT which has been determined to be semi-crystalline, TQ1 has been observed to be an amorphous polymer from dynamic mechanical thermal analysis (DMTA) [13].

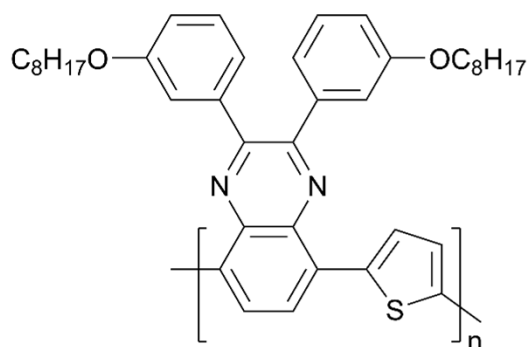


Figure 3.2: Molecular structure of TQ1 donor polymer.

For chapter 7, TQ1 was synthesised according to literature [5]. The molecular weight of TQ1 was determined via Gel Permeation Chromatography using trichlorobenzene at 150 °C, giving a number average molecular weight (M_n) of 52.6 kg/mol with PDI of 3.29 relative to polystyrene standard. TQ1 was paired with PC₆₁BM, with a w/w ratio of 1:2, to form an active layer blend during ink preparation.

3.2.3. Synthesis of PDCBT

The third donor polymer that was investigated in this thesis was poly[5,5'-bis(2-butyloctyl)-(2,2'-bithiophene)-4,4'-dicarboxylate-alt-5,5'-2,2'-bithiophene] (PDCBT) (structure seen in *Figure 3.3*), a highly crystalline polymer [14] that has been demonstrated higher efficiencies, either paired with fullerene [14-16], or non-fullerene small molecule acceptors [16-18], achieving an efficiency of 8.0% and 11.1% when paired with PC₇₁BM [16] or ITIC [16], respectively.

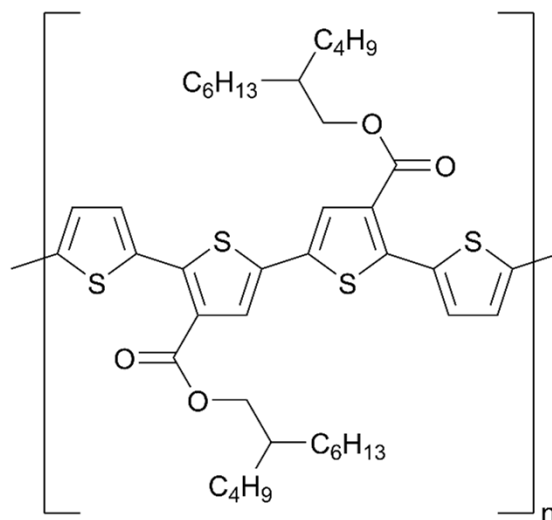


Figure 3.3: Molecular structure of PDCBT donor polymer.

For chapter 7, PDCBT was synthesised following an unpublished procedure, based on the following published work [14, 19, 20]. The molecular weight of PDCBT was determined via Gel Permeation Chromatography using trichlorobenzene at 150 °C, giving a number average molecular weight (M_n) of 22.3 kg/mol with PDI of 7.13 relative to polystyrene standard. During active layer ink preparation, PDCBT was paired with ITIC, with a w/w ratio of 1:1.

3.2.4. Synthesis of ITIC

A common alternative to fullerene acceptors, 3,9-bis(2-methylene-(3-(1,1-dicyanomethylene)-indanone))-5,5,11,11-tetrakis(4-hexylphenyl)-dithieno[2,3-d':2',3'-d']-s-indaceno[1,2-b:5,6-b']dithiophene (ITIC) (structure seen in *Figure 3.4*) is a non-fullerene small molecule acceptor which exhibits a strong and broad absorption in the visible light range [21]. The acceptor has worked effectively with PDCBT [16-18], PTB7-Th [21-23], PBDB-T [24-26]. The highest efficiency achieved with the ITIC acceptor was when paired with the donor polymer, PBDB-T, reaching an efficiency of 11.28% [24]. ITIC has also been demonstrated to be used as an effective acceptor material for blade [27] and slot-die [28] coated devices. For chapter 7, ITIC was synthesised following an unpublished procedure, based on the following published work [21, 29, 30].

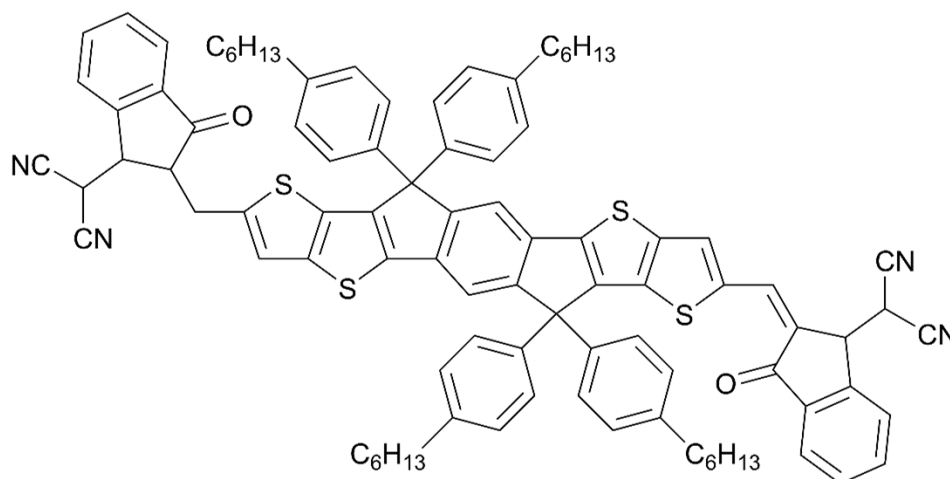


Figure 3.4: Molecular structure of ITIC small-molecule acceptor.

3.2.5. Zinc Oxide nanoparticle synthesis and ink preparation

When shifting from small-scale to scalable OPV fabrication, zinc oxide nanoparticles (ZnO NPs) are commonly used as the electron transport layer [1, 31-33]. Unlike with spin-coating, which initially forms a layer of ZnO precursor prior to annealing (as high as 200 °C), resulting in film thin over the ITO [34], the ZnO NPs must be formed within the ink prior to depositing over the ITO or active layer (depending on device structuring). This is to avoid device and substrate damage that would otherwise be experienced at such high annealing temperatures. To date, ZnO NPs has been demonstrated successful on roll-to-roll [1, 35, 36] and large active area [37, 38] device fabrication.

The preparation of a ZnO NP dispersion was based on a previously published procedure [39]. To achieve an ideal processing concentration, acetone (Chem-supply, 99.9%) was added to the NP precipitate until a concentration of approximately 40 mg mL⁻¹ was achieved. Afterwards, 2-(2-methoxyethoxy)acetic acid (MEA) (Sigma Aldrich) (5% w/w in relation to ZnO NP) was then added to the dispersion to stabilise the NPs. The ink was left to stir variously overnight to ensure the mixing of the MEA with the ZnO NP dispersion. The Ink was stored under dark conditions at room temperature.

3.2.6. Ink preparation of PEDOT:PSS

Poly(3,4-ethylenedioxythiophene):polystyrene sulfonate (PEDOT:PSS) is a polymer mixture of two ionomers (structure seen in *Figure 3.5*). Commonly used for solution-processed organic electrodes [40-43] or interfacial layer between the metallic electrode and active layer [44-46], PEDOT:PSS has been demonstrated to be processable via different printing [47-50] and coating [51-53] conditions.

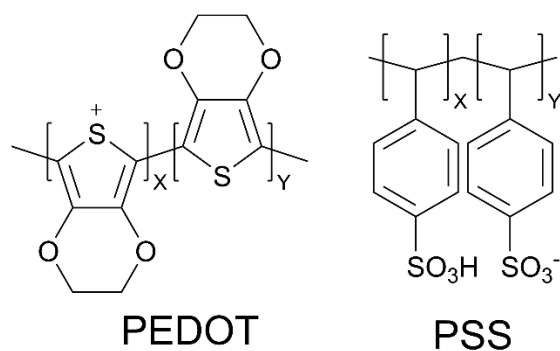


Figure 3.5: Molecular structure of PEDOT and PSS ionomers.

For OPVs that were prepared via a conventional device configuration (seen in *Figure 2.4* in *Chapter 2, Section 6.*), PEDOT:PSS ink was prepared based on previous literature that deposit the material via roll-to-roll slot-die coating [36, 54]. This was achieved by mixing PH1000 (Ossila) (37.5% v/v), Milli-Q® water (37.5% v/v), Isopropanol (19.9% v/v), Dimethylsulfoxide (1.0% v/v) and Zonyl® FSO fluorosurfactant (0.1% v/v). The ink was sonicated with a sonication probe at 20% amplitude for 3 x 30s (30s rest between each burst) with a S&M: 630-0419 probe head. The resulting ink was stored in a fridge (5 °C).

3.3. Device fabrication

There are a variety of printing methods that can be implemented for the roll-to-roll technique, each with their own advantages. The types of printing/coating techniques include; slot-die coating [55], screen printing [56], spray-coating [57], inkjet printing [58] and blade coating [59]. These methods can print devices over a large surface area, allowing for inexpensive production on the meter scale. For this project, a combination of spin-coating and slot-die coating will be implemented. A detailed explanation and comparison of the different printing techniques can be found in *Chapter 2*, while this chapter goes into more depth in associated with slot-die coating.

3.3.1. Spin-coating

Spin-coated devices allow for the fabrication of rigid devices that are relatively easy to produce. To adjust the thickness of films produced, the adjusting of ink concentration and spin-rate can allow for rough thickness control. It is common practice in OPV fabrication to perform spin-coating under nitrogen-atmosphere inside a glovebox. The reason for this is that some materials, especially high-performing donor polymers and acceptor materials, are sensitive to moisture and photo-oxidation [60-63]. By conducting OPV fabrication in nitrogen-atmosphere, it reduces the presence of oxygen and moisture, and thus, reduces the impact of these degradation pathways on device performance.

3.3.2. Slot-die coating

Improving roll-to-roll printed devices is labour intensive and requires a significant number of materials, the fabrication technique generally produces meters of devices per print, having a surface area several magnitudes higher than a single spin-coated device. Resulting in a lot of materials possibly wasted when trying to adjust the printing conditions.

A potential bridging instrument between spin coating and roll-to-roll printing is the mini-roll coater (MRC); a large drum that prints on a flexible substrate. As less substrate is required for device fabrication with the MRC, less materials are required for each strip printed, resulting in less resources wasted, while allowing for methods of improvement against printing.

In this thesis, the MRC from FOM technologies, was implemented for OPV fabrication. The components of the MRC include:

- A Drum with adjustable speed and heating
- A Slot-die head with adjustable height and positioning
- A Syringe-pump with adjustable flow rate

To allow for ease-of-use and a reduced cost, fabrication of devices occur in ambient conditions. This means that printed layers will be exposed during the fabrication process. The printing parameters that can be adjusted includes temperature, drum speed, and coating ink concentration and flow rate. Adjusting these parameters allow for the optimising of film quality and the thickness variation of the printed films.

3.3.2.1. Thickness calculations

For slot-die coating, wet (Equation 3.1) and dry (Equation 3.2) film thicknesses of the layers can be calculated according to:

$$d_{wet} = \frac{f}{S w} \quad (3.1) \quad \& \quad d_{dry} = \frac{f c}{S w \rho} \quad (3.2)$$

where d is the thickness in cm, f is the flow rate in $\text{cm}^3 \text{min}^{-1}$ (mL min^{-1}), S is the drum rotation speed in cm min^{-1} , w is the meniscus guide width in cm, c is the solid content in the ink in g cm^{-3} , and ρ is the density of the dried coating in g cm^{-3} [64, 65]. The density of the donor polymer can be estimated at 1 g cm^{-3} and PC₆₁BM with a material density of 1.5 g cm^{-3} [66].

Another equation for calculating the dry film thickness using low viscosity inks can be seen below:

$$d = k \frac{f c S^{2/3}}{T w \rho} \quad (3.3)$$

where k is a proportionality constant and l is the shim length in cm [1, 2]. Unlike *Equation 3.1 & 3.2*, Hong *et al.* found, how by using low viscosity inks, that the increase web speed results have an increase in thickness, as there is an increase in shear forces that result in more ink being removed from the meniscus. They also state there is a direct relation between thickness and temperature [67].

Michels *et al.* proposed that a combination of the two equations (*Equation 3.2 and Equation 3.3*) has an influence, with relatively low substrate speeds predominately following *Equation 3.2* as the thickness of the film is predominately related to evaporation. For high relatively fast substrate speeds, the thickness strongly related to shear forces between the meniscus and substrate, with properties following *Equation 3.3*. It is noted that this proposed theory was investigated for zone-casting coating method with a dilute solution 3 mg mL^{-1} [69]. As thickness places a significant role in device performance, using the right theoretical model is important for determining the correct printing parameters for meniscus-guided coating.

3.3.2.2. Slot-die coating window

For the deposition via slot-die coating, it is important to adjust the printing parameters to allow for the coating of uniform and defect free film. To achieve this, two stable menisci must be maintained, seen upstream and downstream in relation to the slot-die. This is done by keeping a desired position and angle of the meniscus during coating. The shape of the menisci and their position are determined by two main factors, the shear forms from the meniscus/substrate interactions, and the pressure drop of the ink as it flows through the thin exit of the slot-die (as seen in *Figure 3.6*).

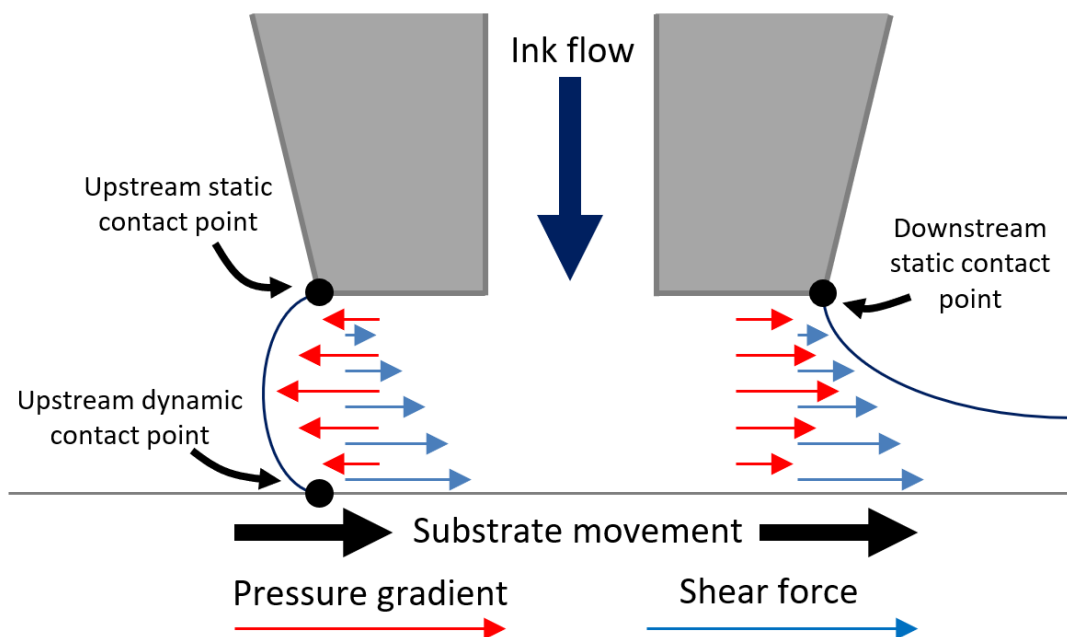


Figure 3.6: Upstream and downstream ink flow with highlighted interaction of the pressure gradient and the shear force of the substrate-liquid interface [70].

By adjusting the pressure gradient (upstream and downstream) and solvent/substrate shear forces, it can influence the shape and stability of the meniscus (seen in *Figure 2.10*). When the correct variables are achieved, a desired meniscus shape occurs, occurring within the “Coating Window”.

Attempting to coat outside the proper range can lead to coating defects including ribbing, chattering, neck-in defects, streaks and air entrainments, in-turn leading towards dry film defects and non-uniformity. These issues can result in a reduction device performance. There are several models that predict the coating window including Capillary Model [71], Viscous Model [72] and Viscocapillary Model of Operating Limits [73]. Printing conditions have an influence over performance of devices fabrications.

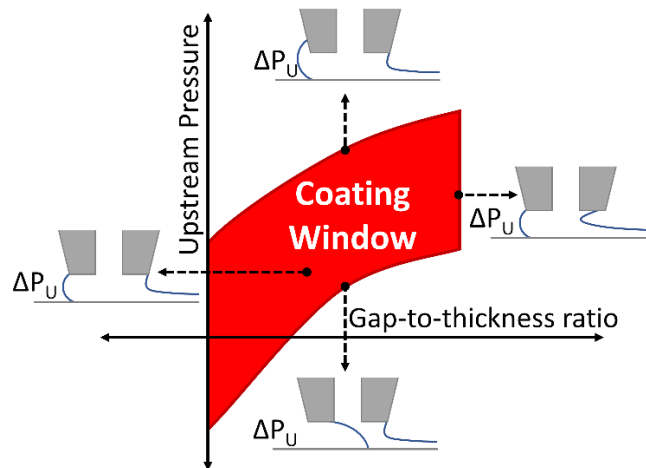


Figure 3.7: Stable coating window based on Capillary Model for slot-die coating that allows for defect-free films [4].

3.3.2.3. *Film defects*

For the fabrication of high-performance devices, it is important that the coated films are relatively uniform and defect-free. Differences in thicknesses can result in reduction a reduction in device efficiency, while defects could lead to complete shorting of the device. For slot-die coating of thin films, there are several defects that could occur, including chattering, ribbing, neck-in, edge defects, bubbles and streaks (seen in *Figure 3.8*).

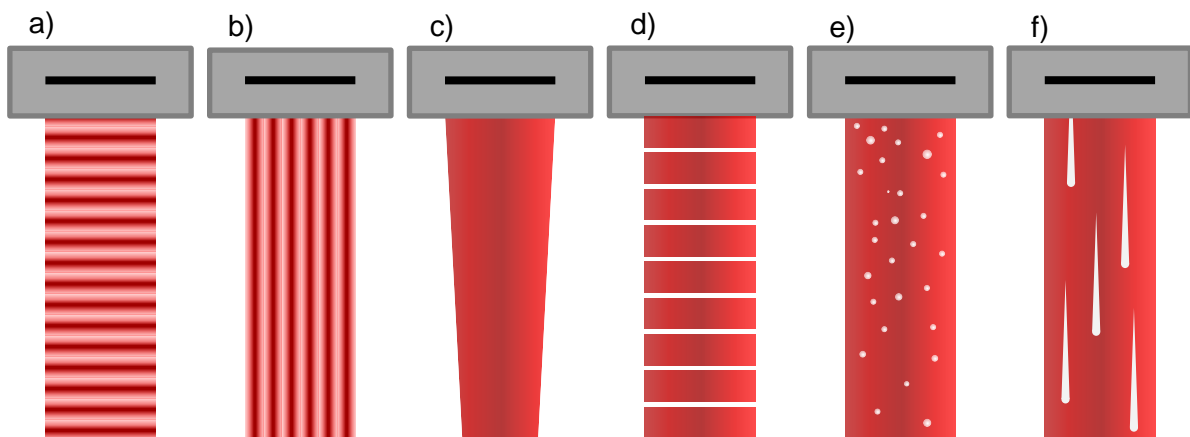


Figure 3.8: Basic schematic of potential film defects from slot-die printing: Chattering (a), ribbing (b), neck-in (c), edge defects (d), bubble (e), and streaks (f).

3.3.2.3.1. Chattering

Chattering (seen in *Figure 3.8a*) involves the film thickness varying constantly perpendicular to the direction of travel, resulting in the presence of horizontal bands. This defect can be caused by the variation in flow rate due to the fluid delivery system or pulsing of the substrate during movement via the roller/drum/stage, roller defects.

In relation to the ink delivery system, the flow rate may be too low, with minor changes in deposition becoming noticeable during coating. By reducing the concentration and increasing the flow rate, this will mitigate the micro-steps during ink flow to the slot-die. For substrate roller/drum/stage, a similar problem could be related to the micro steps present from slow movement of the stage. As such, increasing substrate speed (and flowrate to compensate) would reduce this effect. As for roller/drum damage would require an engineering solution, as the drum/roller needs to be relatively smooth. Lastly, a variation of upstream pressure can be mitigated.

3.3.2.3.2. Ribbing

Unlike chattering, ribbing (seen in *Figure 3.8b*) appears as a result of variation in film thickness parallel to the direction of travel, resulting in bands along the vertical direction. This film defect can be caused by high-shear forces due to the fast movement of the substrate or low pressure at the slot-die exit. For high shear forces, a fast substrate speed and low flow pressure from the slot-die can result in high forces interacting with the ink in the meniscus. To reduce the high-shear forces, decreasing the substrate speed, increasing the flow rate (and thus flow pressure), or reduce distance between the upstream lip and substrate would reduce the shear forces.

If there is low pressure at the slot-die exit, the said pressure can be increased by reducing the shim-thickness, increase viscosity of the ink, or by adding a vacuum box (engineering solution). Lastly, upstream pressure can be increased by reducing the gap between the substrate and slot-die. Another source of this film defect is if there are localised defects on the slot-die head, resulting in a non-uniform flow of ink. This requires repair or replacement of slot-die parts.

3.3.2.3.3. Neck-in

Neck-in (seen in *Figure 3.8c*) occurs across the length of the film at the edges, with a gradient decrease in the coating width, where the thickness along the edges increases as the coating width decreases. A neck-in defect can occur due to a mismatch between the flow rate and substrate speed caused by the acceleration of the ink and shear forces. This can result in a significant difference between the flow rate and substrate speed, causing the solution on the edges to accelerate towards the centre of the film. This can be solved by either lowering the web speed or reducing shim thickness.

Another cause of neck-in defect is the high shear forces that result in the contraction of the meniscus towards the centre leading to higher flow rates at the edges. This can result due to high viscosity and high surface tension from the ink, and/or strong interactions between the ink and the substrate. This can be resolved by reducing the viscosity and/or surface tension of the ink. Surfactants can also be added to the ink to reduce ink/substrate interactions [74].

3.3.2.3.4. Edge defects

There are several types of edge defects that can occur during coating, including where the thickness at the edges of the film is typically increasing, or the variation in position of the coating edge is going in and out along the length of the coating (seen in *Figure 3.8d*). This can be caused by the transition as the meniscus goes on and off the substrate, due to the difference within the surface energy of various regions on the substrate. This can lead to changes to how the ink wets the film. The solution to this is to ensure that the substrate of the substrate surface is homogeneous.

3.3.2.3.5. Bubbling

Bubbling (seen in *Figure 3.8e*) occurs when there is air present within the wet film, resulting in gaps to be present in the dry film. This can occur due to air entrainment in the original solution, or some leakage with the fluid delivery system, otherwise via entrapment from instability of the upstream or downstream section of the meniscus.

Air entrainment can be prevented by removing any air present in the solution and ensuring that there are no gaps between the connectors and adaptors within the delivery system. As for air entrapment, improving the stability of the meniscus by improving pressure stability upstream and downstream can result in reduction of bubbles appearing.

3.3.2.3.6. Streaks

For streaks to form on the film (seen in *Figure 3.8f*), there are several sources. One such is substrate defects such as dust or dirt particles, which can obstruct the meniscus from touching the source. This can be simply solved with proper cleaning of the substrate prior to printing. Another source is obstructions either in the slot-die or on the lip, blocking the flow of ink. This can occur from either improper cleaning of the substrate, or the build-up of aggregation (commonly observed with PEDOT:PSS). Again, proper cleaning to remove blockages will solve this issue. Lastly, any damage to the slot-die, bends, scratches, or deformation can result in non-uniform flow of ink to the meniscus. Careful handling of the slot-die will prevent this issue from occurring.

3.3.2.3. *Thin film deposition for OPV fabrication*

For the deposition of thin films using solution-based slot-die coating methods, a flexible substrate was attached to Mini-roll coater (FOM) with temperature and rotation speed controls (seen in *Figure 3.9*). Selected ink was feed from a plastic syringe attached to a syringe pump (World Precision Instruments), through a plastic hose and fed to a slot-die coating head connected to the MRC. Specific coating conditions used in the thesis can found in the *Experimentation Section of Chapters 4 to 7*.



Figure 3.9: Image of the MRC used throughout the thesis. Included in the image of active materials being deposited from the slot-die coating head.

Upon completion of the deposition of solution-based layers, the substrate can be cut into smaller pieces and used for several purposes. This includes being stored under dark nitrogen conditions for material analysis, as well as into a vacuum chamber to deposit the remaining layers to form a complete OPV device.

3.4. Device electrical analysis

3.4.1. Electron and hole mobility measurements

Electron and hole mobility play a key role in the current density of OPVs. To measure the mobility of active materials and interface layers, dark-JV curves are recorded of specially designed devices. For specific materials of interest with no injection of holes or electrons with the device, ohmic contact devices can be used to produce a linear JV-curve. Otherwise, devices that either block the movement of electrons or holes are fabricated, resulting a typical JV-curve [75].

For the analysis of the typical looking IV-curves, fitting can be applied based on a simplified single space-charge limited current (SCLC) equation dependant on mobility (*Equation 3.4*). The equation is based on an idealised model based on unipolar injection of charge carried from an ohmic contact into the bulk of a semiconductor, where it is assumed that the device contains ohmic contacts and diffusion-free currents from unipolar charge carriers for a single discrete distribution of shallow traps [76, 77]. The relationship between current-density and voltage is given (*Equation 3.4*):

$$J = \frac{9}{8} \varepsilon_0 \varepsilon_r \mu_{e,h} \frac{V^2}{L^3} \quad (3.4)$$

where $\varepsilon_0 \varepsilon_r$ is the permittivity of the material of interest, $\mu_{e,h}$ is the charge mobility of electrons and/or holes (h), V is the voltage across the device, and L is the thickness of the film [78]. This equation holds if mobility is field independent, however, for conjugated materials, which has varying levels of disorder, has found that carrier mobility goes as follows (*Equation 3.5*):

$$\mu_{e,h} = \mu_{e0,h0} e^{\gamma \sqrt{E}} \quad (3.5)$$

where E is the electric field, $\mu_{e0,h0}$ is the zero-field mobility, and γ is the field dependence prefactor [79]. This leads to an adjusted equation for SCLC fitting equation (*Equation 3.6*).

$$J = \frac{9}{8} \varepsilon_0 \varepsilon_r \mu_{e0,h0} e^{0.89\gamma \sqrt{E}} \frac{V^2}{L^3} \quad (3.6)$$

For fitting, the built-in voltage (V_{bi}) and series resistance is subtracted from the experimental data via either experimental or data-fitting means. By fitting with *Equation 3.6* and using the fitting values in *Equation 3.5*, the hole or electron mobility can be calculated. These are important for determination of how electron and hole mobility is affected with the addition of material, interfacial layers, or the degradation of the device (i.e., how the changes in the active layer results in the change in mobility).

Though SCLC are relatively easy to perform experimentally, there has been careful analysis of the experimental data using the above-mentioned models, with several assumptions made to allow for appropriate data fitting. Also, as the SCLC relies on ohmic contact, which Katagiri *et al.* found could be easily impacted by devices that had been annealed at elevated temperatures, such as the high temperatures influence of the contact interface at the ITO electrode, it is obstructing the ohmic contact [80]. SCLC can also be heavily influenced by device preparation, especially at the electrode interface, making it difficult to compare with other published values using the same modelling technique.

3.4.2. Charge Extraction by Linearly Increasing Voltage (CELIV)

Charge extraction by linearly increasing voltage (CELIV) technique relies on the extraction of thermally generated carriers by applying linearly increasing voltage (seen in *Figure 3.10*), allowing for the mobility to be obtained from the peak extraction time of the corresponding transient [81, 82]. Where the population of thermally generated carriers are low, such as for organic semi-conductors, an input light pulse can be employed to allow for the photogeneration of charge, with the technique being referred to as photo-CELIV [83-85].

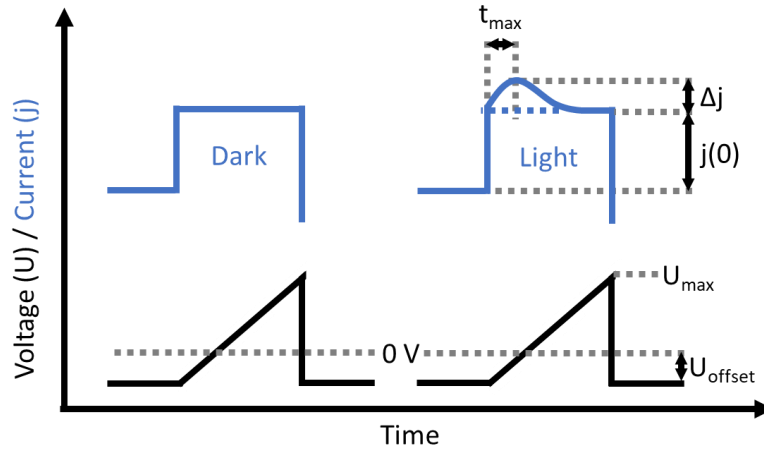


Figure 3.10: Schematic of pulse response from the photo-CELIV technique, showing for dark and light responses. Adapted from Mozer *et al.*, 2005 [85].

From the time when the extraction current reaches its maximum, the mobility can be determined by the following equation (*Equation 3.7*) [81, 85]:

$$\mu = \frac{2 d^2}{3 A t_{max}^2 [1 + 0.36 \frac{\Delta j}{j(0)}]} \text{ if } \Delta j \leq j(0) \quad (3.7)$$

where A is the voltage ramp ($A = \frac{dU}{dt}$), d is the thickness of the sample device, t_{max} is the time position of the maximum extraction current, and $j(0)$ is the capacity displacement current ($j(0) = \frac{A \times \epsilon \epsilon_0}{d}$). In experimental results from photo-CELIV, the $j(0)$ is determined by measuring the dark extraction current, while Δj is measured from the dark extraction current, with the maximum current at t_{max} (as seen in *Figure 3.10*). One advantage of photo-CELIV is it can allow for charge mobility to be measured for OPV that have been annealed at a range of annealing temperatures and times [80].

3.4.4. 4-point probe

For the measurement of sheet resistance, a four-point probe connected to a source meter applies a constant current to the film and records the external voltage. The following calculation is used to determine the sheet resistance (*Equation 3.8*):

$$R_S = 4.53 \times \frac{V}{I} \quad (3.8)$$

where I is the current in amps and V is the recorded in voltage, with the 4.53 correction factor where the sample edge/probe distance is greater than probe-to-probe separation [9]. This equation works for measurements done with probes with constant spacing, a thickness that is less than 40% of the spacing, and the edges of the film are 4 times the spacing distance from the measurement point.

3.4.5. Solar simulation

For the measurement of the efficiency of the fabrication of OPV devices, the use of a solar simulator is used to generate a JV-curve. The setup of the solar simulator includes a current-voltage source, 150 W xenon lamp, filtered to give a 100 mWcm^{-2} at AM 1.5 and is calibrated using a silicon reference cell with NIST traceable certification.

3.5. Material characterisation techniques

3.5.1. Neutral Impact Collision Ion Scattering Spectroscopy

Neutral impact collision ion scattering spectroscopy (NICISS) measurements were carried out to determine the depth profile of elements of interest and the elemental ratio present at the near surface of materials. To achieve this, the sample is bombarded with pulse of lightweight projectiles (such as He^+) with a known kinetic energy, where the projectiles are backscattered away from the sample and towards a time-of-flight (ToF) detector [87, 88] (seen in *Figure 3.11*).

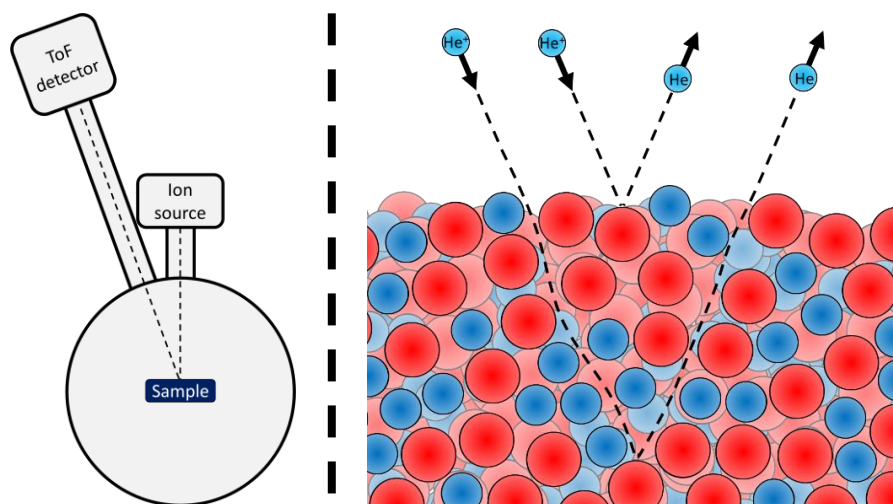


Figure 3.11: Basic schematic of NICISS instrument (LEFT) and elastic and inelastic energy loss due to projectiles colliding with the sample (RIGHT). Schematics adapted from Andersson, 2014 [10].

The technique relies on two types of energy loss, elastic, and in-elastic energy loss. For elastic energy loss, this occurs upon the collision of the projectiles with the atoms in the sample. As elements have varying mass depending on nuclei population, this energy loss can allow for the determination of the elements present in the sample. As for in-elastic energy loss, the projectiles lose energy as they travel through the bulk of the sample, resulting in low energy scattering and electronic excitations (stopping power) [89].

With the combination of elastic and in-elastic collisions, the concentration depth profile for specific elements within the sample can be measured, provided that said atom is heavier than the projectile. Though the concentration depth profile cannot be observed with this technique, instead a recoil hydrogen background can be found in the spectra, which can be removed during data analysis (seen in *Figure 3.12*) [90].

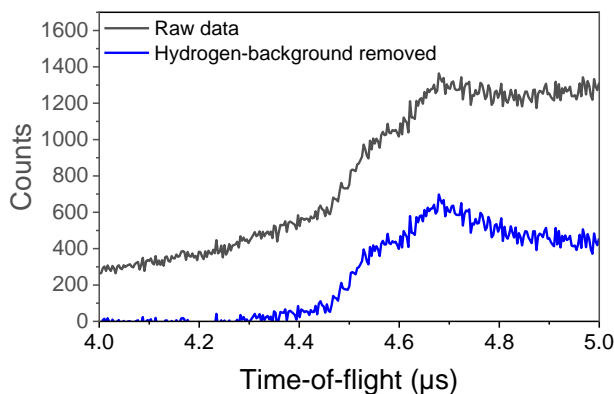


Figure 3.12: Sulphur spectra feature (4.5 μs), with and without hydrogen background.

The technique has a high resolution of $\sim 3 \text{ \AA}$, with the ability to provide a depth profile of elemental composition of up to 300 \AA [87]. This technique can also be used to determine the thickness of ultrathin films ($<15 \text{ nm}$) as well as investigate material diffusion. For this work, NICISS was carried with the use of helium ions (He^+) with a beam energy of 3 keV and a current density around $0.1 \mu\text{A mm}^{-2}$, with the beam normal to the solid surface. The ion beam was chopped into pulses with periods of $20 \mu\text{s}$ with a duty cycle less than 0.1% for the time-of-flight analysis.

Most backscattered projectiles are in a neutral state and were detected at a deflection angle of 165° with detection by microchannel plates. The anode pulses were then registered as digital signals by a multichannel analyser. In combination with the helium projectiles, there is also the detection of hydrogen atoms from the surface. The helium ions sputter off the hydrogen from the hydrocarbons at the surface. These hydrogens are detected at a wide range of energies, forming a broad background [91], especially when measuring samples that hydrocarbon compounds.

For analysis, the hydrogen background is fitted with a low-order polynomial. The Step height between the hydrogen background and helium spectra are adjusted until an appropriated background is fitted. The step height used to fit the background for each elemental spectra can be divided to determine the elemental ratio, as the step height between the helium spectra and background is dependent on the amount of given element present at the near surface ($15\text{-}30 \text{ nm}$ depth).

3.5.2. Atomic Force Microscopy

This is one method for investigating the changes occurring for the surface with atomic force microscopy (AFM). By using a tapping-mode for soft samples, the technique provides a topography map of the surface of a soft film such as the active layer of OPVs. The tapping mode of AFM operates with the use of an oscillating cantilever with a fine point which is used for interacting with the sample. For determining the oscillating frequency, a laser is reflected on the back of the cantilever and received by photodiodes. Any deviations from the setpoint result in the sample height adjusting until desired oscillation occurs, with new height recorded. This continuous feedback loop occurs without the scan, until a topography map is produced.

Roughness values were calculated from five height maps ($5\ \mu\text{m} \times 5\ \mu\text{m}$) from the sample, calculating as Root mean square deviation (R_q). Roughness was calculated with NanoScope Analysis. The AFM has also been employed to investigate possible likeliness of delamination or de-wetting having occurred for layered films [92]. An increase of R_q could be related to layers becoming apart.

3.5.3. X-ray Photoelectron Spectroscopy

X-ray photoelectron spectroscopy (XPS) is a surface-sensitive quantitative and qualitative technique based on the photoelectric effect. X-ray photons of discrete energy interact with the material, with the electrons in the valence band being ejected. The electron kinetic energy is recorded, and the following calculation is done (*Equation 3.9*):

$$E_{binding} = E_{photon} - (E_{kinetic} + \phi) \quad (3.9)$$

where $E_{binding}$ is the binding energy of the electron, E_{photon} is the energy of x-ray photons, $E_{kinetic}$ is the measured kinetic energy of the electron by the instrument, and ϕ is the work function of the analyser. With this calculation, the energy level and thus, the chemical composition can be determined. With peak fitting, the height of the peaks can be used to determine the elemental and/or covalent ratio. This technique has an effective depth is 1-3 nm, depending on the material of interest.

3.5.4. Grazing-Incidence Wide-Angle X-ray Scattering

Grazing-incidence wide-angle x-ray scattering (GIWAXS) is a scattering technique that is used to determine molecular packing and orientation associated with the BHJ of the active layer. Using an x-ray of discrete energy at a wide angle (1 to 45°), the photons interact with the nano-structuring, being scattered towards a photodiode area detector. This scattering produces a 2D map of photon intensity. The advantage of using GIWAXS over conventional x-ray powder diffraction (i.e. XRD) in investigating thin films, is that the technique only requires a small sample volume for the x-rays to interact with [93].

3.5.5. Ultraviolet Photoelectron Spectroscopy

Ultraviolet photoelectron spectroscopy (UPS) is a surface-sensitive technique that is used to determine molecular orbital energies in the valence region. To achieve this, the incident ultraviolet photons interact with the electrons bound to the atoms within material, with the energy of the photon being enough for the electrons bound in the valence and conductive band to be emitted from the material. The kinetic energy of the photoelectron is determined by the following (Equation 3.10):

$$E_K = E_{photon} - I \quad (3.10)$$

where $E_{kinetic}$ is the kinetic energy of the photoelectron, E_{photon} is the energy of the photons and I is the ionization energy of which is required to “eject” a single charge from either the ground or excited state. The method can also be used to determine the work function of the material. The technique works by emitting UV radiation towards the sample. This radiation is absorbed by the electrons in the valence band and then is ejected. The kinetic energy of the emitted photoelectron is then measured.

3.5.6. Stylus Profilometer

Thickness of films is critical for the performance of OPV devices. To allow for routine measurements of such films, a stylus profilometer will be used to measure the thickness of thick films such as the active layer (~200 nm), PEDOT:PSS (~50 nm) and ZnO NP (~35 nm). The stylus profilometer is a contact technique that traces the topography of the surface, with change in stylus height being recorded. To achieve this, a constant force is applied by the stylus onto the surface, the instrument detects a change in force being applied, and the height of the stylus will be adjusted accordingly.

The technique can measure a height ranging from 1 mm down to 1 nm, depending on instrument and sample. Thickness is determined by the height difference between the substrate and film, with the measurements occurring as fabricated scratches acting as troughs. The profilometer, with x and y axis motors, can perform 2D scans, allowing for the mapping of the surface of samples.

3.5.7. Auger Electron Spectroscopy

Auger electron spectroscopy (AES) is a surface-sensitive quantitative and qualitative technique based on the Auger effect. Electrons are used to remove the inner most electrons, leaving behind a hole. As this is an unstable state, the hole can be filled by an outer shell electron, resulting in a release of energy. This energy can then be coupled to the second outer most electron, allowing for the electron to be emitted from orbit if the energy is greater than the orbital binding energy [94, 95].

The kinetic energy of the ejected electrons is associated with the energy of the core level (E_{Core}), as well as the first outer (E_{1st}) and second outer levels (E_{2nd}) (as seen *Equation 3.11*) [96]:

$$E_{kinetic} = E_{Core} - E_{1st} - E_{2nd} \quad (3.11)$$

For the analysis of the of the AES spectra, the data set is smoothed, then derived (s9d5) (*seen in Figure 3.13*). The peak height is then measured for observed peaks and matched with expected elements present in the spectra. Atomic concentration is then calculated based on the specific selectivity values for given element.

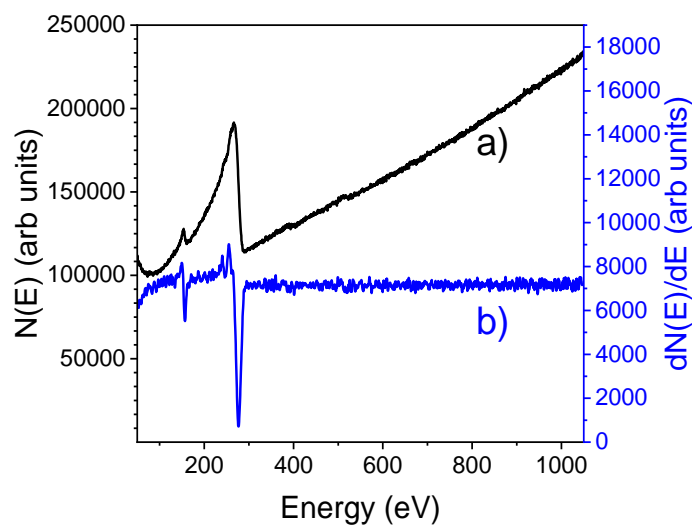


Figure 3.13: Spectra of raw AES data a) and data that has been smoothed and derived b). The AES spectra was from the surface of a PPDT2FBT:PC₆₁BM thin film.

For this thesis, measurements were performed using a PHI 710 Scanning Auger Nanoprobe system SEM using an acceleration voltage that was 10 kV and emission current that was 1 nA. Spectra were collected via point scans as specific locations on the sample. The Auger spectra were filtered and analysed, as well as element concentrations calculated with MultiPak Spectrum. Elemental orbital energies and selectivity values were based on the *Handbook of Auger Electron Microscopy* by Childs *et al.*, 1997 [97].

3.5.8. Dynamic Mechanical Thermal Analysis

Dynamic mechanical thermal analysis (DMTA) is a power instrument, investigating the thermal behaviours of materials, showing details such as the location of glass transitions; a transition for which a polymer transfers from glass-like properties to rubbery-like behaviour. To achieve this, the instrument measures the viscoelastic properties via mechanical stress, such as tension, bending, shear, and compression. As stress (σ) is applied oscillating a force at a known frequency and amplitude (σ_0), the strain (ϵ_0) is measure by associating it with the oscillating displacement (*seen in Figure 3.14*).

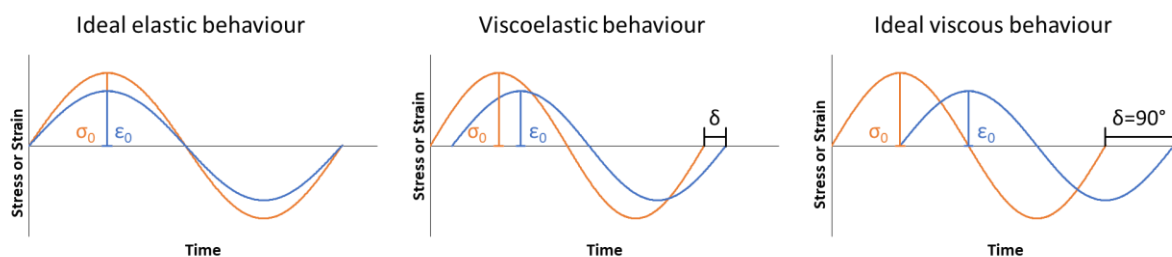


Figure 3.14: Trends in the stress & strain of Ideal elastic, viscous and Viscoelastic behaviour materials.

For an ideal elastic material, there is no phase difference between stress and strain, while for an ideal viscous material, there is a phase shift of 90° . The equations for stress and strains are as follows:

$$\text{Stress: } \sigma = \sigma_0 \sin(t\omega + \delta) \quad (3.12)$$

$$\text{Strain: } \varepsilon = \varepsilon_0 \sin(t\omega) \quad (3.13)$$

for the thermal analysis of materials, an oscillating force of known amplitude and frequency is maintained, while a temperature sweep is applied. During the sweep, there is an instrument the storage and loss modulus, as well as $\tan(\delta)$. The storage modulus is related to the stored energy in the material, while the loss modulus is related to the loss of energy related to friction. Lastly, the $\tan \delta$ is related to the material's damping behaviour. Equations for these components are found below:

$$\text{Storage modulus: } E' = \frac{\sigma_0}{\varepsilon_0} \cos \delta \quad (3.14)$$

$$\text{Loss modulus: } E'' = \frac{\sigma_0}{\varepsilon_0} \sin \delta \quad (3.15)$$

$$\text{Tangent: } \tan \delta = \frac{E''}{E'} \quad (3.16)$$

To prepare the samples, a coating of organic material is drop-cast onto a free-standing glass mesh, allowing for the film to be strengthened without influencing the physical properties of the sample. The sample is then attached to the DMTA via a tension clamp setup (seen in *Figure 3.15*).

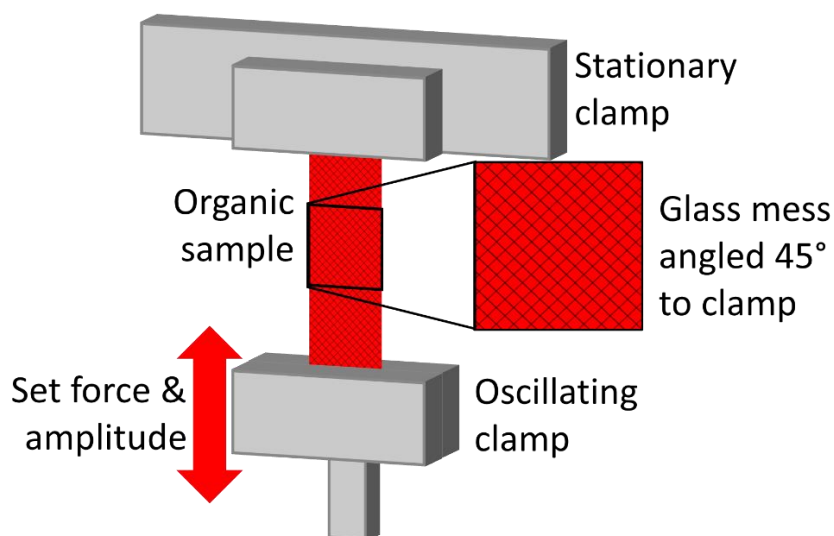


Figure 3.15: Basic schematic of DMTA with tension clamps attachment. Adapted from Sharma *et al.*, 2019 [21].

This technique has previously been demonstrated to improve the understanding of thermomechanical properties of several organic materials, including but not limited to TQ1, P3HT and PCDTBT polymers [13, 98].

In this thesis, DMTA was conducted on a DMA Q800 (TA Instruments) equipped with a liquid nitrogen cooling apparatus. The DMTA samples were prepared by repeatedly drop-casting the respective solutions on pre-cut glass mesh as described in previous literature [13, 98]. The prepared samples were dried under high vacuum of approximately 6×10^{-7} torr overnight. The measurements were performed in a strain-controlled tension mode at a heating rate of $3 \text{ }^\circ\text{C min}^{-1}$ from -110 to $300 \text{ }^\circ\text{C}$ under a nitrogen atmosphere at a frequency of 1 Hz. The annealing of samples was done in the DMA instrument under a nitrogen atmosphere for 30 min. The storage modulus (E'), loss modulus (E'') and $\text{Tan } \delta$ were recorded as a function of temperature for each sample.

3.6. References

1. Song, S., Lee, K. T., Koh, C. W., Shin, H., Gao, M., Woo, H. Y., Vak, D., and Kim, J. Y., Hot slot die coating for additive-free fabrication of high performance roll-to-roll processed polymer solar cells. *Energy & Environmental Science*, **2018**. 11 (11), 3248-3255.
2. Nguyen, T. L., Choi, H., Ko, S. J., Uddin, M. A., Walker, B., Yum, S., Jeong, J. E., Yun, M. H., Shin, T. J., and Hwang, S., Semi-crystalline photovoltaic polymers with efficiency exceeding 9% in a~ 300 nm thick conventional single-cell device. *Energy & Environmental Science*, **2014**. 7 (9), 3040-3051.
3. Mainville, M., Tremblay, V., Fenniri, M. Z., Laventure, A., Farahat, M. E., Ambrose, R., Welch, G. C., Hill, I. G., and Leclerc, M., Water Compatible Direct (Hetero)arylation Polymerization of PPDT2FBT: A Pathway Towards Large-Scale Production of Organic Solar Cells. *Asian Journal of Organic Chemistry*, **2020**. 9 (9), 1318-1325.
4. Morin, P.-O., Bura, T., Sun, B., Gorelsky, S. I., Li, Y., and Leclerc, M., Conjugated polymers à la carte from time-controlled direct (hetero) arylation polymerization. *ACS Macro Letters*, **2015**. 4 (1), 21-24.
5. Wang, E., Hou, L., Wang, Z., Hellström, S., Zhang, F., Inganäs, O., and Andersson, M. R., An easily synthesized blue polymer for high-performance polymer solar cells. *Advanced Materials*, **2010**. 22 (46), 5240-5244.
6. Andersson, L. M., Fully Slot–Die-Coated All-Organic Solar Cells. *Energy Technology*, **2015**. 3 (4), 437-442.
7. Bjuggren, J. M., Sharma, A., Gedefaw, D., Elmas, S., Pan, C., Kirk, B., Zhao, X., Andersson, G., and Andersson, M. R., Facile Synthesis of an Efficient and Robust Cathode Interface Material for Polymer Solar Cells. *ACS Applied Energy Materials*, **2018**. 1 (12), 7130-7139.
8. Wang, Y., Jafari, M. J., Wang, N., Qian, D., Zhang, F., Ederth, T., Moons, E., Wang, J., Inganäs, O., Huang, W., and Gao, F., Light-induced degradation of fullerenes in organic solar cells: a case study on TQ1:PC71BM. *Journal of Materials Chemistry A*, **2018**. 6 (25), 11884-11889.
9. Karuthedath, S., Gorenflot, J., Melianas, A., Kan, Z., Kemerink, M., and Laquai, F., Buildup of Triplet-State Population in Operating TQ1:PC71BM Devices Does Not Limit Their Performance. *The Journal of Physical Chemistry Letters*, **2020**. 11 (8), 2838-2845.
10. Karuthedath, S., Melianas, A., Kan, Z., Pranculis, V., Wohlfahrt, M., Khan, J. I., Gorenflot, J., Xia, Y., Inganäs, O., Gulbinas, V., Kemerink, M., and Laquai, F., Thermal annealing reduces geminate recombination in TQ1:N2200 all-polymer solar cells. *Journal of Materials Chemistry A*, **2018**. 6 (17), 7428-7438.
11. Xia, Y., Musumeci, C., Bergqvist, J., Ma, W., Gao, F., Tang, Z., Bai, S., Jin, Y., Zhu, C., and Kroon, R. J. J. o. M. C. A., Inverted all-polymer solar cells based on a quinoxaline–thiophene/naphthalene-diimide polymer blend improved by annealing. **2016**. 4 (10), 3835-3843.
12. Kim, Y., Yeom, H. R., Kim, J. Y., and Yang, C., High-efficiency polymer solar cells with a cost-effective quinoxaline polymer through nanoscale morphology control induced by practical processing additives. *Energy & Environmental Science*, **2013**. 6 (6), 1909-1916.
13. Sharma, A., Pan, X., Campbell, J. A., Andersson, M. R., and Lewis, D. A., Unravelling the thermomechanical properties of bulk heterojunction blends in polymer solar cells. *Macromolecules*, **2017**. 50 (8), 3347-3354.
14. Zhang, M., Guo, X., Ma, W., Ade, H., and Hou, J., A polythiophene derivative with superior properties for practical application in polymer solar cells. *Advanced Materials*, **2014**. 26 (33), 5880-5885.
15. Jang, S.-Y., Kim, I.-b., Kim, Y., Lim, D.-H., Kang, H., Heeney, M., and Kim, D.-Y., Facile Direct C-H Arylation Polymerization of Conjugated Polymer, PDCBT, for Organic Solar Cells. *Macromolecular Rapid Communications*, **2022**. 43 (20), 2200405.
16. Wang, J., Zheng, Z., Zhang, D., Zhang, J., Zhou, J., Liu, J., Xie, S., Zhao, Y., Zhang, Y., Wei, Z., Hou, J., Tang, Z., and Zhou, H., Regulating Bulk-Heterojunction Molecular Orientations through Surface Free Energy Control of Hole-Transporting Layers for High-Performance Organic Solar Cells. *Advanced Materials*, **2019**. 31 (17), 1806921.

17. Qin, Y., Uddin, M. A., Chen, Y., Jang, B., Zhao, K., Zheng, Z., Yu, R., Shin, T. J., Woo, H. Y., and Hou, J., Highly Efficient Fullerene-Free Polymer Solar Cells Fabricated with Polythiophene Derivative. *Advanced Materials*, **2016**. 28 (42), 9416-9422.
18. Su, Y.-A., Maebayashi, N., Fujita, H., Lin, Y.-C., Chen, C.-I., Chen, W.-C., Michinobu, T., Chueh, C.-C., and Higashihara, T., Development of Block Copolymers with Poly(3-hexylthiophene) Segments as Compatibilizers in Non-Fullerene Organic Solar Cells. *ACS Applied Materials & Interfaces*, **2020**. 12 (10), 12083-12092.
19. Sonar, P., Singh, S. P., Soh, M. S., and Li, Y., Ambipolar polymeric semiconductor materials and organic electronic devices. **2014**, Google Patents.
20. Jang, S. Y., Kim, I. b., Kim, Y., Lim, D. H., Kang, H., Heeney, M., and Kim, D. Y., Facile Direct C-H Arylation Polymerization of Conjugated Polymer, PDCBT, for Organic Solar Cells. *Macromolecular Rapid Communications*, **2022**. 43 (20), 2200405.
21. Lin, Y., Wang, J., Zhang, Z. G., Bai, H., Li, Y., Zhu, D., and Zhan, X., An electron acceptor challenging fullerenes for efficient polymer solar cells. *Advanced materials*, **2015**. 27 (7), 1170-1174.
22. Gurney, R. S., Li, W., Yan, Y., Liu, D., Pearson, A. J., and Wang, T., Morphology and efficiency enhancements of PTB7-Th: ITIC nonfullerene organic solar cells processed via solvent vapor annealing. *Journal of Energy Chemistry*, **2019**. 37, 148-156.
23. Wang, X., Yang, Y., He, Z., Wu, H., and Cao, Y., Influence of the acceptor crystallinity on the open-circuit voltage in PTB7-Th: ITIC organic solar cells. *Journal of Materials Chemistry C*, **2019**. 7 (47), 14861-14866.
24. Zhao, W., Qian, D., Zhang, S., Li, S., Inganäs, O., Gao, F., and Hou, J., Fullerene-Free Polymer Solar Cells with over 11% Efficiency and Excellent Thermal Stability. *Advanced Materials*, **2016**. 28 (23), 4734-4739.
25. Li, S., Ye, L., Zhao, W., Zhang, S., Mukherjee, S., Ade, H., and Hou, J., Energy-Level Modulation of Small-Molecule Electron Acceptors to Achieve over 12% Efficiency in Polymer Solar Cells. *Advanced Materials*, **2016**. 28 (42), 9423-9429.
26. Doumon, N. Y., Houard, F. V., Dong, J., Yao, H., Portale, G., Hou, J., and Koster, L. J. A., Energy level modulation of ITIC derivatives: Effects on the photodegradation of conventional and inverted organic solar cells. *Organic Electronics*, **2019**. 69, 255-262.
27. Zhang, L., Lin, B., Hu, B., Xu, X., and Ma, W., Blade-Cast Nonfullerene Organic Solar Cells in Air with Excellent Morphology, Efficiency, and Stability. *Advanced Materials*, **2018**. 30 (22), 1800343.
28. Destouesse, E., Top, M., Lamminaho, J., Rubahn, H. G., Fahlteich, J., and Madsen, M., Slot-die processing and encapsulation of non-fullerene based ITO-free organic solar cells and modules. *Flexible and Printed Electronics*, **2019**. 4 (4), 045004.
29. Xu, Y. X., Chueh, C. C., Yip, H. L., Ding, F. Z., Li, Y. X., Li, C. Z., Li, X., Chen, W. C., and Jen, A. K. Y., Improved charge transport and absorption coefficient in indacenodithieno [3, 2-b] thiophene-based ladder-type polymer leading to highly efficient polymer solar cells. *Advanced materials*, **2012**. 24 (47), 6356-6361.
30. Cui, Y., Ren, H., Yu, J., Wang, Z., and Qian, G., An indanone-based alkoxy silane dye with second order nonlinear optical properties. *Dyes and Pigments*, **2009**. 81 (1), 53-57.
31. Carlé, J. E., Andreasen, B., Tromholt, T., Madsen, M. V., Norrman, K., Jørgensen, M., and Krebs, F. C., Comparative studies of photochemical cross-linking methods for stabilizing the bulk hetero-junction morphology in polymer solar cells. *Journal of Materials Chemistry*, **2012**. 22 (46), 24417-24423.
32. Eggenhuisen, T. M., Galagan, Y., Biezemans, A. F. K. V., Slaats, T. M. W. L., Voorthuizen, W. P., Kommeren, S., Shanmugam, S., Teunissen, J. P., Hadipour, A., Verhees, W. J. H., Veenstra, S. C., Coenen, M. J. J., Gilot, J., Andriessen, R., and Groen, W. A., High efficiency, fully inkjet printed organic solar cells with freedom of design. *Journal of Materials Chemistry A*, **2015**. 3 (14), 7255-7262.
33. Sundaresan, C., Alem, S., Radford, C. L., Grant, T. M., Kelly, T. L., Lu, J., Tao, Y., and Lessard, B. H., Changes in Optimal Ternary Additive Loading when Processing Large Area Organic Photovoltaics by Spin- versus Blade-Coating Methods. *Solar RRL*, **2021**. 5 (10), 2100432.

34. Sun, Y., Seo, J. H., Takacs, C. J., Seifert, J., and Heeger, A. J., Inverted Polymer Solar Cells Integrated with a Low-Temperature-Annealed Sol-Gel-Derived ZnO Film as an Electron Transport Layer. *Advanced Materials*, **2011**. 23 (14), 1679-1683.
35. Na, S.-I., Seo, Y.-H., Nah, Y.-C., Kim, S.-S., Heo, H., Kim, J.-E., Rolston, N., Dauskardt, R. H., Gao, M., Lee, Y., and Vak, D., High Performance Roll-to-Roll Produced Fullerene-Free Organic Photovoltaic Devices via Temperature-Controlled Slot Die Coating. **2019**. 29 (6), 1805825.
36. Hart, A. S., Andersen, T. R., Griffith, M. J., Fahy, A., Vaughan, B., Belcher, W. J., and Dastoor, P. C., Roll-to-roll solvent annealing of printed P3HT : ICXA devices. *RSC Advances*, **2019**. 9 (72), 42294-42305.
37. Hösel, M., Søndergaard, R. R., Angmo, D., and Krebs, F. C., Comparison of Fast Roll-to-Roll Flexographic, Inkjet, Flatbed, and Rotary Screen Printing of Metal Back Electrodes for Polymer Solar Cells. *Advanced Engineering Materials*, **2013**. 15 (10), 995-1001.
38. Krebs, F. C., Fyenbo, J., and Jørgensen, M., Product integration of compact roll-to-roll processed polymer solar cell modules: methods and manufacture using flexographic printing, slot-die coating and rotary screen printing. *Journal of Materials Chemistry*, **2010**. 20 (41), 8994-9001.
39. Krebs, F. C., Air stable polymer photovoltaics based on a process free from vacuum steps and fullerenes. *Solar Energy Materials and Solar Cells*, **2008**. 92 (7), 715-726.
40. Lee, D. J., Heo, D. K., Yun, C., Kim, Y. H., and Kang, M. H., Solution-processed semitransparent inverted organic solar cells from a transparent conductive polymer electrode. *ECS Journal of Solid State Science and Technology*, **2019**. 8 (2), Q32.
41. Li, Y., Mao, L., Gao, Y., Zhang, P., Li, C., Ma, C., Tu, Y., Cui, Z., and Chen, L., ITO-free photovoltaic cell utilizing a high-resolution silver grid current collecting layer. *Solar energy materials and solar cells*, **2013**. 113, 85-89.
42. Muhsin, B., Roesch, R., Gobsch, G., and Hoppe, H., Flexible ITO-free polymer solar cells based on highly conductive PEDOT:PSS and a printed silver grid. *Solar Energy Materials and Solar Cells*, **2014**. 130, 551-554.
43. Jang, H., Kim, M. S., Jang, W., Son, H., Wang, D. H., and Kim, F. S., Highly conductive PEDOT: PSS electrode obtained via post-treatment with alcoholic solvent for ITO-free organic solar cells. *Journal of Industrial and Engineering Chemistry*, **2020**. 86, 205-210.
44. Eom, S. H., Park, H., Mujawar, S. H., Yoon, S. C., Kim, S.-S., Na, S.-I., Kang, S.-J., Khim, D., Kim, D.-Y., and Lee, S.-H., High efficiency polymer solar cells via sequential inkjet-printing of PEDOT:PSS and P3HT:PCBM inks with additives. *Organic Electronics*, **2010**. 11 (9), 1516-1522.
45. Meng, Y., Hu, Z., Ai, N., Jiang, Z., Wang, J., Peng, J., and Cao, Y., Improving the Stability of Bulk Heterojunction Solar Cells by Incorporating pH-Neutral PEDOT:PSS as the Hole Transport Layer. *ACS Applied Materials & Interfaces*, **2014**. 6 (7), 5122-5129.
46. Seo, J. H., Koo, J.-R., Lee, S. J., Seo, B. M., and Kim, Y. K., Efficient organic photovoltaic devices by using PEDOT: PSSs with excellent hole extraction ability. *Journal of Nanoscience and Nanotechnology*, **2011**. 11 (8), 7307-7310.
47. Sankaran, S., Glaser, K., Gärtner, S., Rödlmeier, T., Sudau, K., Hernandez-Sosa, G., and Colmann, A., Fabrication of polymer solar cells from organic nanoparticle dispersions by doctor blading or ink-jet printing. *Organic Electronics*, **2016**. 28, 118-122.
48. Kommeren, S., Coenen, M. J. J., Eggenhuisen, T. M., Slaats, T. W. L., Gorter, H., and Groen, P., Combining solvents and surfactants for inkjet printing PEDOT:PSS on P3HT/PCBM in organic solar cells. *Organic Electronics*, **2018**. 61, 282-288.
49. Pali, L. S., Jindal, R., and Garg, A., Screen printed PEDOT:PSS films as transparent electrode and its application in organic solar cells on opaque substrates. *Journal of Materials Science: Materials in Electronics*, **2018**. 29 (13), 11030-11038.
50. Ylikunnari, M., Välimäki, M., Väisänen, K.-L., Kraft, T. M., Sliz, R., Corso, G., Po, R., Barbieri, R., Carbonera, C., Gorni, G., and Vilkmann, M., Flexible OPV modules for highly efficient indoor applications. *Flexible and Printed Electronics*, **2020**. 5 (1), 014008.
51. Strohm, S., Machui, F., Langner, S., Kubis, P., Gasparini, N., Salvador, M., McCulloch, I., Egelhaaf, H. J., and Brabec, C. J., P3HT: non-fullerene acceptor based large area, semi-transparent PV modules with power conversion efficiencies of 5%, processed by industrially scalable methods. *Energy & Environmental Science*, **2018**. 11 (8), 2225-2234.

52. Miranda, B. H., Corrêa, L. d. Q., Soares, G. A., Martins, J. L., Lopes, P. L., Vilela, M. L., Rodrigues, J. F., Cunha, T. G., Vilaça, R. d. Q., and Castro-Hermosa, S., Efficient fully roll-to-roll coated encapsulated organic solar module for indoor applications. *Solar Energy*, **2021**. 220, 343-353.
53. Hoff, A., Gasonoo, A., Pahlevani, M., and Welch, G. C., An Alcohol-Soluble N-Annulated Perylene Diimide Cathode Interlayer for Air-Processed, Slot-Die Coated Organic Photovoltaic Devices and Large-Area Modules. *Solar RRL*, **2022**. 6 (11), 2200691.
54. Andersen, T. R., Cooling, N. A., Almyahi, F., Hart, A. S., Nicolaidis, N. C., Feron, K., Noori, M., Vaughan, B., Griffith, M. J., Belcher, W. J., and Dastoor, P. C., Fully roll-to-roll prepared organic solar cells in normal geometry with a sputter-coated aluminium top-electrode. *Solar Energy Materials and Solar Cells*, **2016**. 149, 103-109.
55. Zimmermann, B., Schleiermacher, H.-F., Niggemann, M., Würfel, U., and Cells, S., ITO-free flexible inverted organic solar cell modules with high fill factor prepared by slot die coating. *Solar Energy Materials and Solar Cells*, **2011**. 95 (7), 1587-1589.
56. Krebs, F. C., Jørgensen, M., Norrman, K., Hagemann, O., Alstrup, J., Nielsen, T. D., Fyenbo, J., Larsen, K., and Kristensen, J., A complete process for production of flexible large area polymer solar cells entirely using screen printing—first public demonstration. *Solar Energy Materials and Solar Cells*, **2009**. 93 (4), 422-441.
57. Susanna, G., Salamandra, L., Brown, T. M., Di Carlo, A., Brunetti, F., and Reale, A., Airbrush spray-coating of polymer bulk-heterojunction solar cells. *Solar Energy Materials and Solar Cells*, **2011**. 95 (7), 1775-1778.
58. Angmo, D., Larsen-Olsen, T. T., Jørgensen, M., Søndergaard, R. R., and Krebs, F. C., Roll-to-Roll Inkjet Printing and Photonic Sintering of Electrodes for ITO Free Polymer Solar Cell Modules and Facile Product Integration. *Advanced Energy Materials*, **2013**. 3 (2), 172-175.
59. Krebs, F. C., Polymer solar cell modules prepared using roll-to-roll methods: knife-over-edge coating, slot-die coating and screen printing. *Solar Energy Materials and Solar Cells*, **2009**. 93 (4), 465-475.
60. Meitzner, R., Faber, T., Alam, S., Amand, A., Roesch, R., Büttner, M., Herrmann-Westendorf, F., Presselt, M., Ciannaruchi, L., and Visoly-Fisher, I., Impact of P3HT materials properties and layer architecture on OPV device stability. *Solar Energy Materials and Solar Cells*, **2019**. 202, 110151.
61. Li, M., Zhang, W., Wang, H., Chen, L., Zheng, C., and Chen, R., Effect of organic cathode interfacial layers on efficiency and stability improvement of polymer solar cells. *RSC advances*, **2017**. 7 (50), 31158-31163.
62. Weng, C.-N., Yang, H.-C., Tsai, C.-Y., Chen, S.-H., Chen, Y.-S., Chen, C.-H., Huang, K.-M., Meng, H.-F., Chao, Y.-C., and Chang, C.-Y., The influence of UV filter and Al/Ag moisture barrier layer on the outdoor stability of polymer solar cells. *Solar Energy*, **2020**. 199, 308-316.
63. Doumon, N. Y., Wang, G., Chiechi, R. C., and Koster, L. J. A., Relating polymer chemical structure to the stability of polymer: fullerene solar cells. *Journal of Materials Chemistry C*, **2017**. 5 (26), 6611-6619.
64. Krebs, F. C., Fabrication and processing of polymer solar cells: a review of printing and coating techniques. *Solar energy materials and solar cells*, **2009**. 93 (4), 394-412.
65. Po, R., Bernardi, A., Calabrese, A., Carbonera, C., Corso, G., and Pellegrino, A., From lab to fab: how must the polymer solar cell materials design change? – an industrial perspective. *Energy & Environmental Science*, **2014**. 7 (3), 925-943.
66. Geens, W., Martens, T., Poortmans, J., Aernouts, T., Manca, J., Lutsen, L., Heremans, P., Borghs, S., Mertens, R., and Vanderzande, D., Modelling the short-circuit current of polymer bulk heterojunction solar cells. *Thin Solid Films*, **2004**. 451-452, 498-502.
67. Hong, S., Lee, J., Kang, H., and Lee, K., Slot-die coating parameters of the low-viscosity bulk-heterojunction materials used for polymer solar cells. *Solar energy materials and solar cells*, **2013**. 112, 27-35.
68. Wu, Q., Guo, J., Sun, R., Guo, J., Jia, S., Li, Y., Wang, J., and Min, J., Slot-die printed non-fullerene organic solar cells with the highest efficiency of 12.9% for low-cost PV-driven water splitting. *Nano Energy*, **2019**. 61, 559-566.

69. Michels, J. J., Zhang, K., Wucher, P., Beaujuge, P. M., Pisula, W., and Marszalek, T., Predictive modelling of structure formation in semiconductor films produced by meniscus-guided coating. *Nature materials*, **2020**, 1-8.
70. Ltd, O. Slot-Die Coating: Theory, Design, & Applications. **2020** [cited 2020 5th December]; Available from: <https://www.ossila.com/pages/slot-die-coating-theory#:~:text=Slot%2Ddie%20coating%20is%20an,positioned%20close%20to%20the%20surface.&text=Slot%2Ddie%20coating%20is%20one,the%20surface%20of%20a%20substrate>.
71. Ding, X., Liu, J., and Harris, T. A., A review of the operating limits in slot die coating processes. *AIChE Journal*, **2016**. 62 (7), 2508-2524.
72. Yuan, S. L., A flow model for non-newtonian liquids inside a slot die. *Polymer Engineering & Science*, **1995**. 35 (7), 577-586.
73. Lee, S. H., Koh, H. J., Ryu, B. K., Kim, S. J., Jung, H. W., and Hyun, J. C., Operability coating windows and frequency response in slot coating flows from a viscocapillary model. *Chemical engineering science*, **2011**. 66 (21), 4953-4959.
74. Zhang, W., Zhao, B., He, Z., Zhao, X., Wang, H., Yang, S., Wu, H., Cao, Y. J. E., and Science, E., High-efficiency ITO-free polymer solar cells using highly conductive PEDOT: PSS/surfactant bilayer transparent anodes. **2013**. 6 (6), 1956-1964.
75. Mihailetchi, V. D., Koster, L. J. A., Blom, P. W., Melzer, C., de Boer, B., van Duren, J. K., and Janssen, R. A., Compositional dependence of the performance of poly (p-phenylene vinylene): methanofullerene bulk-heterojunction solar cells. *Advanced Functional Materials*, **2005**. 15 (5), 795-801.
76. Rose, A., Space-Charge-Limited Currents in Solids. *Physical Review*, **1955**. 97 (6), 1538-1544.
77. Haneef, H. F., Zeidell, A. M., and Jurchescu, O. D., Charge carrier traps in organic semiconductors: a review on the underlying physics and impact on electronic devices. *Journal of Materials Chemistry C*, **2020**. 8 (3), 759-787.
78. Murgatroyd, P., Theory of space-charge-limited current enhanced by Frenkel effect. *Journal of Physics D: Applied Physics*, **1970**. 3 (2), 151.
79. Goh, C., Kline, R. J., McGehee, M. D., Kadnikova, E. N., and Fréchet, J. M., Molecular-weight-dependent mobilities in regioregular poly (3-hexyl-thiophene) diodes. *Applied Physics Letters*, **2005**. 86 (12), 122110.
80. Katagiri, C. and Nakayama, K.-i., Comparison of the carrier mobilities of annealed P3HT films by using charge carrier extraction by linearly increasing voltage and space-charge limited current. *Molecular Crystals and Liquid Crystals*, **2016**. 629 (1), 193-199.
81. Juška, G., Arlauskas, K., Viliūnas, M., and Kočka, J., Extraction current transients: new method of study of charge transport in microcrystalline silicon. *Physical review letters*, **2000**. 84 (21), 4946.
82. Juška, G., Arlauskas, K., Viliūnas, M., Genevičius, K., Österbacka, R., and Stubb, H., Charge transport in π -conjugated polymers from extraction current transients. *Physical Review B*, **2000**. 62 (24), R16235.
83. Stephen, M., Genevičius, K., Juška, G., Arlauskas, K., and Hiorns, R. C., Charge transport and its characterization using photo-CELIV in bulk heterojunction solar cells. *Polymer International*, **2017**. 66 (1), 13-25.
84. Chen, S., Choudhury, K. R., Subbiah, J., Amb, C. M., Reynolds, J. R., and So, F., Photo-Carrier Recombination in Polymer Solar Cells Based on P3HT and Silole-Based Copolymer. *Advanced Energy Materials*, **2011**. 1 (5), 963-969.
85. Mozer, A. J., Sariciftci, N. S., Lutsen, L., Vanderzande, D., Österbacka, R., Westerling, M., and Juška, G., Charge transport and recombination in bulk heterojunction solar cells studied by the photoinduced charge extraction in linearly increasing voltage technique. *Applied Physics Letters*, **2005**. 86 (11), 112104.
86. Algahtani, F., Thulasiram, K., Mohd Nasir, N., and Holland, A., Four point probe geometry modified correction factor for determining resistivity. **2013**.
87. Andersson, G. and Ridings, C., Ion scattering studies of molecular structure at liquid surfaces with applications in industrial and biological systems. *Chemical reviews*, **2014**. 114 (17), 8361-8387.

88. Andersson, G. and Morgner, H., Impact collision ion scattering spectroscopy (ICISS) and neutral impact collision ion scattering spectroscopy (NICISS) at surfaces of organic liquids. *Surface science*, **1998**. 405 (1), 138-151.
89. Wang, C., Kan, A., Liu, Z., Zhang, G., Lin, X., and Fu, H., Using neutral impact collision ion scattering spectroscopy and angular resolved X-ray photoelectron spectroscopy to analyze surface structure of surfactant solutions. *Colloid and Polymer Science*, **2015**. 293, 1655-1666.
90. Andersson, G., Krebs, T., and Morgner, H., Activity of surface active substances determined from their surface excess. *Physical Chemistry Chemical Physics*, **2005**. 7 (1), 136-142.
91. Ridings, C., Lockett, V., and Andersson, G., Significant changes of the charge distribution at the surface of an ionic liquid due to the presence of small amounts of water. *Physical Chemistry Chemical Physics*, **2011**. 13 (48), 21301-21307.
92. Greenbank, W., Hirsch, L., Wantz, G., and Chambon, S., Interfacial thermal degradation in inverted organic solar cells. *Applied Physics Letters*, **2015**. 107 (26), 263301.
93. Perlich, J., Rubeck, J., Botta, S., Gehrke, R., Roth, S., Ruderer, M., Prams, S., Rawolle, M., Zhong, Q., and Körstgens, V., Grazing incidence wide angle x-ray scattering at the wiggler beamline BW4 of HASYLAB. *Review of Scientific Instruments*, **2010**. 81 (10), 105105.
94. Chang, C. C., Auger electron spectroscopy. *Surface Science*, **1971**. 25 (1), 53-79.
95. Gunawardane, R. P. and Arumainayagam, C. R., Auger electron spectroscopy, in *Handbook of applied solid state spectroscopy*. 2006, Springer. p. 451-483.
96. Briggs, D., Practical surface analysis. *Auger and X-Ray Photoelectron Spectroscopy*, **1990**. 1, 151-152.
97. Childs, K. D., Carlson, B. A., LaVanier, L. A., Moulder, J. F., Paul, D. F., Stickle, W. F., and Watson, D. G., Handbook of Auger Electron Microscopy. 3rd ed. 1997, Eden Prairie, Minnesota: Physical Electronics, Inc.
98. Sharma, A., Pan, X., Bjuggren, J. M., Gedefaw, D., Xu, X., Kroon, R., Wang, E., Campbell, J. A., Lewis, D. A., and Andersson, M. R., Probing the relationship between molecular structures, thermal transitions, and morphology in polymer semiconductors using a woven glass-mesh-based DMTA technique. *Chemistry of Materials*, **2019**. 31 (17), 6740-6749.

CHAPTER 4 – INTRODUCING NEAT FULLERENES TO IMPROVE THE THERMAL STABILITY OF SLOT-DIE COATED ORGANIC SOLAR CELLS

This chapter is a reformatted text that has been published in Materials Advances. See the Contextual Statement for details on the contributions of the co-authors to the journal version of this article.

Reference for the journal version:

Kirk, B., Pan, X., Jevric, M., Andersson, G., & Andersson, M. R., Introducing neat fullerenes to improve the thermal stability of slot-die coated organic solar cells. Materials Advances, 2022, 3(6), 2838-2849.

4.1. Overview

For organic photovoltaics (OPVs) to be considered commercially viable, the devices should not only achieve high performances, but also have relatively long lifespans. In fact, a major source of lifespan reduction is associated with the "burn-in" process, resulting in a sharp initial reduction in performance. PPDT2FBT:PC₇₁BM and PPDT2FT:PC₆₁BM both represent highly robust and efficient cells when fabricated under ambient conditions via slot-die coating and have been shown to be tolerant to elevated temperatures. With accelerated thermal aging at 120 °C, such devices were found to be affected by the burn-in process, greatly diminishing their efficiency. The addition of pristine C₇₀, to the PPDT2FBT:PC₆₁BM bulk-heterojunction (BHJ) was found to improve the thermal stability of slot-die coated OPVs at high temperatures while the addition of C₆₀ speeds up the burn-in process. Initially, the ink preparation for the active layer and fabrication conditions for slot-die coating were optimised to improve the flexible device performance for PPDT2FBT:PC₇₁BM and PPDT2FBT:PC₆₁BM cells, reaching a power conversion efficiency (PCE) of 8.49% and 7.63%, respectively. A subsequent investigation into the thermal stability of PPDT2FBT:PC₆₁BM devices at 85 °C found no significant burn-in process that reduces device performance, which was evidenced at 120 °C, but a continuous degradation process that slowly reduces the device performance. We have found that the addition of 5.0% w/w of C₇₀ (with respect to PCBM) into the active layer blend suppressed the thermal degradation at 120 °C, compared to the binary blend. Dynamic mechanical thermal analysis (DMTA) measurements on the bulk-heterojunction blends further revealed that the thermal behaviour is significantly changed after the addition of small amounts of C₇₀. When compared with the addition of neat C₆₀, a known nucleating agent, the addition of C₇₀ instead appeared to inhibit crystal formation and growth, rather than induce the formation of many smaller crystals. We anticipate that this improved formulation will improve the device lifetimes significantly at lower temperatures.

4.2. Introduction

Organic photovoltaics (OPVs) have seen increased interest over the past decade owing to its potential to be fabricated as flexible devices, roll-to-roll processability and relatively low fabrication cost [1-3]. Since the early developmental stages of OPVs, fullerenes have been the most widely used acceptor materials, especially PC₆₁BM, due to the materials relatively low production cost [4]. To enhance the absorption of visible light and increase the power conversion efficiency, PC₇₁BM was also introduced early in the development of OPVs [5]. Recently there has been significant increase in record power conversion efficiencies (PCEs), exceeding 18% for single junction devices [6-8]. This is mainly due to the development of strongly absorbing acceptor molecules; however, these molecules are normally produced via multi-step synthesis and are therefore quite expensive to produce. The development of efficient small-scale laboratory fabricated devices has prompted a shift towards large-scale devices which could potentially be used for commercial purposes. In order to fulfill this vision, several coating techniques, including slot-die [9-11], blade [12, 13], screen [14-16] and spray coating [17-19], are currently being investigated to reduce the performance gap between small and large area devices. The advantage of these techniques over small-scale spin-coated devices is the relatively low material wastage and feasibility of upscaling (>1 m²) fabrication of flexible devices. Recently, there has been increased interest in these materials for their potential usage as indoor solar cells [20].

Though performance is an important aspect of OPV development, material/fabrication cost and stability are areas that are not as extensively investigated when it comes to large-area devices. For OPV technologies to be competitive with other types of photovoltaic devices, they need to be relatively in-expensive to manufacture and have a comparable lifespan (at least 10 years) [21]. There are several mechanisms of degradation that have been identified to have significant influence on the lifetime of OPVs. These include thermal [22, 23], oxygen and moisture [24, 25], UV radiance [26, 27] and mechanical [9, 28, 29] degradation. These factors are responsible for two significant decay trends of PCE: burn-in and linear degradation [30-32]. For burn-in, the performance drop is relatively quick and is usually where the largest decrease in performance occurs, however, the impact of this degradation decreases as time progresses [32-34]. After the burn-in, a linear degradation occurs, resulting in a relatively low rate of decay in PCE. It has been shown that the origin behind severe burn-in losses in many systems depends on morphological changes in the active material [33-35].

The continuous illumination of the sun can result in an increase in the working temperature of the OPV in outdoor fixtures. It is known that polymers have structural mobility, especially if the environmental temperature exceeds their glass transition temperatures [36, 37]. This can result in a change of morphology, such as degree of phase separation, over time, for donor-acceptor blends.

In the case of polymer:fullerene composites, the thermal energy can lead to the crystallization of the polymer and fullerene components, which leads to a decreased performance [38, 39]. The formation of large crystals when exposed to heat can lead to a reduction in performance as inefficient exciton dissociation can occur and charge transfer decreases as a result from decrease of the donor/acceptor interfaces. To address fullerene crystallization, one reported method mentioned using nucleating agents to limit the size of fullerene crystallites in the active layer, thus improving the thermal stability [40, 41]. Lindqvist *et al.* demonstrated that the addition of as little 2% w/w C₆₀ improved the thermal stability of TQ1:PC₆₁BM based OPVs, even when heated up to 130 °C, which is above the glass transition temperature of this particular bulk-heterojunction (BHJ) [42].

There are several active materials that have been shown to reach high performances, with some reaching beyond 18% for single junction OPVs [6-8]. However, most of these high performing materials were only fabricated into small-scale cells using rigid glass substrate, and the deposition process was protected by nitrogen, which is not easily applicable to large-scale printing/coating method. As of 2021, the highest efficiency to be achieved for large area (≥ 1 cm²) OPVs has been 12.6% [43]. In addition, these high performing materials are also known to have complex synthesis and require many purification steps that make them expensive to upscale and thus, less desirable to use in the fabrication of large-area OPVs [44, 45]. As seen in *Table B1* in Appendix B, the high performing materials (PM6, ITIC & Y6) are far more expensive than more maturely developed materials (C₆₀, PC₆₁BM, PC₇₁BM, P3HT).

Poly[(2,5-bis(2hexyldecyloxy)phenylene)-alt-(5,6-difluoro-4,7-di(thiophen-2-yl)benzo[c][1,2,5]thiadiazole)]: [6,6]-phenyl-C₆₁-butyric acid ester (PPDT2FBT:PC₆₁BM) is a promising material combination that can be used as the donor:acceptor material in slot-die coated devices (*Figure 4.a*). These organic materials have been used to fabricate devices via slot-die coating (rigid [46] & flexible [47] substrates) with minimal performance losses upon upscaling. In addition, these materials are relatively in-expensive and the synthesis is scalable [48]. Lastly, there is a relatively small gap between spin-coated and slot-die coated PPDT2FBT:PC₇₁BM devices, with efficiencies reaching up to 9.39% [49] and 7.61% [47] respectively.

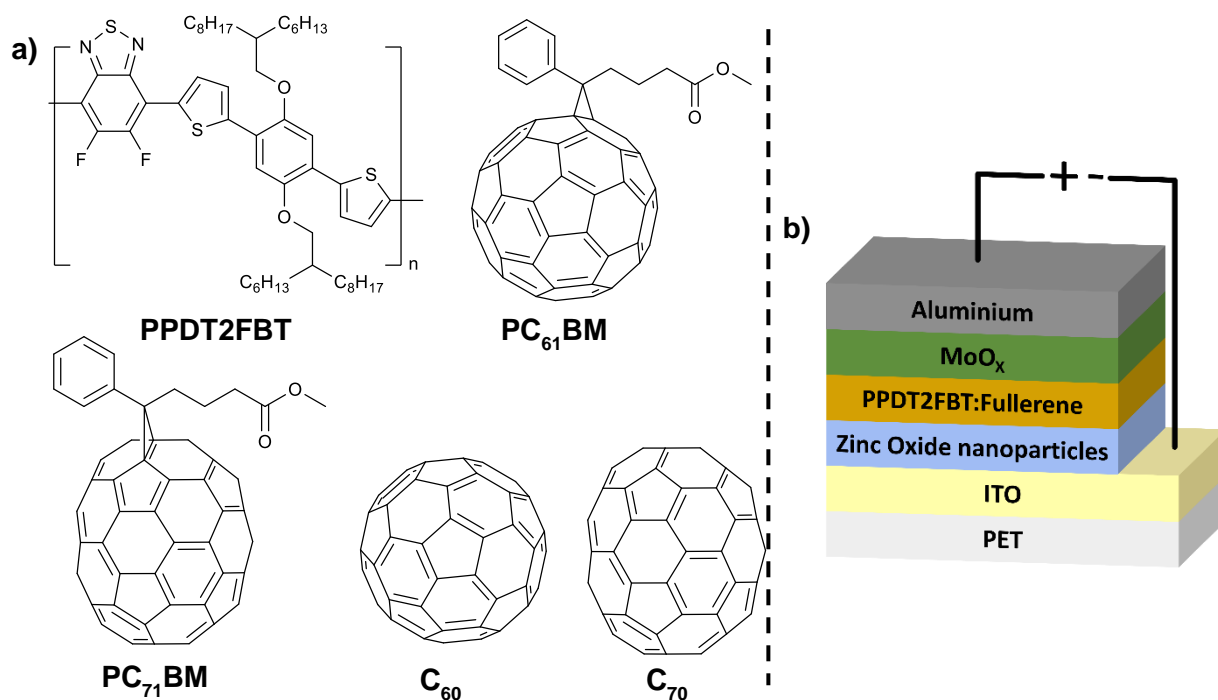


Figure 4.1: (a) Chemical structure of PPDT2FBT, C₆₀, C₇₀, PC₆₁BM and PC₇₁BM; (b) schematic illustration of inverted OPV structure used in this work.

A few studies have investigated the stability of spin-coated and slot-die devices using PPDT2FBT:PCBM. In 2014, Nguyen *et al.* showed that PPDT2FBT:PC₇₁BM based devices were thermally robust at 130 °C for 200 hours of temporal stability (Cycling between room temperature and 130 °C) [49]. Later in 2018, UV activated crosslinkers were added to fix the morphology in the PPDT2FBT:PC₇₁BM active layer was reported, having found such crosslinker addition to improve the thermal stability of OPVs at 120 °C. In addition, subjecting these devices to continual illumination for 40 hrs, resulted in minimal decrease in efficiency [50]. As for slot-die coated devices, Song *et al.* briefly highlighted the impact that solvents and solvent additives could have on the thermal degradation at 25 °C & 120 °C as well as photodegradation under ambient conditions. The conclusion of this work was, that the addition of a high boiling point - low vapour pressure solvent additive reduced the overall stability of PPDT2FBT:PC₇₁BM devices [47].

In this work, we have investigated the thermal stability of slot-die coated inverted devices made of PPDT2FBT:PC₆₁BM (Figure 4.b). Before investigating the thermal stability, coating conditions were adjusted to optimise the performance of slot-die coated PPDT2FBT:PC₇₁BM and PPDT2FBT:PC₆₁BM devices. These devices were all fabricated on flexible PET/ITO substrates via a slot-die coating technique under ambient conditions. The initial stability studies revealed that up to 85 °C under nitrogen storage condition the PPDT2FBT:PC₆₁BM devices are relatively stable and do not suffer from severe loss of the efficiency. To further study the thermal stability, devices were aged at 120 °C to accelerate the degradation. This revealed a significant thermal “burn-in” degradation that can be suppressed by the addition of C₇₀ into the active layer.

We found that the major source of degradation was from the crystallization of fullerene, verified by characterisation using scanning electron microscopy (SEM) and Auger electron spectroscopy (AES) techniques. Dynamic mechanical thermal analysis (DMTA) was implemented to investigate the thermal properties of the neat polymer and the bulk-heterojunction blends, and this revealed that the thermal behaviour is significantly changed after the addition of small amounts of C₇₀.

4.3. Experimental section

4.3.1. Materials

Donor material poly[(2,5-bis(2hexyldecyloxy)phenylene)-alt-(5,6-difluoro-4,7-di(thiophen-2-yl)benzo[c][1,2,5]thiadiazole)] (PPDT2FBT) was synthesised using a direct arylation polymerisation according to literature [51]. The molecular weight of PPDT2FBT was determined via Gel Permeation Chromatography (Agilent 1260 Infinity II High-Temperature GPC System) using trichlorobenzene at 150 °C, giving a number average molecular weight (M_n) of 50 of kg/mol with a PDI of 2.60 relative to polystyrene standards.

The ZnO NP dispersion was prepared following a previously published procedure [52]. To achieve an ideal processing concentration, acetone (Chem-supply, 99.9%) was added to the NP precipitate until a concentration of approximately 40 mg mL⁻¹ was achieved. Afterwards, 2-(2-methoxyethoxy)acetic acid (Sigma Aldrich) (5% w/w in relation to ZnO NP) was then added to the dispersion to stabilise the NPs.

Small molecule acceptors [[6,6]-phenyl-C61-butyric acid ester (PC₆₁BM), [6,6]-phenyl-C71-butyric acid ester (PC₇₁BM), and neat fullerenes (C₆₀ & C₇₀) were purchased from Solenne BV. Solvents ortho-dichlorobenzene, chlorobenzene and 1-chloronaphthalene were purchased from Sigma Aldrich, whereas chloroform (CHCl₃) was purchased from Chem-Supply. All solvents were used directly without purification.

4.3.2. Device fabrication

Slot-die coated devices were fabricated in a PET/ITO/ZnO NP/BHJ layer/MoO_x/Al device configuration for the three BHJ layers of PPDT2FBT:PC₆₁BM, PPDT2FBT:PC₇₁BM & PPDT2FBT:PC₆₁BM:C₇₀. Active layer ink was prepared by dissolving materials, with a donor:acceptor weight ratio of 1:2, in ortho-dichlorobenzene (total 25 mg mL⁻¹ or 14 mg mL⁻¹) with 0.5% V/V of 1-chloronaphthalene at 60 °C overnight.

The flexible ITO substrate (50 ohm/sq, Dongguan Hongdian Technology Co.) was attached to a mini-roll coater (FOM technologies) with slot-die attachment and wiped with isopropanol soaked TerriWipes at a rotation speed of 2 m min⁻¹ prior to fabrication. The tubing and slot-die head was cleaned with chloroform prior to assembly and between the change of deposition material. Layer deposition was processed under ambient conditions.

The ZnO NP layer (35 nm) was deposited using 0.1 mL min⁻¹ flow-rate, a drum speed of 1.0 m min⁻¹ and drum temperature at 70 °C to achieve a strip width of around 13 mm. The BHJ layer (150 – 200 nm) was deposited via varying flow rate and drum speed at a drum temperature at 70 °C to obtain a strip width of around 13 mm. Wet and dry thickness for both the ZnO NP and BHJ layers were calculated according to *Equation B1 & B2* in Appendix B.

After slot-die coating, the MoO_x and aluminium was deposited via the following method. The MoO_x (12nm) was thermally deposited on the BHJ layer under high vacuum using a Covap thermal evaporation system (Angstrom Engineering). This was followed by the evaporation of the Al electrode (80 nm) using a shadow mask, defining the active area to 0.1 cm².

Devices were measured using an Oriel Solar simulator fitted with a 150 W Xeon lamp (Newport), filtered to give an output of 100 mW cm⁻² at AM 1.5 (air mass) standard and calibrated using a silicon reference cell with NIST traceable certification. Device testing was conducted under ambient conditions. For investigating performance and material degradation, PET/ITO/ZnO NP/BHJ layer/MoO_x/Al & PET/ITO/ZnO NP/BHJ device configurations were used, respectively. Thermal annealing and aging were conducted on a hotplate in a nitrogen-filled glove-box with minimal light exposure.

4.3.3. Square-Wave Voltammetry

Square-wave voltammetry (SWV) measurements were carried out for the determination of the oxidation/reduction potentials, and in turn, the highest occupied molecular orbital (HOMO) and/or lowest unoccupied molecular orbital (LUMO) energy levels of PPDT2FBT, PC₇₁BM, PC₆₁BM, C₇₀ & C₆₀. An AUTOLAB PGSTAT (Metrohm AG) instrument using three-electrode setup with platinum wires, both the working electrode (WE) and counter electrode (CE) and an Ag/Ag⁺ reference electrode was used. Detailed experimental details can be found in *Appendix B*.

4.3.4. Scanning Electron Microscopy

Measurements were performed using Inspect F50 scanning electron microscopy (<https://doi.org/10.25957/flinders.sem>) equipped with a field emission gun (FEI Company) and a secondary electron detector. The acceleration voltage was 10 kV, and the working distance of 10 mm. The samples were not coated with any conducting layers.

4.3.5. Auger Electron Spectroscopy

Measurements were performed using a PHI 710 Scanning Auger Nanoprobe system using an acceleration voltage was 10 kV and emission current was 1 nA. Spectra were collected via point scans as specific locations on the sample (SEM images of scan locations can be found in *Figure B3* in *Appendix B*). The Auger spectra were filtered and analysed, as well as element concentrations calculated with MultiPak Spectrum.

4.3.6. Dynamic Mechanical Thermal Analysis

The dynamic mechanical thermal analysis (DMTA) was conducted on a DMA Q800 (TA Instruments) equipped with a liquid nitrogen cooling apparatus. The DMTA samples were prepared by repeatedly drop-casting the respective solutions on pre-cut glass mesh as described in previous literature [53, 54]. Sample preparation and instrument conditions can be found in *Appendix B*.

4.4. Results and Discussion

4.4.1. Adjustment of the slot-die coating conditions

To compare the thermal stability of scalable OPVs, PPDT2FBT:PC₆₁BM devices were fabricated on flexible ITO-coated PET in air using a mini-roll coater. OPV devices were fabricated with the inverted structure of ITO/ZnO NPs/PPDT2FBT:PC₆₁BM/MoO_x/aluminium (as seen in *Figure 4.b*). The coating conditions were adjusted to optimise the PCEs and PPDT2FBT:PC₇₁BM devices were also prepared to further improve the efficiency.

To optimise the slot-die coated devices, the drum-speed, flow rate and ink concentration were adjusted for the active layer. The ZnO NP layer that is coated over the ITO electrode is kept constant. By analysing the Current Density/Voltage (JV) curves of the devices, the short-circuit current density (J_{SC}), open-circuit voltage (V_{OC}), Fill-factor (FF) and power conversion efficiency (PCE) were extracted. The device characteristics under different fabrication conditions are listed in *Table B2* in the *Appendix B*.

When decreasing the drum speed (and proportionately the flow-rate), it was found that despite the same theoretical thickness, the efficiency of these devices had increased. This optimisation of drum/substrate speed has been observed in literature [47] and is suspected to be associated with the shear forces between the substrate and meniscus, allowing for a more ideal active layer deposition. It is also worth noting that the active layer of PPDT2FBT:PC₆₁BM can be coated as a thicker layer [49, 55] allowing for improved efficiency. This is evident when increasing the flow-rate to allow for an increase in the theoretical thickness from 150 nm to 200 nm.

Lastly, using an appropriate concentration was important for active material deposition. At 14 mg mL⁻¹, it was difficult to keep the coating width at 13 mm (width of the slot-die coater), resulting in over-flow along the width of the strip. This was recognized by increasing the concentration to 25 mg mL⁻¹ (and adjusting flow-rate accordingly) to improve efficiency. Overall, by adjusting coating conditions for PPDT2FBT:PC₇₁BM and PPDT2FBT:PC₆₁BM, an optimised PCE of 8.49% and 7.63% was achieved, respectively, when using an ink total concentration of 25 mg min⁻¹ and a drum speed of 0.2 m min⁻¹ (data can be found in *Table B2* in *Appendix B*).

For the investigation of device stability, it was decided to investigate PC₆₁BM as the fullerene acceptor rather than PC₇₁BM. As mentioned previously, cost is an important factor when aiming towards commercialisation of OPVs. As such, it is known that PC₇₁BM is quite expensive when compared with PC₆₁BM[41], making it less feasible for upscaled devices, despite the improved performance.

4.4.2. Storage and thermal stability of PPDT2FBT:PC₆₁BM devices

To understand the stability of PPDT2FBT:PC₆₁BM based OPVs and study the influence of storage conditions, we have carried out stability test by storing the devices under nitrogen conditions at room temperature (RT) and at elevated temperatures. As for the thermal stability measurements, we have used 85 °C to start with, there is a consensus for this temperature in thermal testing [56, 57]. The unencapsulated device characteristics trends with aging time are shown in *Figure 4.2*, comparing the device aging with and without heating in dark and under nitrogen, while device characterisation was performed in air at room temperature. Tables of the detailed data can be found in the supplementary information (Table A3 and A4).

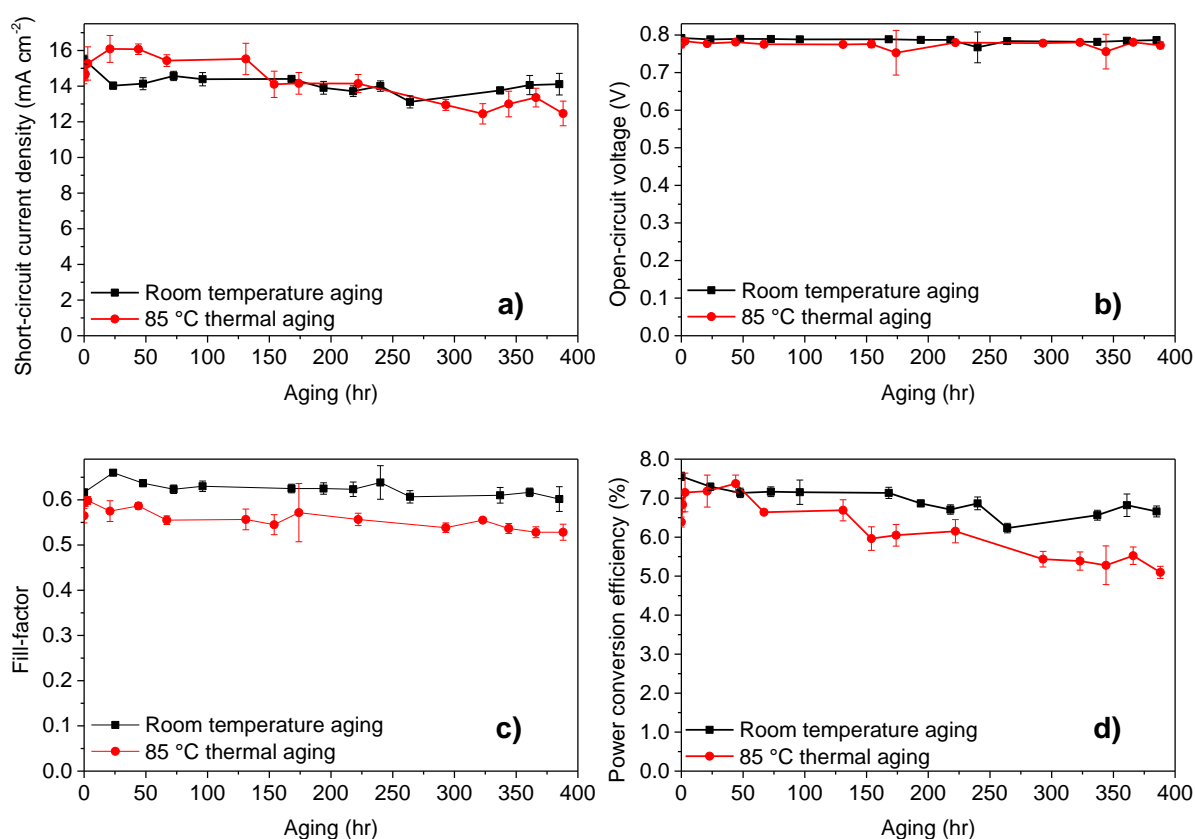


Figure 4.2: Device characteristic trends at room temperature aging and thermal aging at 85 °C under nitrogen of PPDT2FBT:PC₆₁BM based OPVs. The results are from an average of 6 cells, with an active area of 0.1 cm².

For these temperatures, no significant burn-in loss was observed, rather, a constant and gradual decrease in the PCE due to the steady decrease in J_{SC} and FF was present. Overall, though there is a gradual decrease in performance for PPDT2FBT:PC₆₁BM devices heated up to the working temperature, there is a lack of a burn-in process that would otherwise significantly decrease the initial performance. It is worth noting that all the devices were taken out from the glove-box prior to J-V testing under ambient condition, the influence of air on the device performance cannot be eliminated.

4.4.3. The influence of the additional C₇₀ on the device performances

Neat fullerene C₇₀ was introduced previously as a third component to TQ1:C₆₀ devices to enhance the performance by improving the thermal stability by suppressing crystal formation [58]. Additionally, the use of C₇₀ as an additive instead of C₆₀ can improve light absorbance, which could potentially improve the current density of the device. Lastly, it was shown, with the support of differential scanning calorimetry (DSC), for the addition of C₇₀ to the TQ1:PC₆₁BM blend, the neat fullerene acted as a nucleating agent, thus, could improve the thermal stability, similar to C₆₀ [42]. The study, did not, however, investigate the thermal degradation of device performance. To study the influence of additional C₇₀ on the photovoltaic performances on PPDT2FBT:PC₆₁BM based OPVs, different amounts of C₇₀ was introduced to the active material blends and the donor-acceptor ratio was kept constant (1:2). The device performances with different additional amount of C₇₀ are listed in *Table 4.1*. It is worth noting that TQ1-polymer is known to be amorphous in nature [59, 60], whereas PPDT2FBT-polymer is known to have semi-crystalline properties [49, 61].

Table 4.1: Device characteristics of PPDT2FBT:fullerene devices with varying weight ratios of PC₆₁BM:C₇₀.

PPDT2FBT:PC ₆₁ BM:C ₇₀ (w:w:w)	J_{SC} (mA cm ⁻²)	V_{OC} (V)	FF	PCE (%)
1:2:0	15.9 ± 0.3	0.80 ± 0.00	0.62 ± 0.01	7.27 ± 0.09
1:1.9:0.1	15.9 ± 0.5	0.74 ± 0.01	0.61 ± 0.01	7.16 ± 0.24
1:1.8:0.2	16.9 ± 0.5	0.72 ± 0.01	0.53 ± 0.02	6.47 ± 0.16
1:1.6:0.4	17.4 ± 1.5	0.70 ± 0.01	0.53 ± 0.03	6.47 ± 0.48

Average Cell No.: 6 cells / Device Area: 0.1 cm²/ Inverted devices

Coating conditions: Flow-rate: 0.050 m min⁻¹ / Drum-speed: 0.2 m min⁻¹/ Ink concentration: 14.0 mg mL⁻¹

It was observed that the addition of more C₇₀ into the active layer led to a significant increase in J_{SC} due to the increased light absorption and a decrease in the V_{OC} . However, the additional of C₇₀ did not improve the PCE. For comparison 5% w/w of C₆₀ with respect to PCBM was also added to the PPDT2FBT:PC₆₁BM blend and was able to achieve an average J_{SC} of 15.6 mA cm⁻², V_{OC} of 0.76 V, FF of 0.57, and PCE of 6.72%. Initially, it was suspected that the energy level alignment of materials was influencing the performance of the devices, especially the V_{OC} .

To confirm this, square-wave voltammetry (SWV) was measured for pristine materials (PPDT2FBT, PC₆₁BM, PC₇₁BM, C₆₀ & C₇₀). The energy level results from the SWV are illustrated in *Figure 4.3*, (SWV curves can be found in the *Appendix B, Figure B1*).

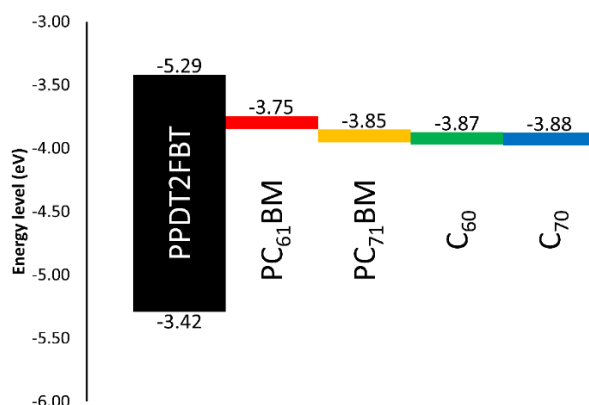


Figure 4.3: Illustration of energy levels of the active layer materials estimated from square-wave voltammetry measurements under identical conditions; PPDT2FBT (HOMO/LUMO), PC₆₁BM, PC₇₁BM, C₆₀ & C₇₀ (LUMO only).

As seen in *Figure 4.3*, there is a reduction between the energy difference between the HOMO_{polymer}/LUMO_{neat fullerene} than that compared to the HOMO_{polymer}/LUMO_{PC₆₁BM}. It has been shown that the open-circuit voltage of OPVs is strongly influenced by the energy difference between the HOMO_{donor} and the LUMO_{acceptor} levels [62, 63]. In the case of the fullerene acceptors, the C₆₀ and C₇₀ have relatively lower LUMO levels (-4.12 and -4.13 eV respectively) when compared with PC₆₁BM and PC₇₁BM (-3.99 and -4.10 eV). Hence, the addition of neat fullerenes to the active layer blend led to the decrease in V_{OC} when compared with the binary system. Furthermore, the increased amount of C₇₀ also resulted in a further decrease in the V_{OC}.

Though C₆₀ was observed to have a higher LUMO level than C₇₀, the addition of C₆₀ resulted in a reduced performance. This difference is accredited the significant decrease in the fill-factor, having dropped down to 0.57. It is known that nucleating agents, such as small molecules, can influence the morphology of active layer blends [64, 65], therefore, the addition of C₆₀ could have negatively influenced the PPDT2FBT:PC₆₁BM blend, resulting in a decreased efficiency.

Overall, the difference in energy level alignment between active layer materials resulted in the reduced performance of the devices. To minimise the impact of the neat fullerene addition on V_{OC}, 5% w/w of C₇₀ was selected for further stability studies and 5% w/w of C₆₀ was also investigated for comparison.

4.4.4. Thermal stability at 120 °C

As discussed above, it is observed that the PPDT2FBT:PC₆₁BM was fairly stable at RT and 85 °C, only showing a slow gradual decrease in J_{SC}, FF, and PCE over long term storage. To test the device stability under accelerated condition, 120 °C was used as the aging temperature, and the device performances were tested for the cells with and without additional neat fullerene.

Furthermore, this temperature has been reported to induce a significant burn-in process to slot-die coated PPDT2FBT:PC₇₁BM inverted devices [47].

Fullerene C₆₀ has been previously reported to improve thermal stability by acting as a nucleating agent when introduced to TQ1:fullerene based devices [42]. In that study C₆₀ was found to be a better nucleating agent for PCBM than C₇₀, however, C₇₀ would result in decreased crystal size and increased crystal population. As of this, C₆₀ and C₇₀ addition to the BHJ was performed to see if it can improve the thermal stability of the devices in this work. The idea is that the nucleating agents will induce the growth of many small crystals instead of a few large ones, resulting in suppressed performance reduction.

With this in mind, PPDT2FBT:PC₆₁BM, PPDT2FBT:PC₆₁BM:C₆₀ and PPDT2FBT:PC₆₁BM:C₇₀ devices were fabricated and thermally aged at 120 °C under dark conditions in under nitrogen atmosphere, while device testing, itself, was performed in air at room temperature. The results of the thermal aging can be seen in *Figure 4.4* (table of results can be found in the *Appendix B*).

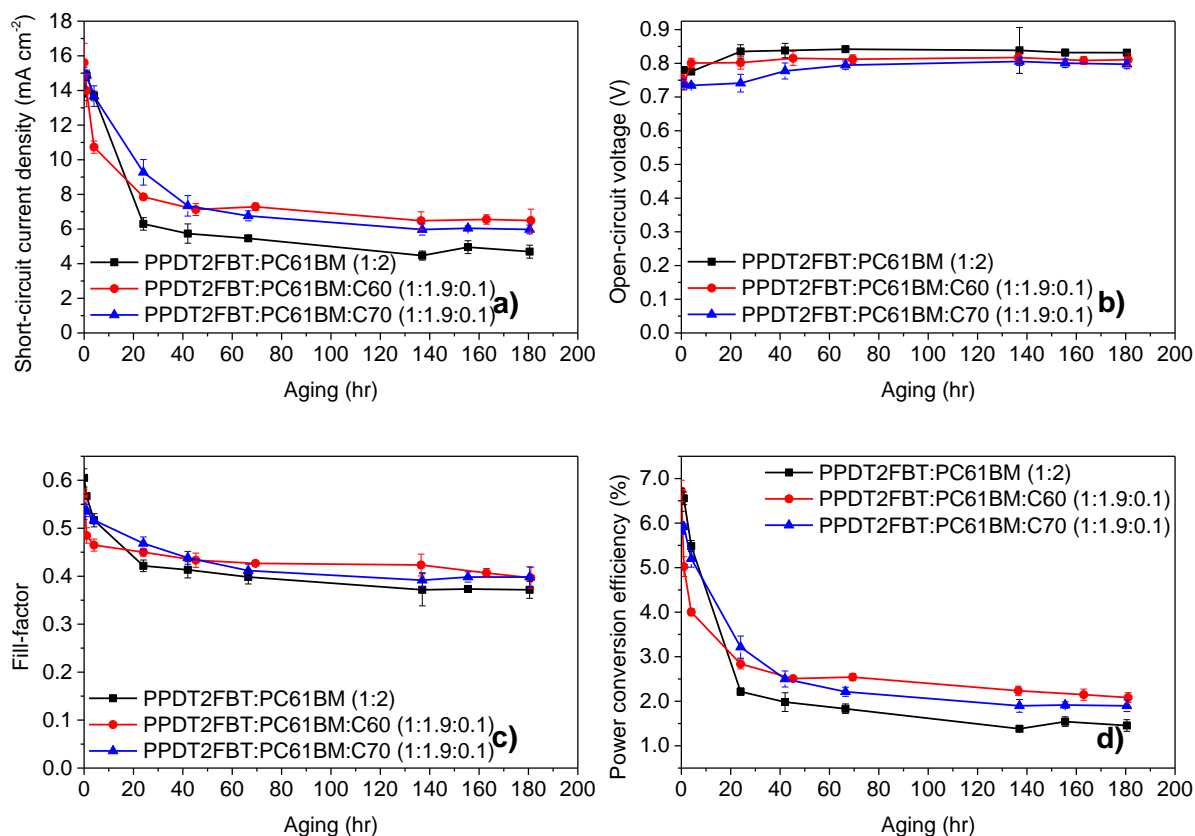


Figure 4.4: Device characteristics trends at 120 °C thermal aging under nitrogen. The results are from an average of 6 cells, with an active area of 0.1 cm².

It was found that when the devices were aged at 120 °C, there are several trends that are common to all systems. Firstly, there is a significant decrease in the J_{SC} and FF with different degrees of thermal “burn-in” occurring in the first 24-48 hours. These changes in J_{SC} and FF are suspected to be a result from the morphology change in the BHJ layer, with the PC₆₁BM likely to crystallize under heated conditions [66, 67]. As for the V_{OC} , all systems had seen an increase within the first 80 hours before remaining constant. The increase in the V_{OC} is likely due to the elimination of the energy disorder at the BHJ/ZnO interface, which has also been observed for BTID-2F:PC₇₁BM devices when stored under dark conditions [68].

With the addition of C₆₀ to the active layer, there is a fast “burn-in” within 4 hours of aging, however, the degree of a performance drop is less than the PPDT2FBT:PC₆₁BM. It is also observed that after the initial burn-in, the devices remained stable with a slightly higher PCE. As for the addition of C₇₀, the burn-in loss is slower, having lasted for around 40 hours instead of 48 hours for the binary blend and 20 hours after the addition of C₆₀. It is also noted that the burn-in loss is less than for PPDT2FBT:PC₆₁BM. Once the burn-in process has passed, the degradation of the ternary blends follows a similar rate to that of the binary PPDT2FBT:PC₆₁BM devices.

Overall, the addition of C₇₀ was able to improve the thermal stability of PPDT2FBT:PC₆₁BM devices by reducing the impact from the thermal burn-in process at 120 °C, whereas the addition of C₆₀, resulted in a sharper burn-in process with slightly more higher performing devices over longer times.

4.4.5. Imaging of microcrystals at BHJ surface

To investigate the morphological change during thermal aging, half-devices (PET/ITO/ZnO NP/BHJ) were heated at 120 °C for 8 hours under nitrogen. The BHJ layers before and after 120 °C heating were characterised under SEM and the images are shown in *Figure 4.5*. Without heating, all BHJ layers were observed to be smooth and free of aggregates/crystals, but after thermal annealing, micro-sized crystals were formed on the BHJ/air surface.

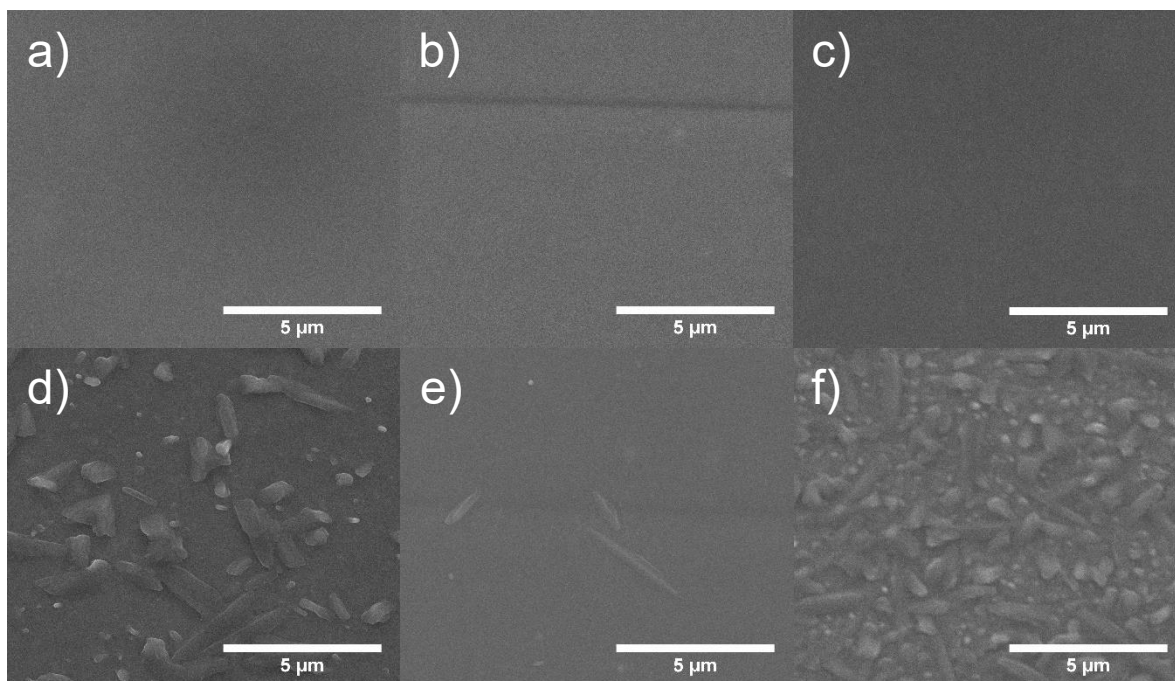


Figure 4.5: SEM images of PPDT2FBT:PC₆₁BM (1:2) (a,d), PPDT2FBT:PC₆₁BM:C₇₀ (1:1.9:0.1) (b,e) & PPDT2FBT:PC₆₁BM:C₆₀ (1:1.9:0.1) (c,f) before (a-c) and after (d-f) heated for 8 h at 120 °C under dark nitrogen conditions.

We also found that different annealed BHJ layers showed slightly different degrees and shapes of crystals on the surface. It was assumed that these crystals on the surface were most likely consisting of PC₆₁BM. For PPDT2FBT:PC₆₁BM, relatively large crystals had appeared on the surface after heating, which could be a result from the crystallisation of PC₆₁BM. In the case of the PPDT2FBT:PC₆₁BM:C₆₀, the size of the crystals is smaller than those seen with PPDT2FBT:PC₆₁BM, the number of them present at the surface has significantly increased. This behaviour is consistent with earlier studies that the addition of C₆₀ can act as a nucleating agent. After the addition of C₇₀, there is a significant reduction of the number of crystals compared to the other samples.

As C₆₀ acts as a nucleating agent, crystal nuclei are formed to allow for crystal growth, thus, more crystals are created. As there is limited space within the film inside the devices, the growth of the crystals is restricted. This can explain why there is a steeper burn-in process as the crystals begin to grow, however, due to the restricted crystal size, the magnitude of the faster decrease is not as severe after the addition of C₇₀ as the decrease seen in the PPDT2FBT:PC₆₁BM. The addition of C₇₀ is significantly reducing the crystallisation rate of PC₆₁BM in the PPDT2FBT:PC₆₁BM blend, visible in both a slower burn in and crystallisation process. In literature, it was determined that the addition of C₇₀ into the TQ1:PC₆₁BM blends, would result in the neat fullerene acting as a nucleating agent[42], however, this does not appear to be the case in this study.

Next, we investigated how the performance degradation differed between devices that were annealed at 120 °C for 24 hours before and after deposition MoO_x/Al on top of the BHJ. As seen in *Figure 4.5*, the crystals had appeared at the top surface of the BHJ, which could result in a layer of fullerene at BHJ/MoO_x interface. The JV-curves of devices at different annealing stages can be seen in *Figure B2* in *Appendix B*.

For devices that were annealed after completion of the fabrication, though there is a change in the shape of the J-V curve, it still showed photovoltaic effect (above 1% PCE). As for those devices heated prior to MoO_x/Al deposition, the efficiency is very low (below 0.1% PCE).

Without the coating on top of the BHJ layers, there is space for the microcrystals to grow above the surface of the BHJ. As for the complete devices, the top and bottom sides of the BHJ are “blocked” by interface materials (MoO_x & ZnO NP respectively), preventing the crystals from growing outside of the layer. This likely explains the performance difference between devices heated before and after MoO_x/ Al deposition.

4.4.6. Elemental characteristics of microcrystals

To further understand the origin of the microcrystals, Auger electron spectroscopy (AES) was used to detect the presence of different elements on different features on the annealed (120 °C, 24 h) PPDT2FBT:PC₆₁BM surface. The advantage of the technique is that it is allowed for specific scanning areas with an effective analysis depth of around 10 nm [69], meaning that the underlying BHJ/Interface/Electrode should not interfere with the measurements. Understanding that the layer consisted of a combination of PPDT2FBT and PC₆₁BM, it was suspected that carbon, nitrogen, oxygen, fluorine, and sulphur peaks would be present in the spectra.

From the AES spectra (*Figure 4.6*), it was found that both carbon (272 eV [70]) and sulphur (152 eV [70]) were the easiest to resolve from the background signal. Whereas oxygen (508 eV [70]) was more difficult to resolve, yet, could still be resolvable in some spectra. Lastly, nitrogen (379 eV [70]) and fluorine (647 eV [70]) were incredibly difficult to resolve from the background, with most times the peaks for these elements not being able to be observed entirely. To give a quantitative comparison between positions, the sulphur to carbon ratio was compared. As of this, the carbon/sulphur ratio was compared to estimate material composition.

This difference in peak intensity can be attributed to two factors, amount of the element present and the sensitivity factor. When operating an electron beam at 10 keV, the sensitivity factors for carbon, nitrogen, oxygen, fluorine and sulphur are 0.28, 0.60, 0.79, 1.91 and 2.43, respectively [71]. As sulphur has a relatively high factor, a low amount of sulphur results in a resolvable peak, whereas carbon, even though having a low factor, there is a large amount of the element present in both materials.

For oxygen, even though it has a lower peak, the element is present in both polymer and fullerene materials. Lastly, both nitrogen and fluorine have a low sensitivity factor, plus is only present in the polymer material, resulting in peak intensities that would be difficult to resolve from the background. As both carbon and sulphur were easy to resolve, the analysis of the spectra involved the comparison between these two elements.

For the investigation, 3 positions were measured using “point scan” of the specific locations. These include short crystals (position 1), long crystals (position 2) and the surface of the active layer (position 3). For the BHJ (position 3), it was suspected that these locations contained a mixture of PC₆₁BM and PPDT2FBT. To determine what material composition the crystals consisted of, it was hypothesised that if a feature was PPDT2FBT, an increase in sulphur would accord compared to position 3 spectra, while a decrease in sulphur would indicate the presence of PC₆₁BM. The experimental spectra from the scans can be found in *Appendix B*, while the resulting atomic composition % can be found in *Table 4.2*.

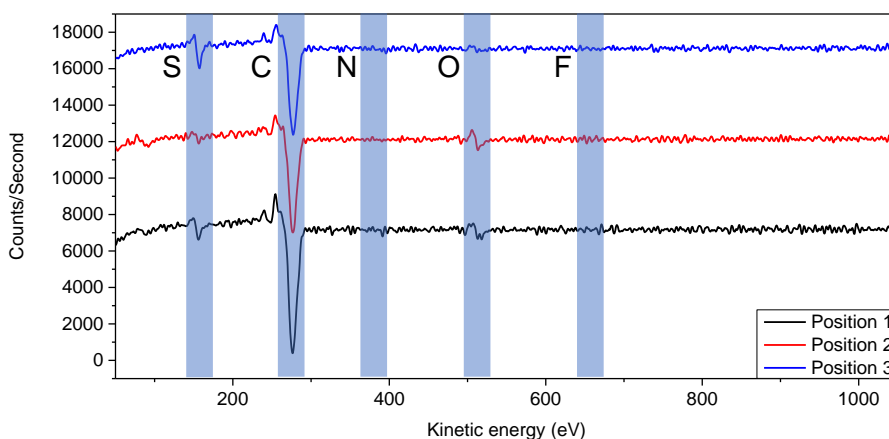


Figure 4.6: Flattened and smoothed Auger spectra of three positions that were measured on the PPDT2FBT:PC₆₁BM surface, including the predicted peak position of elements of interest. The spectra are an average of 5 different scanning areas.

Table 4.2: Atomic percentages of carbon and sulphur at three different locations. Percentages are calculated in relation to the presence of carbon and sulphur only.

Position	Description	Carbon %	Sulphur %
1	“Short” crystal	98.2 ± 0.2	1.8 ± 0.2
2	“Long” crystal	98.4 ± 0.3	1.6 ± 0.3
3	BHJ Surface	96.5 ± 0.2	3.5 ± 0.2

From the *Table 4.2*, position 1 and 2, scanning on the crystals, show a decrease in the presence when compared with position 3. The two crystal positions are within significant figures of each other. Also, from the scans, the oxygen peaks associated with position 2 & 3 are resolvable. This supports the hypothesis that the micro-crystals that formed during thermal aging at 120 °C consists of PC₆₁BM. In cases that sulphur is detected, it is likely as the fullerene grows and moves up from the surface, some of the polymer is taken up with it, remaining on the surface of the crystal.

Another likely source of sulphur is the surroundings of the crystal being detected, with the diameter of the beam during the scan being approximately 650 nm. As some of the crystals had similar sizes as the beam, it is likely that the beam was also analysing the surface of the BHJ, especially for position 1 scans. Overall, with support from the Auger microscopy measurements, it is likely that the microcrystals at the surface of the BHJ consists of fullerene.

4.4.7. Thermal analysis

In OPV research, dynamic mechanical thermal analysis (DMTA) technique was previously used to understand the thermal transitions of pure materials and blends and is a useful tool to characterise the morphology of BHJ layer [54, 72, 73]. In this work, it was used to understand the effect of annealing on the BHJ layers and to study the difference among binary blend and the ternary ones with the addition of C₆₀ or C₇₀.

In the DMTA scans, E' reflects the stiffness, E'' peak feature suggests the thermal transitions, and $\tan \delta = E''/E'$. Traditionally, the peak temperature of the tan delta peak is commonly used to define the thermal transition temperatures.

The DMTA scans of pure PPDT2FBT and BHJ blends are presented in *Figure 4.7*. To reduce the number of conjugated materials, woven glass fibre mesh was used as a support, thus the absolute value of E' cannot be used to characterise the sample rigidity. Instead, the trend of E' and E'' change during heating is the main focus in the following discussion. Similar sample dimensions and amounts of materials are used so qualitative comparison of the data in *Figure 4.7* can be made.

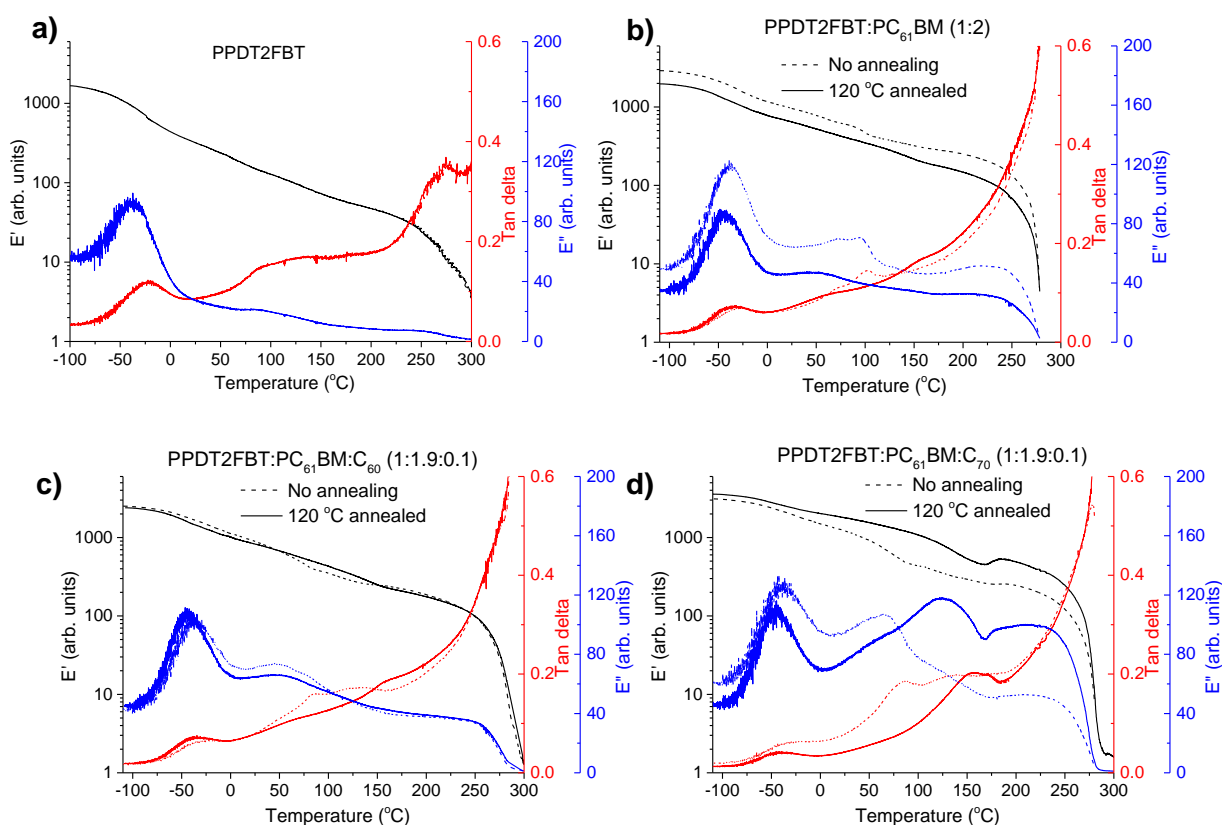


Figure 4.7: DMTA plots of pristine PPDT2FBT (a), PPDT2FBT:PC₆₁BM (b), PPDT2FBT:PC₆₁BM:C₆₀ (c) and PPDT2FBT:PC₆₁BM:C₇₀ (d) before and after annealing (30 min).

For pure PPDT2FBT, one sub- T_g is observed at around -25 °C (extracted from $\tan \delta$ peak temperature), and no clear T_g was detected, indicating the lack of amorphous phase in the solid state[54] of the pure polymer, in accordance with previously published works describing similar polymers [54, 74]. In the case of PPDT2FBT:PC₆₁BM blend, the sub- T_g peaks can still be clearly detected and there is no shift of the peak temperature, which further confirmed that this feature is not originated from a glass transition. When no annealing was applied on the binary sample before the DMTA measurement, one extra thermal relaxation was found at ~100 °C, seen by the E'' peak, which is not observable from the sample annealed at 120 °C for 30 min. This result indicates that the binary blend exhibits some mobility during heating, thus changes in the morphology of BHJ is expected when annealed at 120 °C. However, no clear cold crystallisation was detected, which seems to conflict with the SEM results. The conflicting results might be caused by the relatively fast heating during DMTA measurement (3 °C min⁻¹) compared to long time annealing (8 hr) of the SEM sample, the growth of crystals in the DMA sample were not quick enough to be reflected in increased E' .

With the addition of C₆₀ into the PPDT2FBT:PC₆₁BM blend, the previously observed feature at ~100 °C in the binary sample is absent (*Figure 5.7c*). The samples before and after annealing show almost identical thermal mechanical properties, suggesting the addition of C₆₀ results in restricted mobility of the BHJ layer, possibly originating from already formed small crystals in the materials.

Differently, introducing C₇₀ to the blend yielded a second transition temperature (tan delta) that shifts from 85 (non-annealed one) to ~155 °C after annealing, which is suspected to be due to the formation of more pure phases, induced by heating. The non-annealed sample showed a minor E' increase at ~ 180 °C, indicating the crystal formation at this high temperature. After annealing at 120 °C for 30 min, clearer crystallisation was observed at 170 °C indicated by the E' increase after the thermal relaxation of the fullerene rich phase [53]. The reason of clearer crystallisation observed in annealed PPDT2FBT:PC₆₁BM:C₇₀ sample is indicative of the small crystal formation during 120 °C annealing, which further grow to larger crystals upon applying high thermal energy. By having the main crystallization at such a higher temperature, this system is expected to be more stable at the described aging condition. From the DMTA measurements it is clear that the addition of C₆₀ and C₇₀ alters the thermal behaviour of the blends in different ways. This explains why, with the addition of C₇₀, the burn-in process rate is slightly slower than that of PPDT2FBT:PC₆₁BM and PPDT2BT:PC₆₁BM:C₆₀ at 120 °C.

We assume that the addition of C₇₀ will increase the thermal stability further at 85 °C based on the results derived from the accelerated aging experiments at 120 °C. Our results indicate that PPDT2FBT:PC₆₁BM:C₇₀ is a promising system for large scale printed OPVs.

4.5. Conclusion

In conclusion, the addition of as low as 5% w/w C₇₀ (in respect to PC₆₁BM) to the slot-die coated bulk-heterojunction of PPDT2FBT:PC₆₁BM was successfully demonstrated to improve the thermal stability. Initially, we have optimised the ink preparation and the coating conditions to reach an average power conversion efficiency of 8.49% and 7.63% for PPDT2FBT:PC₇₁BM and PPDT2FBT:PC₆₁BM devices, respectively. A subsequent investigation of the thermal stability of PPDT2FBT:PC₆₁BM at 85 °C revealed that there was no burn-in loss as was observed in 120 °C aged devices. With support of scanning electron microscopy and Auger electron spectroscopy, it was found that the growth of fullerene-rich crystals in the bulk-heterojunction is the likely source of thermal degradation at 120 °C.

Addition of C₆₀ to the PPDT2FBT:PC₆₁BM appeared to act as a nucleating agent, with increased number and reduced size of the crystals. In comparison with the addition of C₇₀ to the PPDT2FBT:PC₆₁BM, the magnitude and rate of the burn-in loss was significantly reduced. Subsequently, the C₇₀ did not appear to behave as a nucleating agent, instead, it was found that the rate of crystal growth reduced with the addition of the neat fullerene. Our results demonstrate that the small addition of C₇₀ could improve the thermal stability of slot-die coated OPVs.

4.6. References

1. Thompson, B. C. and Fréchet, J. M. J., Polymer–Fullerene Composite Solar Cells. *Angewandte Chemie International Edition*, **2008**. 47 (1), 58-77.
2. Beaujuge, P. M. and Fréchet, J. M. J., Molecular Design and Ordering Effects in π -Functional Materials for Transistor and Solar Cell Applications. *Journal of the American Chemical Society*, **2011**. 133 (50), 20009-20029.
3. Andersen, T. R., Almyahi, F., Cooling, N. A., Elkington, D., Wiggins, L., Fahy, A., Feron, K., Vaughan, B., Griffith, M. J., and Mozer, A. J., Comparison of inorganic electron transport layers in fully roll-to-roll coated/printed organic photovoltaics in normal geometry. *Journal of Materials Chemistry A*, **2016**. 4 (41), 15986-15996.
4. Hummelen, J. C., Knight, B. W., LePeq, F., Wudl, F., Yao, J., and Wilkins, C. L., Preparation and characterization of fulleroid and methanofullerene derivatives. *The Journal of Organic Chemistry*, **1995**. 60 (3), 532-538.
5. Wienk, M. M., Kroon, J. M., Verhees, W. J. H., Knol, J., Hummelen, J. C., van Hal, P. A., and Janssen, R. A. J., Efficient Methano[70]fullerene/MDMO-PPV Bulk Heterojunction Photovoltaic Cells. *Angewandte Chemie International Edition*, **2003**. 42 (29), 3371-3375.
6. Bao, S., Yang, H., Fan, H., Zhang, J., Wei, Z., Cui, C., and Li, Y., Volatilizable Solid Additive-Assisted Treatment Enables Organic Solar Cells with Efficiency over 18.8% and Fill Factor Exceeding 80%. *Advanced Materials*, **2021**. 33 (48), 2105301.
7. Cai, Y., Li, Y., Wang, R., Wu, H., Chen, Z., Zhang, J., Ma, Z., Hao, X., Zhao, Y., Zhang, C., Huang, F., and Sun, Y., A Well-Mixed Phase Formed by Two Compatible Non-Fullerene Acceptors Enables Ternary Organic Solar Cells with Efficiency over 18.6%. *Advanced Materials*, **2021**. 33 (33), 2101733.
8. Song, J., Zhu, L., Li, C., Xu, J., Wu, H., Zhang, X., Zhang, Y., Tang, Z., Liu, F., and Sun, Y., High-efficiency organic solar cells with low voltage loss induced by solvent additive strategy. *Matter*, **2021**. 4 (7), 2542-2552.
9. Zimmermann, B., Schleiermacher, H.-F., Niggemann, M., Würfel, U., and Cells, S., ITO-free flexible inverted organic solar cell modules with high fill factor prepared by slot die coating. *Solar Energy Materials and Solar Cells*, **2011**. 95 (7), 1587-1589.
10. Wu, Q., Guo, J., Sun, R., Guo, J., Jia, S., Li, Y., Wang, J., and Min, J., Slot-die printed non-fullerene organic solar cells with the highest efficiency of 12.9% for low-cost PV-driven water splitting. *Nano Energy*, **2019**. 61, 559-566.
11. Zhao, H., Zhang, L., Naveed, H. B., Lin, B., Zhao, B., Zhou, K., Gao, C., Zhang, C., Wang, C., and Ma, W., Processing-Friendly Slot-Die-Cast Nonfullerene Organic Solar Cells with Optimized Morphology. *ACS Applied Materials & Interfaces*, **2019**. 11 (45), 42392-42402.
12. Zhang, L., Xu, X., Lin, B., Zhao, H., Li, T., Xin, J., Bi, Z., Qiu, G., Guo, S., Zhou, K., Zhan, X., and Ma, W., Achieving Balanced Crystallinity of Donor and Acceptor by Combining Blade-Coating and Ternary Strategies in Organic Solar Cells. *Advanced Materials*, **2018**. 30 (51), 1805041.
13. Pérez-Gutiérrez, E., Lozano, J., Gaspar-Tánori, J., Maldonado, J.-L., Gómez, B., López, L., Amores-Tapia, L.-F., Barbosa-García, O., and Percino, M.-J., Organic solar cells all made by blade and slot–die coating techniques. *Solar Energy*, **2017**. 146, 79-84.
14. Krebs, F. C., Jørgensen, M., Norrman, K., Hagemann, O., Alstrup, J., Nielsen, T. D., Fyenbo, J., Larsen, K., and Kristensen, J., A complete process for production of flexible large area polymer solar cells entirely using screen printing—first public demonstration. *Solar Energy Materials and Solar Cells*, **2009**. 93 (4), 422-441.
15. Ylikunnari, M., Välimäki, M., Väisänen, K.-L., Kraft, T. M., Sliz, R., Corso, G., Po, R., Barbieri, R., Carbonera, C., Gorni, G., and Vilkmann, M., Flexible OPV modules for highly efficient indoor applications. *Flexible and Printed Electronics*, **2020**. 5 (1), 014008.
16. He, P., Cao, J., Ding, H., Liu, C., Neilson, J., Li, Z., Kinloch, I. A., and Derby, B., Screen-Printing of a Highly Conductive Graphene Ink for Flexible Printed Electronics. *ACS Applied Materials & Interfaces*, **2019**. 11 (35), 32225-32234.
17. Susanna, G., Salamandra, L., Brown, T. M., Di Carlo, A., Brunetti, F., and Reale, A., Airbrush spray-coating of polymer bulk-heterojunction solar cells. *Solar Energy Materials and Solar Cells*, **2011**. 95 (7), 1775-1778.

18. Jiang, Z., Rahmanian, R., Soltanian, S., Nouri, R., and Servati, P. Single-pass Spray-coated Flexible Organic Solar Cells Using Graphene Transparent Electrodes. in *2019 IEEE International Flexible Electronics Technology Conference (IFETC)*. 2019.
19. Waheed, S., Pareek, S., Sharma, P., and Karak, S., Performance improvement of ultrasonic spray deposited polymer solar cell through droplet boundary reduction assisted by acoustic substrate vibration. *Semiconductor Science and Technology*, **2020**.
20. Ryu, H. S., Park, S. Y., Lee, T. H., Kim, J. Y., and Woo, H. Y., Recent progress in indoor organic photovoltaics. *Nanoscale*, **2020**. 12 (10), 5792-5804.
21. Søndergaard, R., Hösel, M., Angmo, D., Larsen-Olsen, T. T., and Krebs, F. C., Roll-to-roll fabrication of polymer solar cells. *Materials today*, **2012**. 15 (1-2), 36-49.
22. Zhang, Z., Miao, J., Ding, Z., Kan, B., Lin, B., Wan, X., Ma, W., Chen, Y., Long, X., Dou, C., Zhang, J., Liu, J., and Wang, L., Efficient and thermally stable organic solar cells based on small molecule donor and polymer acceptor. *Nature Communications*, **2019**. 10 (1), 3271.
23. Zheng, N., Mahmood, K., Zhong, W., Liu, F., Zhu, P., Wang, Z., Xie, B., Chen, Z., Zhang, K., Ying, L., Huang, F., and Cao, Y., Improving the efficiency and stability of non-fullerene polymer solar cells by using N2200 as the Additive. *Nano Energy*, **2019**. 58, 724-731.
24. Meitzner, R., Faber, T., Alam, S., Amand, A., Roesch, R., Büttner, M., Herrmann-Westendorf, F., Presselt, M., Ciommaruchi, L., and Visoly-Fisher, I., Impact of P3HT materials properties and layer architecture on OPV device stability. *Solar Energy Materials and Solar Cells*, **2019**. 202, 110151.
25. Li, M., Zhang, W., Wang, H., Chen, L., Zheng, C., and Chen, R., Effect of organic cathode interfacial layers on efficiency and stability improvement of polymer solar cells. *RSC advances*, **2017**. 7 (50), 31158-31163.
26. Weng, C.-N., Yang, H.-C., Tsai, C.-Y., Chen, S.-H., Chen, Y.-S., Chen, C.-H., Huang, K.-M., Meng, H.-F., Chao, Y.-C., and Chang, C.-Y., The influence of UV filter and Al/Ag moisture barrier layer on the outdoor stability of polymer solar cells. *Solar Energy*, **2020**. 199, 308-316.
27. Doumon, N. Y., Wang, G., Chiechi, R. C., and Koster, L. J. A., Relating polymer chemical structure to the stability of polymer: fullerene solar cells. *Journal of Materials Chemistry C*, **2017**. 5 (26), 6611-6619.
28. Muhsin, B., Roesch, R., Gobsch, G., and Hoppe, H., Flexible ITO-free polymer solar cells based on highly conductive PEDOT:PSS and a printed silver grid. *Solar Energy Materials and Solar Cells*, **2014**. 130, 551-554.
29. Sun, Y., Meng, L., Wan, X., Guo, Z., Ke, X., Sun, Z., Zhao, K., Zhang, H., Li, C., and Chen, Y., Flexible High-Performance and Solution-Processed Organic Photovoltaics with Robust Mechanical Stability. *Advanced Functional Materials*, **2021**. 31 (16), 2010000.
30. Kang, H., Kim, G., Kim, J., Kwon, S., Kim, H., and Lee, K., Bulk-heterojunction organic solar cells: Five core technologies for their commercialization. *Advanced Materials*, **2016**. 28 (36), 7821-7861.
31. Greenbank, W., Djeddaoui, N., Destouesse, E., Lamminaho, J., Prete, M., Boukezzi, L., Ebel, T., Bessissa, L., Rubahn, H.-G., Turkovic, V., and Madsen, M., Degradation Behavior of Scalable Nonfullerene Organic Solar Cells Assessed by Outdoor and Indoor ISOS Stability Protocols. *Energy Technology*, **2020**. 8 (12), 2000295.
32. Duan, L. and Uddin, A., Progress in Stability of Organic Solar Cells. *Advanced Science*, **2020**. 7 (11), 1903259.
33. Li, N., Perea, J. D., Kassar, T., Richter, M., Heumueller, T., Matt, G. J., Hou, Y., Güldal, N. S., Chen, H., and Chen, S., Abnormal strong burn-in degradation of highly efficient polymer solar cells caused by spinodal donor-acceptor demixing. *Nature communications*, **2017**. 8 (1), 1-9.
34. Chochos, C. L., Leclerc, N., Gasparini, N., Zimmerman, N., Tatsi, E., Katsouras, A., Moschovas, D., Serpetzoglou, E., Konidakis, I., and Fall, S., The role of chemical structure in indacenodithienothiophene-alt-benzothiadiazole copolymers for high performance organic solar cells with improved photo-stability through minimization of burn-in loss. *Journal of Materials Chemistry A*, **2017**. 5 (47), 25064-25076.
35. Tong, X., Wang, N., Slootsky, M., Yu, J., and Forrest, S. R., Intrinsic burn-in efficiency loss of small-molecule organic photovoltaic cells due to exciton-induced trap formation. *Solar energy materials and solar cells*, **2013**. 118, 116-123.

36. Paci, B., Generosi, A., Rossi Albertini, V., Perfetti, P., de Bettignies, R., Leroy, J., Firon, M., and Senten, C., Controlling photoinduced degradation in plastic photovoltaic cells: A time-resolved energy dispersive x-ray reflectometry study. *Applied physics letters*, **2006**. 89 (4), 043507.
37. Andreasen, J. W., Gevorgyan, S. A., Schlepütz, C. M., and Krebs, F. C., Applicability of X-ray reflectometry to studies of polymer solar cell degradation. *Solar energy materials and solar cells*, **2008**. 92 (7), 793-798.
38. Yang, X., Loos, J., Veenstra, S. C., Verhees, W. J., Wienk, M. M., Kroon, J. M., Michels, M. A., and Janssen, R. A., Nanoscale morphology of high-performance polymer solar cells. *Nano letters*, **2005**. 5 (4), 579-583.
39. Krebs, F. C., Alstrup, J., Spanggaard, H., Larsen, K., and Kold, E., Production of large-area polymer solar cells by industrial silk screen printing, lifetime considerations and lamination with polyethyleneterephthalate. *Solar Energy Materials and Solar Cells*, **2004**. 83 (2), 293-300.
40. Lindqvist, C., Sanz-Velasco, A., Wang, E., Bäcke, O., Gustafsson, S., Olsson, E., Andersson, M. R., and Müller, C., Nucleation-limited fullerene crystallisation in a polymer–fullerene bulk-heterojunction blend. *Journal of Materials Chemistry A*, **2013**. 1 (24), 7174-7180.
41. Lindqvist, C., Stability of Bulk-heterojunction Blends for Solar Cell Applications. 2014: Chalmers University of Technology.
42. Lindqvist, C., Bergqvist, J., Feng, C. C., Gustafsson, S., Bäcke, O., Treat, N. D., Bounioux, C., Henriksson, P., Kroon, R., Wang, E., Sanz-Velasco, A., Kristiansen, P. M., Stingelin, N., Olsson, E., Inganäs, O., Andersson, M. R., and Müller, C., Fullerene nucleating agents: a route towards thermally stable photovoltaic blends. *Advanced Energy Materials*, **2014**. 4 (9), 1301437.
43. Distler, A., Brabec, C. J., and Egelhaaf, H.-J., Organic photovoltaic modules with new world record efficiencies. *Progress in Photovoltaics: Research and Applications*, **2021**. 29 (1), 24-31.
44. Moser, M., Wadsworth, A., Gasparini, N., and McCulloch, I., Challenges to the Success of Commercial Organic Photovoltaic Products. *Advanced Energy Materials*, **2021**. 11 (18), 2100056.
45. Osedach, T. P., Andrew, T. L., and Bulović, V., Effect of synthetic accessibility on the commercial viability of organic photovoltaics. *Energy & Environmental Science*, **2013**. 6 (3), 711-718.
46. Dayneko, S. V., Pahlevani, M., and Welch, G. C., Indoor Photovoltaics: Photoactive Material Selection, Greener Ink Formulations, and Slot-Die Coated Active Layers. *ACS Applied Materials & Interfaces*, **2019**. 11 (49), 46017-46025.
47. Song, S., Lee, K. T., Koh, C. W., Shin, H., Gao, M., Woo, H. Y., Vak, D., and Kim, J. Y., Hot slot die coating for additive-free fabrication of high performance roll-to-roll processed polymer solar cells. *Energy & Environmental Science*, **2018**. 11 (11), 3248-3255.
48. Mainville, M., Tremblay, V., Fenniri, M. Z., Laventure, A., Farahat, M. E., Ambrose, R., Welch, G. C., Hill, I. G., and Leclerc, M., Water Compatible Direct (Hetero)arylation Polymerization of PPDT2FBT: A Pathway Towards Large-Scale Production of Organic Solar Cells. *Asian Journal of Organic Chemistry*, **2020**. 9 (9), 1318-1325.
49. Nguyen, T. L., Choi, H., Ko, S. J., Uddin, M. A., Walker, B., Yum, S., Jeong, J. E., Yun, M. H., Shin, T. J., and Hwang, S., Semi-crystalline photovoltaic polymers with efficiency exceeding 9% in a ~ 300 nm thick conventional single-cell device. *Energy & Environmental Science*, **2014**. 7 (9), 3040-3051.
50. Wu, S.-C., Strover, L. T., Yao, X., Chen, X.-Q., Xiao, W.-J., Liu, L.-N., Wang, J., Visoly-Fisher, I., Katz, E. A., and Li, W.-S., UV-Cross-linkable Donor–Acceptor Polymers Bearing a Photostable Conjugated Backbone for Efficient and Stable Organic Photovoltaics. *ACS Applied Materials & Interfaces*, **2018**. 10 (41), 35430-35440.
51. Morin, P.-O., Bura, T., Sun, B., Gorelsky, S. I., Li, Y., and Leclerc, M., Conjugated polymers à la carte from time-controlled direct (hetero) arylation polymerization. *ACS Macro Letters*, **2015**. 4 (1), 21-24.
52. Krebs, F. C., Air stable polymer photovoltaics based on a process free from vacuum steps and fullerenes. *Solar Energy Materials and Solar Cells*, **2008**. 92 (7), 715-726.

53. Sharma, A., Pan, X., Campbell, J. A., Andersson, M. R., and Lewis, D. A., Unravelling the thermomechanical properties of bulk heterojunction blends in polymer solar cells. *Macromolecules*, **2017**. *50* (8), 3347-3354.
54. Sharma, A., Pan, X., Bjuggren, J. M., Gedefaw, D., Xu, X., Kroon, R., Wang, E., Campbell, J. A., Lewis, D. A., and Andersson, M. R., Probing the relationship between molecular structures, thermal transitions, and morphology in polymer semiconductors using a woven glass-mesh-based DMTA technique. *Chemistry of Materials*, **2019**. *31* (17), 6740-6749.
55. Shin, S.-C., Koh, C. W., Vincent, P., Goo, J. S., Bae, J.-H., Lee, J.-J., Shin, C., Kim, H., Woo, H. Y., and Shim, J. W., Ultra-thick semi-crystalline photoactive donor polymer for efficient indoor organic photovoltaics. *Nano Energy*, **2019**. *58*, 466-475.
56. Reese, M. O., Gevorgyan, S. A., Jørgensen, M., Bundgaard, E., Kurtz, S. R., Ginley, D. S., Olson, D. C., Lloyd, M. T., Morvillo, P., Katz, E. A., Elschner, A., Haillant, O., Currier, T. R., Shrotriya, V., Hermenau, M., Riede, M., R. Kirov, K., Trimmel, G., Rath, T., Inganäs, O., Zhang, F., Andersson, M., Tvingstedt, K., Lira-Cantu, M., Laird, D., McGuinness, C., Gowrisanker, S., Pannone, M., Xiao, M., Hauch, J., Steim, R., DeLongchamp, D. M., Rösch, R., Hoppe, H., Espinosa, N., Urbina, A., Yaman-Uzunoglu, G., Bonekamp, J.-B., van Breemen, A. J. J. M., Giroto, C., Voroshazi, E., and Krebs, F. C., Consensus stability testing protocols for organic photovoltaic materials and devices. *Solar Energy Materials and Solar Cells*, **2011**. *95* (5), 1253-1267.
57. Khenkin, M. V., Katz, E. A., Abate, A., Bardizza, G., Berry, J. J., Brabec, C., Brunetti, F., Bulović, V., Burlingame, Q., and Di Carlo, A., Consensus statement for stability assessment and reporting for perovskite photovoltaics based on ISOS procedures. *Nature Energy*, **2020**. *5* (1), 35-49.
58. de Zerio Mendaza, A. D., Bergqvist, J., Bäcke, O., Lindqvist, C., Kroon, R., Gao, F., Andersson, M. R., Olsson, E., Inganäs, O., and Müller, C., Neat C 60: C 70 buckminsterfullerene mixtures enhance polymer solar cell performance. *Journal of Materials Chemistry A*, **2014**. *2* (35), 14354-14359.
59. Wang, E., Bergqvist, J., Vandewal, K., Ma, Z., Hou, L., Lundin, A., Himmelberger, S., Salleo, A., Müller, C., and Inganäs, O., Conformational disorder enhances solubility and photovoltaic performance of a thiophene–quinoxaline copolymer. *Advanced Energy Materials*, **2013**. *3* (6), 806-814.
60. Bergqvist, J., Lindqvist, C., Bäcke, O., Ma, Z., Tang, Z., Tress, W., Gustafsson, S., Wang, E., Olsson, E., and Andersson, M. R., Sub-glass transition annealing enhances polymer solar cell performance. *Journal of Materials Chemistry A*, **2014**. *2* (17), 6146-6152.
61. Kang, H., Uddin, M. A., Lee, C., Kim, K.-H., Nguyen, T. L., Lee, W., Li, Y., Wang, C., Woo, H. Y., and Kim, B. J., Determining the role of polymer molecular weight for high-performance all-polymer solar cells: its effect on polymer aggregation and phase separation. *Journal of the American Chemical Society*, **2015**. *137* (6), 2359-2365.
62. Mühlbacher, D., Scharber, M., Morana, M., Zhu, Z., Waller, D., Gaudiana, R., and Brabec, C., High photovoltaic performance of a low-bandgap polymer. *Advanced Materials*, **2006**. *18* (21), 2884-2889.
63. Brabec, C. J., Sariciftci, N. S., and Hummelen, J. C., Plastic solar cells. *Advanced functional materials*, **2001**. *11* (1), 15-26.
64. Sharenko, A., Gehrig, D., Laquai, F., and Nguyen, T.-Q., The Effect of Solvent Additive on the Charge Generation and Photovoltaic Performance of a Solution-Processed Small Molecule:Perylene Diimide Bulk Heterojunction Solar Cell. *Chemistry of Materials*, **2014**. *26* (14), 4109-4118.
65. Liao, S.-H., Jhuo, H.-J., Yeh, P.-N., Cheng, Y.-S., Li, Y.-L., Lee, Y.-H., Sharma, S., and Chen, S.-A., Single Junction Inverted Polymer Solar Cell Reaching Power Conversion Efficiency 10.31% by Employing Dual-Doped Zinc Oxide Nano-Film as Cathode Interlayer. *Scientific Reports*, **2014**. *4* (1), 6813.
66. Zhao, J., Swinnen, A., Van Assche, G., Manca, J., Vanderzande, D., and Mele, B. V., Phase diagram of P3HT/PCBM blends and its implication for the stability of morphology. *The Journal of Physical Chemistry B*, **2009**. *113* (6), 1587-1591.
67. Bertho, S., Janssen, G., Cleij, T. J., Conings, B., Moons, W., Gadisa, A., D'Haen, J., Goovaerts, E., Lutsen, L., and Manca, J., Effect of temperature on the morphological and

- photovoltaic stability of bulk heterojunction polymer: fullerene solar cells. *Solar Energy Materials and Solar Cells*, **2008**. 92 (7), 753-760.
68. Sun, R., Deng, D., Guo, J., Wu, Q., Guo, J., Shi, M., Shi, K., Wang, T., Xue, L., and Wei, Z., Spontaneous open-circuit voltage gain of fully fabricated organic solar cells caused by elimination of interfacial energy disorder. *Energy & Environmental Science*, **2019**. 12 (8), 2518-2528.
69. Gunawardane, R. P. and Arumainayagam, C. R., Auger electron spectroscopy, in *Handbook of applied solid state spectroscopy*. 2006, Springer. p. 451-483.
70. Vickerman, J. C. and Gilmore, I. S., Surface analysis: the principal techniques. 2011: John Wiley & Sons.
71. Childs, K. D., Carlson, B. A., LaVanier, L. A., Moulder, J. F., Paul, D. F., Stickle, W. F., and Watson, D. G., Handbook of Auger Electron Microscopy. 3rd ed. 1997, Eden Prairie, Minnesota: Physical Electronics, Inc.
72. Yu, L., Qian, D., Marina, S., Nugroho, F. A. A., Sharma, A., Hultmark, S., Hofmann, A. I., Kroon, R., Benduhn, J., and Smilgies, D.-M., Diffusion-Limited Crystallization: A Rationale for the Thermal Stability of Non-Fullerene Solar Cells. *ACS applied materials & interfaces*, **2019**. 11 (24), 21766-21774.
73. Pan, X., Sharma, A., Gedefaw, D., Kroon, R., de Zerio, A. D., Holmes, N. P., Kilcoyne, A. L. D., Barr, M. G., Fahy, A., and Marks, M., Environmentally friendly preparation of nanoparticles for organic photovoltaics. *Organic Electronics*, **2018**. 59, 432-440.
74. Balar, N., Siddika, S., Kashani, S., Peng, Z., Rech, J. J., Ye, L., You, W., Ade, H., and O'Connor, B. T., Role of Secondary Thermal Relaxations in Conjugated Polymer Film Toughness. *Chemistry of Materials*, **2020**. 32 (15), 6540-6549.

CHAPTER 5 – INVESTIGATING DEGRADATION PATHWAYS ASSOCIATED WITH WORKING AND ACCELERATED THERMAL CONDITIONS

5.1. Overview

Thermal stability of OPVs is a significant challenge for the technology to overcome before aiming for commercialisation, however, due to the varying materials that can be used in OPV fabrication, finding strategies for reducing this degradation becomes extremely difficult. Not only that, but majority of the strategies have only been demonstrated on non-scalable fabrication procedures, with scalability only being hypothesised. Lastly, the temperature used for thermal degradation studies is inconsistent between literature, ranging from 80 °C to 180 °C. The purpose of heating the devices at these excessively high temperatures is usually to either accelerate the degradation of the OPV (shortening experiment time), or how high device can reach before major degradation is observed. The issue with these higher temperatures, however, is they result in inducing new degradation pathways, with methods and strategies for improving thermal stability influencing said degradation pathway.

In this chapter, we have demonstrated a method of investigating the thermal degradation of active layer blend PPDT2FBT:PC₆₁BM, a system that has been shown to work effectively when fabricated using roll-to-roll printing, by combining spectroscopy and microscopy techniques, with the dynamic mechanical thermal analysis. This allowed for the determination of thermal behaviour of the blend, how it changes upon annealing, and how they relate the degradation seen in the blend.

The chapter also investigated the difference in degradation that are observed at different annealing temperatures. In this work, we investigated at two temperatures degradation temperatures, 85 °C, accepted by the community as a temperature used for thermal degradation studies under dark storage conditions, and 120 °C: An accelerated temperature that has been used in previous literature using PPDT2FBT:PC₆₁BM degradation studies.

5.2. Introduction

In the previous chapter, it was found that the addition of neat fullerene C₇₀ into PPDT2FBT:PC₆₁BM during the ink preparation stage, allowed for the improvement of the thermal stability at 120 °C, with the support of scanning electron microscopy (SEM) and dynamic mechanical thermal analysis (DMTA) to determine how the neat fullerene influenced the thermal properties of the active layer. Yet, one question arises, does the neat fullerene improve the thermal degradation at 85 °C? In theory, the increase of the annealing temperature would simply accelerate the rate of degradation associated with the main degradation pathway, however, such a temperature increase may lead to the induction of other degradation pathways. This means that methods could be reducing a degradation pathway that may otherwise not be present at the working temperature.

With the push towards cost-effective, accessible, renewable energy sources, there has been an increased interest towards the research and development of organic photovoltaics (OPVs). Their potential is owed to their ability to be fabricated as thin, lightweight and flexible devices using roll-to-roll coating/printing methods with low manufacturing cost, especially when compared to conventional silicon solar panels [1-3]. In the past decade, there has been significant improvements of device performance for OPV technology, leading power conversion efficiencies (PCEs), exceeding 19% for single junction devices [4, 5].

Though performance is an important aspect for the development of OPVs, other factors include fabrication cost and device stability are areas that are just as important yet has seen less research focus. For OPV devices to be competitive to other photovoltaic devices, including silicon-based solar cells, they need to improve in cost-effectiveness, as well as expanding on the average lifespan [6]. In terms of stability, there are five major factors that can negatively impact the device performances of during normal operation of OPVs; including thermal [7, 8], oxygen and moisture [9, 10], UV radiance [11, 12] and mechanical [13-15] degradation. These factors are responsible for two significant decay trends of PCE: burn-in and linear degradation [16-18]. More details in relation to OPV degradation can be found in *Chapter 2*.

In terms of thermal stability, continuous illumination from a light source can result in an increase of the working temperature, especially when operating in outdoor conditions with direct sun-exposure. As majority of OPVs contain a bulk-heterojunction structured active layer, there is a risk of the thermal energy would allow the motion of active materials, resulting in a change in morphology in the active layer, especially when the temperature exceeds glass transitions of the active layer blend [19, 20]. This elevated temperature may also lead to degradation via the material diffusion at the interface between electrodes and interface layers [21-23].

As to date, it has been agreed that 65-85 °C as the working temperature, or known as the high temperature dark storage, which is accepted by the International Summit on OPV Stability (ISOS) consensus test community [24]. As such, a few reported works conduct thermal degradation studies at this working temperature [22, 23, 25-30]. This includes Chaturvedi *et al.* who investigate the degradation of different device configurations of PTB7-Th:IEICO-4F devices for an period of 750 h (31 days) [31], while Wu *et al.* used 85 °C for 4000 minutes (2.7 days) to demonstrate their improved thermal stability using a newly synthesised donor polymer, PMZ2, when compared with PM6 [32]. The issue that can be associated with this working temperature is for more thermal robust devices, a massive amount of time, sometimes surpassing 1 month, is needed for a significant amount of degradation to occur [25, 26]. This length of time to generate data can result in difficulties comparing materials and strategies for improving device lifespan, slowing down the rate of research output.

To resolve this issue, higher temperatures are implemented to allow for accelerated thermal degradation OPV devices, shortening the thermal degradation test to be less than a month [7, 8, 33], depending on the specific temperature used. Through a few papers that compare device stability at higher accelerating degradation temperatures with the accepted working temperature [34-36], this appears to be more the exception rather than the rule. To date, the alternative thermal degradation temperatures that have been used include 80 °C [37-39], 90 °C [34], 100 °C [8, 33, 40], 110 °C [41], 120 °C [36, 42], 130 °C [43], 140 °C [44], 150 °C [45-47], 160 °C [34], and even up to 180 °C [7].

In issue that arises is the potential for new degradation pathways to form at such elevated temperatures that would not otherwise have been experienced when OPV work at standard conditions. For example, He *et al.* had observed that for an inverted OPV configuration, heating up to 200 °C caused silver penetrating into the active layer, resulting in a reduction of device performance, which was not observed at lower temperatures [34]. Whereas for Jang *et al.* had observed that when comparing PTB7:PC₇₁BM that were either fabricated using single deposition or sequential deposition of the active layer, heating at 80 °C for 10 days showed minimal change in degradation, while 140 °C heating resulted in significant burn-in degradation for the single deposition devices [35]. Lastly, Xu *et al.* had shown that for following thermal degradation test with a 10 °C temperature step increase every 5 mins PBTTT-EFT:PC₇₁BM started to degrade significantly after 80 °C, whereas PBTTT-EFT:PC₇₁BM started at 100 °C [36].

One promising active layer material blend for scalable OPV fabrication is Poly[(2,5-bis(2hexyldecyloxy)phenylene)-alt-(5,6-difluoro-4,7-di(thiophen-2-yl)benzo[c][1,2,5]thiadiazole)]:[6,6]-phenyl-C61-butyric acid ester (PPDT2FBT:PC₆₁BM) (structures seen in *Figure 4.1a*), specially, when the material is deposited via slot-die coated.

Achieving a moderate PCE values of 9.39% [48] and 9.1% [49] when incorporating PC₇₁BM and PC₆₁BM in spin-coating, respectively, PPDT2FBT:PCBM has also been effectively slot-die coated at a variety of scales with minimal performance loss [42, 50-52].

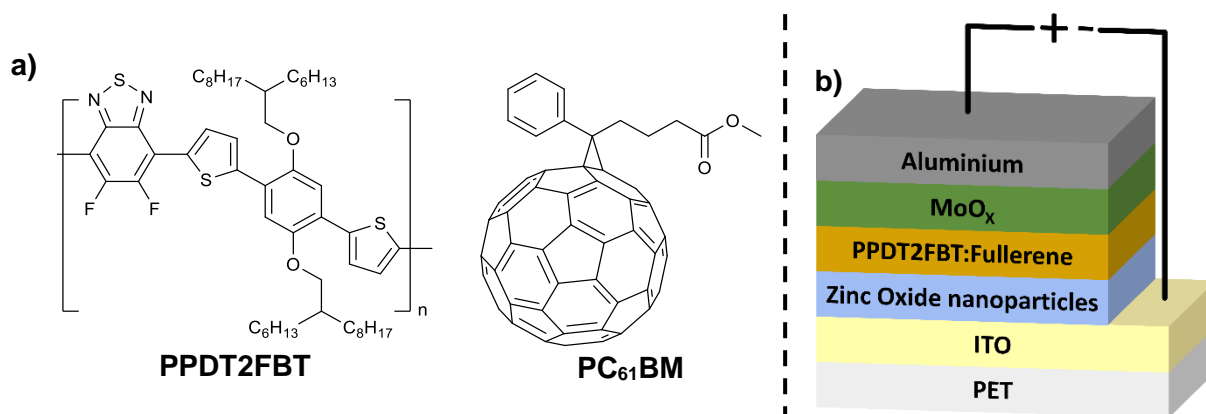


Figure 5.1: (a) Chemical structure of PPDT2FBT & PC₆₁BM, (b) schematic illustration of inverted OPV structure used in this work.

A handful of studies have been performed to investigate the stability of both slot-die and spin-coated PPDT2FBT:PC₆₁BM devices. For lower temperature degradation (60 °C) under constant illumination and without humidity control, Mainville *et al.* observed that the PPDT2FBT:PC₆₁BM devices lasted 220 hours (9 days) before the performance dropped below 80% of the initial PCE [52].

In our previous work, it was found that the addition of neat fullerene C₇₀ into PPDT2FBT:PC₆₁BM during the ink preparation stage improved the thermal stability at 120 °C, revealed from SEM and DMTA results [51]. Yet, one question arises, can the neat fullerene improve the thermal stability of PPDT2FBT:PC₆₁BM based devices upon 85 °C heating? To solve this question, this work firstly aimed at investigating the major degradation pathway associated with 85 °C and 120 °C heating, focusing on the change of thermal properties of materials and blends when exposed to elevated temperatures for specific amounts of time. Afterwards, we investigated how the addition of C₇₀ impacts the thermal degradation at the accepted working temperature.

5.3. Experimental section

5.3.1. Materials

Donor material poly[(2,5-bis(2hexyldecyloxy)phenylene)-alt-(5,6-difluoro-4,7-di(thiophen-2-yl)benzo[c][1,2,5]thiadiazole)] (PPDT2FBT) was synthesised using a direct arylation polymerisation according to literature [53]. The molecular weight of PPDT2FBT was determined via Gel Permeation Chromatography (Agilent 1260 Infinity II High-Temperature GPC System) using trichlorobenzene at 150 °C, giving a number average molecular weight (M_n) of 27 of kg/mol with a PDI of 3.5 relative to polystyrene standards.

The ZnO nanoparticle (NP) dispersion was prepared following a previously published procedure [54]. To achieve an ideal processing concentration, acetone (Chem-supply, 99.9%) was added to the NP precipitate until a concentration of approximately 40 mg mL⁻¹ was achieved. Afterwards, 2-(2-methoxyethoxy)acetic acid (Sigma Aldrich) (5% w/w in relation to ZnO NP) was then added to the dispersion to stabilise the NPs.

Small molecule fullerene acceptor [[6,6]-phenyl-C₆₁-butyric acid ester (PC₆₁BM) were purchased from Solenne BV. Solvents ortho-dichlorobenzene, chlorobenzene and 1-chloronaphthalene were purchased from Sigma Aldrich, whereas chloroform (CHCl₃) was purchased from Chem-Supply. All solvents were used directly without purification.

5.3.2. Device fabrication

Slot-die coated devices were fabricated in a PET/ITO/ZnO NP/BHJ layer/MoO_x/Al device configuration for the BHJ layer of PPDT2FBT:PC₆₁BM. Active layer ink was prepared by dissolving materials, with a donor:acceptor weight ratio of 1:2, in ortho-dichlorobenzene (total 25 mg mL⁻¹ or 14 mg mL⁻¹) with 0.5% V/V of 1-chloronaphthalene at 60 °C overnight.

The flexible ITO substrate (50 ohm/sq, Dongguan Hongdian Technology Co.) was attached to a mini-roll coater (FOM technologies) with slot-die attachment (13 mm width meniscus guide) and wiped with isopropanol soaked TerriWipes at a rotation speed of 2 m min⁻¹ prior to fabrication. The tubing and slot-die head was cleaned with chloroform prior to assembly and between the change of deposition material. Layer deposition was processed under ambient conditions.

The ZnO NP layer (35 nm) was deposited using 0.1 mL min⁻¹ flow-rate, a drum speed of 1.0 m min⁻¹ and drum temperature at 70 °C to achieve a strip width of around 13 mm. The BHJ layer (150 – 200 nm) was deposited via varying flow rate and drum speed at a drum temperature at 70 °C to obtain a strip width of around 13 mm. Wet and dry thickness for both the ZnO NP and BHJ layers were calculated according to *Equation C1 & C2* in *Appendix C*.

After slot-die coating, the MoO_x and aluminium was deposited via the following method. The MoO_x (12nm) was thermally deposited on the BHJ layer under high vacuum using a Covap thermal evaporation system (Angstrom Engineering). This was followed by the evaporation of the Al electrode (80 nm) using a shadow mask, defining the active area to 0.1 cm².

Devices were measured using an Oriel Solar simulator fitted with a 150 W Xeon lamp (Newport), filtered to give an output of 100 mW cm⁻² at AM 1.5 (air mass) standard and calibrated using a silicon reference cell with NIST traceable certification.

Device testing was conducted under ambient conditions. For investigating performance and material degradation, PET/ITO/ZnO NP/BHJ layer/MoO_x/Al & PET/ITO/ZnO NP/BHJ device configurations were used, respectively. Thermal annealing and aging were conducted on a hotplate in a nitrogen-filled glove-box with minimal light exposure.

5.3.3. Scanning Electron Microscopy

Measurements were performed using Inspect F50 scanning electron microscopy (<https://doi.org/10.25957/flinders.sem>) equipped with a field emission gun (FEI Company) and a secondary electron detector. The acceleration voltage was 10 kV, and the working distance of 10 mm. The samples were not coated with any conducting layers. ImageJ was used to analysis the surface features that were observed on the thermally aged samples.

5.3.4. Stylus Profilometry

Measurements were performed using the Bruker DektakXT stylus profilometer, equipped with a 2 µm probe, and 2-dimensional stage movement controllers. The vertical measurement range of the profilometer was set to 6.5 µm.

5.3.5. Auger Electron Spectroscopy

Measurements were performed using a PHI 710 Scanning Auger Nanoprobe system using an acceleration voltage was 10 kV and emission current was 1 nA. Spectra were collected via point scans as specific locations on the sample (SEM images of scan locations can be found in *Table D2 & D3* in *Appendix D*). The Auger spectra were filtered and analysed, as well as element concentrations calculated with MultiPak Spectrum. The peak height to atomic concentration values for specific elements were based on previously published work.

5.3.6. Neutral Impact Collision Ion Scattering Spectroscopy (NICISS)

Elemental depth profiling at depth resolution of a few Angstroms (Å) was performed using the neutral impact collision ion scattering spectroscopy, based on previous experiments with the technique [55-57]. Pulses of positively-charge helium ions with a kinetic energy of 3 keV were used as projectiles, which were backscattered from the sample and towards a time-of-flight (ToF) detector, with a count rate of approximately 200 counts/second.

Analysis of NICISS spectra is based on previous literature that had determined the composition of the surface and near surface of a blend of P3HT:PCBM, identifying a layered structure at the surface [55]. The known bulk concentration of a sample is used to convert the measured count rate into concentration [58].

5.3.7. Dynamic Mechanical Thermal Analysis

The dynamic mechanical thermal analysis (DMTA) was conducted on a DMA Q800 (TA Instruments) equipped with a liquid nitrogen cooling apparatus. The DMTA samples were prepared by repeatedly drop-casting the respective solutions on pre-cut glass mesh as described in previous literature [59, 60]. Sample preparation and instrument conditions can be found in *Appendix C*. Preheating of samples were performed under dark, nitrogen conditions.

5.4. Results and discussion

5.4.1. Device performance stability

As determined in previous work, PPDT2FBT:PC₆₁BM devices appeared to be fairly stable when thermally annealed at 85 °C for the duration of over 2 weeks, especially when compared to dark, room temperature aging [51]. As seen in *Figure 5.2*, after two weeks for thermal testing, there was not significant burn-in, with a small linear degradation pattern being followed.

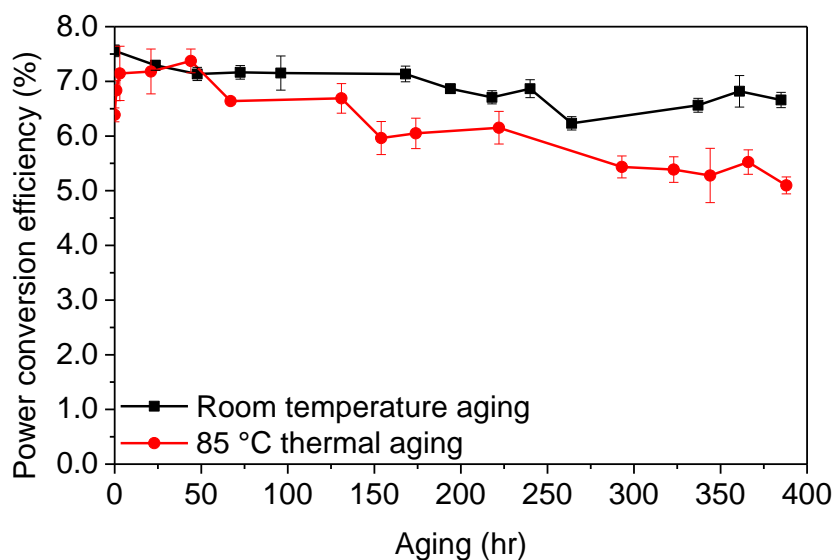


Figure 5.2: Device degradation at 85 °C and room temperature.

As such, it was decided, to extend the range of time for the thermal degradation test from 2 week as previously attempted, to 6 months. This was suspected to allow for a more significant performance decrease to be observed. As a further comparison, the 120 °C thermal degradation test that was performed in *Chapter 4* was overlaid.

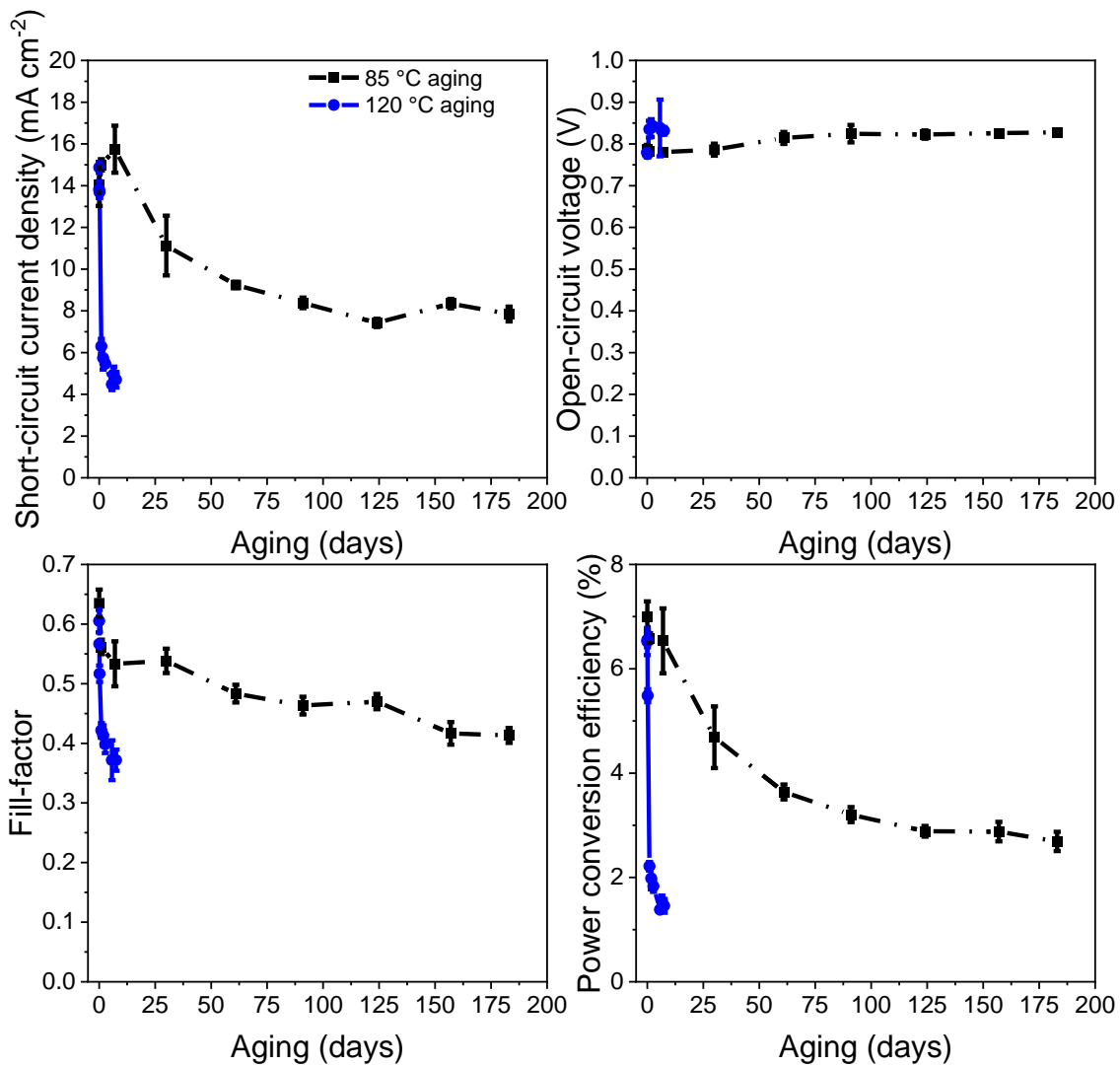


Figure 5.3: Thermal degradation behaviour between devices that are annealed at either 85 °C or 120 °C.

From *Figure 5.2*, the 85 °C degradation behaviour for 3 weeks had the appearance of following a linear trend, indicating the lack of burn-in degradation, however, when the range of degradation is increased to 6 months (*seen in Figure 5.3*), the burn-in trend is more distinguishable, lasting around 120-150 days. This indicates that the source of burn-in degradation takes a relatively long time to degrade the PPDT2FBT:PC₆₁BM devices at 85 °C, especially when compared to the 120 °C degradation trend. Another interesting observation is the magnitude of burn-in degradation when comparing PPDT2FBT:PC₆₁BM devices annealed at 85 °C or 120 °C.

Firstly, it is found that the rate of degradation at 120 °C is significantly faster than at 85 °C. When the 120 °C degradation is fitted with the 85 °C data set, the burn-in degradation appears to occur 90 times faster than the accepted high thermal storage temperature. Another observation found that the magnitude of the initial burn-in degradation is worse for the accelerated temperature, when compared to the working temperature.

So far, there has been extensive effort to correlate the lifespan of accelerated degradation of OPVs with typical lifespan of devices operating under normal conditions. Majority of OPV degradation in terms of the PCE can be approximated to follow an exponential model. As such, there has been literature that aims at using an Arrhenius-type model to predict the device lifespan based on accelerating aging conditions [24, 61]:

$$k_{deg} = A \exp\left(-\frac{E_a}{RT}\right) \quad (5.1)$$

where A is the reaction dependant constant, E_a is the activation energy of the degradation process, R is the gas constant, and T is the temperature in Kelvin. Assuming the degradation follows this simple model, it is evident that the device performance decay is heavily dependent on temperature. There have been several publications that have either demonstrated an Arrhenius-type degradation [62-65]. It is worth pointing out that this method is proposed to be used to predict chemical-based degradation (i.e., photo-degradation), where the increase in temperature will increase chemical degradation.

From the results in *Figure 5.3*, the rate of degradation, when increasing the degradation temperature from 85 °C to 120 °C, resulted in an increase decay a factor of 90 (x26 per 10 °C increase), whereas on paper, that followed the Arrhenius model. showed an increase in decay rate by a factor of 2 per 10 °C increase [62]. It is also observed that the decay magnitude between 85 °C and 120 °C for PPDT2FBT:PC₆₁BM would be the same if degradation is simply increased, where instead the 120 °C aged devices has been observed to have a larger decrease.

As such, it was initially hypothesised as what is causing the burn-in degradation magnitude difference: 1) New degradation pathway has been introduced at the accelerated temperature, resulting in two major degradation sources, or 2) the new dominate degradation at the higher temperature outpaces the previously dominate degradation source at the lower temperature. To investigate further, the surface of the thermally degraded devices was investigated with scanning electron microscopy (SEM).

5.4.2. Bulk heterojunction degradation investigation

To investigate the morphological changes of the active layer (PPDT2FBT:PC₆₁BM), the half devices were heated at 85 °C under dark nitrogen conditions. The BHJ after different annealing time (1, 3 & 6 months) were characterised via SEM with the images shown in *Figure 5.4*.

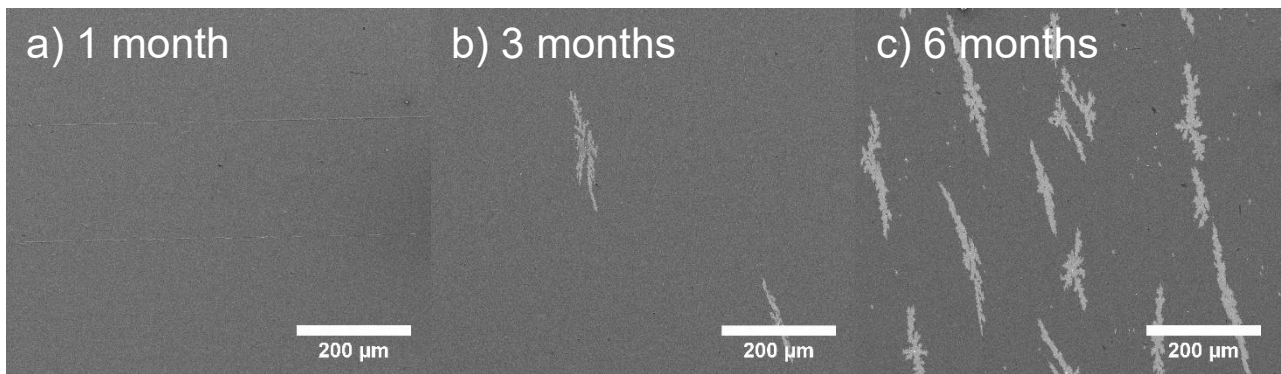


Figure 5.4: SEM of PPDT2FBT:PC₆₁BM BHJ surface after either annealing at 85 °C for either 1 month, 3 months or 6 months.

Before heating, the surface of the BHJ appeared relatively smooth and feature-less. After one month of annealing at 85 °C, no significant change to the active layer was observed, while the BHJ layer still remained relatively featureless. At 3 months of annealing at 85 °C, the appearance of micro-features was observed. The features appeared relatively flat and long (~200 μm length, ~30 μm width), and share a similar orientation along the layer surface. After 6 months, the population of these features increased, yet the size remained the same. Another observation associated with the features is that they appeared to present at the very surface of the active layer, with no noticeable shadows around the crystals. To confirm this, stylus profilometry of the features was performed to see if the height map is distinguishable from the BHJ surface (seen in *Figure 5.5*).

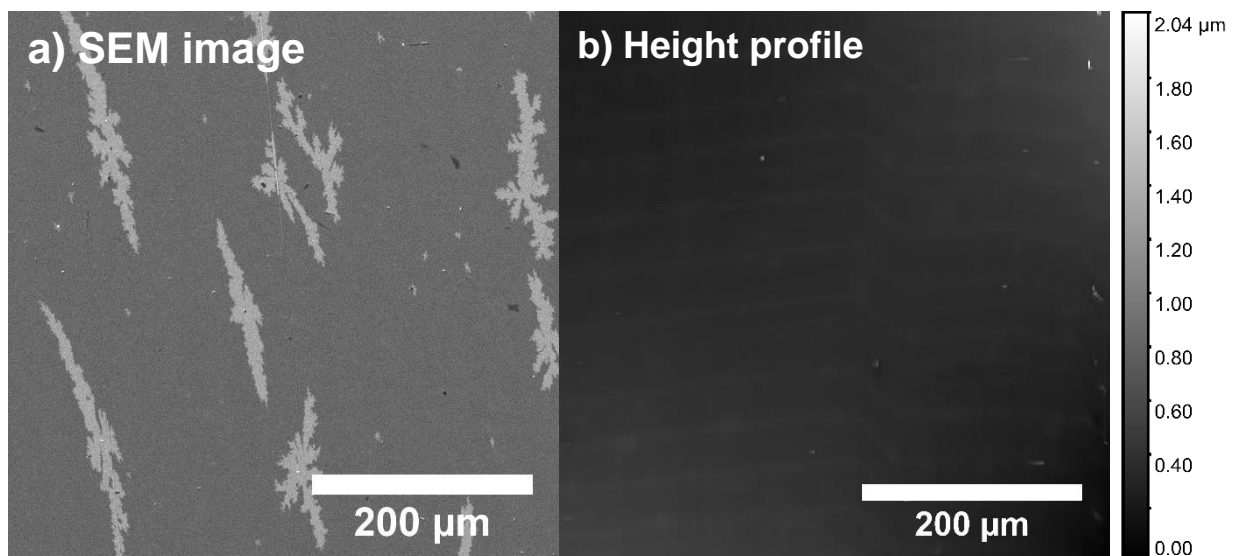


Figure 5.5: Surface comparison of BHJ that was annealed at 85 °C for 6 months: a) SEM image, and b) stylus profilometry height image.

With the comparison of SEM images with the profilometer map, it can be seen that there is no significant height features that would be expected to be observed for crystals growing out of the surface. The small bright spots, however, are suspected to be associated with aggregates that were present prior to thermal annealing, or potential contaminants. As for PPDT2FBT:PC61BM film annealed at 120 °C for 8 hours, there appears to be 3-dimensional microcrystals that are distinguishable from the surface of the active layer (seen in *Figure 5.6*).

From previous studies, with the utilization of AES, that these microcrystals were likely to be PC₆₁BM [51]. The question then arises, are that flat features observed in 85 °C aged PPDT2FBT:PC₆₁BM composed of PC₆₁BM, similar to 120 °C aged active layer, or is the composition of something else? To resolve this matter, techniques such as AES and neutral impact collision ion scattering spectroscopy (NICISS) were utilised.

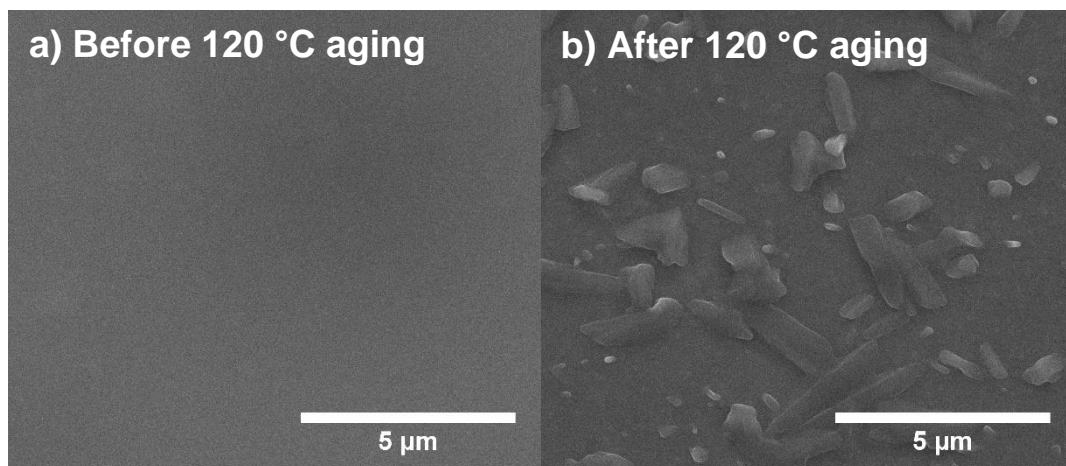


Figure 5.6: SEM of PPDT2FBT:PC₆₁BM BHJ surface before (a) and after (b) annealing 120 °C for 8 hours.

5.4.3. Elemental characteristics of microfeatures

To determine the element composition of the microfeatures on the surface of PPDT2FBT:PC₆₁BM that had appeared after two annealing temperatures (85 °C for 3 months, and 120 °C for 24 hours), Auger electron spectroscopy (AES) was performed. The advantage of this technique is its effective depth (~10 nm), allowing for appropriate surface analysis of the features, thus, minimising the effect of the underlying BHJ, interface, nor electrode underneath. Based on the molecular structure of the photoactive materials present in the BHJ, carbon, sulphur, nitrogen, oxygen, and fluorine would be detectable from the presence of PPDT2FBT, while the presence of PC₆₁BM would result in the signal from only carbon and oxygen.

From the resulting AES spectra (as seen in *Figure 5.7*), the presence of sulphur (152 eV), carbon (272 eV) and oxygen (508 eV) were resolvable from the background, whereas nitrogen (379 eV) and Fluorine (647 eV) were not noticeable. The difference in peak can be explained by two potential factors, the varying number of atoms per element, as well as the sensitivity factor (dependant on the element). When operating the AES with an electron beam energy of 10 keV, the sensitivity factors for carbon, nitrogen, oxygen, fluorine & sulphur are 0.28, 0.60, 0.79, 1.61 & 2.43, respectively [66]. Firstly, due to the relatively high sensitivity factor, even a small amount of sulphur allows for a significant peak to be observed separately from the background, whereas for carbon, the high amount present in both the polymer and fullerene allows for a large peak to be present.

As for nitrogen and oxygen, their low sensitivity factor and low atomic concentration leads to the peaks being either difficult to distinguish, or unable to see from the background. What is difficult to

explain is, though having a high sensitivity factor, the Fluorine peak is unable to be distinguished from the background of the AES spectra, even though the element is present in PPDT2FBT.

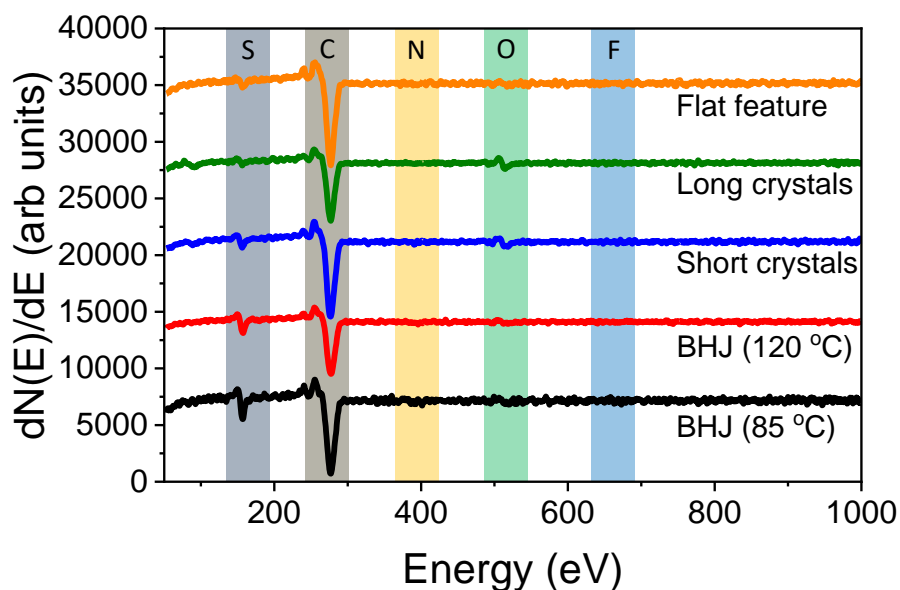


Figure 5.7: Smoothed and derived Auger spectra of specific features found on the surface of PPDT2FBT:PC₆₁BM annealed at either 85 °C or 120 °C. Highlighted are the predicted peak positions of elements suspected to be present at the surface. The spectra are an average of 5 different scanning locations.

As the sulphur and carbon peaks were the two largest peaks to be constantly significant from the background spectra, the sulphur/carbon ratio was used to determine the PPDT2FBT:PC₆₁BM ratio of both the surface of the BHJ, and the microfeatures. As supported in previous work, the AES was able to determine that annealing of PPDT2FBT:PC₆₁BM BHJ at 120 °C for 24 hours resulted in the formation of PC₆₁BM microcrystals.

As a theoretical comparison of atomic percentages of carbon and sulphur, it is expected that PPDT2FBT, containing 52 carbons & 3 sulphurs per repeating unit, would have a carbon and sulphur atomic percentage of 94.5% and 5.5% respectively, whereas PC₆₁BM would have 100% carbon due to no sulphur being present in the molecule. As such, the change in sulphur atomic percentage can be implemented for determining the unit:molecule ratio of polymer:fullerene at specific locations.

Table 5.1: Calculated atomic percentages of carbon and sulphur at various locations based on Auger electron spectroscopy measurements. Percentages are calculated in relation to the presence of carbon and Sulphur only.

Location	%Carbon	%Sulphur
BHJ (85 °C annealed)	96.0% ± 0.5%	4.0% ± 0.5%
BHJ (120 °C annealed)	96.4% ± 0.2%	3.6% ± 0.2%
Short crystals	98.2% ± 0.2%	1.8% ± 0.2%
Long crystals	98.3% ± 0.2%	1.7% ± 0.2%
Flat crystal	98.0% ± 0.5%	2.0% ± 0.5%
PPDT2FBT	96.2% ± 0.8%	3.8% ± 0.8%

From the AES results, the surface of the BHJ appears to have a high percentage of PPDT2FBT polymer, rather than PC₆₁BM. This is supported by investigating the atomic percentage between sulphur and carbon. When measuring the surface of a thin film containing pristine PPDT2FBT, the amount of sulphur was determined to be $3.8 \pm 0.8\%$, while the BHJ had a percentage for $4.0 \pm 0.5\%$. Regardless of annealing temperature, the BHJ surface (not including crystals) appeared to have a high concentration of polymer at the surface.

When investigating the composition of the crystals, sulphur/carbon ratio was also calculated; with a minimal change to the ratio indicating polymer crystallisation, while a significant decrease indicating fullerene crystallisation. A significant decrease of the sulphur percentage was found for all three shapes of crystals examined, with measures over 3-dimensional (short and long) and flat crystals having sulphur percentage of $1.8 \pm 0.2\%$, $1.7 \pm 0.2\%$ & $2.0 \pm 0.5\%$, respectively. Though fullerene crystals do not contain sulphur atoms within their molecular structure, there were still sulphur features observed in the AES spectra. For the 3-dimensional crystals, it is suspected that these crystals grow within the BHJ before migrating to the surface.

This crystal migration has been reported by Zhong *et al.*, with the PC₆₁BM crystallisation being investigated for a polymer:fullerene BHJ under post-annealing conditions [67]. This may result in some of the polymer position at the surface to be taken up with the crystal, as well as increased phase separation leading to an increase in exciton recombination. As for the flat feature, it was damaged while scanning with the electron beam, with a possibility of exposing the underlying BHJ layer. Otherwise, the thickness of these flat crystals is smaller than the effective depth of AES measurements, resulting in some of the polymer underneath being detected.

Lastly, for all three crystal types that have been observed for PPDT2FBT:PC₆₁BM, showed sulphur present in the spectra. There are a few variables that could result in the Sulphur peak appearing, including the beam radius being large enough to incorporate the BHJ surrounding the crystal, the migration of crystal brings up some of the polymer on its surface, and/or the BHJ underneath the crystals and features being within the effective depth of the spectroscopy method.

5.5.4. Depth profiling of bulk-heterojunction surface containing microfeatures

To support the observations found from AES and SEM, an elemental depth profiling method known as neutral impact collision ion scattering spectroscopy (NICISS) was performed on the thermal degraded active layer samples. The advantage of the method of AES is its ability to determine the concentration of elements at a specific depth, as well as the total concentration within the effective depth. The downside of this method is that it uses a projectile beam that is relatively large when compared with AES, having a beam diameter of 1 mm. As such, both the surface of the BHJ and any features present due to annealing impact the depth profile during the measurement. As such, to allow for accurate analysis, the depth profile is compared with the SEM images and AES spectra.

Initially, NCISS measurement was performed on a pristine PPDT2FBT film (~100 nm thickness) that was slot-die coated over a PET/ITO/ZnO NP substrate. Afterwards, PPDT2FBT:PC₆₁BM samples were measured at specific thermal aging conditions, non-annealed, 85 °C for 6 months and 120 °C for 24 hours (seen in *Figure 5.8*). In all NCISS spectra, sulphur (S), fluorine (F), oxygen (O), nitrogen (N) and carbon (C) was observed.

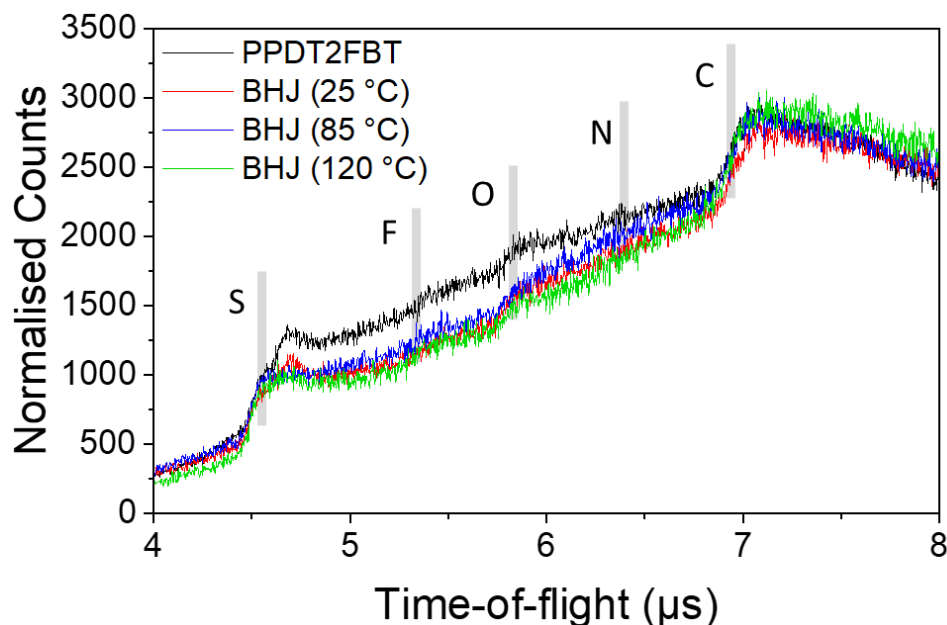


Figure 5.8: NCISS ToF spectra of either pristine PPDT2FBT (black line) or PPDT2FBT:PC₆₁BM BHJ (coloured lines). The BHJ is either non-annealed (25 °C) (red line), aged at 85 °C for 6 months (blue) or aged at 120 °C for 24 hours (green line). Counts are normalised based on carbon peak height. Spectra features due to sulphur, fluorine, oxygen, nitrogen, and carbon are marked with vertical bars.

From the raw spectra of PPDT2FBT polymer, both the sulphur and carbon features are significant in the spectra, due to that sulphur has a relative larger atomic diameter compared with other non-metal atoms, while the polymer has a large number of carbon atoms per repeating unit. Other atoms (fluorine, oxygen, and nitrogen) though are observed in the spectra, their lack of size makes it difficult to determine the concentration of the elements accurately. As sulphur does not present in the PC₆₁BM molecule, it can be predicted that the concentration of sulphur in the depth-profile correlated with the concentration of PPDT2FBT. As such, it was used to determine the composition of the BHJ surface that has not been thermally aged.

To convert the ToF spectra into a concentration depth profile, a data conversion method that has been previously published was implemented [68]. To convert the count rate to concentration, the sulphur step height of the count rate was based on the step height of carbon, with the S:C height ratio from the PPDT2FBT being the reference for 100% polymer composition, and a ratio of 0 being 100% fullerene composition. This relative measurement for S concentration was used for the depth profile in *Figure 5.9*.

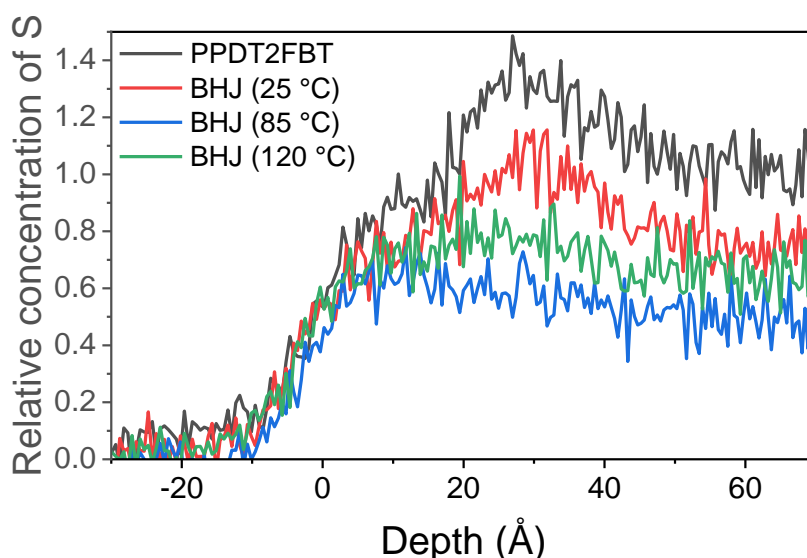


Figure 5.9: Concentration depth profiles of either pristine PPDT2FBT (black line) or PPDT2FBT:PC61BM BHJ (coloured lines). The BHJ is either non-annealed (25 °C) (red line), aged at 85 °C for 6 months (blue) or aged at 120 °C for 24 hours (green line).

When comparing the concentration depth profile of pristine polymer with the BHJ samples, they all have a similar feature offset at 0 Å, where zero depth points to the outermost layer, and an increase in depth indicates the bulk materials. In this case, for all sample surface, there is a presence of polymer at the surface.

As such, the polymer at the surface facilitates charge transportation and collection for inverted organic devices. The concentration of the S, however, indicates a depletion of this polymer at the surface of BHJ after the annealing when compared to the pristine polymer sample. The other observation is associated with height a 50 – 70 Å, indicating a reduction of polymer composition in the bulk of the sample of the BHJ, when compared to the pristine polymer sample. When comparing 85 °C and 120 °C aged BHJ surfaces, it can be observed that the 85 °C near surface has noticeably less surface, than compared with the 120 °C sample. This with observation, the next stage was to use the step height of the spectra in Figure 5.9 to calculate the polymer and fullerene percentages at the near surface (seen in *Table 5.2*).

Table 5.2: Step height of the count rate for sulphur and carbon, step height ratio and calculated material composition of polymer in the PPDT2DBT, as well as non-annealed and annealed BHJ. The material composition was calculated based on the C:S step height ratio of pristine PPDT2FBT.

Sample	Step height (arb units)		S:C step height ratio	Material composition	
	Sulphur	Carbon		Polymer	Fullerene
PPDT2FBT	4800	65000	0.074	100%	0%
BHJ 25 °C	3900	71000	0.055	74%	26%
BHJ 85 °C	2800	77000	0.036	49%	51%
BHJ 120 °C	4000	89000	0.045	61%	39%

By calculating the material composition based on the S:C step height ratio, it is found that the bulk of the BHJ contained a mixture of polymer and fullerene materials. Based on theoretical calculations of PPDT2FBT repeating unit : Fullerene molecule ratio based on a 1:2 w/w ratio, it is expected the unit:molecule ratio would be 1:9.5 throughout the entire layer. Instead, the calculated ratio is closer to 3:4, indicating that there is an enrichment of polymer at the surface.

When the BHJ is annealed at 120 °C for 24 hours, there is a decrease in sulphur compared to non-annealed BHJ. When compared to the SEM images, despite the surface being covered in fullerene crystals, the NICISS spectra still showed a presence of sulphur from the polymer. It is suspected that there is still a layer of BHJ over the fullerene crystals, where the crystal either formed near the BHJ surface, or the crystals migrated to the surface.

As for the BHJ that was annealed at 85 °C, it is far less polymer at the near-surface compared both to non-annealed and 120 °C annealed samples. Unlike 3-dimensional fullerene crystals that may have polymer at their surface due to either the migrate or formation said crystals near the surface of the active layer, it is suspect the flat features on the surface of the 85 °C annealed sample to be purely PC₆₁BM within the effective depth of the NICISS. To support this argument, the percentage of PC₆₁BM determined from the NICISS was compared with the surface area of the flat features observed from the SEM (seen in *Figure 5.10*).

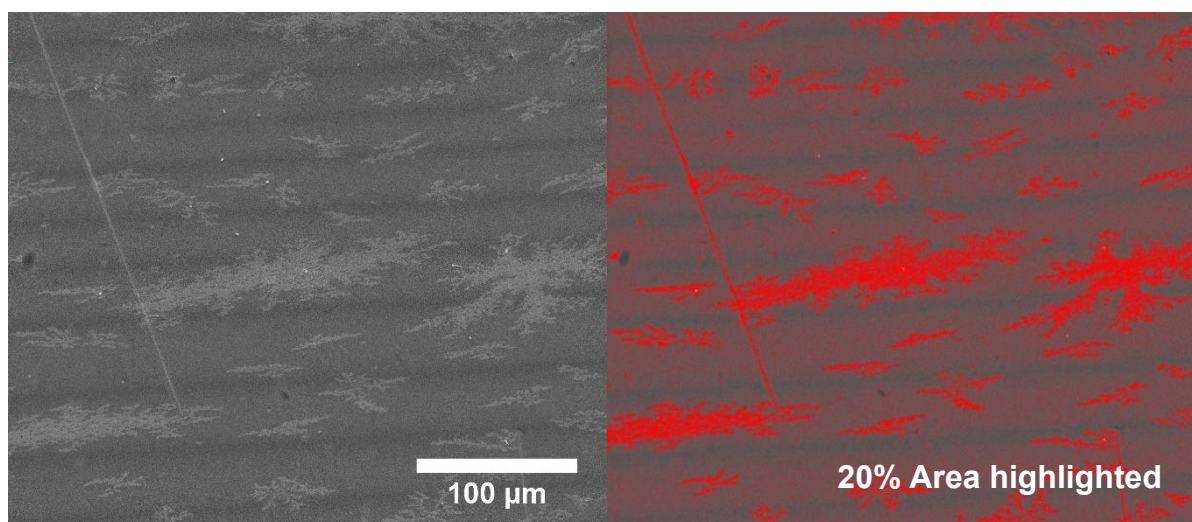


Figure 5.10: SEM surface of PPDT2FBT:PC₆₁BM active layer aged at 85 °C for 6 months (LEFT), with highlighted area used for determining area of flat fullerene features.

With the SEM image of the active layer surface, the bright area of the surface was measured with ImageJ, using the measure threshold function. From the images, it was found the surface area consisted of approximately 20% of flat fullerene features. In terms with the NICISS, the difference in the bulk polymer composition between non-annealed and 85 °C aged BHJ is by a reduction of approximately 20%, thus an increase of fullerene by the same amount, supporting the observation that the increase in fullerene at the surface and near-surface is from the flat features.

By implementing SEM, AES and NCISS to investigate the flat features at the surface of the PPDT2FBT:PC₆₁BM blend after being thermally aged 85 °C, they are likely to be rich in PC₆₁BM. As for 120 °C, the NCISS supports the observation from AES that there may be PPDT2FBT polymer on the surface of the 3-dimensional fullerene crystals.

4.5.5. Thermal degradation behaviour

One technique that has been implemented in the investigation of the thermal behaviour of OPV active layer blends is the dynamic mechanical thermal analysis (DMTA), a useful method for understanding the thermal transitions of pure materials and blends, as well as a tool to understand the morphology of the BHJ layer [60, 69, 70]. In this work, this technique was used to investigate the thermal behaviour of the active layer blend., Dynamic Mechanic Thermal Analysis (DMTA). This method relies on the changes of the viscoelastic properties as the material is subjected to a constant increase in temperature.

To investigate these viscoelastic properties, an oscillating mechanical strain (i.e., tension) with known amplitude and frequency is applied, will the movement of the sample under oscillation is observed. This allows for values of storage modulus (E'), Loss modulus (E'') and Tan delta (=E'/E''), where E' reflects the stiffness of the sample, E'' peaks features suggest thermal transitions, while traditionally, tan delta defines the temperature of these transitions.

In previous work, DMTA was demonstrated to show how the addition of C₇₀ was able to influence the thermal properties of PPDT2FBT:PC₆₁BM, resulting in the fullerene crystallisation to occur at a higher temperature [51]. In this work, the purpose of the DMTA measurements was to observe how the thermal transitions changed as the samples experienced different temperatures and durations of annealing. It was hypothesised that, as the morphology changes, that there may be a shift in certain thermal transitions.

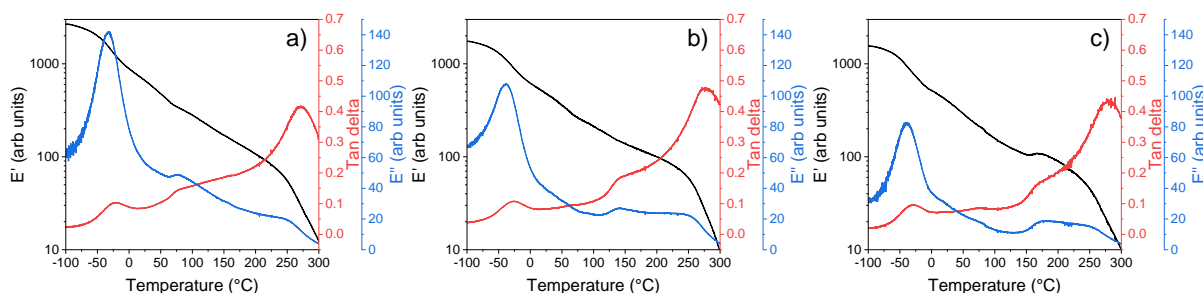


Figure 5.11: DMTA of pure PPDT2FBT after thermal annealing: a) 40 °C for 30 minutes, b) 85 °C for 24 hours, and c) 120 °C for 24 hours.

For pure PPDT2FBT polymer (seen in *Figure 5.11a*), one sub-glass transition (sub- T_g) was observed at around $-25\text{ }^\circ\text{C}$ (having been determined from tan delta peak), while no clear T_g was detected with DMTA, indicating the lack of amorphous phase in the solid state [60], which in previously published work, had been observed for similar polymers [60, 71]. This conclusion can be supported by previous literature, where grazing-incidence wide-angle x-ray scattering (GIWAXS), found the PPDT2FBT to be semi-crystalline polymer [48, 72]. There also appears to be a thermal transition at $75\text{ }^\circ\text{C}$ yet appears relatively minor when compared to the sub- T_g transition.

When the PPDT2FBT is subjected to annealing at elevated temperature for 24 hours prior to DMTA measurements (seen in *Figure 5.11b & c*), this transition appears to shift, with the feature located at $140\text{ }^\circ\text{C}$ and $175\text{ }^\circ\text{C}$ after annealing at $85\text{ }^\circ\text{C}$ and $120\text{ }^\circ\text{C}$, respectively. It is also observed that, at this feature at $40\text{ }^\circ\text{C}$ and $85\text{ }^\circ\text{C}$, there is a small increase in stiffness, while at $120\text{ }^\circ\text{C}$ pre-annealing, the stiffness increase is significant. It is suspected that this feature is associated with the crystallisation of the PPDT2FBT. The shift of the peak could be associated with the polymer re-orientating itself. As semi-crystalline polymers may have several transitions present during sample heating, including T_g , cold crystallisation and melting [73]. As the size/thickness of these layers are changed, so too do the temperatures these transitions occur at including T_g [74] and cold-crystallisation [73]. Based on the DMTA results, the heating of the polymer likely leads to increased phase size of semi-crystalline PPDT2FBT, before cold-crystallisation is observed. It is also found that the sub- T_g did not see any significant temperature shift, regardless of the change in pre-annealing conditions.

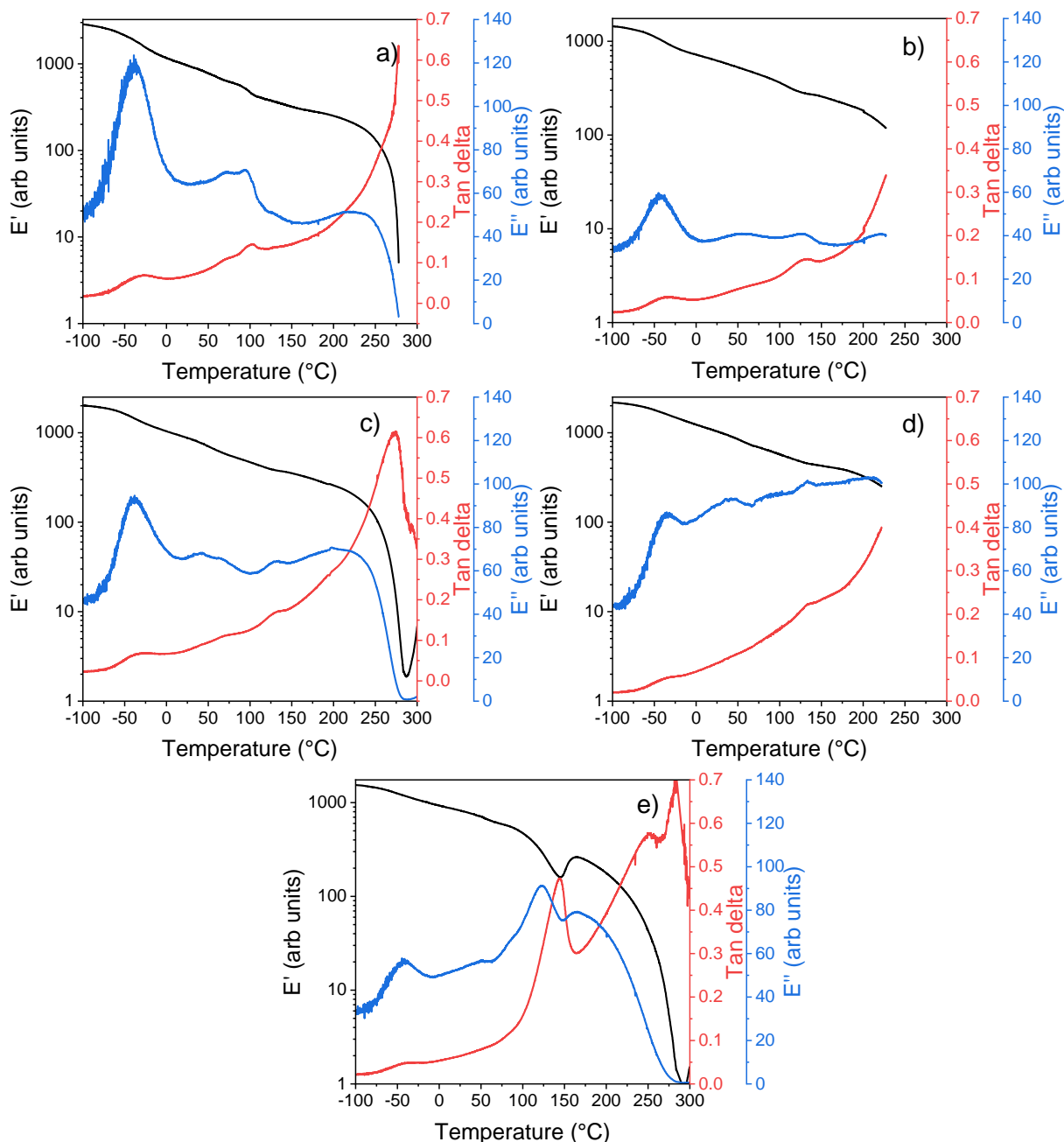


Figure 5.12: DMTA of PPDT2FBT:PC₆₁BM samples after thermal annealing: a) 40 °C for 30 minutes, as well as b) 85 °C for 30 minutes, c) 8 hours, d) 15 hours, and e) 1 week.

For PPDT2FBT:PC₆₁BM blend (As seen in *Figure 5.12*), the sub- T_g peak is still clearly observed, with no significant peak shift in relation to temperature, which supports that this feature is not originated from the glass transition. For the blend has been annealed at 40 °C (to remove thermal history [70]), one extra thermal relaxation at ~100 °C, seen by the E'' peak, as well as a thermal transition without stiffness change at ~70 °C. After annealing the samples at 85 °C for certain amounts of times, it is observed that ~100 °C thermal relaxation peak shifts to ~130 °C after 30 minutes / 15 hours, while the thermal transition at ~70 °C shifts to a lower temperature at ~50 °C.

This shift in the ~ 100 °C thermal relaxation is suspected to be associated with the cold crystallisation of PC₆₁BM, especially when, after 1 week of pre-annealing at 85 °C resulted in E' increase from ~ 100 °C to ~ 145 °C, indicating the formation of crystals. This feature has also been observed in previous literature, which attributed the stiffness trend to the cold crystallisation of Y6 at 190 °C [75].

As the SEM images showed a lack of 3-dimensional fullerenes on the 85 °C annealed PPDT2FBT:PC₆₁BM surface, it can be speculated that this crystal formation occurred once a higher temperature was reached during the DMTA measurement. As such, the DMTA supported the idea that the annealing at 85 °C results in the change in morphology, allowing for purer PC₆₁BM and polymer phases to form. Once these phases have increased in purity, and potentially in size, a substantial amount of crystallisation can be observed from the DMTA.

The increase in the suspected PC₆₁BM cold crystallisation temperature initially found at ~ 100 °C and shifted at ~ 130 °C is likely due to the increased size in fullerene phase. As discussed previously, that there is a size dependency for thermal transitions [73, 74]. Based on these observations, as the blend is heated at 85 °C, the fullerene phase in the blend increases in size and purity, before reaching a point where, during the DMTA measurement, the fullerene cold crystallisation can significantly influence the stiffness of the sample.

The last observation found with the 85 °C aged PPDT2FBT:PC₆₁BM, the feature at -25 °C, which is confirmed to be the sub-T_g of the PPDT2FBT polymer (seen in *Figure 5.11*), does not appear to significantly shift in temperature position. With the axis of the E'' kept constant, it appears that the height of the E'' peak reduces as the PPDT2FBT:PC₆₁BM blend is annealed at 85 °C, even after 30 minutes. This embrittlement of the Sub-T_g has been previously observed for epoxies, with the side-chains of the polymers becoming more restricted in its movement.

In the case of PPDT2FBT, the change in morphology of the blend could lead to restricted side chain movement, either due to fullerene molecules getting in-between the side chains, or the rearrangements of the polymers. It is well known that the height of E'' is dependent on the dimension and mass of the sample, thus, making it difficult to compare between samples. Later in the work, a sample that was pre-heated and remeasured was performed.

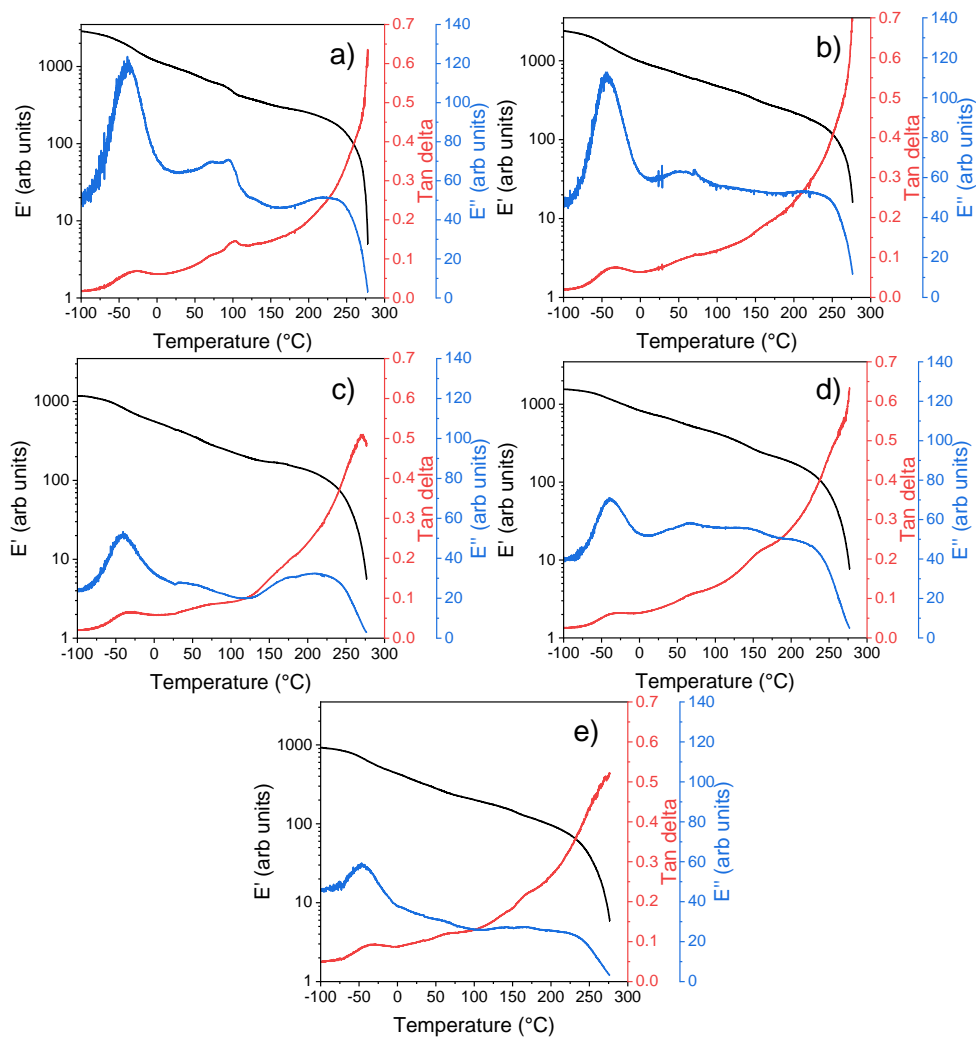


Figure 5.13: DMTA of PPDT2FBT:PC₆₁BM samples after thermal annealing: a) 40 °C for 30 minutes, as well as b) 120 °C for 30 minutes, c) 8 hours, d) 15 hours, and e) 1 week.

Unlike the 85 °C pre-annealed PPDT2FBT:PC₆₁BM blends, the samples that had experienced different annealing times at 120 °C resulted in the 100 °C thermal transition feature mostly disappearing. It is expected that during the annealing of the sample at the higher temperature, the PC₆₁BM may experience crystallisation, meaning that when the DMTA scans at elevated temperatures, such crystallisation behaviour would not be observed. It is also observed that there are insignificant spectra different between the 120 °C annealed samples at various times, with it being attributed the lack of morphology mobility after annealing for 30 minutes.

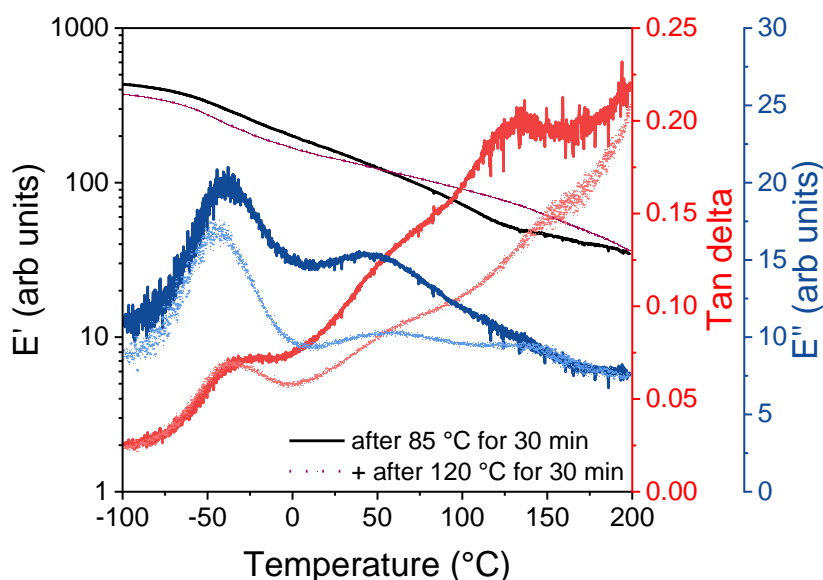


Figure 5.14: DMTA of PPDT2FBT:PC₆₁BM sample after thermal annealing after annealing at 85 °C for 30 minutes (solid line), while the same sample was annealed at 120 °C for 30 minutes and measured again (dotted line)

In terms of the sub- T_g , the 85 °C annealing of the sample resulted in similar thermal behaviour as seen in *Figure 5.12*. A sub- T_g was observed at -40 °C with a peak height of 20, a E'' at 46 °C with a peak height of 15, and cold-crystallisation feature at 133 °C. When the same sample was annealed at 120 °C for 30 minutes, several changes are observed. Similar with *Figure 5.13*, the cold-crystallisation is not observable in the DMTA spectra, while both the sub- T_g and thermal relaxation both saw a decrease in peak height, down to 15 and 10, respectively.

5.5. Conclusion

In this work, it was observed that, when thermally degrading the PPBT2FBT:PC₆₁BM at two different annealing temperatures, working temperature (85 °C) and accelerated temperature (120 °C), the dominate degradation pathway of the active layer appeared to be significantly different. Specifically, while PC₆₁BM crystals appeared at the surface after annealing at the accelerated temperature, the working temperature results in relatively large, yet flat PC₆₁BM features. This observation was supported by combining scanning electron microscopy, Auger electron spectroscopy and 2D-sylus profilometry.

By implementing the DMTA technique to study the change in thermal behaviour after annealing the PPDT2FBT:PC₆₁BM blends, it was found that the major degradation pathway at 120 °C is associated with fullerene crystallisation, while 85 °C resulted in significant changes to the morphology, with the increased phase separation between PPDT2FBT and PC₆₁BM. In summary, this work highlights the importance of performing thermal degradation studies at accepted annealing temperatures, regardless of whether higher accelerated degradation temperatures were required to observe a significant performance reduction.

5.6. References

1. Thompson, B. C. and Fréchet, J. M. J., Polymer–Fullerene Composite Solar Cells. *Angewandte Chemie International Edition*, **2008**. 47 (1), 58-77.
2. Beaujuge, P. M. and Fréchet, J. M. J., Molecular Design and Ordering Effects in π -Functional Materials for Transistor and Solar Cell Applications. *Journal of the American Chemical Society*, **2011**. 133 (50), 20009-20029.
3. Andersen, T. R., Almyahi, F., Cooling, N. A., Elkington, D., Wiggins, L., Fahy, A., Feron, K., Vaughan, B., Griffith, M. J., and Mozer, A. J., Comparison of inorganic electron transport layers in fully roll-to-roll coated/printed organic photovoltaics in normal geometry. *Journal of Materials Chemistry A*, **2016**. 4 (41), 15986-15996.
4. Zhu, L., Zhang, M., Xu, J., Li, C., Yan, J., Zhou, G., Zhong, W., Hao, T., Song, J., Xue, X., Zhou, Z., Zeng, R., Zhu, H., Chen, C.-C., MacKenzie, R. C. I., Zou, Y., Nelson, J., Zhang, Y., Sun, Y., and Liu, F., Single-junction organic solar cells with over 19% efficiency enabled by a refined double-fibril network morphology. *Nature Materials*, **2022**. 21 (6), 656-663.
5. Wei, Y., Chen, Z., Lu, G., Yu, N., Li, C., Gao, J., Gu, X., Hao, X., Lu, G., Tang, Z., Zhang, J., Wei, Z., Zhang, X., and Huang, H., Binary Organic Solar Cells Breaking 19% via Manipulating the Vertical Component Distribution. *Advanced Materials*, **2022**. 34 (33), 2204718.
6. Søndergaard, R., Hösel, M., Angmo, D., Larsen-Olsen, T. T., and Krebs, F. C., Roll-to-roll fabrication of polymer solar cells. *Materials today*, **2012**. 15 (1-2), 36-49.
7. Zhang, Z., Miao, J., Ding, Z., Kan, B., Lin, B., Wan, X., Ma, W., Chen, Y., Long, X., Dou, C., Zhang, J., Liu, J., and Wang, L., Efficient and thermally stable organic solar cells based on small molecule donor and polymer acceptor. *Nature Communications*, **2019**. 10 (1), 3271.
8. Zheng, N., Mahmood, K., Zhong, W., Liu, F., Zhu, P., Wang, Z., Xie, B., Chen, Z., Zhang, K., Ying, L., Huang, F., and Cao, Y., Improving the efficiency and stability of non-fullerene polymer solar cells by using N2200 as the Additive. *Nano Energy*, **2019**. 58, 724-731.
9. Meitzner, R., Faber, T., Alam, S., Amand, A., Roesch, R., Büttner, M., Herrmann-Westendorf, F., Presselt, M., Ciommaruchi, L., and Visoly-Fisher, I., Impact of P3HT materials properties and layer architecture on OPV device stability. *Solar Energy Materials and Solar Cells*, **2019**. 202, 110151.
10. Li, M., Zhang, W., Wang, H., Chen, L., Zheng, C., and Chen, R., Effect of organic cathode interfacial layers on efficiency and stability improvement of polymer solar cells. *RSC advances*, **2017**. 7 (50), 31158-31163.
11. Weng, C.-N., Yang, H.-C., Tsai, C.-Y., Chen, S.-H., Chen, Y.-S., Chen, C.-H., Huang, K.-M., Meng, H.-F., Chao, Y.-C., and Chang, C.-Y., The influence of UV filter and Al/Ag moisture barrier layer on the outdoor stability of polymer solar cells. *Solar Energy*, **2020**. 199, 308-316.
12. Doumon, N. Y., Wang, G., Chiechi, R. C., and Koster, L. J. A., Relating polymer chemical structure to the stability of polymer: fullerene solar cells. *Journal of Materials Chemistry C*, **2017**. 5 (26), 6611-6619.
13. Muhsin, B., Roesch, R., Gobsch, G., and Hoppe, H., Flexible ITO-free polymer solar cells based on highly conductive PEDOT:PSS and a printed silver grid. *Solar Energy Materials and Solar Cells*, **2014**. 130, 551-554.
14. Zimmermann, B., Schleiermacher, H.-F., Niggemann, M., Würfel, U., and Cells, S., ITO-free flexible inverted organic solar cell modules with high fill factor prepared by slot die coating. *Solar Energy Materials and Solar Cells*, **2011**. 95 (7), 1587-1589.
15. Sun, Y., Meng, L., Wan, X., Guo, Z., Ke, X., Sun, Z., Zhao, K., Zhang, H., Li, C., and Chen, Y., Flexible High-Performance and Solution-Processed Organic Photovoltaics with Robust Mechanical Stability. *Advanced Functional Materials*, **2021**. 31 (16), 2010000.
16. Kang, H., Kim, G., Kim, J., Kwon, S., Kim, H., and Lee, K., Bulk-heterojunction organic solar cells: Five core technologies for their commercialization. *Advanced Materials*, **2016**. 28 (36), 7821-7861.

17. Greenbank, W., Djeddaoui, N., Destouesse, E., Lamminaho, J., Prete, M., Boukezzi, L., Ebel, T., Bessissa, L., Rubahn, H.-G., Turkovic, V., and Madsen, M., Degradation Behavior of Scalable Nonfullerene Organic Solar Cells Assessed by Outdoor and Indoor ISOS Stability Protocols. *Energy Technology*, **2020**. 8 (12), 2000295.
18. Duan, L. and Uddin, A., Progress in Stability of Organic Solar Cells. *Advanced Science*, **2020**. 7 (11), 1903259.
19. Paci, B., Generosi, A., Rossi Albertini, V., Perfetti, P., de Bettignies, R., Leroy, J., Firon, M., and Sentein, C., Controlling photoinduced degradation in plastic photovoltaic cells: A time-resolved energy dispersive x-ray reflectometry study. *Applied physics letters*, **2006**. 89 (4), 043507.
20. Andreasen, J. W., Gevorgyan, S. A., Schlepütz, C. M., and Krebs, F. C., Applicability of X-ray reflectometry to studies of polymer solar cell degradation. *Solar energy materials and solar cells*, **2008**. 92 (7), 793-798.
21. Greenbank, W., Rolston, N., Destouesse, E., Wantz, G., Hirsch, L., Dauskardt, R., and Chambon, S., Improved mechanical adhesion and electronic stability of organic solar cells with thermal ageing: the role of diffusion at the hole extraction interface. *Journal of Materials Chemistry A*, **2017**. 5 (6), 2911-2919.
22. Sung, Y. M., Huang, Y. C., Chien, F. S. S., and Tsao, C. S., Mechanism and Analysis of Thermal Burn-In Degradation of OPVs Induced by Evaporated HTL. *IEEE Journal of Photovoltaics*, **2019**. 9 (3), 694-699.
23. Greenbank, W., Hirsch, L., Wantz, G., and Chambon, S., Interfacial thermal degradation in inverted organic solar cells. *Applied Physics Letters*, **2015**. 107 (26), 263301.
24. Reese, M. O., Gevorgyan, S. A., Jørgensen, M., Bundgaard, E., Kurtz, S. R., Ginley, D. S., Olson, D. C., Lloyd, M. T., Morvillo, P., Katz, E. A., Elschner, A., Haillant, O., Currier, T. R., Shrotriya, V., Hermenau, M., Riede, M., R. Kirov, K., Trimmel, G., Rath, T., Inganäs, O., Zhang, F., Andersson, M., Tvingstedt, K., Lira-Cantu, M., Laird, D., McGuinness, C., Gowrisanker, S., Pannone, M., Xiao, M., Hauch, J., Steim, R., DeLongchamp, D. M., Rösch, R., Hoppe, H., Espinosa, N., Urbina, A., Yaman-Uzunoglu, G., Bonekamp, J.-B., van Breemen, A. J. J. M., Girotto, C., Voroshazi, E., and Krebs, F. C., Consensus stability testing protocols for organic photovoltaic materials and devices. *Solar Energy Materials and Solar Cells*, **2011**. 95 (5), 1253-1267.
25. Park, S., Park, S. H., Jin, H., Yoon, S., Ahn, H., Shin, S., Kwak, K., Nah, S., Shin, E.-Y., Noh, J. H., Min, B. K., and Son, H. J., Important role of alloyed polymer acceptor for high efficiency and stable large-area organic photovoltaics. *Nano Energy*, **2022**. 98, 107187.
26. Son, H. J., Park, H.-K., Moon, J. Y., Ju, B.-K., and Kim, S. H., Thermal degradation related to the PEDOT:PSS hole transport layer and back electrode of the flexible inverted organic photovoltaic module. *Sustainable Energy & Fuels*, **2020**. 4 (4), 1974-1983.
27. Li, Z., Ho Chiu, K., Shahid Ashraf, R., Fearn, S., Dattani, R., Cheng Wong, H., Tan, C.-H., Wu, J., Cabral, J. T., and Durrant, J. R., Toward Improved Lifetimes of Organic Solar Cells under Thermal Stress: Substrate-Dependent Morphological Stability of PCDTBT:PCBM Films and Devices. *Scientific Reports*, **2015**. 5 (1), 15149.
28. Bolognesi, M., Prosa, M., Tessarolo, M., Donati, G., Toffanin, S., Muccini, M., and Seri, M., Impact of environmentally friendly processing on polymer solar cells: Performance, thermal stability and morphological study by imaging techniques. *Solar Energy Materials and Solar Cells*, **2016**. 155, 436-445.
29. Lee, H., Sohn, J., Tyagi, P., and Lee, C., Crystallinity dependent thermal degradation in organic solar cell. *Applied Physics Letters*, **2017**. 110 (5), 053301.
30. Wang, Z., Nian, Y., Jiang, H., Pan, F., Hu, Z., Zhang, L., Cao, Y., and Chen, J., High Voc ternary nonfullerene polymer solar cells with improved efficiency and good thermal stability. *Organic Electronics*, **2019**. 69, 174-180.
31. Chaturvedi, N., Gasparini, N., Corzo, D., Bertrandie, J., Wehbe, N., Troughton, J., and Baran, D., All Slot-Die Coated Non-Fullerene Organic Solar Cells with PCE 11%. *Advanced Functional Materials*, **2021**. n/a (n/a), 2009996.
32. Wu, J., Guo, X., Xiong, M., Xia, X., Li, Q., Fang, J., Yan, X., Liu, Q., Lu, X., Wang, E., Yu, D., and Zhang, M., Modulating the nanoscale morphology on carboxylate-pyrazine containing terpolymer toward 17.8% efficiency organic solar cells with enhanced thermal stability. *Chemical Engineering Journal*, **2022**. 446, 137424.

33. Hong, L., Yao, H., Cui, Y., Yu, R., Lin, Y.-W., Chen, T.-W., Xu, Y., Qin, J., Hsu, C.-S., Ge, Z., and Hou, J., Simultaneous Improvement of Efficiency and Stability of Organic Photovoltaic Cells by using a Cross-Linkable Fullerene Derivative. *Small*, **2021**. 17 (24), 2101133.
34. He, Y., Heumüller, T., Lai, W., Feng, G., Classen, A., Du, X., Liu, C., Li, W., Li, N., and Brabec, C. J., Evidencing Excellent Thermal- and Photostability for Single-Component Organic Solar Cells with Inherently Built-In Microstructure. *Advanced Energy Materials*, **2019**. 9 (21), 1900409.
35. Jang, Y., Ju Cho, Y., Kim, M., Seok, J., Ahn, H., and Kim, K., Formation of Thermally Stable Bulk Heterojunction by Reducing the Polymer and Fullerene Intermixing. *Scientific Reports*, **2017**. 7 (1), 9690.
36. Xu, X., Fukuda, K., Karki, A., Park, S., Kimura, H., Jinno, H., Watanabe, N., Yamamoto, S., Shimomura, S., and Kitazawa, D., Thermally stable, highly efficient, ultraflexible organic photovoltaics. *Proceedings of the National Academy of Sciences*, **2018**. 115 (18), 4589-4594.
37. Ding, K., Li, Y., and Forrest, S. R., Characterizing and Improving the Thermal Stability of Organic Photovoltaics Based on Halogen-Rich Non-Fullerene Acceptors. *ACS Applied Materials & Interfaces*, **2022**. 14 (4), 5692-5698.
38. Xu, Y., Yuan, J., Zhou, S., Seifrid, M., Ying, L., Li, B., Huang, F., Bazan, G. C., and Ma, W., Ambient Processable and Stable All-Polymer Organic Solar Cells. *Advanced Functional Materials*, **2019**. 29 (8), 1806747.
39. Kim, M., Park, S., Ryu, D. Y., and Kim, K., Improving thermal stability of organic photovoltaics via constructing interdiffused bilayer of polymer/fullerene. *Polymer*, **2016**. 103, 132-139.
40. Xian, K., Zhang, S., Xu, Y., Liu, J., Zhou, K., Peng, Z., Li, M., Zhao, W., Chen, Y., Fei, Z., Hou, J., Geng, Y., and Ye, L., Refining acceptor aggregation in nonfullerene organic solar cells to achieve high efficiency and superior thermal stability. *Science China Chemistry*, **2023**. 66 (1), 202-215.
41. Wang, Z., Hong, Z., Zhuang, T., Chen, G., Sasabe, H., Yokoyama, D., and Kido, J., High fill factor and thermal stability of bilayer organic photovoltaic cells with an inverted structure. *Applied Physics Letters*, **2015**. 106 (5), 053305.
42. Song, S., Lee, K. T., Koh, C. W., Shin, H., Gao, M., Woo, H. Y., Vak, D., and Kim, J. Y., Hot slot die coating for additive-free fabrication of high performance roll-to-roll processed polymer solar cells. *Energy & Environmental Science*, **2018**. 11 (11), 3248-3255.
43. Yin, J., Zhou, W., Zhang, L., Xie, Y., Yu, Z., Shao, J., Ma, W., Zeng, J., and Chen, Y., Improved Glass Transition Temperature towards Thermal Stability via Thiols Solvent Additive versus DIO in Polymer Solar Cells. *Macromolecular Rapid Communications*, **2017**. 38 (20), 1700428.
44. Zhang, C., Mumyatov, A., Langner, S., Perea, J. D., Kassar, T., Min, J., Ke, L., Chen, H., Gerasimov, K. L., Anokhin, D. V., Ivanov, D. A., Ameri, T., Osvet, A., Susarova, D. K., Unruh, T., Li, N., Troshin, P., and Brabec, C. J., Overcoming the Thermal Instability of Efficient Polymer Solar Cells by Employing Novel Fullerene-Based Acceptors. *Advanced Energy Materials*, **2017**. 7 (3), 1601204.
45. Chao, Y.-C., Chuang, C.-H., Hsu, H.-L., Wang, H.-J., Hsu, Y.-C., Chen, C.-P., and Jeng, R.-J., Enhanced thermal stability of organic photovoltaics via incorporating triphenylamine derivatives as additives. *Solar Energy Materials and Solar Cells*, **2016**. 157, 666-675.
46. Grant, T. M., Gorisse, T., Dautel, O., Wantz, G., and Lessard, B. H., Multifunctional ternary additive in bulk heterojunction OPV: increased device performance and stability. *Journal of Materials Chemistry A*, **2017**. 5 (4), 1581-1587.
47. Feng, W., Lin, Z., Cui, J., Lv, W., Wang, W., and Ling, Q., Photoactive layer crosslinking in all-polymer solar cells: Stabilized morphology and enhanced thermal-stability. *Solar Energy Materials and Solar Cells*, **2019**. 200, 109982.
48. Nguyen, T. L., Choi, H., Ko, S. J., Uddin, M. A., Walker, B., Yum, S., Jeong, J. E., Yun, M. H., Shin, T. J., and Hwang, S., Semi-crystalline photovoltaic polymers with efficiency exceeding 9% in a ~ 300 nm thick conventional single-cell device. *Energy & Environmental Science*, **2014**. 7 (9), 3040-3051.

49. Du, Z., Mainville, M., Vollbrecht, J., Dixon, A. L., Schopp, N., Schrock, M., Peng, Z., Huang, J., Chae, S., Ade, H., Leclerc, M., Reddy, G. N. M., and Nguyen, T.-Q., Insights into Bulk-Heterojunction Organic Solar Cells Processed from Green Solvent. *Solar RRL*, **2021**. 5 (8), 2100213.
50. Dayneko, S. V., Pahlevani, M., and Welch, G. C., Indoor Photovoltaics: Photoactive Material Selection, Greener Ink Formulations, and Slot-Die Coated Active Layers. *ACS Applied Materials & Interfaces*, **2019**. 11 (49), 46017-46025.
51. Kirk, B., Pan, X., Jevric, M., Andersson, G., and Andersson, M. R., Introducing neat fullerenes to improve the thermal stability of slot-die coated organic solar cells. *Materials Advances*, **2022**.
52. Mainville, M., Tremblay, V., Fenniri, M. Z., Laventure, A., Farahat, M. E., Ambrose, R., Welch, G. C., Hill, I. G., and Leclerc, M., Water Compatible Direct (Hetero)arylation Polymerization of PPDT2FBT: A Pathway Towards Large-Scale Production of Organic Solar Cells. *Asian Journal of Organic Chemistry*, **2020**. 9 (9), 1318-1325.
53. Morin, P.-O., Bura, T., Sun, B., Gorelsky, S. I., Li, Y., and Leclerc, M., Conjugated polymers à la carte from time-controlled direct (hetero) arylation polymerization. *ACS Macro Letters*, **2015**. 4 (1), 21-24.
54. Krebs, F. C., Air stable polymer photovoltaics based on a process free from vacuum steps and fullerenes. *Solar Energy Materials and Solar Cells*, **2008**. 92 (7), 715-726.
55. Schmerl, N. and Andersson, G., A layered structure at the surface of P3HT/PCBM blends. *Physical Chemistry Chemical Physics*, **2011**. 13 (33), 14993-15002.
56. Alghamdi, A. R., Bjuggren, J. M., Pan, X., Andersson, M. R., and Andersson, G. G., Dipole Formation at Active Materials/P(NDI3N-T-Br) Interface in Organic-Based Photovoltaic. *Macromolecular Materials and Engineering*, **2022**. 307 (10), 2200303.
57. Alghamdi, A. R., Kirk, B. P., Kocak, G., Andersson, M. R., and Andersson, G. G., Modification of the Surface Composition of PTB7-Th: ITIC Blend Using an Additive. *Molecules*, **2022**. 27 (19), 6358.
58. Andersson, G. and Morgner, H., Impact collision ion scattering spectroscopy (ICISS) and neutral impact collision ion scattering spectroscopy (NICISS) at surfaces of organic liquids. *Surface science*, **1998**. 405 (1), 138-151.
59. Sharma, A., Pan, X., Campbell, J. A., Andersson, M. R., and Lewis, D. A., Unravelling the thermomechanical properties of bulk heterojunction blends in polymer solar cells. *Macromolecules*, **2017**. 50 (8), 3347-3354.
60. Sharma, A., Pan, X., Bjuggren, J. M., Gedefaw, D., Xu, X., Kroon, R., Wang, E., Campbell, J. A., Lewis, D. A., and Andersson, M. R., Probing the relationship between molecular structures, thermal transitions, and morphology in polymer semiconductors using a woven glass-mesh-based DMTA technique. *Chemistry of Materials*, **2019**. 31 (17), 6740-6749.
61. Jørgensen, M., Norrman, K., and Krebs, F. C., Stability/degradation of polymer solar cells. *Solar Energy Materials and Solar Cells*, **2008**. 92 (7), 686-714.
62. Gevorgyan, S. A., Jørgensen, M., and Krebs, F. C., A setup for studying stability and degradation of polymer solar cells. *Solar Energy Materials and Solar Cells*, **2008**. 92 (7), 736-745.
63. Schuller, S., Schilinsky, P., Hauch, J., and Brabec, C. J., Determination of the degradation constant of bulk heterojunction solar cells by accelerated lifetime measurements. *Applied Physics A*, **2004**. 79 (1), 37-40.
64. De Bettignies, R., Leroy, J., Firon, M., and Sentain, C., Accelerated lifetime measurements of P3HT:PCBM solar cells. *Synthetic Metals*, **2006**. 156 (7), 510-513.
65. Chang, B., Cheng, H.-W., Lin, Y.-C., Wang, H.-C., Chen, C.-H., Nguyen, V.-T., Yang, Y., and Wei, K.-H., Incorporating Indium Selenide Nanosheets into a Polymer/Small Molecule Binary Blend Active Layer Enhances the Long-Term Stability and Performance of Its Organic Photovoltaics. *ACS Applied Materials & Interfaces*, **2020**. 12 (49), 55023-55032.
66. Childs, K. D., Carlson, B. A., LaVanier, L. A., Moulder, J. F., Paul, D. F., Stickle, W. F., and Watson, D. G., Handbook of Auger Electron Microscopy. 3rd ed. 1997, Eden Prairie, Minnesota: Physical Electronics, Inc.
67. Zhong, H., Yang, X., deWith, B., and Loos, J., Quantitative Insight into Morphology Evolution of Thin PPV/PCBM Composite Films upon Thermal Treatment. *Macromolecules*, **2006**. 39 (1), 218-223.

68. Andersson, G. and Morgner, H., Investigations on solutions of tetrabutylonium salts in formamide with NICISS and ICISS: concentration depth profiles and composition of the outermost layer. *Surface science*, **2000**. 445 (1), 89-99.
69. Yu, L., Qian, D., Marina, S., Nugroho, F. A. A., Sharma, A., Hultmark, S., Hofmann, A. I., Kroon, R., Benduhn, J., and Smilgies, D.-M., Diffusion-Limited Crystallization: A Rationale for the Thermal Stability of Non-Fullerene Solar Cells. *ACS applied materials & interfaces*, **2019**. 11 (24), 21766-21774.
70. Pan, X., Sharma, A., Gedefaw, D., Kroon, R., de Zerio, A. D., Holmes, N. P., Kilcoyne, A. L. D., Barr, M. G., Fahy, A., and Marks, M., Environmentally friendly preparation of nanoparticles for organic photovoltaics. *Organic Electronics*, **2018**. 59, 432-440.
71. Balar, N., Siddika, S., Kashani, S., Peng, Z., Rech, J. J., Ye, L., You, W., Ade, H., and O'Connor, B. T., Role of Secondary Thermal Relaxations in Conjugated Polymer Film Toughness. *Chemistry of Materials*, **2020**. 32 (15), 6540-6549.
72. Shin, S.-C., Koh, C. W., Vincent, P., Goo, J. S., Bae, J.-H., Lee, J.-J., Shin, C., Kim, H., Woo, H. Y., and Shim, J. W., Ultra-thick semi-crystalline photoactive donor polymer for efficient indoor organic photovoltaics. *Nano Energy*, **2019**. 58, 466-475.
73. Hajduk, B., Bednarski, H., and Trzebicka, B., Temperature-Dependent Spectroscopic Ellipsometry of Thin Polymer Films. *The Journal of Physical Chemistry B*, **2020**. 124 (16), 3229-3251.
74. El Ouakili, A., Vignaud, G., Balnois, E., Bardeau, J.-F., and Grohens, Y., Multiple glass transition temperatures of polymer thin films as probed by multi-wavelength ellipsometry. *Thin Solid Films*, **2011**. 519 (6), 2031-2036.
75. Pan, X., Bjuggren, J. M., Jevric, M., Tan, W. L., McNeill, C. R., and Andersson, M. R., Achieving High-Efficiency Organic Photovoltaics from a New Completely Amorphous Donor Polymer. *Chemistry of Materials*, **2022**. 34 (11), 5103-5115.

CHAPTER 6 – INTRODUCING NON-FULLERENE ADDITIVES TO IMPROVE THE THERMAL STABILITY OF SLOT-DIE COATED ORGANIC PHOTOVOLTAICS

6.1. Overview

In the field of OPVs, solid additives have gained interest towards their potential to improve both the device performance and photo/thermal stability when added to the active layer blend. Currently, there has been discussion on how these additives can influence the physical and chemical properties of the BHJ morphology, however, due to the wide range of additive available to test with, it is difficult to gain a consensus precise mechanisms involved with the interactions between additives and active materials. The other issue is that majority of research involving solid additives fabricated via small-scale spin-coating, with the addition of additives to the active layer being assumed to be scalable.

In this chapter, three solid additives, piperazine (PP), 4'-bipiperidine (BP), and polyacenaphthylene (PAN) were chosen based on previously published work having shown their influence over the polymer:fullerene active layer blend. Using slot-die coating, it was found that when adding the additives to PPDT2FBT:PC₆₁BM blends, were able to influence the thermal stability of OPV devices. Specifically, improving the stability at 120 °C, while negatively influencing the stability at 85 °C.

When combining scanning electron microscopy (SEM) imaging with the dynamic mechanical thermal analysis (DMTA) technique, these additives were able to slow down the fullerene crystallisation growth rate at 120 °C, allowing for improved thermal stability. Whereas at 85 °C, it was found that these additives allowed for fullerene crystallisation to occur at the lower temperature, allowing for the formation of both fullerene crystals and flat fullerene features to be observable at the surface of the active layer. This work has shown that, despite the additives were able have a positive influence over the thermal stability of OPVs, it is important to investigate said stability at lower aging temperatures.

6.2. Introduction

Organic photovoltaics (OPV) have shown potential towards the next generation of photovoltaic (PV) technology due to its cost effectiveness, potential for lightweight and flexible panel design, as well as the ability to be fabrication with roll-to-roll compatible processes. In the past decade, there has been rapid progress in the power conversion efficiency (PCE) of OPVs, reaching beyond 19% for single junction devices [1, 2]. OPVs have also been demonstrated to work effectively under lowlight conditions, including under the presence of indoor lights [3-5], allowing for devices to apply towards light recycling and indirect light harvesting.

Despite these advantages, there are two factors that are important for the development of OPV technology towards commercialisation, device stability, and fabrication scalability, which has been mentioned in detail in *Chapter 2*. In terms of OPV device stability, it has been found that several sources of degradation can reduce the overall lifespan, including thermal [6, 7], oxygen and moisture [8, 9], UV radiance [10, 11] and mechanical [12-14] degradation. The influence of these degradation sources can lead to an initial significant exponential decay, known as burn-in, as well as a slow linear decay of the PCE [15-17]. An example of this decay behaviour can be seen in *Chapter 5*, with the degradation behaviour being observed for PPDT2FBT:PC₆₁BM devices thermally aged at 85 °C under dark nitrogen conditions.

In terms of thermal stability, continuous illumination from a light source can result in an increase of the working temperature, especially when operating in outdoor conditions with direct sun-exposure. As majority of OPVs contain a bulk-heterojunction structured active layer, there is a risk of the thermal energy would allow the movement of active materials, resulting in a change in morphology in the active layer, especially when the temperature exceeds any major thermal transitions of the materials contained in the active layer blend, such as glass-transition and cold-crystallisation [18, 19]. This elevated temperature may also lead to degradation via the material diffusion at the interface of electrodes and transport/extraction/interface layers [20-22].

Recently, solid additives have gained increased interest towards their ability to improve active layer, specifically allow for control over the morphology, simple post treatments and enhancement of device stability. Since this is a relatively new area in OPV development, there is minimal knowledge associated with mechanisms of how solid additive influence the active materials and the morphology. Some additives that have been investigated in published literature can be found in *Figure 6.1*.

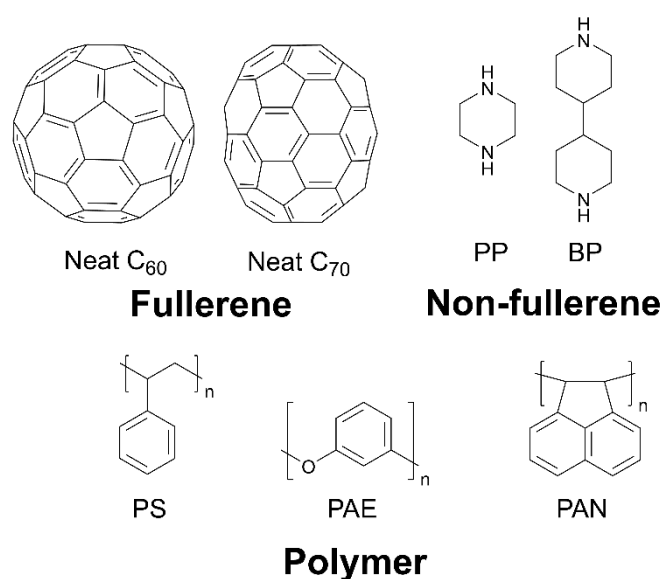


Figure 6.1: Chemical structures of some solid additives that have been investigated in previously published worked.

One such additive, piperazine (PP), has been shown to work effectively at improving the thermal stability of polymer:fullerene based OPVs. For example, Yan *et al.* demonstrated that the addition of 3% w/w Piperazine into the active layer (P3HT:PCBM) improved the light degradation (without presence of oxygen) [23]. It was lately determined by Yan *et al.* that the addition of piperazine functioned as a dopant, allowing for improved electron mobility of the PCBM, while also improving photo-oxidation stability [24].

With the successful demonstration of PP in polymer:fullerene additives, few research groups were aimed at determining what interactions were involved with influencing device performance and stability. In one paper, Zhang *et al.* concluded that the addition of piperazine improved stability by having the N-H function groups intermolecularly bonding with the S, N & O elements that are present in either PC₆₁BM or the PCE11 polymer (hydrogen bonds). This helps reduce movement of the BHJ upon experiencing heated conditions [25]. Whereas a paper by Yan *et al.* concluded that the addition of piperazine to P3HT:Bis-PC₆₁BM improved the photo-oxidation stability by suppressing Mo⁶⁺ reduction (C₆₀ addition as well) at the BHJ/MoO_x interface [26].

A similar material to piperazine, 4,4'-bipiperidine (BP) is a small molecule that combines two 6-member rings connected by a single carbon bond, with each ring containing a single nitrogen atom. This molecule has an increased melting point of 170-172 °C (bp 274-782 °C) when compared with piperazine (mp 106 °C, bp 146 °C). From preliminary search of available literature, BP has alone been used to improve the thermal stability of perovskite solar cells, allowing for the improved crystallinity and reduction in defect sites in the perovskite materials [27].

Another type of non-volatile additive is the use of insulating polymers, such as polystyrene (PS), poly(aryl ether) (PAE) and polyacenaphthylene (PAN), and their derivatives. For PS, Wang *et al.* investigated the addition of 5% w/w of PS when mixed with PBDB-T and ITIC, showing an improvement the device performance by influencing the phase separation and structuring of the morphology, suspecting that due to the low glassing temperature of PS, allowing it the polymer to fill in interspace between phases [28]. Also hypothesised to be able to improve the charge carrier mobility and lifetime. Another paper published by Liu *et al.* found that when mixing PS with PM6:BTP-BO-4Cl resulted in the reduction of device performance, with the reduction in charge carrier mobility and reduced mechanical properties of the active layer blend .

Another insulating polymer, poly(aryl ether) (PAE) and their derivatives have been shown to improve the thermal stability of OPV devices when added to the additive layer [29-33]. Han *et al.* observed that the addition of 5% w/w of the ridged high T_g polymer, poly(aryl ether)-based polymer to the active layer ink (containing PM6:Y6) prior to deposition, was able to form faster the morphology of the BHJ, allowing for an extended lifespan when exposed to 85 °C annealing conditions. This insulating polymer has also been demonstrated to effectively improve photo/thermal stability of pseudo planar heterojunction (sequentially-deposited) active layer [34].

Another material that has been shown to work effectively at improving the thermal stability of OPVs is the addition of polyacenaphthylene (PAN). A high T_g polymer Insulator, it had been demonstrated by Chen *et al.* (2021), that when adding PAN to PTB7-Th:EH-IDTBR blends, it was able to improve the thermal stability by reducing the crystal growth of the acceptor by having the polymer additive between the acceptor compounds [35]. Though, it was also shown adding too much of the insulator resulted in a reduction of the J_{sc} and leading to a decrease in device performance. Besides this paper, initial searches show that there is no other literature that has tried to explain the mechanisms behind the PAN additive's influence over the BHJ. The other issue is that the thermal stability measurements were conducted at a much higher degradation temperature (150 °C).

One last solid-additive type that has been investigated in previous literature, as well as in this thesis work (*Chapter 4*), is the addition of neat fullerenes. With the addition of neat C_{60} to an active layer containing a blend polymer:fullerene, the additive can act as a nucleating agent, allowing for a reduced size for fullerene crystallisation due to space-limitation in the active, resulting in improved thermal stability [36-39]. Whereas for the addition of neat C_{70} to the active layer resulted in changes to the morphological thermal behaviour, leading to a decrease in fullerene crystallisation rate and population [39]. Both the addition of neat C_{60} and C_{70} into the PPDT2FBT:PC₆₁BM active layer blend has been investigated by this thesis work (*Chapter 4*).

Overall, there is an array of solid additives that have been investigated for both polymer:fullerene and polymer:non-fullerene systems, however, there is a knowledge gap when understanding the role these additives play at influencing the thermal properties of BHJ. Secondly, majority of solid-additive research have been conducted on small-scale spin-coated, leaving the scalability of solid additives to be speculated. As such, this research not only aimed at investigating the influence these additives have on the thermal behaviour, but if these actives can be utilised in OPV that have been fabricated using scalable coating methods, such as slot-die coating.

To investigate the impact of non-volatile on the thermal properties of an active layer, active materials Poly[(2,5-bis(2hexyldecyloxy)phenylene)-alt-(5,6-difluoro-4,7-di(thiophen-2-yl)benzo[c][1,2,5]thiadiazole)]: [6,6]-phenyl-C₆₁-butyric acid ester (PPDT2FBT:PC₆₁BM) (structures seen in *Figure 6.2a*) was chosen for this work due to its ability to be slot-die processable, while having a relatively high thermal stability. To date, device performance of 9.39% [40] and 9.1% [41] when incorporating PC₇₁BM and PC₆₁BM in spin-coating, respectively, PPDT2FBT:PCBM has been demonstrated to effectively slot-die coated at a variety of scales with minimal performance loss [39, 42-44].

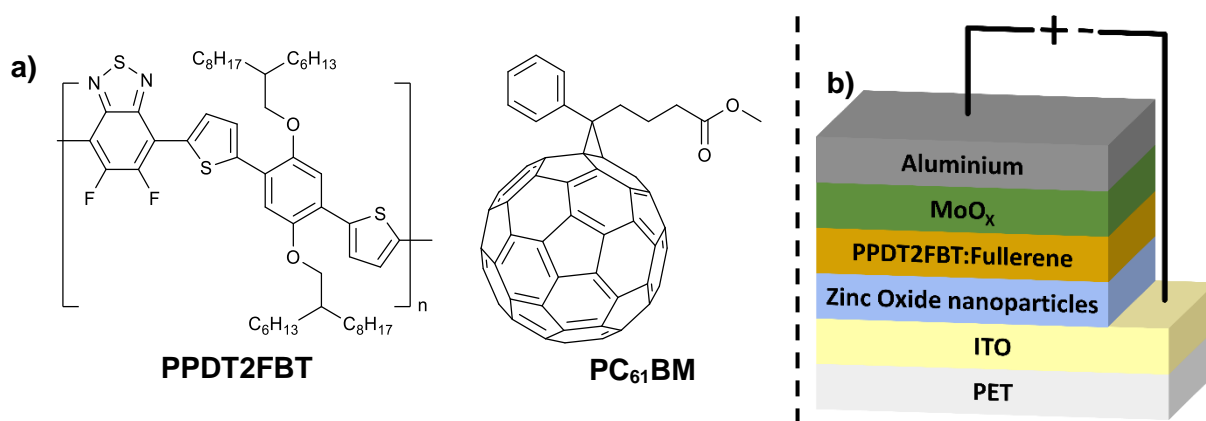


Figure 6.2: (a) Chemical structure of PPDT2FBT & PC₆₁BM, (b) schematic illustration of inverted OPV structure used in this work.

A handful of studies have been performed to investigate the stability of both slot-die and spin-coated PPDT2FBT:PC₆₁BM devices. For lower temperature degradation (60 °C), paired with constant illumination and no humidity control, Mainville *et al.* observed that the PPDT2FBT:PC₆₁BM devices lasted 220 hours (9 days) before degradation below 80% initial PCE [44].

The aim of the chapter is to investigate a few small molecule and insulator materials that can be used as additives to influence the thermal behaviour of the polymer:fullerene BHJ, thus, decreasing the thermal degradation. The molecules of interest include piperazine (PP), 4,4'-biperadine (BP), and polyacenaphthylene (PAN) (seen in *Figure 6.3*).

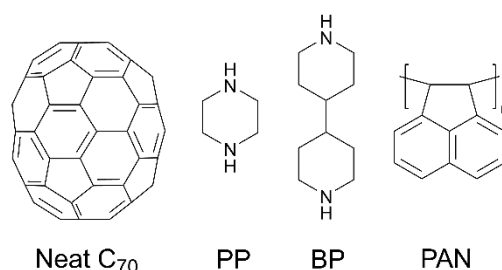


Figure 6.3: Chemical structure of Neat C₇₀, piperazine (PP), 4,4'-biperadine (BP), and polyacenaphthylene (PAN).

The thermal degradation studies include investigating the stability at both the working (85 °C) and accelerated (120 °C) temperatures. Lastly, the influence on the thermal behaviour of the blends were investigated with analytical methods such as scanning electron microscopy (SEM), Auger electron microscopy (AEM), and dynamics mechanical thermal analysis (DMTA).

6.3. Experimental section

6.3.1. Materials

Donor material poly[(2,5-bis(2hexyldecyloxy)phenylene)-alt-(5,6-difluoro-4,7-di(thiophen-2-yl)benzo[c][1,2,5]thiadiazole)] (PPDT2FBT) was synthesised using a direct arylation polymerisation according to literature [45]. The molecular weight of PPDT2FBT was determined via Gel Permeation Chromatography (Agilent 1260 Infinity II High-Temperature GPC System) using trichlorobenzene at 150 °C, giving a number average molecular weight (M_n) of 50 of kg/mol with a PDI of 2.60 relative to polystyrene standards.

The ZnO NP dispersion was prepared following a previously published procedure [46]. To achieve an ideal processing concentration, acetone (Chem-supply, 99.9%) was added to the NP precipitate until a concentration of approximately 40 mg mL⁻¹ was achieved. Afterwards, 2-(2-methoxyethoxy)acetic acid (Sigma Aldrich) (5% w/w in relation to ZnO NP) was then added to the dispersion to stabilise the NPs.

Piperazine, 4,4'-Bipiperidine & Polyacenaphthylene were purchased from Sigma-Aldrich, Tokyo Chemical Industry & Sigma-Aldrich respectively. Small molecule acceptors [[6,6]-phenyl-C61-butyric acid ester (PC₆₁BM), and neat fullerenes (C₇₀) were purchased from Solenne BV. Solvents ortho-dichlorobenzene, chlorobenzene and 1-chloronaphthalene were purchased from Sigma Aldrich, whereas chloroform (CHCl₃) was purchased from Chem-Supply. All solvents were used directly without purification.

6.3.2. Device fabrication

Slot-die coated devices were fabricated in a PET/ITO/ZnO NP/BHJ layer/MoO_x/Al device configuration for BHJ layers of PPDT2FBT:PC₆₁BM. Active layer ink was prepared by dissolving materials, with a donor:acceptor weight ratio of 1:2, in ortho-dichlorobenzene (total 25 mg mL⁻¹) with 0.5% V/V of 1-chloronaphthalene at 60 °C overnight.

The flexible ITO substrate (50 ohm/sq, Dongguan Hongdian Technology Co.) was attached to a mini-roll coater (FOM technologies) with slot-die attachment and wiped with isopropanol soaked TerriWipes at a rotation speed of 2 m min⁻¹ prior to fabrication. The tubing and slot-die head was cleaned with chloroform prior to assembly and between the change of deposition material. Layer deposition was processed under ambient conditions.

The ZnO NP layer (35 nm) was deposited using 0.1 mL min⁻¹ flow-rate, a drum speed of 1.0 m min⁻¹ and drum temperature at 70 °C to achieve a strip width of around 13 mm. The BHJ layer (150 – 200 nm) was deposited via varying flow rate and drum speed at a drum temperature at 70 °C to obtain a strip width of around 13 mm. Wet and dry thickness for both the ZnO NP and BHJ layers were calculated according to *Equation C1 & C2 in Appendix C*.

After slot-die coating, the MoO_x and aluminium was deposited via the following method. The MoO_x (12nm) was thermally deposited on the BHJ layer under high vacuum using a Covap thermal evaporation system (Angstrom Engineering). This was followed by the evaporation of the Al electrode (80 nm) using a shadow mask, defining the active area to 0.1 cm².

Devices were measured using an Oriel Solar simulator fitted with a 150 W Xeon lamp (Newport), filtered to give an output of 100 mW cm⁻² at AM 1.5 (air mass) standard and calibrated using a silicon reference cell with NIST traceable certification. Device testing was conducted under ambient conditions. For investigating performance and material degradation, PET/ITO/ZnO NP/BHJ layer/MoO_x/Al & PET/ITO/ZnO NP/BHJ device configurations were used, respectively. Thermal annealing and aging were conducted on a hotplate in a nitrogen-filled glovebox with minimal light exposure.

6.3.3. Atomic Force Microscopy

Measurements were performed using a Bruker Multimode atomic force microscopy (AFM) in tapping mode, with the instrument measuring the height of the surface during scans. Surface measurements from the AFM were analysed with NanoScope Analysis 2.0.

6.3.4. Scanning Electron Microscopy

Measurements were performed using Inspect F50 scanning electron microscopy (<https://doi.org/10.25957/flinders.sem>) equipped with a field emission gun (FEI Company) and a secondary electron detector. The acceleration voltage was 10 kV, and the working distance of 10 mm. The samples were not coated with any conducting layers.

6.3.5. Charge Carrier Dynamics

Photo charge extraction by linearly increasing voltage (photo-CELIV), transient photovoltage (TPV) and time-resolved charge extraction (TRCE) were conducted using commercially available PAIOS 2 system (Fluxim AG). For carrier transport and recombination data, light pulse from a white LED (Cree, xp-g) was simultaneous with the application of either a linearly increasing voltage (photo-CELIV) or square-step voltage (TPV) to extract photogenerated charges. The current transients were recorded by the integrated PAIOS hardware.

6.3.6. Dynamic Mechanical Thermal Analysis

The dynamic mechanical thermal analysis (DMTA) was conducted on a DMA Q800 (TA Instruments) equipped with a liquid nitrogen cooling apparatus. The DMTA samples were prepared by repeatedly drop-casting the respective solutions on pre-cut glass mesh as described in previous literature [47, 48]. Sample preparation and instrument conditions can be found in *Appendix C*.

6.4. Results and discussion

6.4.1. Device performance Influence due to additives in the Bulk Heterojunction

From previously published work, it has been shown that the presence of solid additives can influence the morphological structure of the bulk heterojunction (BHJ), resulting in a change in performance conversion efficiency (PCE). As such, it was important to investigate how the addition of additives, specifically piperazine (PP), 4,4'-bipiperadine (BP) and polyacenaphthylene (PAN) had on the device performance of PPDT2FBT:PC₆₁BM. The initial device performance characteristics of devices each of these additives in the BHJ can be seen in *Table 6.1*. Performance results for the addition of neat C₇₀ were initially gathered from *Chapter 4*.

Table 6.1: Device performance based on PPDT2FBT:PC₆₁BM devices with and without solid additives. Additives include neat C₇₀, piperazine (PP), 4,4'-bipiperadine (BP), polyacenaphthylene (PAN). The results are from an average of 6 cells, with an active area of 0.1 cm².

Active layer material	Age (days)	J _{SC} (mA cm ⁻²)	V _{OC} (V)	FF	PCE (%)
PPDT2FBT:PC ₆₁ BM (1:2)	0	15.9 ± 0.6	0.78 ± 0.01	0.61 ± 0.01	7.63 ± 0.20
PPDT2FBT:PC ₆₁ BM:C ₇₀ (1:1.9:0.1)	0	15.9 ± 0.5	0.74 ± 0.01	0.61 ± 0.01	7.16 ± 0.24
PPDT2FBT:PC ₆₁ BM:PP (1:2:0.03)	0	17.0 ± 0.8	0.76 ± 0.01	0.58 ± 0.02	7.51 ± 0.13
PPDT2FBT:PC ₆₁ BM:BP (1:2:0.03)	0	15.8 ± 0.2	0.67 ± 0.01	0.49 ± 0.01	5.16 ± 0.09
PPDT2FBT:PC ₆₁ BM:BP (1:2:0.003)	0	17.8 ± 0.3	0.77 ± 0.01	0.59 ± 0.01	8.03 ± 0.10
	1	17.4 ± 0.1	0.77 ± 0.01	0.60 ± 0.01	7.95 ± 0.08
PPDT2FBT:PC ₆₁ BM: PAN (1:2:0.03)	0	17.9 ± 0.4	0.78 ± 0.01	0.62 ± 0.01	8.68 ± 0.17
	1	16.5 ± 0.5	0.78 ± 0.01	0.63 ± 0.01	8.11 ± 0.17

As discussed in the thesis work, it was observed that the addition of neat C₇₀ to the PPDT2FBT:PC₆₁BM blend had led to a decrease in V_{OC}. This decrease had been found to be related to be associated with the energy alignment between PPDT2FBT and C₇₀. When compared with the lowest unoccupied molecular orbital (LUMO) of PC₆₁BM, the LUMO for C₇₀ is significantly lower [39]. As the V_{OC} is strongly influenced by the energy difference between the highest occupied molecular orbital (HOMO) of the donor and the LUMO of the acceptor [49, 50], the decrease in the LUMO from the C₇₀ leads to a reduced energy gap with the PPDT2FBT HOMO, thus, reducing the V_{OC} of the device. As low amount of C₇₀ had been added, minimal impact to the performance, while the FF and J_{SC} remained constant.

For the addition of PP to the BHJ had minimal influence of the J_{SC} and V_{OC} , however, there was a slight reduction in the FF, resulting in the reduction in the PCE. As for BP, adding the same amount as the addition of PP, led to a reduction in both V_{OC} and FF, thus, a reduction of PCE. By reducing the additive amount of BP by a factor of ten, led to an improvement in J_{SC} , thus, improving the performance of the PCE. After one day of storage aging in a glovebox, the device performance remained the same. Lastly, the addition of PAN led to the improvement of the JSC, leading to a device performance that is comparable with PPDT2FBT:PC₇₁BM devices (as seen in *Chapter 5*). After one day of storage aging in a glovebox, the device performance dropped by 0.5%, due to the decrease in J_{SC} .

Overall, the addition of solid additive, either PP, BP, or PAN, could improve the device performance by increasing the J_{SC} . From the preliminary investigation with the addition of 1.0% w/w BP, adding too much of this additive resulted in a reduction in V_{OC} and FF, thus reducing PCE, yet 0.1% w/w addition led to a performance increase. In previous literature, it is suspected that additives such as PP [24] and insulating polymers [28] could improve J_{SC} due to improvement of charge-mobility.

6.4.2. Influence of solid additives over the Charge Carrier mobility

From *Section 6.4.1*, it appears the solid additives had a ranging influence over the atomic force microscopy (AFM) images (see *Figure D1* in *Appendix D*) of the surface of the BHJ, where there appears to be minimal impact to the surface morphology. This is an indication that the additives have an insignificant impact towards the morphology. This also explains how, though in some cases where additives improve performance, the fill-factor does not increase, as morphology can affect the fill-factor as it is dependent on exciton recombination.

Another explanation for the change in device performance could be explained by the influence of the carrier charge mobility and lifetime in the active layer. From previously published work, additives were able to influence the charge mobility, resulting in a significant change over the PCE, either by acting as a dopant [24], or filling in interspace between phases in the active layer [28]. Carrier charge mobility was determined with photo-CELIV (seen in *Figure 6.4*), while lifetime was determined with TPV and TRCE (seen in *Figure 6.5*).

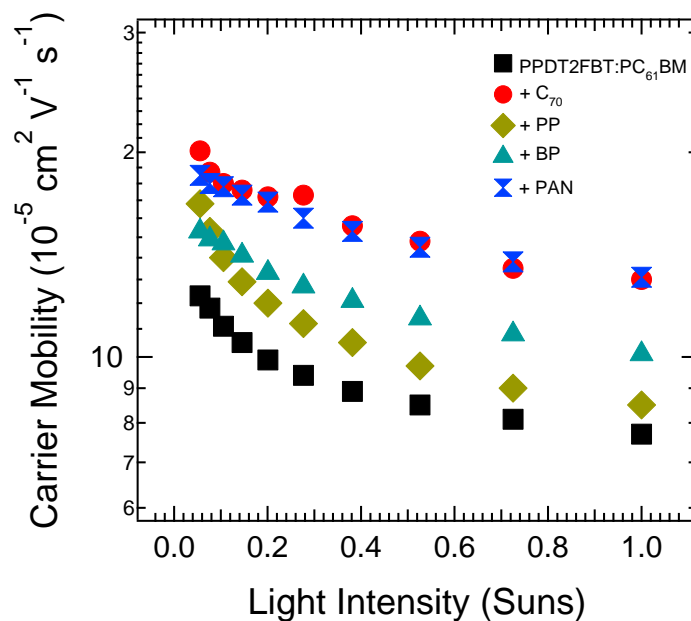


Figure 6.4: Charge carrier mobility in PPDT2FBT:PC₆₁BM devices as a function of light intensity, with the active layer either with or without various solid additives.

For the carrier mobility in relation to light intensity in *Figure 6.4*, there is a noticeable increase in charge carrier mobility for devices that contain solid additives in the active layer, compared to those that do not. The addition of C₇₀ and PAN appeared to have the most significant increase in charge carrier mobility, while PP and BP was observed to have a moderate increase in mobility.

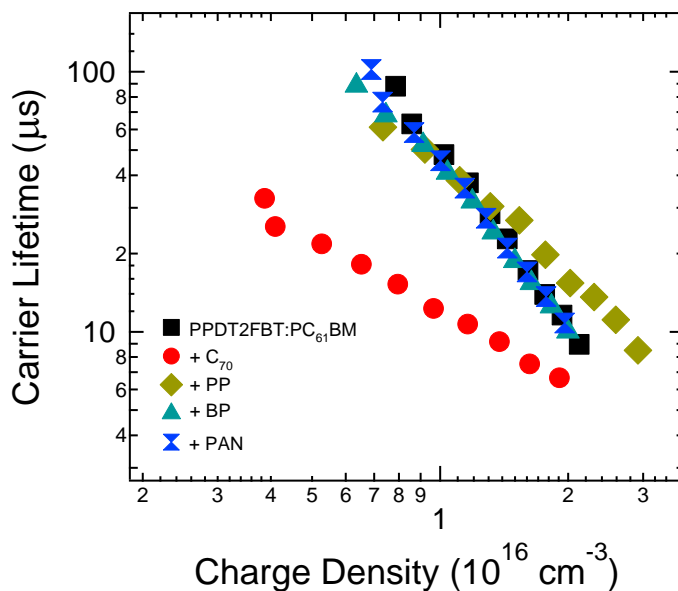


Figure 6.5: Carrier Lifetime of PPDT2FBT:PC₆₁BM devices as a function of charge Density, with the active layer either with or without various solid additives.

In terms of data relating carrier lifetime to charge density (seen in *Figure 6.5*), it was observed that for the addition of neat C₇₀, there was a significant decrease in carrier lifetime, whereas the addition of other additives appeared to have minimal impact on the lifetime.

Table 6.2: Charge carrier mobility, lifetime and PCE measurements of PPDT2FBT:PC₆₁BM based on BHJs either without or with solid additives.

Device	Mobility (10 ⁻⁵ cm ² V ⁻¹ s ⁻¹)	Lifetime	PCE (%)
PPDT2FBT:PC ₆₁ BM (1:2)	7.7 ± 0.3	2.29	7.63 ± 0.20
PPDT2FBT:PC ₆₁ BM:C ₇₀ (1:1.9:0.1)	13.0 ± 2.3	0.90	7.16 ± 0.24
PPDT2FBT:PC ₆₁ BM:PP (1:2:0.03)	8.5 ± 0.5	1.42	7.51 ± 0.13
PPDT2FBT:PC ₆₁ BM:BP (1:2:0.003)	10.1 ± 1.0	1.82	8.03 ± 0.10
PPDT2FBT:PC ₆₁ BM:PAN (1:2:0.03)	13.1 ± 1.2	2.05	8.68 ± 0.17

From the electrical analysis of the devices with and without solid additives, it is observed that the addition of either C₇₀, PP, BP or PAN were able to improve the charge carrier mobility, however, any decrease in photocharge lifetime appears to nullify these increases. This is evident with the addition of neat C₇₀, though significantly improving the charge carrier mobility, also saw a significant decrease in lifetime when compared with the standard BHJ. Other additive included have lower amounts of decrease in their lifetime, while having either slight increase in charge carrier mobility, in terms of PP addition, or moderate increase for the addition of BP to the active layer. As such the addition of PAN, the insulating polymer was able significantly increase the charge carrier mobility, without significantly decreasing exciton lifetime. This explains for the addition of PAN, which is suspected to have minimal impact on exciton formation was able to improve the PCE of the PPDT2FBT:PC₆₁BM OPV devices. In terms of charge mobility, there are several factors that can improve it for the active layer, including reduction of space between phases, improved material packing, and doping of fullerenes.

6.4.3. Thermal stability of PPDT2FBT:PC₆₁BM devices

From previously published work, it was found that PPDT2FBT:PC₆₁BM were fairly stable at 85 °C after two weeks of degradation, as only the linear degradation pattern had been observed [39]. As such, to observe a more significant degradation pathway, 120 °C was initial chosen as at this temperature, a significant burn-in can be observed prior to a linear degradation. Four systems that were investigated include PPDT2FBT:PC₆₁BM with either 1.0% w/w PP, 0.1% w/w BP, 1.0% w/w PAN, or without an additive added during the ink preparation stage. The aging of PPDT2FBT:PC₆₁BM with and without additives at 120 °C can be found in

Figure 6.6.

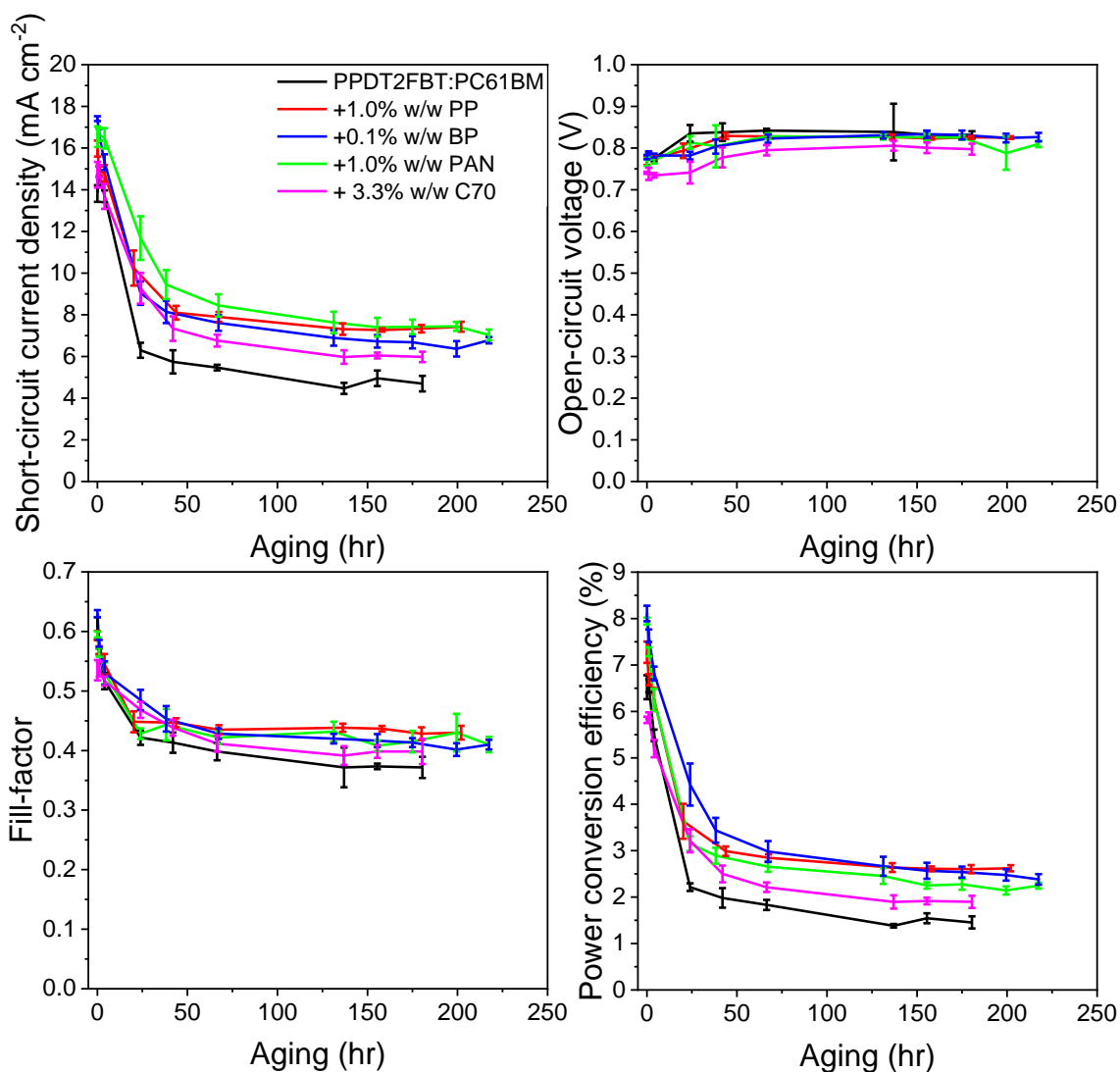


Figure 6.6: Device characteristics trends at 120 °C thermal aging under nitrogen. The results are from an average of 6 cells, with an active area of 0.1 cm².

It was found that when the devices were aged at 120 °C, there were several trends that were common, regardless of active layer composition. Firstly, there was a significant decrease in the J_{SC} and FF, which are suspected to be a result from the change in morphology in the BHJ, with the PC₆₁BM being likely to crystallise at this elevated temperature [51, 52]. This has also been confirmed in *Chapter 5*, with fullerene having grown and migrated to the surface of the BHJ. As for the V_{OC} , there had been observed a steady increase with the first 80 hours of aging, before remaining constant onwards to up to 200 hours. This observed increase was suspected to be likely due to the elimination of the energy disorder at the BHJ/ZnO interface, which has been observed by Sun *et al.* for BTID-2F:PC₇₁BM devices when stored under dark conditions [53].

For devices containing either PP, BP, or PAN as an additive, it was found that the magnitude of the “burn-in” degradation had reduced for both J_{SC} and V_{OC} resulting in a reduced impact on the “burn-in” behaviour for the PCE. Afterwards, all systems were observed to have a similar linear degradation behaviour, indicating that the additives were able to influence a degradation pathway that is present at the first 80 hours of 120 °C aging.

When comparing the systems with different additives, the BHJ which contained a small amount of PAN had a slightly slowly burn-in degradation rate for the J_{SC} and PCE, whereas those with either PP or BP had a very similar degradation pattern. It is likely that these three additives, though varying in molecular structure, may have a similar influence over the morphology of the BHJ, with PAN possibly having a slightly different physical behaviour when compared with PP or BP.

Before proceeding with investigating the influence the additives had over the thermal behaviour of PPDT2FBT:PC₆₁BM, it was critical to also investigate thermal aging at 85 °C. Firstly, to allow for realistic comparison of thermal degradation with previously published work, it has been agreed by the International Summit on OPV Stability (ISOS) consensus test community that 85 °C is classified as the high temperature for dark storage aging, otherwise known as the working temperature [54]. With this agreement, this temperature the most widely implemented temperatures for investigating thermal degradation of OPV devices [21, 22, 55-60]. Lastly, previous work in *Chapter 5* found that when comparing thermal degradation pathways for PPDT2FBT:PC₆₁BM, 120 °C aging resulted in the formation and migration of fullerene crystals, while at 85 °C resulted in 200 µm length features at the surface of the BHJ, which was found to have high concentrations of PC₆₁BM. This had led to the conclusion that the two aging temperatures had different dominate degradation pathways.

With these observations in mind, the next step was determined if the additives could reduce the degradation rate of the devices under working temperatures (85 °C) under dark, nitrogen conditions. The aging of PPDT2FBT:PC₆₁BM with and without additives at 85 °C can be in *Figure 6.7*.

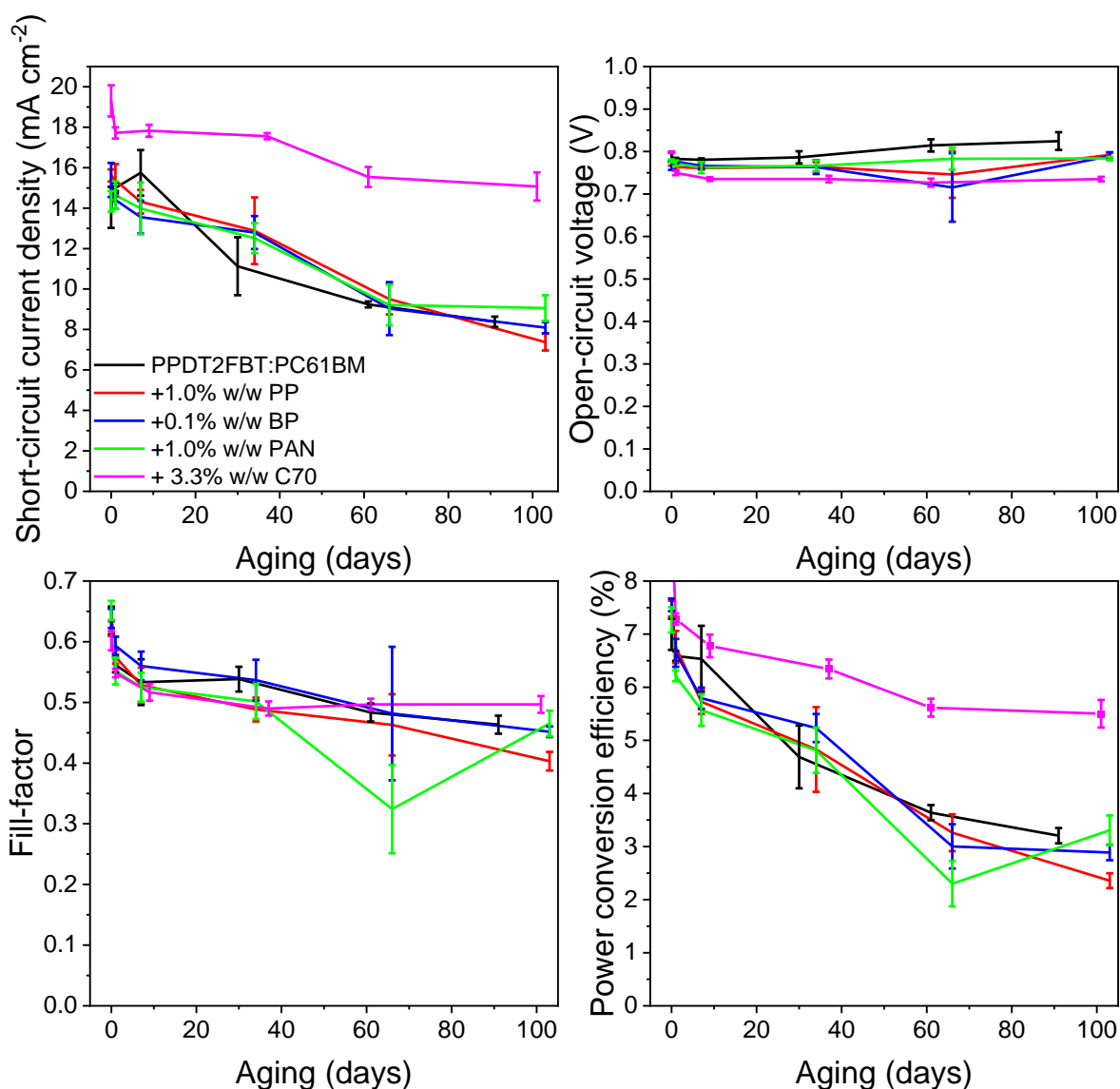


Figure 6.7: Device characteristics trends at 85 °C thermal aging under nitrogen. The results are from an average of 6 cells, with an active area of 0.1 cm².

Unlike what was observed for 120 °C aging (seen in

Figure 6.6), regardless of whether the BHJ contained additives or not, the degradation pattern at 85 °C appeared to be relatively similar. As the dominated degradation pathway for PPDT2FBT:PC₆₁BM is significantly different for 85 °C and 120 °C, it is suspected that the additives were only influencing one suspect of BHJ degradation, that being PC₆₁BM crystallisation.

6.4.4. Bulk heterojunction degradation investigation at 120 °C and 85 °C

To investigate the morphological changes of the BHJ containing PPDT2FBT:PC₆₁BM (with or without additives), half devices (PET/ITO/ZnO NPs/BHJ) were prepared and heated at either 120 °C or 85 °C under nitrogen conditions. Due to the difference in degradation rate for the two degradation temperatures, half-devices that were exposed to 120 °C annealing was aged for 24 hours, while half-devices under 85 °C annealing was aged for 1 month. After thermal aging, the

surface of the BHJ were characterised via scanning electron microscopy (SEM), with the resulting images found in *Figure 6.8*.

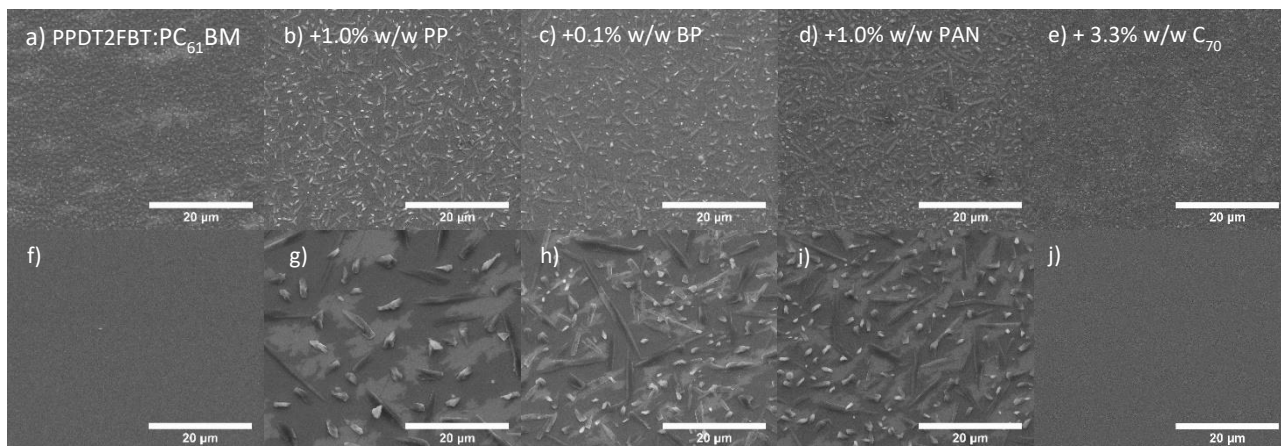


Figure 6.8: SEM images of PPDT2FBT:PC₆₁BM surface after annealing at either 120 °C for 24 hours (a-e) or 85 °C for 1 month (f-j). The active layer either contained no additives (a, f), 1.0% w/w PP (b, g), 0.1% w/w BP (c, h), 1.0% w/w PAN (d, i) or 3.3% w/w C₇₀.

For PPDT2FBT:PC₆₁BM aged at 120 °C for 24 hours, micro-crystals were observed to have grown and migrated to the surface, with previous work from *Chapter 4* supporting that these fullerene crystals. As for the half-device aged at 85 °C for 1 month, no noticeable features were observable, being too short of aging period for features to be observed as noted in *Chapter 5*.

For additive-containing BHJs after annealing at 120 °C, regardless of the additive, fullerene crystals had on the surface, however, size and population number was noticeably different. With additives present in the active layer, though the number of crystals present at the surface increased, the size of these crystals was significantly smaller. This meant that the growth rate of the fullerene crystals was likely being slowed by the addition of additives, while the increase in population meant that eventual size of said crystals would be limited due to space limitation of the BHJ.

As for additive-containing BHJs after annealing for 85 °C for 1 month, both 3-dimensional crystals and flat fullerene features had been observed at the surface of the active layer. This makes it significantly different to the aging of the BHJ without additives after 1 month, there were no noticeable features at the surface, flat fullerene features had been observed after 3 months of thermal aging at 85 °C. Secondly, the 3-dimensional crystals had only been observed at 120 °C annealing.

From initial SEM results, it had been observed that the addition of either PP, BP or PAN were able to influence the crystal growth rate and population of 3-dimensional fullerene crystals for 120 °C. Though, at 85 °C, it appears that the additives have lowered the temperature required for fullerene crystal growth, while speeding up the growth of flat fullerene features at the surface. When

observing the surface at a large magnification (seen in *Figure 6.9*), it appears that in some cases, the flat fullerene feature is on top of the fullerene crystal.

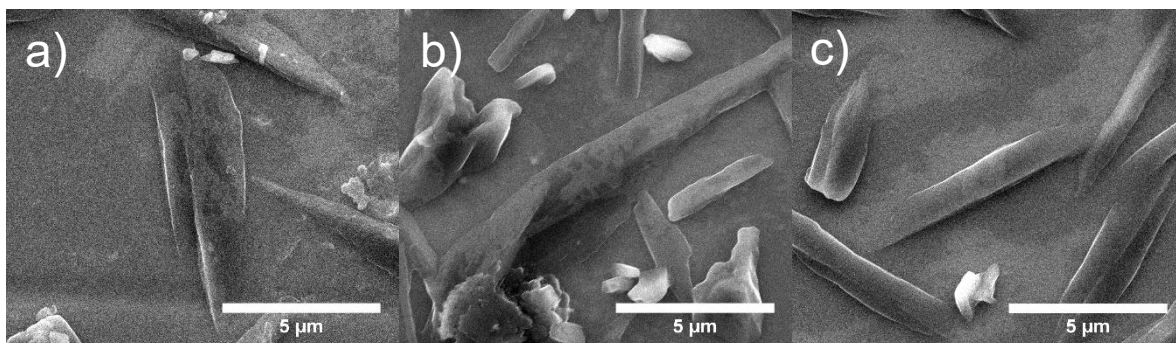


Figure 6.9: SEM images of PPDT2FBT:PC₆₁BM surface after annealing at 85 °C for 1 month. The active layer either contained (a) 1.0% w/w PP, (b) 0.1% w/w BP or (c) 1.0% w/w PAN.

From these observations, it is suspected that the flat fullerene features form at the top surface of the BHJ, resulting in a contrast in the SEM imaging. At the same time, the fullerene crystals likely grow within the BHJ, or near the surface. As the large crystals grow under the surface of the active layer, the surface is pulled up with it, resulting the flat feature (and some polymer) laying over the crystals.

6.4.5. Thermal Analysis

Dynamic mechanical thermal analysis (DMTA) is a technique that has been previously implemented for the understanding of thermal transitions and behaviour of both pristine materials, as well as blends, allowing for it to be a useful tool to characterise the morphology of BHJ layers [48, 61, 62]. In this work, this technique was used to investigate the impact different additives had on the thermal behaviour of the active layer blend. This method relies on the changes of the viscoelastic properties as the material is subjected to a constant increase in temperature.

To investigate these viscoelastic properties, an oscillating mechanical strain (i.e., tension) with known amplitude and frequency is applied, and the stress of the sample under oscillation is observed. This allows for values of storage modulus (E'), Loss modulus (E'') and Tan delta ($=E'/E''$), where E' reflects the stiffness of the sample, E'' peaks features suggest thermal transitions, while traditionally, tan delta defines the temperature of these transitions.

In previous work, DMTA was demonstrated to show how the addition of C₇₀ was able to influence the thermal properties of PPDT2FBT:PC₆₁BM, resulting in the fullerene crystallisation to occur at a higher temperature [39]. In this work, the purpose of the DMTA measurements was to observe how the thermal transitions were influenced by different additives (*Figure 6.10*), as well as how the additives impacted the changes in thermal behaviour.

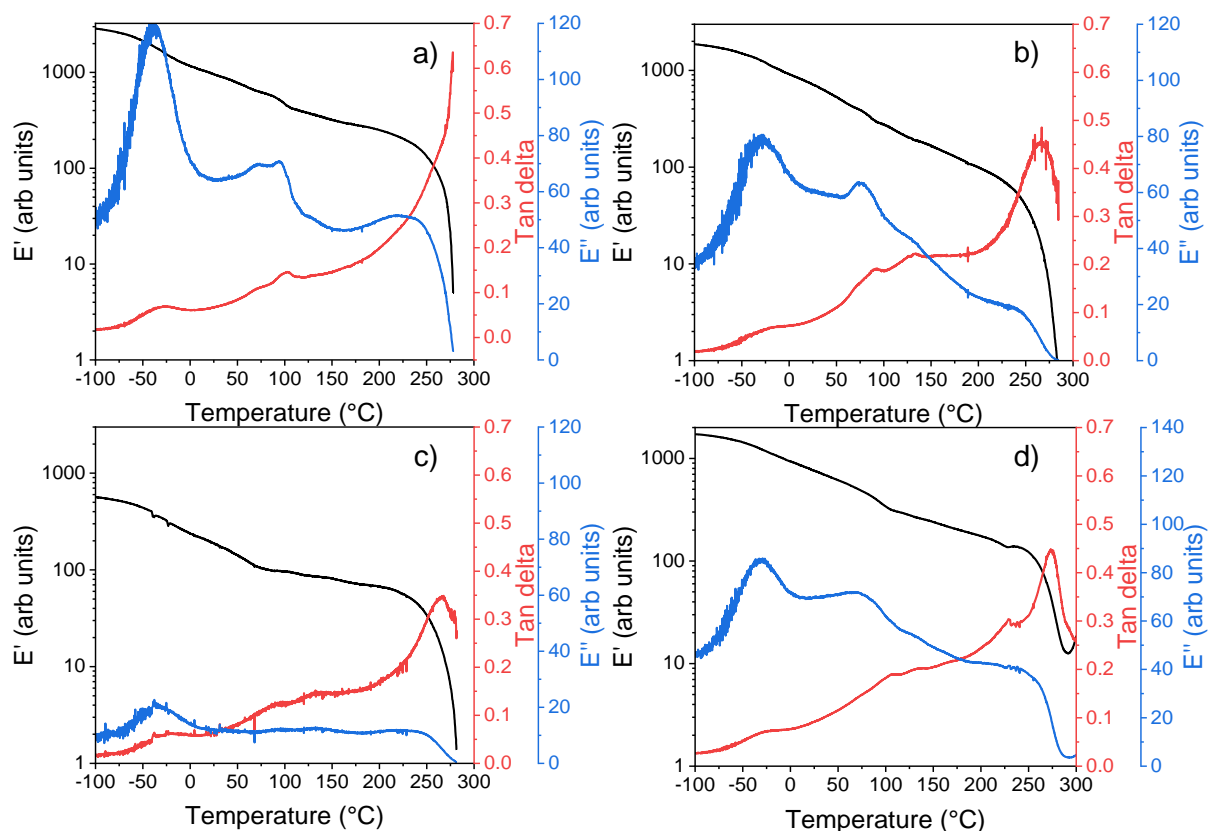


Figure 6.10: DMTA plots of PPDT2FBT:PC₆₁BM, either (a) without additive, with (b) 1.0% w/w PP, (c) 0.1% w/w BP, or (d) 1.0% w/w PAN. All samples were pre-annealed at 40 °C for 30 minutes prior to measurements.

For the PPDT2FBT:PC₆₁BM blend (*Figure 6.10a*), there is a sub-glassing transition (sub- T_g) observed at approximately -25 °C (having been determined from the tan delta peak), with the sub- T_g determined to be related to the polymer. This was based on previous work on the DMTA measurements performed on pure PPDT2DFBT [39]. There was also an extra thermal relaxation feature at ~100 °C, seen by the E'' peak, as well as a thermal transition without significant E' change at ~70 °C.

With the addition of PP (*Figure 6.10b*) or BP (*Figure 6.10c*) to the active material blend, the ~70 °C thermal transition appeared to disappear, while the ~100 °C thermal relaxation feature reduced in temperature to ~90 °C. In *Chapter 5*, it was suspected this thermal relaxation feature was associated with the cold crystallisation of PC₆₁BM, as upon annealing PPDT2FBT:PC₆₁BM blends at 85 °C after at least 30 minutes. In this case, it appears the addition of either PP or BP to the active layer blend had reduced the thermal energy required for PC₆₁BM crystallisation to occur. This could explain why for 85 °C aging, fullerene crystals were observed at the surface of the BHJ.

As for the blend with the addition of PAN (*Figure 6.10d*), the thermal relation feature appears to at the same temperature of ~100 °C, yet, where similar to the addition of PP and BP, the thermal transition at ~70 °C had disappeared. Despite the similarity in thermal degradation behaviour as the other additives, it appears that the PAN additive has a different interaction with the PPDT2FBT:PC₆₁BM.

For a more in-depth analysis of the thermal behaviour of the different systems (with or without PAN), the samples were annealed at either 85 °C or 120 °C prior to DMTA measurements (seen in Figure 6.11).

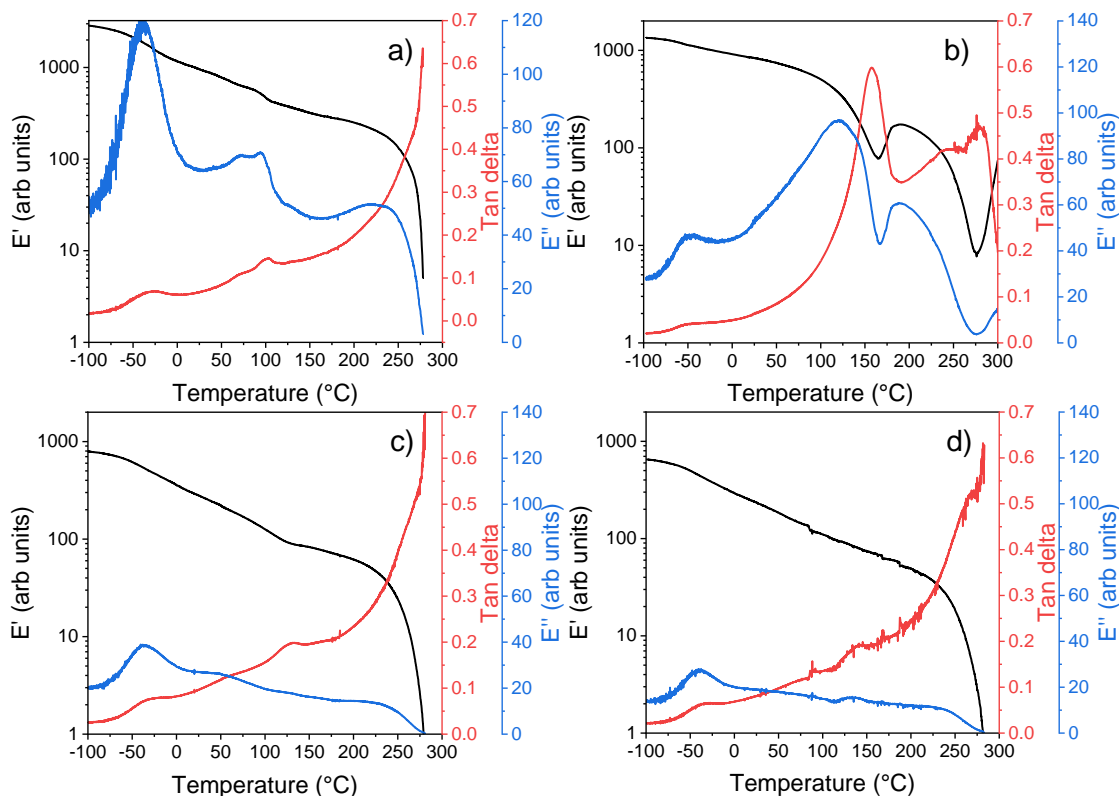


Figure 6.11: DMTA plots of PPDT2FBT:PC₆₁BM + 1.0% w/w PAN, which the blends having been pre-annealed at either (a) 40 °C for 30 minutes, (b) 120 °C for 30 minutes, (c) 85 °C for 30 minutes or (d) 24 hours. Pre-annealing was performed prior to measurements.

When the PPDT2FBT:PC₆₁BM + 1.0% w/w PAN blend was annealed at 120 °C for 30 minutes, the thermal relaxation feature shifted from ~100 °C to ~155 °C, while a E' increase at ~160 °C after a clear drop, indicating thermal relaxation followed by cold crystallisation. This feature has been observed previously in *Chapter 5* for PPDT2FBT:PC₆₁BM that had been annealed at 85 °C for 1 week, with the observation being determined to be likely to formation for purer PC₆₁BM and polymer phases at the lower annealing temperature, which then allowed for a substantial of crystallisation to be detected from the DMTA. The feature had also been observed for PPDT2FBT:PC₆₁BM:C₇₀ when annealed at 120 °C for 24 hours, where it was determined that the addition of the neat fullerene to the blend reduced the PC₆₁BM crystal growth rate [39]. Based on these observations, it is suspected that, similar with the addition of neat C₇₀, the addition of PAN to PPDT2FBT:PC₆₁BM restricted the growth rate of the fullerene crystals, allowing for the cold crystallisation to be significantly distinguishable once the DMTA reached the higher temperature.

Whereas for pre-annealing of the blend at 85 °C for 30 minutes, the thermal relaxation feature shifted from ~100 °C to ~130 °C. After annealing for 24 hours, the thermal relaxation feature disappears from the DMTA measurements.

With collaboration with the SEM, with the crystals appearing at the surface of the BHJ, it is suspected that annealing of the blend led to small crystallisation to already form, meaning that any small amount of non-crystallised fullerene phase was not significant enough to be detectable by the DMA. From the DMTA measurements, it is clear that the addition of PP, BP and PAN could alter the thermal behaviour of PPDT2FBT:PC₆₁BM blends, with PP and BP have similar behaviour altering properties. The DMTA measurements were also able to show how the additives were both able to reduce the crystal growth rate at 120 °C while allowing for fullerene crystals to easily grow at 85 °C.

6.5. Conclusion

The work in this chapter has shown how thermal degradation at two annealing temperatures, 85 °C and 120 °C, were influenced with the addition of neat fullerenes, specifically neat C₇₀, piperazine (PP), 4,4'-bipieradine (BP), and polyacenaphthylene (PAN). Though PP, BP and PAN were able to improve thermal stability of PPDT2FBT:PC₆₁BM devices at 120 °C, only the addition of C₇₀ was able to reduce thermal degradation at both 120 °C and 85 °C.

When investigating the thermal behaviour with scanning electron microscopy and dynamic thermal analysis, it was found that the addition of either PP, BP or PAN were able to reduce the rate of crystallisation, however, they allow for fullerene crystallisation to occur at lower temperatures, as well as accelerate the growth of flat fullerene features at the surface of the active layer. Whereas the addition of C₇₀ was able to reduce the rate and population of fullerene crystallisation growth, as well as slow down the formation of flat fullerene features.

In short, the work has demonstrated the importance of verifying the degradation studies at accepted annealing temperature, even through the active layer materials, blends and the use of additives were able to improve stability at higher aging temperatures. This is due to the uncertainty that such blends and conditions would allow for improved stability at lower temperatures.

6.6. References

1. Zhu, L., Zhang, M., Xu, J., Li, C., Yan, J., Zhou, G., Zhong, W., Hao, T., Song, J., Xue, X., Zhou, Z., Zeng, R., Zhu, H., Chen, C.-C., MacKenzie, R. C. I., Zou, Y., Nelson, J., Zhang, Y., Sun, Y., and Liu, F., Single-junction organic solar cells with over 19% efficiency enabled by a refined double-fibril network morphology. *Nature Materials*, **2022**. 21 (6), 656-663.
2. Ding, G., Chen, T., Wang, M., Xia, X., He, C., Zheng, X., Li, Y., Zhou, D., Lu, X., Zuo, L., Xu, Z., and Chen, H., Solid Additive-Assisted Layer-by-Layer Processing for 19% Efficiency Binary Organic Solar Cells. *Nano-Micro Letters*, **2023**. 15 (1), 92.
3. Cui, Y., Hong, L., and Hou, J., Organic photovoltaic cells for indoor applications: opportunities and challenges. *ACS applied materials & interfaces*, **2020**. 12 (35), 38815-38828.
4. Ylikunnari, M., Välimäki, M., Väisänen, K.-L., Kraft, T. M., Sliz, R., Corso, G., Po, R., Barbieri, R., Carbonera, C., Gorni, G., and Vilkmann, M., Flexible OPV modules for highly efficient indoor applications. *Flexible and Printed Electronics*, **2020**. 5 (1), 014008.
5. Yang, S. S., Hsieh, Z. C., Keshtov, M. L., Sharma, G. D., and Chen, F. C., Toward High-Performance Polymer Photovoltaic Devices for Low-Power Indoor Applications. *Solar RRL*, **2017**. 1 (12), 1700174.
6. Zhang, Z., Miao, J., Ding, Z., Kan, B., Lin, B., Wan, X., Ma, W., Chen, Y., Long, X., Dou, C., Zhang, J., Liu, J., and Wang, L., Efficient and thermally stable organic solar cells based on small molecule donor and polymer acceptor. *Nature Communications*, **2019**. 10 (1), 3271.
7. Zheng, N., Mahmood, K., Zhong, W., Liu, F., Zhu, P., Wang, Z., Xie, B., Chen, Z., Zhang, K., Ying, L., Huang, F., and Cao, Y., Improving the efficiency and stability of non-fullerene polymer solar cells by using N2200 as the Additive. *Nano Energy*, **2019**. 58, 724-731.
8. Meitzner, R., Faber, T., Alam, S., Amand, A., Roesch, R., Büttner, M., Herrmann-Westendorf, F., Presselt, M., Ciamparuchi, L., and Visoly-Fisher, I., Impact of P3HT materials properties and layer architecture on OPV device stability. *Solar Energy Materials and Solar Cells*, **2019**. 202, 110151.
9. Li, M., Zhang, W., Wang, H., Chen, L., Zheng, C., and Chen, R., Effect of organic cathode interfacial layers on efficiency and stability improvement of polymer solar cells. *RSC advances*, **2017**. 7 (50), 31158-31163.
10. Weng, C.-N., Yang, H.-C., Tsai, C.-Y., Chen, S.-H., Chen, Y.-S., Chen, C.-H., Huang, K.-M., Meng, H.-F., Chao, Y.-C., and Chang, C.-Y., The influence of UV filter and Al/Ag moisture barrier layer on the outdoor stability of polymer solar cells. *Solar Energy*, **2020**. 199, 308-316.
11. Doumon, N. Y., Wang, G., Chiechi, R. C., and Koster, L. J. A., Relating polymer chemical structure to the stability of polymer: fullerene solar cells. *Journal of Materials Chemistry C*, **2017**. 5 (26), 6611-6619.
12. Muhsin, B., Roesch, R., Gobsch, G., and Hoppe, H., Flexible ITO-free polymer solar cells based on highly conductive PEDOT:PSS and a printed silver grid. *Solar Energy Materials and Solar Cells*, **2014**. 130, 551-554.
13. Zimmermann, B., Schleiermacher, H.-F., Niggemann, M., Würfel, U., and Cells, S., ITO-free flexible inverted organic solar cell modules with high fill factor prepared by slot die coating. *Solar Energy Materials and Solar Cells*, **2011**. 95 (7), 1587-1589.
14. Sun, Y., Meng, L., Wan, X., Guo, Z., Ke, X., Sun, Z., Zhao, K., Zhang, H., Li, C., and Chen, Y., Flexible High-Performance and Solution-Processed Organic Photovoltaics with Robust Mechanical Stability. *Advanced Functional Materials*, **2021**. 31 (16), 2010000.
15. Kang, H., Kim, G., Kim, J., Kwon, S., Kim, H., and Lee, K., Bulk-heterojunction organic solar cells: Five core technologies for their commercialization. *Advanced Materials*, **2016**. 28 (36), 7821-7861.
16. Greenbank, W., Djeddaoui, N., Destouesse, E., Lamminaho, J., Prete, M., Boukezzi, L., Ebel, T., Bessissa, L., Rubahn, H.-G., Turkovic, V., and Madsen, M., Degradation Behavior of Scalable Nonfullerene Organic Solar Cells Assessed by Outdoor and Indoor ISOS Stability Protocols. *Energy Technology*, **2020**. 8 (12), 2000295.
17. Duan, L. and Uddin, A., Progress in Stability of Organic Solar Cells. *Advanced Science*, **2020**. 7 (11), 1903259.

18. Paci, B., Generosi, A., Rossi Albertini, V., Perfetti, P., de Bettignies, R., Leroy, J., Firon, M., and Senten, C., Controlling photoinduced degradation in plastic photovoltaic cells: A time-resolved energy dispersive x-ray reflectometry study. *Applied physics letters*, **2006**. 89 (4), 043507.
19. Andreasen, J. W., Gevorgyan, S. A., Schlepütz, C. M., and Krebs, F. C., Applicability of X-ray reflectometry to studies of polymer solar cell degradation. *Solar energy materials and solar cells*, **2008**. 92 (7), 793-798.
20. Greenbank, W., Rolston, N., Destouesse, E., Wantz, G., Hirsch, L., Dauskardt, R., and Chambon, S., Improved mechanical adhesion and electronic stability of organic solar cells with thermal ageing: the role of diffusion at the hole extraction interface. *Journal of Materials Chemistry A*, **2017**. 5 (6), 2911-2919.
21. Sung, Y. M., Huang, Y. C., Chien, F. S. S., and Tsao, C. S., Mechanism and Analysis of Thermal Burn-In Degradation of OPVs Induced by Evaporated HTL. *IEEE Journal of Photovoltaics*, **2019**. 9 (3), 694-699.
22. Greenbank, W., Hirsch, L., Wantz, G., and Chambon, S., Interfacial thermal degradation in inverted organic solar cells. *Applied Physics Letters*, **2015**. 107 (26), 263301.
23. Yan, L., Yi, J., Chen, Q., Dou, J., Yang, Y., Liu, X., Chen, L., and Ma, C.-Q., External load-dependent degradation of P3HT:PC61BM solar cells: behavior, mechanism, and method of suppression. *Journal of Materials Chemistry A*, **2017**. 5 (20), 10010-10020.
24. Yan, L., Wang, Y., Wei, J., Ji, G., Gu, H., Li, Z., Zhang, J., Luo, Q., Wang, Z., Liu, X., Xu, B., Wei, Z., and Ma, C.-Q., Simultaneous performance and stability improvement of polymer:fullerene solar cells by doping with piperazine. *Journal of Materials Chemistry A*, **2019**. 7 (12), 7099-7108.
25. Zhang, C., Heumueller, T., Leon, S., Gruber, W., Burlafinger, K., Tang, X., Perea, J. D., Wabra, I., Hirsch, A., Unruh, T., Li, N., and Brabec, C. J., A top-down strategy identifying molecular phase stabilizers to overcome microstructure instabilities in organic solar cells. *Energy & Environmental Science*, **2019**. 12 (3), 1078-1087.
26. Yan, L., Gu, H., Li, Z., Zhang, J., Yang, Y., Wang, H., Liu, X., Wei, Z., Luo, Q., and Ma, C.-Q., The interfacial degradation mechanism of polymer:fullerene bis-adduct solar cells and their stability improvement. *Materials Advances*, **2020**. 1 (5), 1307-1317.
27. Li, Y., Zhang, J., Xiang, J., Hu, H., Zhong, H., and Shi, Y., A Novel 4,4'-Bipiperidine-Based Organic Salt for Efficient and Stable 2D-3D Perovskite Solar Cells. *ACS Applied Materials & Interfaces*, **2022**. 14 (19), 22324-22331.
28. Wang, M., Liu, S., You, P., Wang, N., Tang, G., Miao, Q., and Yan, F., Insulating Polymers for Enhancing the Efficiency of Nonfullerene Organic Solar Cells. *Solar RRL*, **2020**. 4 (6), 2000013.
29. Brand, V., Bruner, C., and Dauskardt, R. H., Cohesion and device reliability in organic bulk heterojunction photovoltaic cells. *Solar Energy Materials and Solar Cells*, **2012**. 99, 182-189.
30. Yu, R., Wu, G., and Tan, Z. a., Realization of high performance for PM6:Y6 based organic photovoltaic cells. *Journal of Energy Chemistry*, **2021**. 61, 29-46.
31. Botkin, J. H., Cotter, R. J., Matzner, M., and Kwiatkowski, G. T., POLY(ARYL ETHER KETONE) BLOCK AND CHAIN-EXTENDED COPOLYMERS .3. PREPARATION AND CHARACTERIZATION OF POLY(ETHER KETONE KETONE) POLY(ETHER SULFONE) BLOCK COPOLYMERS. *MACROMOLECULES*, **1993**. 26 (9), 2372-2376.
32. Han, J., Bao, F., Wang, X., Huang, D., Yang, R., Yang, C., Jian, X., Wang, J., Bao, X., and Chu, J., Identifying tunneling effects of poly (aryl ether) matrices and boosting the efficiency, stability, and stretchability of organic solar cells. *Cell Reports Physical Science*, **2021**. 2 (5), 100408.
33. Han, J., Bao, F., Huang, D., Wang, X., Yang, C., Yang, R., Jian, X., Wang, J., Bao, X., and Chu, J., A universal method to enhance flexibility and stability of organic solar cells by constructing insulating matrices in active layers. *Advanced Functional Materials*, **2020**. 30 (38), 2003654.
34. Han, J., Xu, H., Paleti, S. H. K., Wen, Y., Wang, J., Wu, Y., Bao, F., Yang, C., Li, X., Jian, X., Wang, J., Karuthedath, S., Gorenflot, J., Laquai, F., Baran, D., and Bao, X., Vertical Stratification Engineering of Insulating Poly(aryl ether)s Enables 18.6% Organic Solar Cells with Improved Stability. *ACS Energy Letters*, **2022**. 7 (9), 2927-2936.

35. Chen, F., Zhang, Y., Wang, Q., Gao, M., Kirby, N., Peng, Z., Deng, Y., Li, M., and Ye, L., High Tg Polymer Insulator Yields Organic Photovoltaic Blends with Superior Thermal Stability at 150 oC. *Chinese Journal of Chemistry*, **2021**. 39 (9), 2570-2578.
36. Lindqvist, C., Sanz-Velasco, A., Wang, E., Bäcke, O., Gustafsson, S., Olsson, E., Andersson, M. R., and Müller, C., Nucleation-limited fullerene crystallisation in a polymer–fullerene bulk-heterojunction blend. *Journal of Materials Chemistry A*, **2013**. 1 (24), 7174-7180.
37. Lindqvist, C., Stability of Bulk-heterojunction Blends for Solar Cell Applications. 2014: Chalmers University of Technology.
38. Lindqvist, C., Bergqvist, J., Feng, C. C., Gustafsson, S., Bäcke, O., Treat, N. D., Bounioux, C., Henriksson, P., Kroon, R., Wang, E., Sanz-Velasco, A., Kristiansen, P. M., Stingelin, N., Olsson, E., Inganäs, O., Andersson, M. R., and Müller, C., Fullerene nucleating agents: a route towards thermally stable photovoltaic blends. *Advanced Energy Materials*, **2014**. 4 (9), 1301437.
39. Kirk, B., Pan, X., Jevric, M., Andersson, G., and Andersson, M. R., Introducing neat fullerenes to improve the thermal stability of slot-die coated organic solar cells. *Materials Advances*, **2022**.
40. Nguyen, T. L., Choi, H., Ko, S. J., Uddin, M. A., Walker, B., Yum, S., Jeong, J. E., Yun, M. H., Shin, T. J., and Hwang, S., Semi-crystalline photovoltaic polymers with efficiency exceeding 9% in a ~ 300 nm thick conventional single-cell device. *Energy & Environmental Science*, **2014**. 7 (9), 3040-3051.
41. Du, Z., Mainville, M., Vollbrecht, J., Dixon, A. L., Schopp, N., Schrock, M., Peng, Z., Huang, J., Chae, S., Ade, H., Leclerc, M., Reddy, G. N. M., and Nguyen, T.-Q., Insights into Bulk-Heterojunction Organic Solar Cells Processed from Green Solvent. *Solar RRL*, **2021**. 5 (8), 2100213.
42. Song, S., Lee, K. T., Koh, C. W., Shin, H., Gao, M., Woo, H. Y., Vak, D., and Kim, J. Y., Hot slot die coating for additive-free fabrication of high performance roll-to-roll processed polymer solar cells. *Energy & Environmental Science*, **2018**. 11 (11), 3248-3255.
43. Dayneko, S. V., Pahlevani, M., and Welch, G. C., Indoor Photovoltaics: Photoactive Material Selection, Greener Ink Formulations, and Slot-Die Coated Active Layers. *ACS Applied Materials & Interfaces*, **2019**. 11 (49), 46017-46025.
44. Mainville, M., Tremblay, V., Fenniri, M. Z., Laventure, A., Farahat, M. E., Ambrose, R., Welch, G. C., Hill, I. G., and Leclerc, M., Water Compatible Direct (Hetero)arylation Polymerization of PPDT2FBT: A Pathway Towards Large-Scale Production of Organic Solar Cells. *Asian Journal of Organic Chemistry*, **2020**. 9 (9), 1318-1325.
45. Morin, P.-O., Bura, T., Sun, B., Gorelsky, S. I., Li, Y., and Leclerc, M., Conjugated polymers à la carte from time-controlled direct (hetero) arylation polymerization. *ACS Macro Letters*, **2015**. 4 (1), 21-24.
46. Krebs, F. C., Air stable polymer photovoltaics based on a process free from vacuum steps and fullerenes. *Solar Energy Materials and Solar Cells*, **2008**. 92 (7), 715-726.
47. Sharma, A., Pan, X., Campbell, J. A., Andersson, M. R., and Lewis, D. A., Unravelling the thermomechanical properties of bulk heterojunction blends in polymer solar cells. *Macromolecules*, **2017**. 50 (8), 3347-3354.
48. Sharma, A., Pan, X., Bjuggren, J. M., Gedefaw, D., Xu, X., Kroon, R., Wang, E., Campbell, J. A., Lewis, D. A., and Andersson, M. R., Probing the relationship between molecular structures, thermal transitions, and morphology in polymer semiconductors using a woven glass-mesh-based DMTA technique. *Chemistry of Materials*, **2019**. 31 (17), 6740-6749.
49. Mühlbacher, D., Scharber, M., Morana, M., Zhu, Z., Waller, D., Gaudiana, R., and Brabec, C., High photovoltaic performance of a low-bandgap polymer. *Advanced Materials*, **2006**. 18 (21), 2884-2889.
50. Brabec, C. J., Sariciftci, N. S., and Hummelen, J. C., Plastic solar cells. *Advanced functional materials*, **2001**. 11 (1), 15-26.
51. Zhao, J., Swinnen, A., Van Assche, G., Manca, J., Vanderzande, D., and Mele, B. V., Phase diagram of P3HT/PCBM blends and its implication for the stability of morphology. *The Journal of Physical Chemistry B*, **2009**. 113 (6), 1587-1591.
52. Bertho, S., Janssen, G., Cleij, T. J., Conings, B., Moons, W., Gadisa, A., D'Haen, J., Goovaerts, E., Lutsen, L., and Manca, J., Effect of temperature on the morphological and

- photovoltaic stability of bulk heterojunction polymer: fullerene solar cells. *Solar Energy Materials and Solar Cells*, **2008**. 92 (7), 753-760.
53. Sun, R., Deng, D., Guo, J., Wu, Q., Guo, J., Shi, M., Shi, K., Wang, T., Xue, L., and Wei, Z., Spontaneous open-circuit voltage gain of fully fabricated organic solar cells caused by elimination of interfacial energy disorder. *Energy & Environmental Science*, **2019**. 12 (8), 2518-2528.
 54. Reese, M. O., Gevorgyan, S. A., Jørgensen, M., Bundgaard, E., Kurtz, S. R., Ginley, D. S., Olson, D. C., Lloyd, M. T., Morvillo, P., Katz, E. A., Elschner, A., Haillant, O., Currier, T. R., Shrotriya, V., Hermenau, M., Riede, M., R. Kirov, K., Trimmel, G., Rath, T., Inganäs, O., Zhang, F., Andersson, M., Tvingstedt, K., Lira-Cantu, M., Laird, D., McGuinness, C., Gowrisanker, S., Pannone, M., Xiao, M., Hauch, J., Steim, R., DeLongchamp, D. M., Rösch, R., Hoppe, H., Espinosa, N., Urbina, A., Yaman-Uzunoglu, G., Bonekamp, J.-B., van Breemen, A. J. J. M., Girotto, C., Voroshazi, E., and Krebs, F. C., Consensus stability testing protocols for organic photovoltaic materials and devices. *Solar Energy Materials and Solar Cells*, **2011**. 95 (5), 1253-1267.
 55. Park, S., Park, S. H., Jin, H., Yoon, S., Ahn, H., Shin, S., Kwak, K., Nah, S., Shin, E.-Y., Noh, J. H., Min, B. K., and Son, H. J., Important role of alloyed polymer acceptor for high efficiency and stable large-area organic photovoltaics. *Nano Energy*, **2022**. 98, 107187.
 56. Son, H. J., Park, H.-K., Moon, J. Y., Ju, B.-K., and Kim, S. H., Thermal degradation related to the PEDOT:PSS hole transport layer and back electrode of the flexible inverted organic photovoltaic module. *Sustainable Energy & Fuels*, **2020**. 4 (4), 1974-1983.
 57. Li, Z., Ho Chiu, K., Shahid Ashraf, R., Fearn, S., Dattani, R., Cheng Wong, H., Tan, C.-H., Wu, J., Cabral, J. T., and Durrant, J. R., Toward Improved Lifetimes of Organic Solar Cells under Thermal Stress: Substrate-Dependent Morphological Stability of PCDTBT:PCBM Films and Devices. *Scientific Reports*, **2015**. 5 (1), 15149.
 58. Bolognesi, M., Prosa, M., Tessarolo, M., Donati, G., Toffanin, S., Muccini, M., and Seri, M., Impact of environmentally friendly processing on polymer solar cells: Performance, thermal stability and morphological study by imaging techniques. *Solar Energy Materials and Solar Cells*, **2016**. 155, 436-445.
 59. Lee, H., Sohn, J., Tyagi, P., and Lee, C., Crystallinity dependent thermal degradation in organic solar cell. *Applied Physics Letters*, **2017**. 110 (5), 053301.
 60. Wang, Z., Nian, Y., Jiang, H., Pan, F., Hu, Z., Zhang, L., Cao, Y., and Chen, J., High Voc ternary nonfullerene polymer solar cells with improved efficiency and good thermal stability. *Organic Electronics*, **2019**. 69, 174-180.
 61. Yu, L., Qian, D., Marina, S., Nugroho, F. A. A., Sharma, A., Hultmark, S., Hofmann, A. I., Kroon, R., Benduhn, J., and Smilgies, D.-M., Diffusion-Limited Crystallization: A Rationale for the Thermal Stability of Non-Fullerene Solar Cells. *ACS applied materials & interfaces*, **2019**. 11 (24), 21766-21774.
 62. Pan, X., Sharma, A., Gedefaw, D., Kroon, R., de Zerio, A. D., Holmes, N. P., Kilcoyne, A. L. D., Barr, M. G., Fahy, A., and Marks, M., Environmentally friendly preparation of nanoparticles for organic photovoltaics. *Organic Electronics*, **2018**. 59, 432-440.

CHAPTER 7 – PRELIMINARY STUDY OF SCALABLE METHODS USED TO INFLUENCE THERMAL BEHAVIOUR OF OPVS

7.1. Overview

With the improvement of OPV performance over the years, there has been increased interest towards more applicational research, however, there is a significant gap between small-scale laboratory-based OPVs, and those fabricated using large-scale industry-based fabrication methods. To resolve this issue, there has been more focus on scalable OPV fabrication, allowing for coating and printing methods that can be upscaled, allowing for the cost-effective testing the scalability of methods for improving device performance and stability. From previous chapters, the major thermal degradation pathway for PPDT2FBT:PC₆₁BM devices that have been fabricated via slot-die coating have been extensively investigated, as well as methods for reducing the impact of said pathway of OPV lifespan. The purpose of this chapter was to investigate the scalability from the mini-roll coater (MRC) towards a roll-to-roll friendly fabrication method.

Initially, when transferring from an inverted OPV configuration to a conventional structure, it was found there was a significant decrease in performance, with a further decrease when increasing the active area from 0.1 cm² to 12.15 cm². Despite the performance decrease, the conventional PPDT2FBT:PC₆₁BM was able to achieve a power conversion efficiency up to 2.3%. As for stability, it was found that the conventional OPVs were less stable than the inverted devices, with the possible cause of the instability being associated with the degradation of the PEDOT:PSS and its interface with the electrode and active layer. When attempting to influence the thermal behaviour of the active layer by adding solid-additives to the blend, it appeared to worsen the effect of the degradation, yet eventually improve performance.

From this chapter, it was found that the fabrication method used by the MRC can allow for the fabrication of scalable OPVs, towards device configurations that are roll-to-roll processable. The chapter has also shown that methods though solid-additives can positively influence the thermal stability of the active layer, they can result in worsening of other degradation pathways associated with interfacial layers, such as PEDOT:PSS.

7.2. Introduction

With the push towards cost-effective, accessible, renewable energy sources, there has been an increased interest towards the research and development of organic photovoltaics (OPVs). Their potential is owed to their ability to be fabricated as thin, lightweight and flexible devices, while able to be made using roll-to-roll coating/printing methods that allow relatively low manufacturing cost, especially when compared to conventional silicon solar panels [1-3].

In the past decade, there has been significant improvements of device performance for OPV technology, with such advances leading power conversion efficiencies (PCEs), exceeding 18% for single junction devices [4-6]. As the performance gap between conventional silicon solar cells and OPVs becomes smaller, the interest towards the application of these devices has strengthened, leading to development of printing and coating conditions that can be upscaled towards an industry setting.

For the past two decades, there was an interest of the upscaled fabrication of OPV modules, with the main focus of using alternative deposition techniques, such as blade coating [7-9], flexography printing [10], gravure printing [11, 12], inkjet printing [13, 14], pad printing [15], rod coating [16], screen printing [17, 18], slot-die coating [19-25] and spray printing [26-30]. As the years went by, there was a shift from large area fabrication to small area, with the focus on reducing the performance gap between spin-coated and alternative printed/coated OPVs. Within the past few years, there has been a renewed interest towards scalable and large area cells and modules, with blade coated [31-34] and slot-die coated [33, 35-38] taking up the majority of the interest in the OPV.

Though this renewed interest towards scalable and large-scale OPV fabrication is a positive step towards applicational use of these devices, there are still a couple of areas that have not received as much attention as compared with device performance. These areas include fabrication cost and device stability, which are areas that are just as important yet have seen less research focus. For OPV devices to be competitive to other photovoltaic devices, including silicon-based solar cells, they need to improve cost-effectiveness, as well as expanding on the average lifespan [39]. In terms of stability, there are five major factors that can negatively impact the device performances during normal operation of OPVs; including thermal [40, 41], oxygen and moisture [42, 43], UV radiance [44, 45] and mechanical [22, 46, 47] degradation. These factors are responsible for two significant decay trends of PCE: burn-in and linear degradation [48-50].

In terms of thermal stability, continuous illumination from a light source can result in an increase of the working temperature, especially when operating in outdoor conditions with direct sun-exposure. As majority of OPVs contain a bulk-heterojunction structured active layer, there is a risk of the thermal energy would allow the movement of active materials, resulting in a change in morphology in the active layer, especially when the temperature exceeds any major thermal transitions of the materials contained in the active layer blend, such as glass-transition and cold-crystallisation [51, 52]. This elevated temperature may also lead to degradation via the material diffusion at the interface of electrodes and transport/extraction/interface layers [53-55].

With those that mention stability in their work, some papers have it as a secondary focus to the research [56-61], while others have stability as a primary focus [37, 53, 62, 63]. Some stability work conducted on OPV fabricated using alternative coating methods, Lee *et al.* having demonstrated the use of low cost-encapsulation for roll-to-roll fabrication for improving stability [37], while Moustafa *et al.* demonstrated for spray coated devices, modifying the ZnO film over the polymer:fullerene film had allowed for improved thermal stability at 85 °C [63]. Lastly, our work (*Chapter 4*) demonstrated how the addition of neat fullerenes into the PPDT2FBT:PC₆₁BM active layer was able to influence the thermal behaviour of the blend, leading to improve the thermal stability of slot-die coated devices [62].

In terms of the thesis work, it was demonstrated for slot-die coated devices prepared using the mini-roll coater (MRC), that the addition of solid-additives (both neat fullerene and non-fullerene) were able to significantly influence the thermal behaviour of the PPDT2FBT:PC₆₁BM blend, leading to changes of the influence of thermal degradation pathways. In the previous work, the active layer material blend that has been extensively investigated is Poly[(2,5-bis(2hexyldecyloxy)phenylene)-alt-(5,6-difluoro-4,7-di(thiophen-2-yl)benzo[c][1,2,5]thiadiazole)]:[6,6]-phenyl-C61-butyric acid ester (PPDT2FBT:PC₆₁BM) (structures seen in *Figure 7.1*), due to its ability to be used in scalable OPV fabrication, as well as initial stability thermal stability.

Achieving a moderate device performance of 9.39% [64] and 9.1% [65] when incorporating PC₇₁BM and PC₆₁BM in spin-coating, respectively, PPDT2FBT:PCBM has been demonstrated to effectively slot-die coated at a variety of scales with minimal performance loss [60, 62, 66, 67]. A handful of studies have been performed to investigate the stability of both slot-die and spin-coated PPDT2FBT:PC₆₁BM devices. For lower temperature degradation (60 °C), paired with constant illumination and no humidity control, Mainville *et al.* observed that the PPDT2FBT:PC₆₁BM devices lasted 220 hours (9 days) before degradation below 80% initial PCE [67].

Another donor polymer of interest that was investigated in this chapter was poly[2,3-bis-(3-octyloxyphenyl)quinoxaline-5,8-diyl-alt-thiophene-2,5-diyl] (TQ1), a easily synthesised D-A type, low band polymer [68]. So far, TQ1 has been demonstrate to achieve moderate performances when paired with either PC₆₁BM [68, 69], PC₇₁BM [69-71] and N2200 [72, 73], achieving a PCE of 4.9% [68], 7.08% [74], 3.15% [73], respectively. Previous literature has also demonstrated the ability of TQ1:fullerene devices to be fabricated using scalable platforms, such as on a mini-roll coater (MRC) [69, 75] and roll-to-roll (R2R) coater [75].

The major difference between TQ1 and PPDT2FBT polymer, is that TQ1 had been determined to be amorphous via DMTA [76]., while PPDT2FBT was been observed to be semi-crystalline. Though both materials blends contain PC₆₁BM, known to be a major source of morphology degradation due to fullerene crystallisation [62, 77, 78], it is possible that changing between donor polymers may influence the thermal behaviour between blends.

A third polymer that was investigated was poly[5,5'-bis(2-butyloctyl)-(2,2'-bithiophene)-4,4'-dicarboxylate-alt-5,5'-2,2'-bithiophene] (PDCBT) (structure seen in *Figure 7.1*), is a highly crystalline polymer that is relatively easy to synthesis. Though able to achieve moderate efficiencies when paired with PC₇₁BM, reaching 8.0% PCE, a higher efficiency of 11.1% was achieved with ITIC [79], making it a more ideal active layer blend compared to fullerene-based system. The ease of synthesis of the donor polymer, as well as relatively high efficiency makes PDCBT an ideal polymer for scalable and large OPV fabrication.

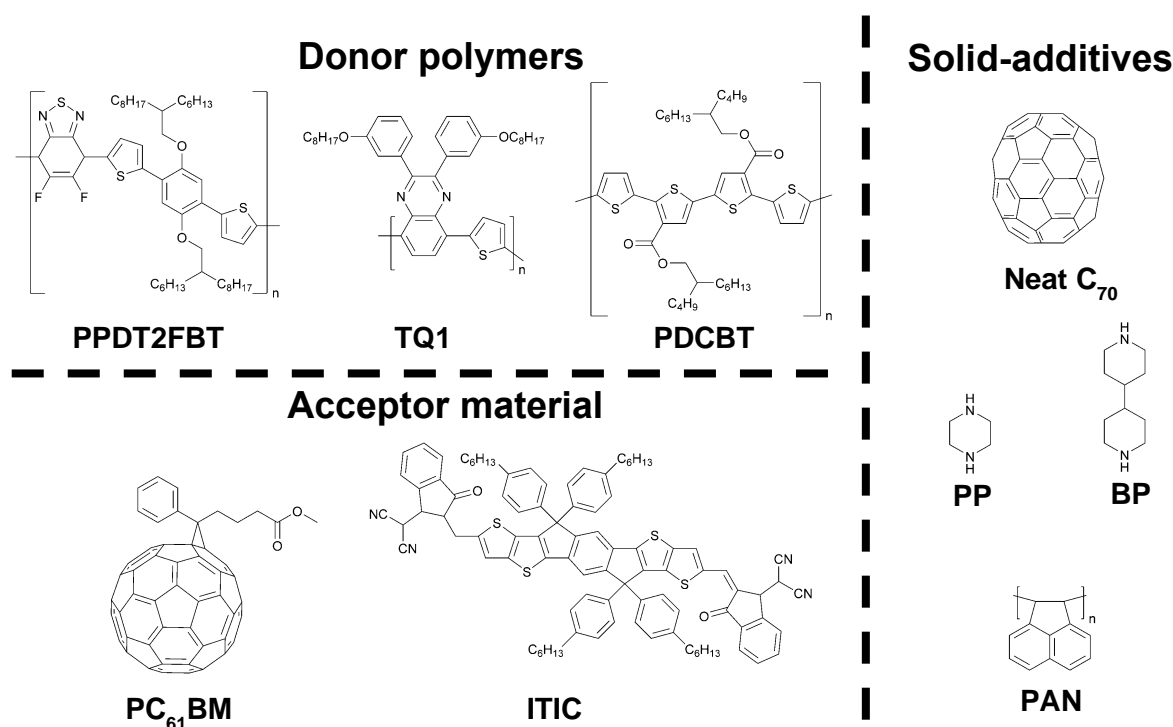


Figure 7.1: Molecular structure of active layer materials, donor polymers and acceptor materials, as well as solid additives investigated in this thesis.

The focus of this chapter is for the preliminary demonstration of the scalability of the research that had been conducted through this thesis. This was achieved by implementing a roll-to-roll friendly device structuring (seen in *Figure 7.2*), which is currently being used for upscaled OPV manufacturing. The chapter also aims to investigate the translatability of the thesis work by comparing the thermal stability and behaviour between three active layer blends; PPDT2FBT:PC₆₁BM, TQ1:PC₆₁BM and PDCBT:ITIC, as well as PPDT2FBT:PC₆₁BM with and with solid additives (structures seen in *Figure 7.1*).

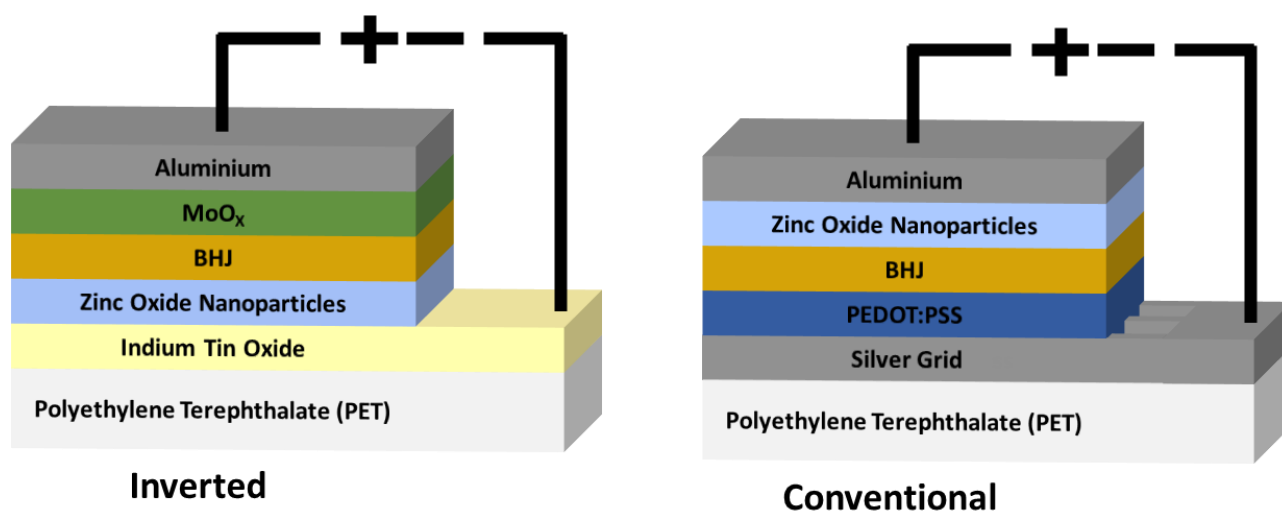


Figure 7.2: Schematic illustration of inverted (LEFT) and conventional (RIGHT) OPV structure used in this chapter.

7.3. Experimental section

7.3.1. Materials

Donor material poly[(2,5-bis(2hexyldecyloxy)phenylene)-alt-(5,6-difluoro-4,7-di(thiophen-2-yl)benzo[c][1,2,5]thiadiazole)] (PPDT2FBT) was synthesised using a direct arylation polymerisation according to literature [80]. The molecular weight of PPDT2FBT was determined via Gel Permeation Chromatography (Agilent 1260 Infinity II High-Temperature GPC System) using trichlorobenzene at 150 °C, giving a number average molecular weight (M_n) of 50 of kg/mol with a PDI of 2.60 relative to polystyrene standards.

Donor material poly[2,3-bis-(3-octyloxyphenyl)quinoxaline-5,8-diyl-alt-thiophene-2,5-diyl] (TQ1) was synthesised according to literature [68]. Detailed synthesis method can be found in *Appendix C*. The molecular weight of TQ1 was determined via Gel Permeation Chromatography using trichlorobenzene at 150 °C, giving a number average molecular weight (M_n) of 52.6 kg/mol with PDI of 3.29 relative to polystyrene standard.

Donor material p''''2,2''''-bis[[[(2-butyloctyl)oxy]carbon]']'2,':5''2''''',2''-quaterthiophen''-5,5''-diyl] (PDCBT) was synthesised following an unpublished procedure, based on the following published work [81-83]. The molecular weight of PDCBT was determined via Gel Permeation Chromatography using trichlorobenzene at 150 °C, giving a number average molecular weight (M_n) of 22.3 kg/mol with PDI of 7.13 relative to polystyrene standard.

Acceptor material 3,9-bis(2-methylene-(3-(1,1-dicyanomethylene)-indanone))-5,5,11,11-tetrakis(4-hexylphenyl)-dithieno[2,3-d':2',3'-d']-s-indaceno[1,2-b:5,6-b']dithiophene (ITIC) was synthesised following an unpublished procedure, based on the following published work [84-86].

PEDOT:PSS was prepared based on previously published procedure [87, 88], by mixing PH1000 (Ossila) (37.5% v/v), Milli-Q® water (37.5% v/v), Isopropanol (19.5% v/v), Dimethylsulfoxide (5.0% v/v) and Zonyl® FSO fluorosurfactant (0.5% v/v). The ink was sonicated with a sonication probe at 40% amplitude for 3 x 30s (30s rest between each burst) with a S&M: 630-0419 probe head. The ink was surrounded by an ice bath to keep the solution cold during sonication.

The ZnO NP dispersion was prepared following a previously published procedure [89]. To achieve an ideal processing concentration, acetone (Chem-supply, 99.9%) or ethanol (Chem-supply, 99.9%) was added to the NP precipitate until a concentration of approximately 40 mg mL⁻¹ was achieved. Afterwards, 2-(2-methoxyethoxy)acetic acid (Sigma Aldrich) (5% w/w in relation to ZnO NP) was then added to the dispersion to stabilise the NPs.

Small molecule fullerene acceptor [[6,6]-phenyl-C₆₁-butyric acid ester (PC₆₁BM) were purchased from Solenne BV. Solvents ortho-dichlorobenzene, chlorobenzene and 1-chloronaphthalene were purchased from Sigma Aldrich, whereas chloroform (CHCl₃) was purchased from Chem-Supply. All solvents were used directly without purification.

7.3.2. Inverted Device fabrication

Slot-die coated devices were fabricated in a PET/ITO/ZnO NP/BHJ layer/MoO_x/Al device configuration for BHJ layers of either PPDT2FBT:PC₆₁BM (1:2 w/w), TQ1:PC₆₁BM (1:2 w/w) or PDCBT:ITIC (1:1 w/w). PPDT2FBT:PC₆₁BM and TQ1:PC₆₁BM ink was prepared by dissolving materials, in ortho-dichlorobenzene (total 25 mg mL⁻¹) with 0.5% V/V of 1-chloronaphthalene at 60 °C overnight. PDCBT:ITIC was prepared by dissolving materials in chloroform (total 10 mg mL⁻¹) at 30 °C overnight.

The flexible ITO-covered Polyethylene terephthalate (PET) substrate (50 ohm/sq, Dongguan Hongdian Technology Co.) was attached to a mini-roll coater (FOM technologies) with slot-die attachment and wiped with isopropanol soaked TerriWipes at a rotation speed of 2 m min⁻¹ prior to fabrication. The tubing and slot-die head was cleaned with chloroform prior to assembly and between the change of deposition material. Layer deposition was processed under ambient conditions.

The ZnO NP layer (35 nm) was deposited using 0.1 mL min⁻¹ flow-rate, a drum speed of 1.0 m min⁻¹ and drum temperature at 70 °C to achieve a strip width of around 13 mm. The BHJ layer (150 – 200 nm) was deposited via varying flow rate and drum speed at a drum temperature at 70 °C to obtain a strip width of around 13 mm. Wet and dry thickness for both the ZnO NP and BHJ layers were calculated according to *Equation C1 & C2* in *Appendix C*.

After slot-die coating, the MoO_x and aluminium was deposited via the following method. The MoO_x (12nm) was thermally deposited on the BHJ layer under high vacuum using a Covap thermal evaporation system (Angstrom Engineering). This was followed by the evaporation of the Al electrode (80 nm) using a shadow mask, defining the active area to 0.1 cm².

7.3.3. Conventional Device fabrication

The procedure for active layer ink preparation, as well as active layer and ZnO NP coating conditions are the same as for 4.3.2. *Inverted Device fabrication*. Slot-die coated devices were fabricated in a PET/Ag/PEDOT:PSS/BHJ layer/ZnO NPs/Al device configuration for the BHJ layer of either PPDT2FBT:PC₆₁BM (1:2 w/w), TQ1:PC₆₁BM (1:2 w/w) or PDCBT:ITIC (1:1 w/w).

Polyethylene terephthalate (PET) (Multapex), with a thickness of 75 μm, was pre-stretched at 160 °C for 2 min. silver ink (Novacentrix PFI-600) was roll-to-roll printed (Grafisk Maskinfabrik Solar-1 Coater) on the PET substrate using a patterned photopolymer flexo plate and 3 cm³m⁻² anilox roller to give a dry silver pattern thickness of approximately 240 nm.

The flexible Ag-patterned PET substrate was attached to a mini-roll coater (FOM technologies) with slot-die attachment and wiped with isopropanol soaked TerriWipes at a rotation speed of 2 m min⁻¹ prior to fabrication. The tubing and slot-die head was cleaned with chloroform prior to assembly and between the change of deposition material. Layer deposition was processed under ambient conditions.

The PEDOT:PSS (150 nm) was deposited using 0.780 mL min⁻¹ flow-rate, a drum speed of 1.5 m min⁻¹ and leaving the drum at room temperature. Post-deposition, the drum was heated up to 70 °C and left at the temperature for 30 min to remove remaining moisture in layer. The BHJ layer (100 – 200 nm) was deposited via varying flow rate and drum speed at a drum temperature at 70 °C to obtain a strip width of around 13 mm.

Lastly, the ZnO NP layer (35 nm) was deposited using 0.1 mL min⁻¹ flow-rate, a drum speed of 1.0 m min⁻¹ and drum temperature at 70 °C to achieve a strip width of around 13 mm. The wet and dry thickness for PEDOT:PSS, BHJ and ZnO NP were calculated according to *Equation C1 & C2* in *Appendix C*.

After slot-die coating, the aluminium was thermally deposited on the ZnO NPs layer via vacuum-based deposition high vacuum using a Covap thermal evaporation system (Angstrom Engineering) using a shadow mask, defining the active area to 0.1 cm². For large-area (12.15 cm²), aluminium is sputtered based on previously published work [87, 88], resulting in an electrode strip with a thickness of 100 nm.

For investigating performance and material degradation, PET/PEDOT:PSS/BHJ/ZnO NP/Al & PET/PEDOT:PSS/BHJ half device configurations were used, respectively. Thermal annealing and aging were conducted on a hotplate in a nitrogen-filled glovebox with minimal light exposure.

7.3.4. Solar simulator

For small area (0.1 cm^2), devices were measured using an Oriel Solar simulator fitted with a 150 W Xeon lamp (Newport), filtered to give an output of 100 mW cm^{-2} at AM 1.5 (air mass) standard and calibrated using a Newport silicon reference cell with NIST traceable certification. For large area (12.15 cm^2), devices were measured using a Newport Class AAA solar simulator, filtered to give an output of 100 mW cm^{-2} at AM 1.5 spectrum standard and calibrated with an FHG-ISE silicon reference cell with NIST traceable certification. For both setups, the testing of OPV devices occurred under ambient conditions.

7.3.5. Scanning Electron Microscopy

Measurements were performed using Inspect F50 scanning electron microscopy (<https://doi.org/10.25957/flinders.sem>) equipped with a field emission gun (FEI Company) and a secondary electron detector. The acceleration voltage was 10 kV, and the working distance of 10 mm. The samples were not coated with any conducting layers.

7.4. Results and discussion

7.4.1. Inverted configuration OPVs

Before converting from inverted to conventional OPV device configuration, the first step was to evaluate a few active layer blends to allow for comparison, specifically, PPDT2FBT:PC₆₁BM, TQ1:PC₆₁BM and PDCBT:ITIC. As mentioned in the introduction, these material blends have been shown previously to be printable via slot-die coating methods, as well as being relatively cheap to synthesis. The device performance of inverted devices can be found in *Table 7.1*.

Table 7.1: Device performance of inverted OPVs, with the performance values based on the specific active layer blend per system. The results are from an average of 6 cells, with an active area of 0.1 cm^2 .

Active material	J_{SC} (mA cm^{-2})	V_{OC} (V)	FF	PCE (%)
PPDT2FBT:PC ₆₁ BM (1:2 w/w)	15.9 ± 0.6	0.78 ± 0.01	0.61 ± 0.03	7.6 ± 0.2
TQ1:PC ₆₁ BM (1:2 w/w)	8.4 ± 0.1	0.76 ± 0.01	0.52 ± 0.05	3.4 ± 0.1
PDCBT:ITIC (1:1)	12.8 ± 0.6	0.92 ± 0.01	0.43 ± 0.02	5.1 ± 0.4

When comparing active layer blends, the PPDT2FBT:PC₆₁BM had the best performance out of the three active layer blends tested, due to its increased J_{SC} and FF, however, the PDCBT:ITIC system was able to yield a significantly higher V_{OC} , reaching an average of 0.92 V. As for TQ1:PC₆₁BM, the performance was relatively low compared to the PPDT2FBT:PC₆₁BM and PDCBT:ITIC blends, as well as when compared with spin-coated devices (PCE 4.9%) [90], yet, this difference between spin and slot-die coating can be explained by the coating conditions from this work not being optimised.

7.4.2. Post-fabrication switching verses pre-aging silver electrode

With the performance for inverted devices gathered, the next stage was to determine a fabrication method for conventional devices that were roll-to-roll friendly, and that could be scaled up to larger active area and coating area. The OPV architecture of PET / Ag grid / PEDOT:PSS (PH1000) / Active layer / ZnO NPs / Al was chosen based on successful demonstration of fabrication using roll-to-roll coating [3, 87]. The other advantage of this configuration is that is shifted away from an ITO-based substrate, allowing for improved mechanical stability and as well as reduced material cost; as ITO requires high energy vacuum technique, while indium being is a fairly rare element.

The one issue with this configuration is associated with the potential to have a significant population for cells that have shorting issues. This can occur during the deposition of the Ag-grid via flexography printing, where though the thickness of the grid should be theoretically 240nm, peaks in film can form, reaching the μm range in height. When a full device is fabricated, this can result in the Ag-peaks reaching within the active layer and/or top electrode, leading to shorting. To resolve this, switching can be performed, where a reverse bias can be applied to the cell, resulting in the burn-out of the short [87, 91]. Switching can also be used to form a de-dope PEDOT:PSS interface with the active layer, which was found to be an effective hole selective layer in solar cells, allowing for the improvement in device performance [92]. From previous work, switching has been demonstrated to be able to be conducted for both small-scale and large-fabrication, with the process being automatable, however, if there are coating errors during fabrication, or a critical procedure failure occurs during switching, the cell will appear burnt or melted, resulting in the destruction of that particular cell [88].

In this work, two methods of Improving device performance, reverse bias switching, or silver electrode aging were used. To age the silver, the PET substrate containing the electrode was left out in ambient conditions, with indoor light exposure. The idea of this was to try and oxide the silver, specifically, the silver peaks that were present and known to lead to device shorting. It was hypothesised that this would lead to a decrease in the number of devices that would early require switching, or the number of completed dead cells. The switching vs aging device performance can be found in *Table 7.2*, where the devices contained an active layer blend of PPDT2FBT:PC₆₁BM.

Table 7.2: Device performance of conventional PPDT2FBT:PC61BM OPVs. The results are from an average of 6 cells, with an active area of 0.1 cm².

Ag aging?	Switched?	J _{sc} (mA cm ⁻²)	V _{oc} (V)	FF	PCE (%)
No	No	9.92 ± 1.05	0.60 ± 0.11	0.28 ± 0.08	1.65 ± 0.77
No	Yes	10.15 ± 0.35	0.72 ± 0.00	0.56 ± 0.03	4.05 ± 0.18
Yes	No	12.79 ± 0.42	0.74 ± 0.00	0.60 ± 0.02	5.63 ± 0.29

For devices that were tested without pre-aging of the substrate, or device switching, were found to have significantly lower J_{sc}, V_{oc}, FF and PCE, with some devices that were not switched appeared to have peak features at -0.1 V and 0.4 V in the JV-curve, while others appear to more resemble more of a straight line rather than an ideal JV curve for solar cells. For the curves containing peak features. It is hypothesised that the PEDOT:PSS is the S-shape can be associated with charge accumulation, possibly in the PEDOT:PSS layer. Similar observations have been found in ITO/PEDOT:PSS systems and been shown to be related to charge accumulation [93, 94]. As for the linear-appearing curves, this is hypothesised to be associated with the shorting of the devices as the bottom and top electrodes have a pathway that allows for charge to travel in both directions freely. This sort of behaviour has been observed in P3HT:PCBM devices that added carbon nanotubes within the active layer, resulting in cases where shorting had occurred in the devices [95].

After switching the devices that contain the peak features, the JV curve appears to switch to a more ideal PV curve, allowing for an improvement of device performance. Whereas for linear-curved devices, some devices could be successfully switched, with possible sources of shorts being burnt out, however, some devices which contain too many sources of shorting resulted in the melting/burning of the cell, resulting in device becoming effectively dead.

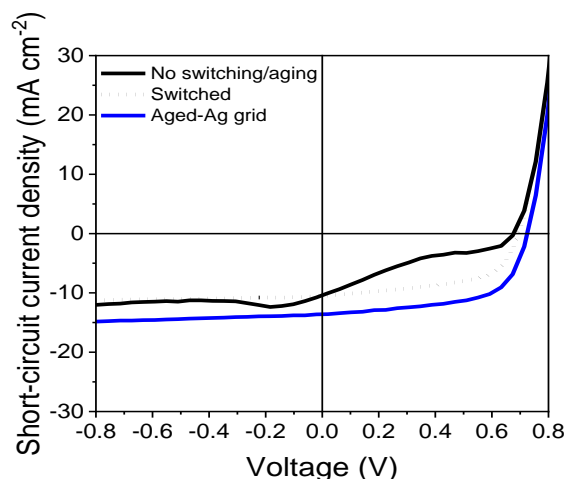


Figure 7.3: JV-curve of PPDT2FBT:PC₆₁BM with different processing conditions, specifically, non-processed, switched and substrate-aged devices.

As for aging of the Ag-grid substrate, the population of dead cells had significantly reduced when compared with non-aged substrate. It is suspected that with the aging of silver under ambient conditions, a layer of insulating silver oxide or silver peaks, allowing for the increase in shunt resistance and reduced population of shorting sources. As this is preliminary work, and outside the focus of the thesis, no further work had been conducted to explain the mechanism associated with the silver aging, however, further research is required to confirm that hypothesis associated with this observation.

7.4.3. Conventional versus inverted OPVs

With a method for fabricating conventional configuration OPVs, next was to compare the device performance of conventional and inverted devices, with these configurations containing active layer blends of either PPDT2FBT:PC₆₁BM, TQ1:PC₆₁BM or PDCBT:ITIC (seen in *Table 7.3*).

Table 7.3: Device performance of inverted and conventional slot-die coated OPVs, with the performance values based on the specific active layer blend per system. The results are from an average of 6 cells, with an active area of 0.1 cm².

Active material	Configuration	J _{sc} (mA cm ⁻²)	V _{oc} (V)	FF	PCE (%)
PPDT2FBT:PC ₆₁ BM (1:2)	Inverted	15.9 ± 0.56	0.78 ± 0.01	0.61 ± 0.03	7.6 ± 0.2
	Conventional	12.8 ± 0.4	0.74 ± 0.00	0.60 ± 0.02	5.6 ± 0.3
TQ1:PC ₆₁ BM (1:2)	Inverted	8.4 ± 0.1	0.76 ± 0.01	0.52 ± 0.05	3.4 ± 0.1
	Conventional	7.1 ± 0.5	0.78 ± 0.06	0.55 ± 0.06	3.1 ± 0.3
PDCBT:ITIC (1:1)	Inverted	12.8 ± 0.6	0.92 ± 0.01	0.43 ± 0.02	5.1 ± 0.4
	Conventional	8.5 ± 0.5	0.82 ± 0.06	0.36 ± 0.03	2.5 ± 0.2

When comparing the device performance between conventional and inverted configurations, there is a noticeable difference in the PCE, with conventional resulting in the lower performance. This difference is associated with two factors, the decrease in the J_{SC} and the V_{OC} . For the discrepancy in J_{SC} , this can be explained by the absorbance of light by the PEDOT:PSS layer vs the ITO layer. For both flexible and rigid substrates containing ITO, it is found to have a relatively high transparency of ~90% at 550 nm, whereas for PEDOT:PSS, this can reduce to 80% depending on the thickness of the films. With the increase in light absorbance from the PEDOT:PSS layer, less light ended up reaching the active layer, reducing the J_{SC} .

As for V_{OC} , it is hypothesised to that replacing the hole transport layer of MoO_x with PEDOT:PSS, as well as replacing the ITO with silver, has resulted in several changes including work function difference between electrodes and interface layers. This has been supported from work by Ratcliff *et al.* that by tuning the ITO work function, were able to adjust the V_{OC} of the OPV devices.

Overall, changing from an inverted to conventional structure resulted in a decrease in the PCE due to a reduction in J_{SC} and V_{OC} . This decrease appears to not be dependent on the active layer materials itself. As PPDT2FBT:PC₆₁BM was able to achieve the highest performance after switching configurations, the remainder of the study will focus on this active layer blend, specifically, the performance at a larger area, as well as its thermal stability. The rest of the chapter will also investigate the influence of solid-additives have on the performance and stability of the conventional PPDT2FBT:PC₆₁BM devices.

7.4.4. Large area conventional devices

With the performance of small area conventional PPDT2FBT:PC₆₁BM devices determined, the next stage was to investigate the impact of increase active area has on the device performance. It is common, when comparing small and large active area OPVs, for the large area to have a reduced PCE [38, 96-98]. There are several sources that can lead to performance reduction, including contact resistance of the interconnections [99] and sheet resistance of electrodes [100], resulting a reduction in J_{SC} , FF and thus, PCE.

For this chapter, a single strip of devices was coated on a single substrate before being separated into small-area (0.1 cm²) and large-area (12.15 cm²) PPDT2FBT:PC₆₁BM devices. Some strips contained either 1.0% w/w piperazine (PP), 0.1 w/w 4,4'-bipiperidine (BP) or 1.0% w/w polyacenaphthylene (PAN) or no additives at all. Device performance of small and large area devices, with or without additives can be seen in *Table 7.4*.

Table 7.4: Device performance conventional OPVs for small and large active area, with the performance values based on the specific active layer blend per system. Small-area devices are an average of 6 cells, while large area is of the highest performance achieved.

Materials	Area (cm ²)	J _{sc} (mA cm ⁻²)	V _{oc} (V)	FF	PCE (%)
PPDT2FBT:PC ₆₁ BM	0.1	9.9 ± 0.8	0.71 ± 0.01	0.45 ± 0.04	3.2 ± 0.3
	12.15	6.0	0.72	0.53	2.3
+3.3% w/w C ₇₀	0.1	9.8 ± 0.1	0.69 ± 0.00	0.54 ± 0.01	3.7 ± 0.1
	12.15	7.1	0.70	0.51	2.5
+1.0% w/w PP	0.1	7.3 ± 0.6	0.73 ± 0.01	0.62 ± 0.01	3.3 ± 0.2
	12.15	7.2	0.73	0.52	2.7
+0.1% w/w BP	0.1	9.8 ± 0.8	0.72 ± 0.00	0.61 ± 0.05	4.3 ± 0.4
	12.15	6.8	0.72	0.57	2.8
+1.0% w/w PAN	0.1	7.6 ± 0.5	0.73 ± 0.02	0.55 ± 0.02	3.1 ± 0.2
	12.15	6.9	0.75	0.52	2.7

When comparing small area devices (0.1 cm²), it is found that they all have similar PCE values (3.1% to 3.3%), except for PPDT2FBT:PC₆₁BM + BP, with an average PCE of 4.3%. This improvement appears to be related to a good J_{sc} and FF compared to the other active layer systems, while the V_{oc} for all systems is around 0.73 V. As found in *Chapter 6*, it had been found that the solid additives were able to influence the performance of polymer:fullerene devices, however, it was found the addition of PAN yielded in a significant improvement in device performance, whereas BP addition only had a minor increase. In this chapter, however, the addition of 0.1% w/w of BP was able to increase the PCE from 3.2% to 4.2% and the addition of 3.3% w/w C₇₀ increase the performance to 3.7%. As for the addition of 1.0% w/w of either PP or PAN, there was an insignificant change to the PCE of the OPV devices.

It is a bit unclear as to why the PAN addition had improved the device performance in *Chapter 6* and not for this chapter work, however, there are a few differences in device fabrication. In the previous chapter, OPV devices followed an inverse architecture (seen in *Figure 7.2*), while the hole transport layer (HTL) consisted of MoO_x and the bottom electrode was ITO. In this work, the OPV device followed a conventional architecture (seen in *Figure 7.2*), while the HTL and bottom electrode was replaced with PEDOT:PSS and a silver grid, respectively. From this detail, it is speculated that the addition of PAN resulted in physical changes to the active layer that are more favourable for the inverted device architecture, and not for conventional. Despite this, the PAN additive, as well as PP did not negatively impact the OPV device performance.

When the active large was increased to 12.15 cm², it was found that PPDT2FBT:PC₆₁BM without solid additives yielded a performance up to 2.3%, whereas devices with solid additives yielded a performance up to 2.7% to 2.8%, a significant difference in PCE. This difference appears to be associated with the change in J_{sc} and FF, while the V_{oc} remains constant without.

Overall, increasing the active area from 0.1 cm² to 12.15 cm² led to a performance decrease of between 13% to 35% the initial PCE.

7.4.5. Device stability under dark nitrogen conditions

Next step was to investigate the influence of changing device architecture had over the overall stability of the device. These changes include 1) replacing the ITO electrode with a silver grid, 2) replacing MoO_x with PEDOT:PSS, and 3) changing from an inverted to a conventional configuration. Though in *Chapter 4 & 5* found a major source of degradation came from the change in morphology of the BHJ in the active layer, this may not be the case of the conventional structure. As such, the first degradation study investigated the aging of the OPVs at room temperature under dark nitrogen conditions (seen in *Figure 7.4*). It is worth highlighting the devices were tested under ambient conditions, while the devices were not encapsulated.

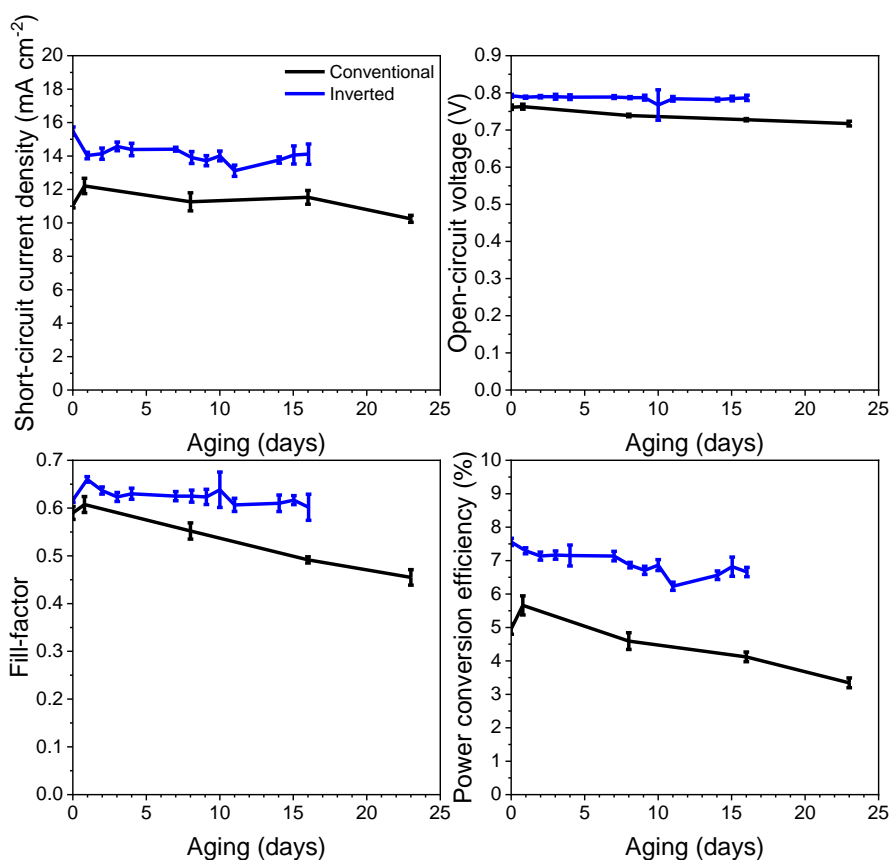


Figure 7.4: Conventional and Inverted PPDT2FBT:PC₆₁BM devices aging at room temperature under nitrogen conditions.

From the previous work conducted in *Chapter 4*, it was observed that, when the inverted PPDT2FBT:PC₆₁BM devices were aged under dark, nitrogen conditions for 20 days, the degradation of PCE appears to be relatively linear, with no apparent burn-in degradation behaviour. The linear degradation behaviour appeared to be equally related to the decrease in J_{sc}, and FF, while the V_{oc} is relatively constant. In this work, it was found that, when compared with inverted devices, conventional PPDT2FBT:PC₆₁BM had a relatively linear degradation trend, with the significant amount of decrease in J_{sc}, V_{oc} and FF, resulting in a decrease in PCE.

Overall, it appears that the conventional device structure is degrading quicker than the inverted structure. One major reason been shown that, with the presence of water, results in the formation and migration of Ag grains into the PEDOT:PSS layer, where with enough time, can migrate to the active layer, leading to a reduction in shunt resistance and thus, reduce the device performance over time [101].

7.4.6. Device stability at elevated temperatures

For further comparison in relation to degradation, conventional and inverted PPDT2FBTLPC₆₁BM degradation at 85 °C was compared together. From the previous work conducted in *Chapter 4*, it was observed that, when the inverted PPDT2FBT:PC₆₁BM devices were aged at 85 °C for 20 days, the degradation of PCE appears to be relatively linear, with no apparent burn-in degradation behaviour. The linear degradation behaviour appeared to be heavily related to the decrease in J_{SC}, while there is a slight decrease in FF, and the V_{OC} is relatively constant.

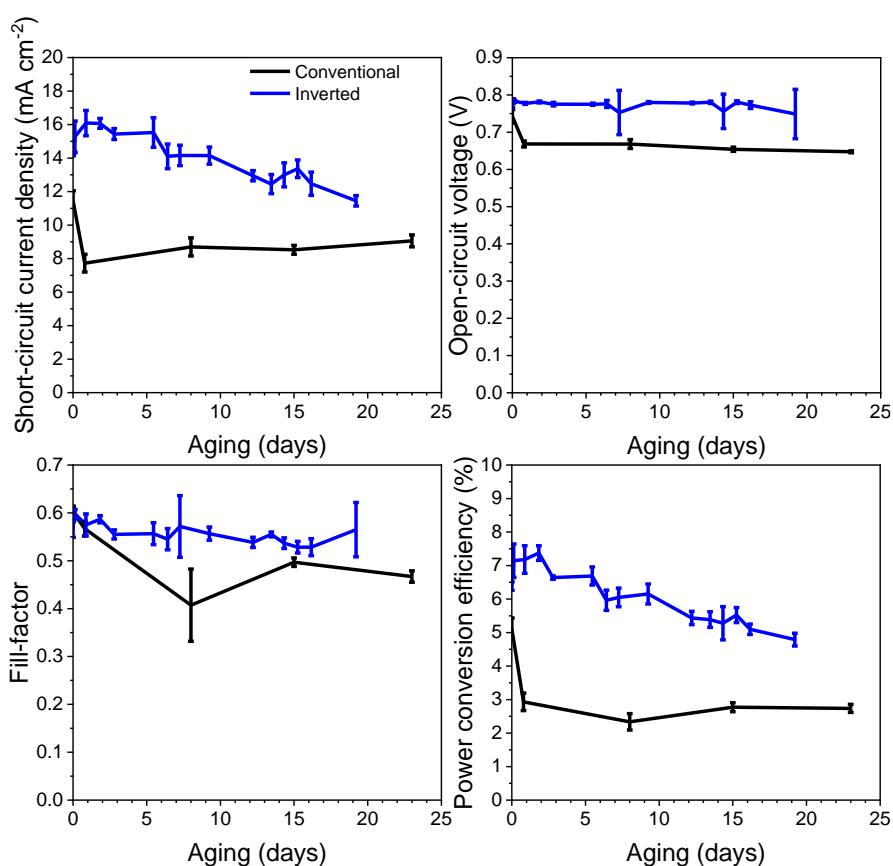


Figure 7.5: Device stability of PPDT2FBT:PC₆₁BM conventional vs Inverted devices that are aged at 85 °C.

Whereas for conventional OPVs, the J_{SC} and V_{OC} were shown to have a similar degradation behaviour, with a quick reduction within a day of aging, before either slightly increase or decrease, in terms of J_{SC} and V_{OC}, respectively. As for the FF, there was a sharp decrease at the 8-day mark, before increasing back to 0.5. With the combination of the changes in J_{SC}, V_{OC} and FF, this has led to a sharp decrease of the PCE after 8 hours, before becoming relatively stable for the past 25 days.

From previous work in *Chapter 5*, it was observed for inverted PPDT2FBT:PC₆₁BM approximately 124 days for the device degrade below 3% PCE. In contrary to conventional PPDT2FBT:PC₆₁BM, it was observed to have degraded within one day for aging at 85 °C, indicating a significantly faster burn-in degradation to have been observed.

With this observation, there were two hypotheses, either the architecture allowed for an acceleration of either fullerene crystallisation or phase separation, otherwise the degradation may be associated with the interface between the active layer and transport layers.

It has been previously published by Son *et al.* that the PEDOT:PSS was a major source of thermal degradation, source the layer itself, as well as the interface between other materials being major sources [102]. For PEDOT:PSS degradation, it has been shown that, though annealing can allow for the removal of moisture for the layer, further annealing can relate in morphological changes, resulting in the reduction of the conductivity [103, 104].

7.4.6. Influence of solid-additives over thermal degradation of conventional OPV

As found earlier in the work, it was observed that there was a significant drop in decrease in device performance when aging at 85 °C. If this sharp decrease was associated with fullerene crystallisation or phase purification, then the addition of solid additives could influence the degradation pattern. As such, based on previous thesis work, the use of C₇₀ could reduce the crystallisation rate and phase separation rate (Chapter 4), while the addition of PP, BP and PAN could reduce the crystallisation rate, yet increase population (Chapter 6).

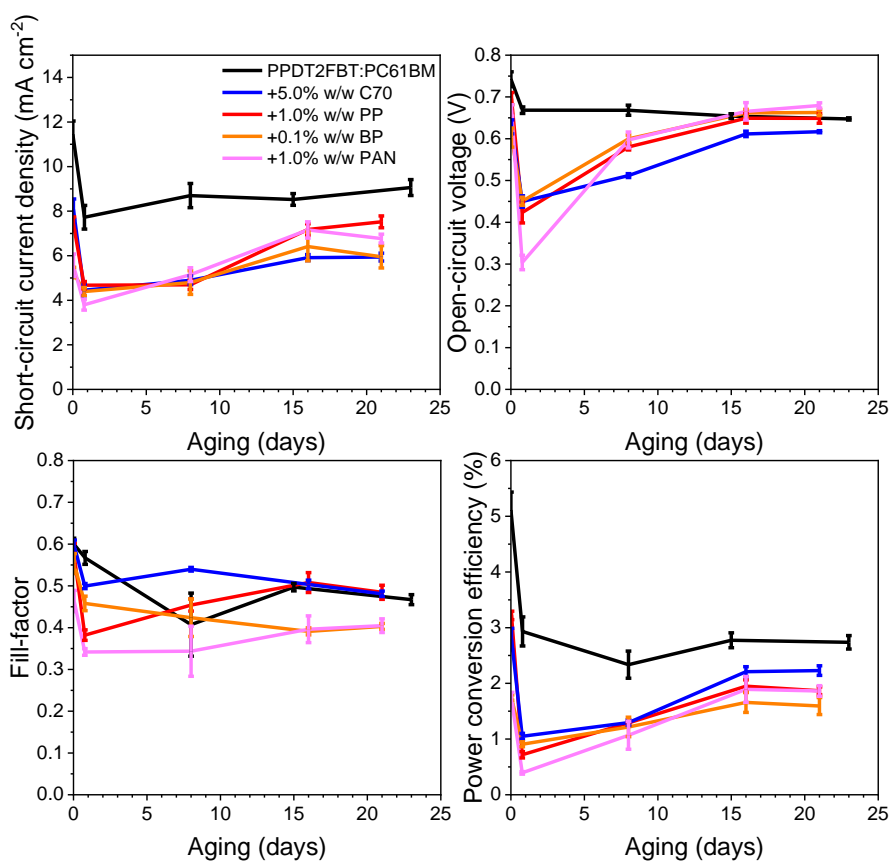


Figure 7.6: PPDT2FBT:PC₆₁BM conventional device thermal aging at 85 °C for different additives. Additions include piperazine (PP), 4,4'-bipiperadine (BP) and polyacenaphthylene (PAN).

When an additive is included in the active layer blend, all additives appear to worsen the magnitude of the V_{OC} degradation, resulting in significant initial performance decrease. Like the standard blend however, as the device continue to age, there is an increase in the V_{OC} , J_{SC} and PCE. A hypothesis of what is occurring is that the crystallisation of PC₆₁BM is preventing Ag migration into the active layer, due to space limitation. For systems containing additives in the active layer, especially those that reduce the crystal growth rate, allows for Ag grain migration into the active layer, leading to a reduction in shunt resistance. Yet, as crystals do increase in size, they are able to push the Ag grains from the active layer, resulting in an increase in shunt resistance, thus, increasing V_{OC} and FF of the devices.

7.4.7. Final discussion of stability of conventional OPV

As it has been observed from the experimental results, the conventional architecture is significantly less stable than the inverted OPVs, with the likely source of said degradation being associated with the PEDOT:PSS layer replacing MoO_x. Though MoO_x not commonly used for large scale device fabrication, it has been investigated extensively towards its influence of the stability of OPVs. Previous literature has support this similar behaviour of inverted device being more stable than conventional [105]. Kundu *et al.* found that, when implementing both configurations with MoO_x and ZnO NPs as transport layers, with the slower degradation for inverted being associated with the MoO_x acting as a barrier, preventing oxygen and silver reaching the active layer [105].

It is worth noting that this may not always be the case, with test conditions playing an important impact on understanding degradation behaviour. Kumar *et al.* found with inverted devices either containing MoO_x or PEDOT:PSS as the hole transport layer, that devices containing MoO_x were more stable under outdoor testing conditions, while both MoO_x and PEDOT:PSS has similar stability when under light aging [106].

As for fullerene crystallisation, there is a possibility that the interfacial layers could influence the crystal population in the active layer when undergoing thermal aging. Li *et al.* found by changing the underlying layer underneath the PCDTBT:PC₆₁BM layer influenced the crystal growth of PC₆₁BM, with the surface energy and roughness leading to increased crystallisation, while ZnO and minimal crystallisation, while PEDOT:PSS could lead to increase crystal population [107].

By comparing literature with the experimental data, it is hypothesised that the dominate degradation pathway for the current conventional OPV device is not associated with the morphology or crystallisation of the active layer, rather the PEDOT:PSS degradation within the layer, or at the interface, where using improved interfacial materials allowing for the improving of morphological stability. To confirm this hypothesis, more time to require degrading the devices and observe and physical features on the active and PEDOT:PSS layer, as well as at the interface.

7.5. Conclusion

To support the scalability of mini-roll coated OPV devices, a conventional device structure that has previously been demonstrated to be roll-to-roll compatible, was implemented in this study. By comparing the device performance of conventional and inverted architectures, with active layers containing either PPDT2FBT:PC₆₁BM, TQ1:PC₆₁BM or PDCBT:ITIC, that there is a small decrease in device performance due the replacement of Zinc Oxide nanoparticles with PEDOT:PSS, resulting in a significant reduction of the J_{sc}. When increasing the active area of PPDT2FBT:PC₆₁BM conventional devices from 0.1 cm² to 12.15 cm², the perform decreased further from 3.2% to 2.3%.

As for the stability, both under dark storage and at 85 °C thermal aging, the conventional PPDT2FBT:PC₆₁BM devices degraded at an accelerated rate compared with inverted devices with the same active material blend. As such, it is suspected that the major source of degradation for these devices is associated with the PEDOT:PSS layer.

7.6. Reference

1. Thompson, B. C. and Fréchet, J. M. J., Polymer–Fullerene Composite Solar Cells. *Angewandte Chemie International Edition*, **2008**. 47 (1), 58-77.
2. Beaujuge, P. M. and Fréchet, J. M. J., Molecular Design and Ordering Effects in π -Functional Materials for Transistor and Solar Cell Applications. *Journal of the American Chemical Society*, **2011**. 133 (50), 20009-20029.
3. Andersen, T. R., Almyahi, F., Cooling, N. A., Elkington, D., Wiggins, L., Fahy, A., Feron, K., Vaughan, B., Griffith, M. J., and Mozer, A. J., Comparison of inorganic electron transport layers in fully roll-to-roll coated/printed organic photovoltaics in normal geometry. *Journal of Materials Chemistry A*, **2016**. 4 (41), 15986-15996.
4. Bao, S., Yang, H., Fan, H., Zhang, J., Wei, Z., Cui, C., and Li, Y., Volatilizable Solid Additive-Assisted Treatment Enables Organic Solar Cells with Efficiency over 18.8% and Fill Factor Exceeding 80%. *Advanced Materials*, **2021**. 33 (48), 2105301.
5. Cai, Y., Li, Y., Wang, R., Wu, H., Chen, Z., Zhang, J., Ma, Z., Hao, X., Zhao, Y., Zhang, C., Huang, F., and Sun, Y., A Well-Mixed Phase Formed by Two Compatible Non-Fullerene Acceptors Enables Ternary Organic Solar Cells with Efficiency over 18.6%. *Advanced Materials*, **2021**. 33 (33), 2101733.
6. Song, J., Zhu, L., Li, C., Xu, J., Wu, H., Zhang, X., Zhang, Y., Tang, Z., Liu, F., and Sun, Y., High-efficiency organic solar cells with low voltage loss induced by solvent additive strategy. *Matter*, **2021**. 4 (7), 2542-2552.
7. Chang, Y.-H., Tseng, S.-R., Chen, C.-Y., Meng, H.-F., Chen, E.-C., Horng, S.-F., and Hsu, C.-S., Polymer solar cell by blade coating. *Organic Electronics*, **2009**. 10 (5), 741-746.
8. Schmidt-Hansberg, B., Sanyal, M., Grossiord, N., Galagan, Y., Baunach, M., Klein, M. F. G., Colsmann, A., Scharfer, P., Lemmer, U., Dosch, H., Michels, J., Barrena, E., and Schabel, W., Investigation of non-halogenated solvent mixtures for high throughput fabrication of polymer–fullerene solar cells. *Solar Energy Materials and Solar Cells*, **2012**. 96, 195-201.
9. Lim, F. J., Ananthanarayanan, K., Luther, J., and Ho, G. W., Influence of a novel fluorosurfactant modified PEDOT:PSS hole transport layer on the performance of inverted organic solar cells. *Journal of Materials Chemistry*, **2012**. 22 (48), 25057-25064.
10. Yu, J.-S., Kim, I., Kim, J.-S., Jo, J., Larsen-Olsen, T. T., Søndergaard, R. R., Hösel, M., Angmo, D., Jørgensen, M., and Krebs, F. C., Silver front electrode grids for ITO-free all printed polymer solar cells with embedded and raised topographies, prepared by thermal imprint, flexographic and inkjet roll-to-roll processes. *Nanoscale*, **2012**. 4 (19), 6032-6040.
11. Cho, C.-K., Hwang, W.-J., Eun, K., Choa, S.-H., Na, S.-I., and Kim, H.-K., Mechanical flexibility of transparent PEDOT:PSS electrodes prepared by gravure printing for flexible organic solar cells. *Solar Energy Materials and Solar Cells*, **2011**. 95 (12), 3269-3275.
12. Yang, J., Vak, D., Clark, N., Subbiah, J., Wong, W. W. H., Jones, D. J., Watkins, S. E., and Wilson, G., Organic photovoltaic modules fabricated by an industrial gravure printing proofer. *Solar Energy Materials and Solar Cells*, **2013**. 109, 47-55.
13. Eom, S. H., Senthilarasu, S., Uthirakumar, P., Hong, C.-H., Lee, Y.-S., Lim, J., Yoon, S. C., Lee, C., and Lee, S.-H., Preparation and characterization of nano-scale ZnO as a buffer layer for inkjet printing of silver cathode in polymer solar cells. *Solar Energy Materials and Solar Cells*, **2008**. 92 (5), 564-570.
14. Eom, S. H., Park, H., Mujawar, S. H., Yoon, S. C., Kim, S.-S., Na, S.-I., Kang, S.-J., Khim, D., Kim, D.-Y., and Lee, S.-H., High efficiency polymer solar cells via sequential inkjet-printing of PEDOT:PSS and P3HT:PCBM inks with additives. *Organic Electronics*, **2010**. 11 (9), 1516-1522.
15. Krebs, F. C., Pad printing as a film forming technique for polymer solar cells. *Solar Energy Materials and Solar Cells*, **2009**. 93 (4), 484-490.
16. Zhu, R., Chung, C.-H., Cha, K. C., Yang, W., Zheng, Y. B., Zhou, H., Song, T.-B., Chen, C.-C., Weiss, P. S., Li, G., and Yang, Y., Fused Silver Nanowires with Metal Oxide Nanoparticles and Organic Polymers for Highly Transparent Conductors. *ACS Nano*, **2011**. 5 (12), 9877-9882.
17. Krebs, F. C., Alstrup, J., Spanggaard, H., Larsen, K., and Kold, E., Production of large-area polymer solar cells by industrial silk screen printing, lifetime considerations and lamination

- with polyethyleneterephthalate. *Solar Energy Materials and Solar Cells*, **2004**. 83 (2), 293-300.
18. Zhang, B., Chae, H., and Cho, S. M., Screen-Printed Polymer:Fullerene Bulk-Heterojunction Solar Cells. *Japanese Journal of Applied Physics*, **2009**. 48 (2R), 020208.
 19. Krebs, F. C., Polymer solar cell modules prepared using roll-to-roll methods: knife-over-edge coating, slot-die coating and screen printing. *Solar Energy Materials and Solar Cells*, **2009**. 93 (4), 465-475.
 20. Krebs, F. C., Fyenbo, J., and Jørgensen, M., Product integration of compact roll-to-roll processed polymer solar cell modules: methods and manufacture using flexographic printing, slot-die coating and rotary screen printing. *Journal of Materials Chemistry*, **2010**. 20 (41), 8994-9001.
 21. Krebs, F. C., Tromholt, T., and Jørgensen, M., Upscaling of polymer solar cell fabrication using full roll-to-roll processing. *Nanoscale*, **2010**. 2 (6), 873-886.
 22. Zimmermann, B., Schleiermacher, H.-F., Niggemann, M., Würfel, U., and Cells, S., ITO-free flexible inverted organic solar cell modules with high fill factor prepared by slot die coating. *Solar Energy Materials and Solar Cells*, **2011**. 95 (7), 1587-1589.
 23. Carlé, J. E., Andreasen, B., Tromholt, T., Madsen, M. V., Norrman, K., Jørgensen, M., and Krebs, F. C., Comparative studies of photochemical cross-linking methods for stabilizing the bulk hetero-junction morphology in polymer solar cells. *Journal of Materials Chemistry*, **2012**. 22 (46), 24417-24423.
 24. Liu, Y., Larsen-Olsen, T. T., Zhao, X., Andreasen, B., Søndergaard, R. R., Helgesen, M., Norrman, K., Jørgensen, M., Krebs, F. C., and Zhan, X., All polymer photovoltaics: From small inverted devices to large roll-to-roll coated and printed solar cells. *Solar Energy Materials and Solar Cells*, **2013**. 112, 157-162.
 25. Hösel, M., Søndergaard, R. R., Angmo, D., and Krebs, F. C., Comparison of Fast Roll-to-Roll Flexographic, Inkjet, Flatbed, and Rotary Screen Printing of Metal Back Electrodes for Polymer Solar Cells. *Advanced Engineering Materials*, **2013**. 15 (10), 995-1001.
 26. Unsworth, N. K., Hancox, I., Dearden, C. A., Howells, T., Sullivan, P., Lilley, R. S., Sharp, J., and Jones, T. S., Highly conductive spray deposited poly(3, 4-ethylenedioxythiophene):poly(styrenesulfonate) electrodes for indium tin oxide-free small molecule organic photovoltaic devices. *Applied Physics Letters*, **2013**. 103 (17), 173304.
 27. Wang, T., Scarratt, N. W., Yi, H., Dunbar, A. D. F., Pearson, A. J., Watters, D. C., Glen, T. S., Brook, A. C., Kingsley, J., Buckley, A. R., Skoda, M. W. A., Donald, A. M., Jones, R. A. L., Iraqi, A., and Lidzey, D. G., Fabricating High Performance, Donor-Acceptor Copolymer Solar Cells by Spray-Coating in Air. *Advanced Energy Materials*, **2013**. 3 (4), 505-512.
 28. Zheng, Y., Wu, R., Shi, W., Guan, Z., and Yu, J., Effect of in situ annealing on the performance of spray coated polymer solar cells. *Solar Energy Materials and Solar Cells*, **2013**. 111, 200-205.
 29. Tait, J. G., Rand, B. P., and Heremans, P., Concurrently pumped ultrasonic spray coating for donor:acceptor and thickness optimization of organic solar cells. *Organic Electronics*, **2013**. 14 (3), 1002-1008.
 30. Colella, S., Mazzeo, M., Melcarne, G., Carallo, S., Ciccarella, G., and Gigli, G., Spray coating fabrication of organic solar cells bypassing the limit of orthogonal solvents. *Applied Physics Letters*, **2013**. 102 (20), 203307.
 31. Distler, A., Brabec, C. J., and Egelhaaf, H.-J., Organic photovoltaic modules with new world record efficiencies. *Progress in Photovoltaics: Research and Applications*, **2021**. 29 (1), 24-31.
 32. Kadam, K. D., Kim, H., Rehman, S., Patil, H., Aziz, J., Dongale, T. D., Khan, M. F., and Kim, D.-k., Optimization of ZnO:PEIE as an Electron Transport Layer for Flexible Organic Solar Cells. *Energy & Fuels*, **2021**. 35 (15), 12416-12424.
 33. Miranda, B. H., Corrêa, L. d. Q., Soares, G. A., Martins, J. L., Lopes, P. L., Vilela, M. L., Rodrigues, J. F., Cunha, T. G., Vilaça, R. d. Q., and Castro-Hermosa, S., Efficient fully roll-to-roll coated encapsulated organic solar module for indoor applications. *Solar Energy*, **2021**. 220, 343-353.
 34. Liao, C.-Y., Hsiao, Y.-T., Tsai, K.-W., Teng, N.-W., Li, W.-L., Wu, J.-L., Kao, J.-C., Lee, C.-C., Yang, C.-M., Tan, H.-S., Chung, K.-H., and Chang, Y.-M., Photoactive Material for

- Highly Efficient and All Solution-Processed Organic Photovoltaic Modules: Study on the Efficiency, Stability, and Synthetic Complexity. *Solar RRL*, **2021**. 5 (3), 2000749.
35. Castro, M. F., Mazzolini, E., Sondergaard, R. R., Espindola-Rodriguez, M., and Andreasen, J. W., Flexible ITO-free roll-processed large-area nonfullerene organic solar cells based on P3HT: O-IDTBR. *Physical Review Applied*, **2020**. 14 (3), 034067.
 36. Chaturvedi, N., Gasparini, N., Corzo, D., Bertrandie, J., Wehbe, N., Troughton, J., and Baran, D., All Slot-Die Coated Non-Fullerene Organic Solar Cells with PCE 11%. *Advanced Functional Materials*, **2021**. n/a (n/a), 2009996.
 37. Lee, C.-Y., Tsao, C.-S., Lin, H.-K., Cha, H.-C., Chung, T.-Y., Sung, Y.-M., and Huang, Y.-C., Encapsulation improvement and stability of ambient roll-to-roll slot-die-coated organic photovoltaic modules. *Solar Energy*, **2021**. 213, 136-144.
 38. Hoff, A., Gasonoo, A., Pahlevani, M., and Welch, G. C., An Alcohol-Soluble N-Annulated Perylene Diimide Cathode Interlayer for Air-Processed, Slot-Die Coated Organic Photovoltaic Devices and Large-Area Modules. *Solar RRL*, **2022**. 6 (11), 2200691.
 39. Søndergaard, R., Hösel, M., Angmo, D., Larsen-Olsen, T. T., and Krebs, F. C., Roll-to-roll fabrication of polymer solar cells. *Materials today*, **2012**. 15 (1-2), 36-49.
 40. Zhang, Z., Miao, J., Ding, Z., Kan, B., Lin, B., Wan, X., Ma, W., Chen, Y., Long, X., Dou, C., Zhang, J., Liu, J., and Wang, L., Efficient and thermally stable organic solar cells based on small molecule donor and polymer acceptor. *Nature Communications*, **2019**. 10 (1), 3271.
 41. Zheng, N., Mahmood, K., Zhong, W., Liu, F., Zhu, P., Wang, Z., Xie, B., Chen, Z., Zhang, K., Ying, L., Huang, F., and Cao, Y., Improving the efficiency and stability of non-fullerene polymer solar cells by using N2200 as the Additive. *Nano Energy*, **2019**. 58, 724-731.
 42. Meitzner, R., Faber, T., Alam, S., Amand, A., Roesch, R., Büttner, M., Herrmann-Westendorf, F., Presselt, M., Ciammaruchi, L., and Visoly-Fisher, I., Impact of P3HT materials properties and layer architecture on OPV device stability. *Solar Energy Materials and Solar Cells*, **2019**. 202, 110151.
 43. Li, M., Zhang, W., Wang, H., Chen, L., Zheng, C., and Chen, R., Effect of organic cathode interfacial layers on efficiency and stability improvement of polymer solar cells. *RSC advances*, **2017**. 7 (50), 31158-31163.
 44. Weng, C.-N., Yang, H.-C., Tsai, C.-Y., Chen, S.-H., Chen, Y.-S., Chen, C.-H., Huang, K.-M., Meng, H.-F., Chao, Y.-C., and Chang, C.-Y., The influence of UV filter and Al/Ag moisture barrier layer on the outdoor stability of polymer solar cells. *Solar Energy*, **2020**. 199, 308-316.
 45. Doumon, N. Y., Wang, G., Chiechi, R. C., and Koster, L. J. A., Relating polymer chemical structure to the stability of polymer: fullerene solar cells. *Journal of Materials Chemistry C*, **2017**. 5 (26), 6611-6619.
 46. Muhsin, B., Roesch, R., Gobsch, G., and Hoppe, H., Flexible ITO-free polymer solar cells based on highly conductive PEDOT:PSS and a printed silver grid. *Solar Energy Materials and Solar Cells*, **2014**. 130, 551-554.
 47. Sun, Y., Meng, L., Wan, X., Guo, Z., Ke, X., Sun, Z., Zhao, K., Zhang, H., Li, C., and Chen, Y., Flexible High-Performance and Solution-Processed Organic Photovoltaics with Robust Mechanical Stability. *Advanced Functional Materials*, **2021**. 31 (16), 2010000.
 48. Kang, H., Kim, G., Kim, J., Kwon, S., Kim, H., and Lee, K., Bulk-heterojunction organic solar cells: Five core technologies for their commercialization. *Advanced Materials*, **2016**. 28 (36), 7821-7861.
 49. Greenbank, W., Djeddaoui, N., Destouesse, E., Lamminaho, J., Prete, M., Boukezzi, L., Ebel, T., Bessissa, L., Rubahn, H.-G., Turkovic, V., and Madsen, M., Degradation Behavior of Scalable Nonfullerene Organic Solar Cells Assessed by Outdoor and Indoor ISOS Stability Protocols. *Energy Technology*, **2020**. 8 (12), 2000295.
 50. Duan, L. and Uddin, A., Progress in Stability of Organic Solar Cells. *Advanced Science*, **2020**. 7 (11), 1903259.
 51. Paci, B., Generosi, A., Rossi Albertini, V., Perfetti, P., de Bettignies, R., Leroy, J., Firon, M., and Sentein, C., Controlling photoinduced degradation in plastic photovoltaic cells: A time-resolved energy dispersive x-ray reflectometry study. *Applied physics letters*, **2006**. 89 (4), 043507.

52. Andreasen, J. W., Gevorgyan, S. A., Schlepütz, C. M., and Krebs, F. C., Applicability of X-ray reflectometry to studies of polymer solar cell degradation. *Solar energy materials and solar cells*, **2008**. 92 (7), 793-798.
53. Greenbank, W., Rolston, N., Destouesse, E., Wantz, G., Hirsch, L., Dauskardt, R., and Chambon, S., Improved mechanical adhesion and electronic stability of organic solar cells with thermal ageing: the role of diffusion at the hole extraction interface. *Journal of Materials Chemistry A*, **2017**. 5 (6), 2911-2919.
54. Sung, Y. M., Huang, Y. C., Chien, F. S. S., and Tsao, C. S., Mechanism and Analysis of Thermal Burn-In Degradation of OPVs Induced by Evaporated HTL. *IEEE Journal of Photovoltaics*, **2019**. 9 (3), 694-699.
55. Greenbank, W., Hirsch, L., Wantz, G., and Chambon, S., Interfacial thermal degradation in inverted organic solar cells. *Applied Physics Letters*, **2015**. 107 (26), 263301.
56. Han, N., Heo, Y.-J., Lee, M., Moon, Y., Yang, D., Kim, Y., and Kim, D.-Y., Introduction of Water Treatment in Slot-Die Coated Organic Solar Cells to Improve Device Performance and Stability. *Advanced Functional Materials*, **2022**. 32 (39), 2204871.
57. Chang, Y.-M., Liao, C.-Y., Lee, C.-C., Lin, S.-Y., Teng, N.-W., and Huei-Shuan Tan, P., All solution and ambient processable organic photovoltaic modules fabricated by slot-die coating and achieved a certified 7.56% power conversion efficiency. *Solar Energy Materials and Solar Cells*, **2019**. 202, 110064.
58. Hoff, A., Gasonoo, A., Pahlevani, M., and Welch, G. C., An Alcohol-Soluble N-Annulated Perylene Diimide Cathode Interlayer for Air-Processed, Slot-Die Coated Organic Photovoltaic Devices and Large-Area Modules. *Solar RRL*, **2022**. 6 (11), 2200691.
59. Chen, C.-T. and Yang, H.-H., Inkjet printing of composite hole transport layers and bulk heterojunction structure for organic solar cells. *Thin Solid Films*, **2022**. 751, 139217.
60. Song, S., Lee, K. T., Koh, C. W., Shin, H., Gao, M., Woo, H. Y., Vak, D., and Kim, J. Y., Hot slot die coating for additive-free fabrication of high performance roll-to-roll processed polymer solar cells. *Energy & Environmental Science*, **2018**. 11 (11), 3248-3255.
61. Wei, J., Zhang, C., Ji, G., Han, Y., Ismail, I., Li, H., Luo, Q., Yang, J., and Ma, C.-Q., Roll-to-roll printed stable and thickness-independent ZnO:PEI composite electron transport layer for inverted organic solar cells. *Solar Energy*, **2019**. 193, 102-110.
62. Kirk, B., Pan, X., Jevric, M., Andersson, G., and Andersson, M. R., Introducing neat fullerenes to improve the thermal stability of slot-die coated organic solar cells. *Materials Advances*, **2022**.
63. Rodríguez-Martínez, X., Riera-Galindo, S., Aguirre, L. E., Campoy-Quiles, M., Arwin, H., and Inganäs, O., Laminated Organic Photovoltaic Modules for Agrivoltaics and Beyond: An Outdoor Stability Study of All-Polymer and Polymer:Small Molecule Blends. *Advanced Functional Materials*, **2023**. 33 (10), 2213220.
64. Nguyen, T. L., Choi, H., Ko, S. J., Uddin, M. A., Walker, B., Yum, S., Jeong, J. E., Yun, M. H., Shin, T. J., and Hwang, S., Semi-crystalline photovoltaic polymers with efficiency exceeding 9% in a ~ 300 nm thick conventional single-cell device. *Energy & Environmental Science*, **2014**. 7 (9), 3040-3051.
65. Du, Z., Mainville, M., Vollbrecht, J., Dixon, A. L., Schopp, N., Schrock, M., Peng, Z., Huang, J., Chae, S., Ade, H., Leclerc, M., Reddy, G. N. M., and Nguyen, T.-Q., Insights into Bulk-Heterojunction Organic Solar Cells Processed from Green Solvent. *Solar RRL*, **2021**. 5 (8), 2100213.
66. Dayneko, S. V., Pahlevani, M., and Welch, G. C., Indoor Photovoltaics: Photoactive Material Selection, Greener Ink Formulations, and Slot-Die Coated Active Layers. *ACS Applied Materials & Interfaces*, **2019**. 11 (49), 46017-46025.
67. Mainville, M., Tremblay, V., Fenniri, M. Z., Laventure, A., Farahat, M. E., Ambrose, R., Welch, G. C., Hill, I. G., and Leclerc, M., Water Compatible Direct (Hetero)arylation Polymerization of PPDT2FBT: A Pathway Towards Large-Scale Production of Organic Solar Cells. *Asian Journal of Organic Chemistry*, **2020**. 9 (9), 1318-1325.
68. Wang, E., Hou, L., Wang, Z., Hellström, S., Zhang, F., Inganäs, O., and Andersson, M. R., An easily synthesized blue polymer for high-performance polymer solar cells. *Advanced Materials*, **2010**. 22 (46), 5240-5244.
69. Bjuggren, J. M., Sharma, A., Gedefaw, D., Elmas, S., Pan, C., Kirk, B., Zhao, X., Andersson, G., and Andersson, M. R., Facile Synthesis of an Efficient and Robust Cathode

- Interface Material for Polymer Solar Cells. *ACS Applied Energy Materials*, **2018**. *1* (12), 7130-7139.
70. Wang, Y., Jafari, M. J., Wang, N., Qian, D., Zhang, F., Ederth, T., Moons, E., Wang, J., Inganäs, O., Huang, W., and Gao, F., Light-induced degradation of fullerenes in organic solar cells: a case study on TQ1:PC71BM. *Journal of Materials Chemistry A*, **2018**. *6* (25), 11884-11889.
 71. Karuthedath, S., Gorenflot, J., Melianas, A., Kan, Z., Kemerink, M., and Laquai, F., Buildup of Triplet-State Population in Operating TQ1:PC71BM Devices Does Not Limit Their Performance. *The Journal of Physical Chemistry Letters*, **2020**. *11* (8), 2838-2845.
 72. Karuthedath, S., Melianas, A., Kan, Z., Pranculis, V., Wohlfahrt, M., Khan, J. I., Gorenflot, J., Xia, Y., Inganäs, O., Gulbinas, V., Kemerink, M., and Laquai, F., Thermal annealing reduces geminate recombination in TQ1:N2200 all-polymer solar cells. *Journal of Materials Chemistry A*, **2018**. *6* (17), 7428-7438.
 73. Xia, Y., Musumeci, C., Bergqvist, J., Ma, W., Gao, F., Tang, Z., Bai, S., Jin, Y., Zhu, C., and Kroon, R. J. J. o. M. C. A., Inverted all-polymer solar cells based on a quinoxaline–thiophene/naphthalene-diimide polymer blend improved by annealing. **2016**. *4* (10), 3835-3843.
 74. Kim, Y., Yeom, H. R., Kim, J. Y., and Yang, C., High-efficiency polymer solar cells with a cost-effective quinoxaline polymer through nanoscale morphology control induced by practical processing additives. *Energy & Environmental Science*, **2013**. *6* (6), 1909-1916.
 75. Andersson, L. M., Fully Slot–Die-Coated All-Organic Solar Cells. *Energy Technology*, **2015**. *3* (4), 437-442.
 76. Sharma, A., Pan, X., Campbell, J. A., Andersson, M. R., and Lewis, D. A., Unravelling the thermomechanical properties of bulk heterojunction blends in polymer solar cells. *Macromolecules*, **2017**. *50* (8), 3347-3354.
 77. Lindqvist, C., Bergqvist, J., Bäcke, O., Gustafsson, S., Wang, E., Olsson, E., Inganäs, O., Andersson, M. R., and Müller, C., Fullerene mixtures enhance the thermal stability of a non-crystalline polymer solar cell blend. *Applied Physics Letters*, **2014**. *104* (15), 153301.
 78. Lindqvist, C., Bergqvist, J., Feng, C. C., Gustafsson, S., Bäcke, O., Treat, N. D., Bounioux, C., Henriksson, P., Kroon, R., Wang, E., Sanz-Velasco, A., Kristiansen, P. M., Stingelin, N., Olsson, E., Inganäs, O., Andersson, M. R., and Müller, C., Fullerene nucleating agents: a route towards thermally stable photovoltaic blends. *Advanced Energy Materials*, **2014**. *4* (9), 1301437.
 79. Wang, J., Zheng, Z., Zhang, D., Zhang, J., Zhou, J., Liu, J., Xie, S., Zhao, Y., Zhang, Y., Wei, Z., Hou, J., Tang, Z., and Zhou, H., Regulating Bulk-Heterojunction Molecular Orientations through Surface Free Energy Control of Hole-Transporting Layers for High-Performance Organic Solar Cells. *Advanced Materials*, **2019**. *31* (17), 1806921.
 80. Morin, P.-O., Bura, T., Sun, B., Gorelsky, S. I., Li, Y., and Leclerc, M., Conjugated polymers à la carte from time-controlled direct (hetero) arylation polymerization. *ACS Macro Letters*, **2015**. *4* (1), 21-24.
 81. Zhang, M., Guo, X., Ma, W., Ade, H., and Hou, J., A polythiophene derivative with superior properties for practical application in polymer solar cells. *Advanced Materials*, **2014**. *26* (33), 5880-5885.
 82. Sonar, P., Singh, S. P., Soh, M. S., and Li, Y., Ambipolar polymeric semiconductor materials and organic electronic devices. **2014**, Google Patents.
 83. Jang, S. Y., Kim, I. b., Kim, Y., Lim, D. H., Kang, H., Heeney, M., and Kim, D. Y., Facile Direct C-H Arylation Polymerization of Conjugated Polymer, PDCBT, for Organic Solar Cells. *Macromolecular Rapid Communications*, **2022**. *43* (20), 2200405.
 84. Xu, Y. X., Chueh, C. C., Yip, H. L., Ding, F. Z., Li, Y. X., Li, C. Z., Li, X., Chen, W. C., and Jen, A. K. Y., Improved charge transport and absorption coefficient in indacenodithieno [3, 2-b] thiophene-based ladder-type polymer leading to highly efficient polymer solar cells. *Advanced materials*, **2012**. *24* (47), 6356-6361.
 85. Lin, Y., Wang, J., Zhang, Z. G., Bai, H., Li, Y., Zhu, D., and Zhan, X., An electron acceptor challenging fullerenes for efficient polymer solar cells. *Advanced materials*, **2015**. *27* (7), 1170-1174.
 86. Cui, Y., Ren, H., Yu, J., Wang, Z., and Qian, G., An indanone-based alkoxy silane dye with second order nonlinear optical properties. *Dyes and Pigments*, **2009**. *81* (1), 53-57.

87. Hart, A. S., Andersen, T. R., Griffith, M. J., Fahy, A., Vaughan, B., Belcher, W. J., and Dastoor, P. C., Roll-to-roll solvent annealing of printed P3HT : ICXA devices. *RSC Advances*, **2019**. 9 (72), 42294-42305.
88. Andersen, T. R., Cooling, N. A., Almyahi, F., Hart, A. S., Nicolaidis, N. C., Feron, K., Noori, M., Vaughan, B., Griffith, M. J., Belcher, W. J., and Dastoor, P. C., Fully roll-to-roll prepared organic solar cells in normal geometry with a sputter-coated aluminium top-electrode. *Solar Energy Materials and Solar Cells*, **2016**. 149, 103-109.
89. Krebs, F. C., Air stable polymer photovoltaics based on a process free from vacuum steps and fullerenes. *Solar Energy Materials and Solar Cells*, **2008**. 92 (7), 715-726.
90. Wang, E., Hou, L., Wang, Z., Hellström, S., Zhang, F., Inganäs, O., and Andersson, M. R., An Easily Synthesized Blue Polymer for High-Performance Polymer Solar Cells. *Advanced Materials*, **2010**. 22 (46), 5240-5244.
91. Andersen, T. R., Weyhe, A. T., Tao, Q., Zhao, F., Qin, R., Zhang, S., Chen, H., and Yu, D., Novel cost-effective acceptor:P3HT based organic solar cells exhibiting the highest ever reported industrial readiness factor. *Materials Advances*, **2020**. 1 (4), 658-665.
92. Larsen-Olsen, T. T., Søndergaard, R. R., Norrman, K., Jørgensen, M., and Krebs, F. C., All printed transparent electrodes through an electrical switching mechanism: A convincing alternative to indium-tin-oxide, silver and vacuum. *Energy & Environmental Science*, **2012**. 5 (11), 9467-9471.
93. Ibrahim, N. Effect of PEDOT:PSS/metal electrodes on the performance of heterojunction solar cells. in *2015 International Conference on Computing, Control, Networking, Electronics and Embedded Systems Engineering (ICCNEEE)*. 2015.
94. Teguh, J. S., Sum, T. C., and Yeow, E. K. L., Effect of charge accumulation on the stability of PEDOT:PSS during device operation. *Chemical Physics Letters*, **2014**. 607, 52-56.
95. Alley, N. J., Liao, K.-S., Andreoli, E., Dias, S., Dillon, E. P., Orbaek, A. W., Barron, A. R., Byrne, H. J., and Curran, S. A., Effect of carbon nanotube-fullerene hybrid additive on P3HT:PCBM bulk-heterojunction organic photovoltaics. *Synthetic Metals*, **2012**. 162 (1), 95-101.
96. Lee, J., Seo, Y.-H., Kwon, S.-N., Kim, D.-H., Jang, S., Jung, H., Lee, Y., Weerasinghe, H., Kim, T., Kim, J. Y., Vak, D., and Na, S.-I., Slot-Die and Roll-to-Roll Processed Single Junction Organic Photovoltaic Cells with the Highest Efficiency. **2019**. 9 (36), 1901805.
97. Zhao, Y., Wang, G., Wang, Y., Xiao, T., Adil, M. A., Lu, G., Zhang, J., and Wei, Z., A Sequential Slot-Die Coated Ternary System Enables Efficient Flexible Organic Solar Cells. *Solar RRL*, **2019**. 3 (3), 1800333.
98. Sankaran, S., Glaser, K., Gärtner, S., Rödlmeier, T., Sudau, K., Hernandez-Sosa, G., and Colsmann, A., Fabrication of polymer solar cells from organic nanoparticle dispersions by doctor blading or ink-jet printing. *Organic Electronics*, **2016**. 28, 118-122.
99. Bernardo, G., Lopes, T., Lidzey, D. G., and Mendes, A., Progress in Upscaling Organic Photovoltaic Devices. *Advanced Energy Materials*, **2021**. 11 (23), 2100342.
100. Pandey, A. K., Nunzi, J. M., Ratier, B., and Moliton, A., Size effect on organic optoelectronics devices: Example of photovoltaic cell efficiency. *Physics Letters A*, **2008**. 372 (8), 1333-1336.
101. Suh, Y., Lu, N., Lee, S. H., Chung, W.-S., Kim, K., Kim, B., Ko, M. J., and Kim, M. J., Degradation of a Thin Ag Layer Induced by Poly(3,4-ethylenedioxythiophene):Polystyrene Sulfonate in a Transmission Electron Microscopy Specimen of an Inverted Polymer Solar Cell. *ACS Applied Materials & Interfaces*, **2012**. 4 (10), 5118-5124.
102. Son, H. J., Park, H.-K., Moon, J. Y., Ju, B.-K., and Kim, S. H., Thermal degradation related to the PEDOT:PSS hole transport layer and back electrode of the flexible inverted organic photovoltaic module. *Sustainable Energy & Fuels*, **2020**. 4 (4), 1974-1983.
103. Giannouli, M., Drakonakis, V. M., Savva, A., Eleftheriou, P., Florides, G., and Choulis, S. A., Methods for improving the lifetime performance of organic photovoltaics with low-costing encapsulation. *ChemPhysChem*, **2015**. 16 (6), 1134-1154.
104. Vitoratos, E., Sakkopoulos, S., Dalas, E., Paliatsas, N., Karageorgopoulos, D., Petraki, F., Kennou, S., and Choulis, S. A., Thermal degradation mechanisms of PEDOT: PSS. *Organic Electronics*, **2009**. 10 (1), 61-66.
105. Kundu, S., Gollu, S. R., Sharma, R., Srinivas, G., Ashok, A., Kulkarni, A., and Gupta, D., Device stability of inverted and conventional bulk heterojunction solar cells with MoO₃ and

- ZnO nanoparticles as charge transport layers. *Organic Electronics*, **2013**. *14* (11), 3083-3088.
106. Kumar, P., Bilen, C., Vaughan, B., Zhou, X., Dastoor, P. C., and Belcher, W. J., Comparing the degradation of organic photovoltaic devices under ISOS testing protocols. *Solar Energy Materials and Solar Cells*, **2016**. *149*, 179-186.
107. Li, Z., Ho Chiu, K., Shahid Ashraf, R., Fearn, S., Dattani, R., Cheng Wong, H., Tan, C.-H., Wu, J., Cabral, J. T., and Durrant, J. R., Toward Improved Lifetimes of Organic Solar Cells under Thermal Stress: Substrate-Dependent Morphological Stability of PCDTBT:PCBM Films and Devices. *Scientific Reports*, **2015**. *5* (1), 15149.

CHAPTER 8 – CONCLUDING SUMMARY

As the global community aims at transferring its energy reliance from polluting non-renewable energy sources to those that have a minimal impact of the environment and human health, there are still challenges that limit these transitions, such as accessibility, reliability, and cost-effectiveness. One promising energy source, photovoltaics (PV), has been shown to be one such example of technology that can lead the energy transition towards being clean, renewable, energy. The issue is, however, their accessibility due to their rigidity and weight means that they are limited to which locations and surfaces they can be installed and operated on.

To allow for PV technology to be more widely accessed globally, new material types, such as organic photovoltaics (OPVs) have shown incredible promise as an energy source to allow for cost-effective and accessible, energy. They can also be designed to be light-weight, flexible, and have the ability to operate under low-light conditions, such as indirect-sunlight and under cloudy conditions [1], as well as from indoor light exposure [2-4]. Though OPVs have shown significant progress in performance, reaching up to 19% power conversion efficiency (PCE) [5, 6], leading to a reduction in the performance gap between OPV and silicon-based PV (26% [7]), however, device lifetime is a major factor that is holding back this technology from being widespread in the commercial market.

One of the most challenging sources of degradation to control is thermal degradation, where due to regular operation of OPVs, especially under continuous illumination from the sun, can lead to an increase in operating temperature, resulting in thermal aging. Though there has been significant investigation towards major thermal degradation pathways [8-13] and strategies for minimising their impact on device lifespan [14-18], many of these strategies that have been tested on small-scale fabrication methods are not translatable to larger scales and OPV manufacturing. As a result, these strategies have only been speculated to improve stability at increased device areas without experimental evidence. The other issue with these strategies is that some have tested on thermally-accelerated aged devices (100 °C – 180 °C [17-29]), where it is assumed that device stability is improved at lower operating temperatures (65 – 85 °C [30]).

The focus of this thesis was to experimentally investigate the degradation behaviour of OPV devices that were fabricated using slot-die coating, a scalable coating method used in large-area manufacturing. The focus was also towards the impact on the change of thermal aging temperatures had on main degradation pathways that were present in OPV aging. To support the argument of the scalability and translatability of the research in this thesis, a device manufacturing method that roll-to-roll compatible [31, 32] was fabricated and tested.

8.1. Summary of conclusions

In chapter 4, it was observed that the PPDT2FBT:fullerene-based devices were thermally stable at 85 °C, yet, showed significant degradation at 120 °C. With the support of scanning electron microscopy (SEM) and Auger electron microscopy (AES), the major source of degradation at 120 °C was associated with fullerene crystallisation, resulting in the decreased device performance in a relatively brief time (24 hours). To reduce the impact of fullerene crystallisation, neat C₆₀ could be added to the additive layer to induce nucleation, resulting a crystal size limit, and thus, reducing the magnitude of degradation. Whereas for the addition of neat C₇₀ led to the reducing of crystal growth rate, rather than nucleation.

To expand on the understanding of the thermal degradation of PPDT2FBT:fullerene devices, in Chapter 5 long-term thermal degradation at 85 °C for 6 months is compared with 120 °C for 20 days. Whereas the 120 °C annealing led to fullerene crystallisation, the 85 °C aging had led to the formation of flat surface features. With the support of SEM, AES, stylus profilometry and neutral impact collision ion scattering spectroscopy (NICISS), it was confirmed that these features also consisted of fullerene. With the support of dynamic mechanical thermal analysis (DMTA), it was concluded that the 85 °C led to morphological changes in the PPDT2FBT:fullerene blend.

With the in-depth insight towards the degradation pathways associated with PPDT2FBT:fullerene, Chapter 6 investigated a range of solid-based additives to influence the thermal degradation pathways, specially, neat C₇₀, piperazine (PP), 4,4'-bipiperidine (BP) and polyacenaphthylene (PAN). In previous literature, these solid-additives had been demonstrated to effectively reduce thermal degradation of the active layer of OPVs at elevated temperatures. At 120 °C, it was observed that all additives were able to influence fullerene crystallisation, with PP, BP and PAN reducing the crystallisation rate, while increasing crystallisation population, leading to a reduced size of crystals due to space-limitation. At 85 °C, however, the addition of PP, BP and PAN in the active layer led to fullerene crystallisation growing at the lower temperature, while speeding up the formation of flat fullerene features. Whereas for neat C₇₀ addition, the rate of flat fullerene feature growth was reduced, and no fullerene crystallisation was observed. Overall, the non-fullerene additives were able to reduce the crystallisation rate at 120 °C, they also allowed for crystallisation to occur at 85 °C, which was otherwise not observed for the standard active layer blend, while the fullerene additive significantly changed the thermal behaviour at both 85 °C and 120 °C, allowing for reduced morphology degradation of the active layer.

To determine the scalability of the results, chapter 7 aimed at following a fabrication process that had been demonstrated in literature to be roll-to-roll scalable. In relation to device performance, it was found the technique for preparing and coating devices containing an active layer of PPDT2FBT:PC₆₁BM, TQ1:PC₆₁BM or PDCBT:ITIC were able to yield decent performances for large active area (12.15 cm²) of 2.3%, 1.7% and 2.0%, respectively .

As for the thermal stability of the PPDT2FBT:PC₆₁BM devices, it was found that the conventional configuration was less stable than the inverted configuration implemented in chapters 4 – 6. This issue was exacerbated upon the addition of solid-additives (neat C₇₀, PP, BP, or PAN). These results highlighted that, though the fabrication technique is relatively scalable to increased active area, the techniques for improving active layer stability may accelerate degradation pathways associated with other layers such as interfacial materials and electrodes.

8.2. Potential for Future research

Through this thesis study, this work has shown, in-depth, the major degradation pathways associated with morphological changes to the active layer containing a polymer:fullerene blend. It has also been shown how these degradation pathways can be influenced with the addition of solid-additives to the active layer, leading to changes to either thermal behaviour of the blend, or crystallisation of the fullerene. Yet, this is only one example of the many active layer blends that exist within the field of OPVs. Even when focusing on materials that can be printed to scale under ambient conditions, there are several active blends that exist, following under the category of either polymer:fullerene, polymer:non-fullerene small molecule, or polymer:polymer. Despite this, this work has demonstrated an array of methods to investigate the thermal degradation behaviour of the active layer.

The other aspect of this thesis work is the control of other degradation sources to purely focus on thermal aging. As such, the high temperature dark storage aging environment was conducted under nitrogen conditions, however, in real operating conditions, OPVs will be exposed to varying levels of light intensity, oxygen and moisture in its surrounds, as well as elevated temperatures [30, 33-35]. It is also expected that the temperature of these devices won't be constant, resulting in thermal cycling between higher and lower temperatures [30, 36, 37]. There are still issues when comparing indoor aging studies using simulated degradation methods, with real-life outdoor conditions [36, 38], however, as Greenbank *et al.* concluded from their outdoor/indoor degradation studies, that range of testing conditions and protocols developed by the international summit on OPV stability (ISOS) community [30] should be implemented before making more accurate conclusions associated with degradation, especially in relation to the active layer [36]. Several published literatures have shown successful demonstrations of comparing ISOS degradation protocols to gain a more insightful understanding in OPV degradation [34, 39-41].

In terms of investigating the thermal behaviour of polymer:fullerene blend throughout this thesis, the DMTA has been demonstrated to be a powerful analysis technique for investigating the changes. From previously published literature, DMTA has predominately been used to investigate the glass transition of select pristine organic samples and material blends [42-44], with some literature focusing on thermal transitional changes upon mixing with different material blends [45] and solvents [46, 47].

Besides the work conducted in this thesis work, there has been a couple of published literature that has used the DMTA to investigate thermal behaviour and morphological changes to thermal stability [48]. This is in contrast to techniques such as grazing-incidence wide angle x-ray scattering (GIWAXS) [25, 49-51] and differential scanning calorimetry (DSC) [25, 49-53], where morphological changes to the active layer have been observed for several systems.

With the strengths of the DMTA technique, and the lack of literature implementing the technique to relate with changes to thermally aged pristine and blend systems, more work can be done to gain an increase in an understanding of active layer blend degradation, and how additives influence thermal behaviour of pristine materials. As mentioned previously, it is suspected that OPV temperature during operation would be fluctuating, rather than being constant. As such, it is important to compare cyclic thermal aging with constant thermal aging, and how thermal transitions are influenced. Previously, the DMTA has been shown to be operational via heating and cooling [48], allowing for the method to be able to pre-age prior to measuring samples.

As observed in Chapter 7, it was noticed that a major source of degradation for the conventional devices was due to PEDOT:PSS degradation, a layer not used for inverted devices used in Chapters 4 – 6. When solid-additives were included into the active layer, there was a significant decay in performance within the first 24 hours, with the decrease likely associated with the accelerated degradation of the PEDOT:PSS.

Overall, the slot-die-based MRC OPV fabrication method has been demonstrated to test the scalability of strategies for influencing thermal stability of the active layer. This thesis work has shown the implementation of the DMTA to investigate morphological and thermal behaviour changes upon thermally aged samples, allowing for determination of degradation pathways. In saying that, further effort is required to gain a more in-depth understanding associated with the thermal behaviour of blends, as well as how different additives interact with individual materials.

8.3. References

1. Holliday, S., Li, Y., and Luscombe, C. K., Recent advances in high performance donor-acceptor polymers for organic photovoltaics. *Progress in Polymer Science*, **2017**. *70*, 34-51.
2. Ylikunnari, M., Välimäki, M., Väisänen, K.-L., Kraft, T. M., Sliz, R., Corso, G., Po, R., Barbieri, R., Carbonera, C., Gorni, G., and Vilkmann, M., Flexible OPV modules for highly efficient indoor applications. *Flexible and Printed Electronics*, **2020**. *5* (1), 014008.
3. Alkhatib, H., Pasquinelli, M., Escoubas, L., Simon, J. J., Pierron, P., and Dkhil, S. B., Lifetime of inkjet printing OPV modules for indoor applications. **2019**.
4. Mainville, M. and Leclerc, M., Recent Progress on Indoor Organic Photovoltaics: From Molecular Design to Production Scale. *ACS Energy Letters*, **2020**. *5* (4), 1186-1197.
5. Zhu, L., Zhang, M., Xu, J., Li, C., Yan, J., Zhou, G., Zhong, W., Hao, T., Song, J., Xue, X., Zhou, Z., Zeng, R., Zhu, H., Chen, C.-C., MacKenzie, R. C. I., Zou, Y., Nelson, J., Zhang, Y., Sun, Y., and Liu, F., Single-junction organic solar cells with over 19% efficiency enabled by a refined double-fibril network morphology. *Nature Materials*, **2022**. *21* (6), 656-663.
6. Ding, G., Chen, T., Wang, M., Xia, X., He, C., Zheng, X., Li, Y., Zhou, D., Lu, X., Zuo, L., Xu, Z., and Chen, H., Solid Additive-Assisted Layer-by-Layer Processing for 19% Efficiency Binary Organic Solar Cells. *Nano-Micro Letters*, **2023**. *15* (1), 92.
7. Yoshikawa, K., Kawasaki, H., Yoshida, W., Irie, T., Konishi, K., Nakano, K., Uto, T., Adachi, D., Kanematsu, M., and Uzu, H., Silicon heterojunction solar cell with interdigitated back contacts for a photoconversion efficiency over 26%. *Nature energy*, **2017**. *2* (5), 17032.
8. Paci, B., Generosi, A., Rossi Albertini, V., Perfetti, P., de Bettignies, R., Leroy, J., Firon, M., and Sentein, C., Controlling photoinduced degradation in plastic photovoltaic cells: A time-resolved energy dispersive x-ray reflectometry study. *Applied physics letters*, **2006**. *89* (4), 043507.
9. Andreasen, J. W., Gevorgyan, S. A., Schlepütz, C. M., and Krebs, F. C., Applicability of X-ray reflectometry to studies of polymer solar cell degradation. *Solar energy materials and solar cells*, **2008**. *92* (7), 793-798.
10. Yang, X., Loos, J., Veenstra, S. C., Verhees, W. J., Wienk, M. M., Kroon, J. M., Michels, M. A., and Janssen, R. A., Nanoscale morphology of high-performance polymer solar cells. *Nano letters*, **2005**. *5* (4), 579-583.
11. Krebs, F. C., Alstrup, J., Spanggaard, H., Larsen, K., and Kold, E., Production of large-area polymer solar cells by industrial silk screen printing, lifetime considerations and lamination with polyethyleneterephthalate. *Solar Energy Materials and Solar Cells*, **2004**. *83* (2), 293-300.
12. Krebs, F. C., Biancardo, M., Winther-Jensen, B., Spanggaard, H., and Alstrup, J., Strategies for incorporation of polymer photovoltaics into garments and textiles. *Solar Energy Materials and Solar Cells*, **2006**. *90* (7-8), 1058-1067.
13. Winther-Jensen, B. and Krebs, F. C., High-conductivity large-area semi-transparent electrodes for polymer photovoltaics by silk screen printing and vapour-phase deposition. *Solar Energy Materials and Solar Cells*, **2006**. *90* (2), 123-132.
14. Lindqvist, C., Sanz-Velasco, A., Wang, E., Bäcke, O., Gustafsson, S., Olsson, E., Andersson, M. R., and Müller, C., Nucleation-limited fullerene crystallisation in a polymer-fullerene bulk-heterojunction blend. *Journal of Materials Chemistry A*, **2013**. *1* (24), 7174-7180.
15. Lindqvist, C., Stability of Bulk-heterojunction Blends for Solar Cell Applications. 2014: Chalmers University of Technology.
16. Lindqvist, C., Bergqvist, J., Feng, C. C., Gustafsson, S., Bäcke, O., Treat, N. D., Bounioux, C., Henriksson, P., Kroon, R., Wang, E., Sanz-Velasco, A., Kristiansen, P. M., Stingelin, N., Olsson, E., Inganäs, O., Andersson, M. R., and Müller, C., Fullerene nucleating agents: a route towards thermally stable photovoltaic blends. *Advanced Energy Materials*, **2014**. *4* (9), 1301437.
17. Feng, W., Lin, Z., Cui, J., Lv, W., Wang, W., and Ling, Q., Photoactive layer crosslinking in all-polymer solar cells: Stabilized morphology and enhanced thermal-stability. *Solar Energy Materials and Solar Cells*, **2019**. *200*, 109982.
18. He, Y., Heumüller, T., Lai, W., Feng, G., Classen, A., Du, X., Liu, C., Li, W., Li, N., and Brabec, C. J., Evidencing Excellent Thermal- and Photostability for Single-Component

- Organic Solar Cells with Inherently Built-In Microstructure. *Advanced Energy Materials*, **2019**. 9 (21), 1900409.
19. Hong, L., Yao, H., Cui, Y., Yu, R., Lin, Y.-W., Chen, T.-W., Xu, Y., Qin, J., Hsu, C.-S., Ge, Z., and Hou, J., Simultaneous Improvement of Efficiency and Stability of Organic Photovoltaic Cells by using a Cross-Linkable Fullerene Derivative. *Small*, **2021**. 17 (24), 2101133.
 20. Xian, K., Zhang, S., Xu, Y., Liu, J., Zhou, K., Peng, Z., Li, M., Zhao, W., Chen, Y., Fei, Z., Hou, J., Geng, Y., and Ye, L., Refining acceptor aggregation in nonfullerene organic solar cells to achieve high efficiency and superior thermal stability. *Science China Chemistry*, **2023**. 66 (1), 202-215.
 21. Zheng, N., Mahmood, K., Zhong, W., Liu, F., Zhu, P., Wang, Z., Xie, B., Chen, Z., Zhang, K., Ying, L., Huang, F., and Cao, Y., Improving the efficiency and stability of non-fullerene polymer solar cells by using N2200 as the Additive. *Nano Energy*, **2019**. 58, 724-731.
 22. Wang, Z., Hong, Z., Zhuang, T., Chen, G., Sasabe, H., Yokoyama, D., and Kido, J., High fill factor and thermal stability of bilayer organic photovoltaic cells with an inverted structure. *Applied Physics Letters*, **2015**. 106 (5), 053305.
 23. Xu, X., Fukuda, K., Karki, A., Park, S., Kimura, H., Jinno, H., Watanabe, N., Yamamoto, S., Shimomura, S., and Kitazawa, D., Thermally stable, highly efficient, ultraflexible organic photovoltaics. *Proceedings of the National Academy of Sciences*, **2018**. 115 (18), 4589-4594.
 24. Song, S., Lee, K. T., Koh, C. W., Shin, H., Gao, M., Woo, H. Y., Vak, D., and Kim, J. Y., Hot slot die coating for additive-free fabrication of high performance roll-to-roll processed polymer solar cells. *Energy & Environmental Science*, **2018**. 11 (11), 3248-3255.
 25. Yin, J., Zhou, W., Zhang, L., Xie, Y., Yu, Z., Shao, J., Ma, W., Zeng, J., and Chen, Y., Improved Glass Transition Temperature towards Thermal Stability via Thiols Solvent Additive versus DIO in Polymer Solar Cells. *Macromolecular Rapid Communications*, **2017**. 38 (20), 1700428.
 26. Zhang, C., Mumyatov, A., Langner, S., Perea, J. D., Kassar, T., Min, J., Ke, L., Chen, H., Gerasimov, K. L., Anokhin, D. V., Ivanov, D. A., Ameri, T., Osvet, A., Susarova, D. K., Unruh, T., Li, N., Troshin, P., and Brabec, C. J., Overcoming the Thermal Instability of Efficient Polymer Solar Cells by Employing Novel Fullerene-Based Acceptors. *Advanced Energy Materials*, **2017**. 7 (3), 1601204.
 27. Chao, Y.-C., Chuang, C.-H., Hsu, H.-L., Wang, H.-J., Hsu, Y.-C., Chen, C.-P., and Jeng, R.-J., Enhanced thermal stability of organic photovoltaics via incorporating triphenylamine derivatives as additives. *Solar Energy Materials and Solar Cells*, **2016**. 157, 666-675.
 28. Grant, T. M., Gorisse, T., Dautel, O., Wantz, G., and Lessard, B. H., Multifunctional ternary additive in bulk heterojunction OPV: increased device performance and stability. *Journal of Materials Chemistry A*, **2017**. 5 (4), 1581-1587.
 29. Zhang, Z., Miao, J., Ding, Z., Kan, B., Lin, B., Wan, X., Ma, W., Chen, Y., Long, X., Dou, C., Zhang, J., Liu, J., and Wang, L., Efficient and thermally stable organic solar cells based on small molecule donor and polymer acceptor. *Nature Communications*, **2019**. 10 (1), 3271.
 30. Reese, M. O., Gevorgyan, S. A., Jørgensen, M., Bundgaard, E., Kurtz, S. R., Ginley, D. S., Olson, D. C., Lloyd, M. T., Morvillo, P., Katz, E. A., Elschner, A., Haillant, O., Currier, T. R., Shrotriya, V., Hermenau, M., Riede, M., R. Kirov, K., Trimmel, G., Rath, T., Inganäs, O., Zhang, F., Andersson, M., Tvingstedt, K., Lira-Cantu, M., Laird, D., McGuinness, C., Gowrisanker, S., Pannone, M., Xiao, M., Hauch, J., Steim, R., DeLongchamp, D. M., Rösch, R., Hoppe, H., Espinosa, N., Urbina, A., Yaman-Uzunoglu, G., Bonekamp, J.-B., van Breemen, A. J. J. M., Giroto, C., Voroshazi, E., and Krebs, F. C., Consensus stability testing protocols for organic photovoltaic materials and devices. *Solar Energy Materials and Solar Cells*, **2011**. 95 (5), 1253-1267.
 31. Andersen, T. R., Almyahi, F., Cooling, N. A., Elkington, D., Wiggins, L., Fahy, A., Feron, K., Vaughan, B., Griffith, M. J., and Mozer, A. J., Comparison of inorganic electron transport layers in fully roll-to-roll coated/printed organic photovoltaics in normal geometry. *Journal of Materials Chemistry A*, **2016**. 4 (41), 15986-15996.
 32. Hart, A. S., Andersen, T. R., Griffith, M. J., Fahy, A., Vaughan, B., Belcher, W. J., and Dastoor, P. C., Roll-to-roll solvent annealing of printed P3HT : ICXA devices. *RSC Advances*, **2019**. 9 (72), 42294-42305.

33. Jørgensen, M., Norrman, K., and Krebs, F. C., Stability/degradation of polymer solar cells. *Solar Energy Materials and Solar Cells*, **2008**. 92 (7), 686-714.
34. Kettle, J., Stoichkov, V., Kumar, D., Corazza, M., Gevorgyan, S. A., and Krebs, F. C., Using ISOS consensus test protocols for development of quantitative life test models in ageing of organic solar cells. *Solar Energy Materials and Solar Cells*, **2017**. 167, 53-59.
35. Bristow, N. and Kettle, J., Outdoor performance of organic photovoltaics: Diurnal analysis, dependence on temperature, irradiance, and degradation. *Journal of Renewable and Sustainable Energy*, **2015**. 7 (1).
36. Greenbank, W., Djeddaoui, N., Destouesse, E., Lamminaho, J., Prete, M., Boukezzi, L., Ebel, T., Bessissa, L., Rubahn, H.-G., Turkovic, V., and Madsen, M., Degradation Behavior of Scalable Nonfullerene Organic Solar Cells Assessed by Outdoor and Indoor ISOS Stability Protocols. *Energy Technology*, **2020**. 8 (12), 2000295.
37. Dolara, A., Fazio, G. d., Leva, S., Manzolini, G., Simonetti, R., and Terenzi, A., Outdoor Assessment and Performance Evaluation of OPV Modules. *IEEE Journal of Photovoltaics*, **2021**. 11 (2), 391-399.
38. Owens, C., Ferguson, G. M., Hermenau, M., Voroshazi, E., Galagan, Y., Zimmermann, B., Rösch, R., Angmo, D., Teran-Escobar, G., Uhrich, C., Andriessen, R., Hoppe, H., Würfel, U., Lira-Cantu, M., Krebs, F. C., and Tanenbaum, D. M., Comparative Indoor and Outdoor Degradation of Organic Photovoltaic Cells via Inter-laboratory Collaboration. *Polymers*, **2016**. 8 (1), 1.
39. Kumar, P., Bilen, C., Vaughan, B., Zhou, X., Dastoor, P. C., and Belcher, W. J., Comparing the degradation of organic photovoltaic devices under ISOS testing protocols. *Solar Energy Materials and Solar Cells*, **2016**. 149, 179-186.
40. dos Reis Benatto, G. A., Roth, B., Corazza, M., Søndergaard, R. R., Gevorgyan, S. A., Jørgensen, M., and Krebs, F. C., Roll-to-roll printed silver nanowires for increased stability of flexible ITO-free organic solar cell modules. *Nanoscale*, **2016**. 8 (1), 318-326.
41. Al-Ahmad, A., Vaughan, B., Holdsworth, J., Belcher, W., Zhou, X., and Dastoor, P., The Role of the Electron Transport Layer in the Degradation of Organic Photovoltaic Cells. *Coatings*, **2022**. 12 (8), 1071.
42. Hajduk, B., Bednarski, H., Jarzabek, B., Janeczka, H., and Nitschke, P., P3HT:PCBM blend films phase diagram on the base of variable-temperature spectroscopic ellipsometry. *Beilstein Journal of Nanotechnology*, **2018**. 9, 1108-1115.
43. Pearson, A. J., Wang, T., Jones, R. A. L., Lidzey, D. G., Staniec, P. A., Hopkinson, P. E., and Donald, A. M., Rationalizing Phase Transitions with Thermal Annealing Temperatures for P3HT:PCBM Organic Photovoltaic Devices. *Macromolecules*, **2012**. 45 (3), 1499-1508.
44. Holmes, N. P., Marks, M., Cave, J. M., Feron, K., Barr, M. G., Fahy, A., Sharma, A., Pan, X., Kilcoyne, D. A. L., Zhou, X., Lewis, D. A., Andersson, M. R., van Stam, J., Walker, A. B., Moons, E., Belcher, W. J., and Dastoor, P. C., Engineering Two-Phase and Three-Phase Microstructures from Water-Based Dispersions of Nanoparticles for Eco-Friendly Polymer Solar Cell Applications. *Chemistry of Materials*, **2018**. 30 (18), 6521-6531.
45. Hopkinson, P. E., Staniec, P. A., Pearson, A. J., Dunbar, A. D. F., Wang, T., Ryan, A. J., Jones, R. A. L., Lidzey, D. G., and Donald, A. M., A Phase Diagram of the P3HT:PCBM Organic Photovoltaic System: Implications for Device Processing and Performance. *Macromolecules*, **2011**. 44 (8), 2908-2917.
46. Sharma, A., Pan, X., Campbell, J. A., Andersson, M. R., and Lewis, D. A., Unravelling the thermomechanical properties of bulk heterojunction blends in polymer solar cells. *Macromolecules*, **2017**. 50 (8), 3347-3354.
47. Pan, X., Sharma, A., Gedefaw, D., Kroon, R., de Zerio, A. D., Holmes, N. P., Kilcoyne, A. L. D., Barr, M. G., Fahy, A., and Marks, M., Environmentally friendly preparation of nanoparticles for organic photovoltaics. *Organic Electronics*, **2018**. 59, 432-440.
48. Erhardt, A., Hochgesang, A., Meichsner, F., and Thelakkat, M., High electron mobility and tuneable glass transition temperature in fullerene-functionalized polynorbornenes. *Journal of Materials Chemistry C*, **2022**. 10 (16), 6419-6428.
49. Chen, F., Zhang, Y., Wang, Q., Gao, M., Kirby, N., Peng, Z., Deng, Y., Li, M., and Ye, L., High Tg Polymer Insulator Yields Organic Photovoltaic Blends with Superior Thermal Stability at 150 oC. *Chinese Journal of Chemistry*, **2021**. 39 (9), 2570-2578.

50. Lee, K. C., An, N. G., Lee, S. M., Heo, J., Kim, D. S., Kim, J. Y., and Yang, C., Influence of the Crystalline Nature of Small Donors Molecules on the Efficiency and Stability of Organic Photovoltaic Devices. *Solar RRL*, **2018**. 2 (4), 1700235.
51. Lee, Y.-H., Chen, W.-C., Chiang, C.-J., Kau, K.-C., Liou, W.-S., Lee, Y.-P., Wang, L., and Dai, C.-A., A new strategy for fabricating organic photovoltaic devices with stable D/A double-channel network to enhance performance using self-assembling all-conjugated diblock copolymer. *Nano Energy*, **2015**. 13, 103-116.
52. Bourque, A. J., Engmann, S., Fuster, A., Snyder, C. R., Richter, L. J., Geraghty, P. B., and Jones, D. J., Morphology of a thermally stable small molecule OPV blend comprising a liquid crystalline donor and fullerene acceptor. *Journal of Materials Chemistry A*, **2019**. 7 (27), 16458-16471.
53. Zhu, M., Kim, H., Jang, Y. J., Park, S., Ryu, D. Y., Kim, K., Tang, P., Qiu, F., Kim, D. H., and Peng, J., Toward high efficiency organic photovoltaic devices with enhanced thermal stability utilizing P3HT-b-P3PHT block copolymer additives. *Journal of Materials Chemistry A*, **2016**. 4 (47), 18432-18443.

APPENDICES

The appendices have been separated into different sections, with the first section, *Appendix A*, containing supportive information for device performance of PPDT2FBT:PC₆₁BM, containing two different batches of PPDT2FBT. *Appendix B*, is the reformatted supportive information document for *Chapter 4*, a reformatted text that has been published in *Materials Advances* (see Contextual statement). *Appendix C & D* is supportive information connected with Chapters 5 – 7, while Appendix C is focused on experimental details, such as material synthesis, slot-die coated thin film thickness calculations and Dynamic mechanical thermal analysis sample preparation. Appendix D is focused on raw data that was gathered for the thesis, including atomic force microscopy images, as well as scan locations and raw Auger electron spectroscopy spectra.

Appendix A – OPV device performances for cells that utilised different PPDT2FBT polymer batches.

In this appendix is the device performance values in relation to two batches of PPDT2FBT that have been used for OPV fabrication in this thesis work. Appendix includes experimental procedure (*Section D.1.*), as well as device performance values from JV-curve characteristics (*Section D.2.*).

A.1. Experimental section

Slot-die coated devices were fabricated in a PET/ITO/ZnO NP/BHJ layer/MoO_x/Al device configuration for the BHJ layer of PPDT2FBT:PC₆₁BM. Active layer ink was prepared by dissolving materials, with a donor:acceptor weight ratio of 1:2, in ortho-dichlorobenzene (total 25 mg mL⁻¹ or 14 mg mL⁻¹) with 0.5% V/V of 1-chloronaphthalene at 60 °C overnight.

The flexible ITO substrate (50 ohm/sq, Dongguan Hongdian Technology Co.) was attached to a mini-roll coater (FOM technologies) with slot-die attachment (13 mm width meniscus guide) and wiped with isopropanol soaked TerriWipes at a rotation speed of 2 m min⁻¹ prior to fabrication. The tubing and slot-die head was cleaned with chloroform prior to assembly and between the change of deposition material. Layer deposition was processed under ambient conditions.

The ZnO NP layer (35 nm) was deposited using 0.1 mL min⁻¹ flow-rate, a drum speed of 1.0 m min⁻¹ and drum temperature at 70 °C to achieve a strip width of around 13 mm. The BHJ layer (150 – 200 nm) was deposited via varying flow rate and drum speed at a drum temperature at 70 °C to obtain a strip width of around 13 mm. Wet and dry thickness for both the ZnO NP and BHJ layers were calculated according to *Equation C1 & C2* in *Appendix C*.

After slot-die coating, the MoO_x and aluminium was deposited via the following method. The MoO_x (12nm) was thermally deposited on the BHJ layer under high vacuum using a Covap thermal evaporation system (Angstrom Engineering). This was followed by the evaporation of the Al electrode (80 nm) using a shadow mask, defining the active area to 0.1 cm².

Devices were measured using an Oriel Solar simulator fitted with a 150 W Xeon lamp (Newport), filtered to give an output of 100 mW cm⁻² at AM 1.5 (air mass) standard and calibrated using a silicon reference cell with NIST traceable certification. Device testing was conducted under ambient conditions.

A.2. Device performance results

Table A1: Device performance based on PPDT2FBT:PC61BM devices with different PPDT2FBT batches (C143 & D173). The results are from an average of 6 cells, with an active area of 0.1 cm².

Active layer	Mn (g/mol)	J _{sc} (mA/cm ²)	V _{oc} (V)	FF	PCE (%)
C143:PC61BM (1:2)	50130	16.0 ± 0.4	0.796 ± 0.00	0.62 ± 0.01	7.92 ± 0.12
D173:PC61BM (1:2)	27455	16.1 ± 0.9	0.781 ± 0.00	0.64 ± 0.01	8.02 ± 0.33

Appendix B – Supporting Information for Chapter 4

Appendix B is the reformatted supportive information associated with *Chapter 4*; a reformatted text that has been published in *Materials Advances* (see Contextual statement). The appendix includes content associated with the cost of active layer materials, theoretical equations for calculating slot-die coated thin films, as well as details for square-wave voltammetry and dynamic mechanical thermal analysis. The appendix also includes supporting data for solar simulation measurements, thermal degradation at 85 °C and 120 °C, Auger electron spectroscopy and square-wave voltammetry. Experimental details can be found in the experimental section in *Section 4.3*, as well as in *Chapter 3 – Methodology*.

B.1. Active material costs

Table B1: Estimated material cost of active layer materials based on a scale of 100 g. Prices gathered in December 2021, proved by Organic Nano Electronic (ONE=1) materials.

Material	USD/g
PBDB-T-2F (PM6)	650
PTB7-Th	550
PPDT2FBT	500
P3HT	120
Y6	650
ITIC	350
C ₆₀	25
C ₇₀	75
PC ₆₁ BM	150
PC ₇₁ BM	300

B.2. Slot-die theoretical thickness

To determine the theoretical thickness of the specific layers coated via slot-die coating, the following equations were employed:

$$d_{wet} = \frac{f}{S w} \quad (B1)$$

$$d_{dry} = \frac{f c}{S w \rho} \quad (B2)$$

Where *d* is the thickness (cm), *f* is the flow rate (cm³ min⁻¹), *S* is the drum rotation speed (cm min⁻¹), *w* is the meniscus guide width (cm), *c* is the solid content in the ink (g cm⁻³) and *ρ* is the density of the dried material [1, 2]. The estimated material density polymer to be 1.0 g mL⁻¹, while the densities for PC₆₁BM & C₆₀ are 1.5 g mL⁻¹ [3] and 1.68 g mL⁻¹ [4] respectively. The material densities of PC₇₁BM & C₇₀ are similar to PC₆₁BM & C₆₀ respectively.

B.3. Square-wave voltammetry

A 0.1M of tetrabutylammonium hexafluorophosphate (Bu_4NPF_6) in anhydrous acetonitrile was used as the electrolyte solution. The recorded square-wave voltammograms were referred to ferrocene/ferrocenium (Fc/Fc^+). The working electrode was coated with sample film by dipping it into the respective solutions. All materials were coated from chlorobenzene solutions. The electrolyte solution was purged with nitrogen gas for a minimum of 10 min prior to each measurement.

During the measurements, the electrolyte solution surface was kept under nitrogen atmosphere to ensure inert conditions. Energy levels of the materials were calculated by setting the peak potential of Fc/Fc^+ versus the normal hydrogen electrode (NHE) to 0.630 V and the NHE versus the vacuum level to 4.5 V [5-7]. That is, $E_{\text{HOMO}} = -(E_{\text{ox,peak}} + 5.13)$ and $E_{\text{LUMO}} = -(E_{\text{red,peak}} + 5.13)$.

B.4. Dynamic mechanical thermal analysis

The blend solutions used were the same as the ones used for solar cell fabrication. The prepared samples were dried under high vacuum of approximately 6×10^{-7} torr overnight. The measurements were performed in a strain-controlled tension mode at a heating rate of $3 \text{ }^\circ\text{C min}^{-1}$ from -110 to $300 \text{ }^\circ\text{C}$ under a nitrogen atmosphere at a frequency of 1 Hz. Short-time (30 min) annealing of samples was done in the DMA instrument under a nitrogen atmosphere for 30 min. Whereas long-time (from 1 hour to 1 week) annealing of the sample was done on a hotplate under dark, nitrogen conditions. The storage modulus (E'), loss modulus (E'') and $\text{Tan } \delta$ were recorded as a function of temperature for each sample.

B.5. Solar simulation results

Table B2: Device characteristics of PPDT2FBT:Fullerene devices under different coating conditions.

Fullerene	Drum speed (m min^{-1})	Flow-rate (mL min^{-1})	Ink Conc (mg mL^{-1})	Theoretical thickness ¹ (nm)	J_{sc} (mA cm^{-2})	V_{oc} (V)	FF	PCE (%)
PC ₇₁ BM	1.0	0.100	25.0	150	11.5 ± 0.5	0.77 ± 0.01	0.61 ± 0.01	5.40 ± 0.27
	1.0	0.200	25.0	300	14.4 ± 0.5	0.76 ± 0.02	0.54 ± 0.02	5.99 ± 0.18
	0.2	0.050	14.0	150	14.6 ± 0.6	0.76 ± 0.01	0.61 ± 0.02	6.71 ± 0.16
	0.2	0.050	14.0	200	17.8 ± 0.2	0.77 ± 0.00	0.59 ± 0.00	8.13 ± 0.08
	0.2	0.028	25.0	200	17.9 ± 0.3	0.77 ± 0.01	0.62 ± 0.01	8.49 ± 0.07
PC ₆₁ BM	1.0	0.100	14.0	150	10.5 ± 0.5	0.77 ± 0.01	0.57 ± 0.04	4.65 ± 0.37
	0.2	0.050	14.0	200	14.8 ± 0.3	0.80 ± 0.00	0.62 ± 0.01	7.27 ± 0.09
	0.2	0.035	25.0	200	15.9 ± 0.6	0.78 ± 0.01	0.61 ± 0.01	7.63 ± 0.20

¹ Thermal thickness calculated using equation 2.

Average Cell No.: 6 cells / Device Area: 0.1 cm^2 / Inverted devices

Table B3: Device characteristics of PPDT2FBT:PC₆₁BM devices aging at room temperature under dark nitrogen conditions.

Aging (hr)	J _{SC} (mA cm ⁻²)	V _{OC} (V)	FF	PCE (%)
0.00	15.5 ± 0.2	0.792 ± 0.00	0.62 ± 0.00	7.56 ± 0.11
23.50	14.0 ± 0.2	0.788 ± 0.00	0.66 ± 0.01	7.29 ± 0.09
47.75	14.1 ± 0.3	0.790 ± 0.00	0.64 ± 0.01	7.14 ± 0.12
72.50	14.6 ± 0.3	0.790 ± 0.01	0.62 ± 0.01	7.17 ± 0.12
96.00	14.4 ± 0.4	0.789 ± 0.01	0.63 ± 0.01	7.15 ± 0.31
168.0	14.4 ± 0.1	0.789 ± 0.00	0.63 ± 0.01	7.14 ± 0.14
194.0	13.9 ± 0.4	0.787 ± 0.00	0.63 ± 0.01	6.87 ± 0.08
218.0	13.7 ± 0.3	0.787 ± 0.01	0.62 ± 0.02	6.71 ± 0.12
240.0	14.0 ± 0.3	0.767 ± 0.04	0.64 ± 0.04	6.87 ± 0.16
264.0	13.1 ± 0.3	0.784 ± 0.01	0.61 ± 0.01	6.23 ± 0.12
337.0	13.8 ± 0.2	0.782 ± 0.00	0.61 ± 0.02	6.56 ± 0.13
361.0	14.1 ± 0.5	0.785 ± 0.01	0.62 ± 0.01	6.82 ± 0.29
385.0	14.1 ± 0.6	0.787 ± 0.01	0.60 ± 0.03	6.66 ± 0.14

Average Cell No.: 6 cells / Device Area: 0.1 cm² / Inverted devices

Table B4: Device characteristics of PPDT2FBT:PC₆₁BM devices aging at 85 °C under dark nitrogen conditions.

Aging (hr)	J _{SC} (mA cm ⁻²)	V _{OC} (V)	FF	PCE (%)
0	14.6 ± 0.4	0.775 ± 0.01	0.57 ± 0.02	6.39 ± 0.13
1	14.7 ± 0.4	0.783 ± 0.01	0.60 ± 0.01	6.83 ± 0.19
3	15.3 ± 0.9	0.784 ± 0.00	0.60 ± 0.01	7.15 ± 0.50
21	16.1 ± 0.8	0.777 ± 0.00	0.58 ± 0.02	7.18 ± 0.41
44	16.1 ± 0.3	0.781 ± 0.00	0.59 ± 0.01	7.37 ± 0.22
67	15.4 ± 0.3	0.775 ± 0.00	0.56 ± 0.01	6.64 ± 0.05
131	15.5 ± 0.9	0.775 ± 0.00	0.56 ± 0.02	6.69 ± 0.27
154	14.1 ± 0.7	0.776 ± 0.01	0.55 ± 0.02	5.96 ± 0.30
174	14.2 ± 0.6	0.753 ± 0.06	0.57 ± 0.06	6.05 ± 0.28
222	14.1 ± 0.5	0.780 ± 0.00	0.56 ± 0.01	6.15 ± 0.30
293	12.9 ± 0.3	0.778 ± 0.00	0.54 ± 0.01	5.44 ± 0.20
323	12.4 ± 0.6	0.780 ± 0.00	0.56 ± 0.01	5.39 ± 0.23
344	13.0 ± 0.7	0.756 ± 0.05	0.54 ± 0.01	5.28 ± 0.50
366	13.4 ± 0.5	0.781 ± 0.00	0.53 ± 0.01	5.52 ± 0.22
388	12.5 ± 0.7	0.773 ± 0.01	0.53 ± 0.02	5.10 ± 0.15

Average Cell No.: 6 cells / Device Area: 0.1 cm² / Inverted devices

B.6. Square-wave results

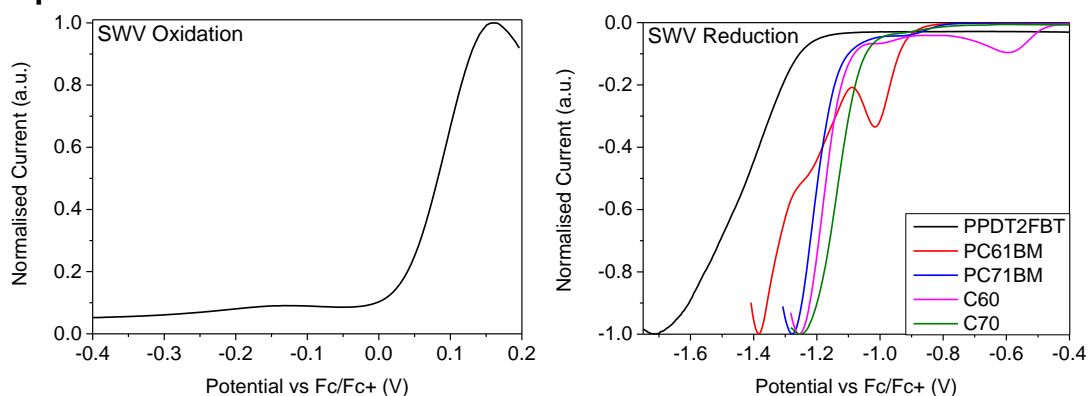


Figure B1: Oxidation square-wave curve of PPDT2FBT (LEFT), as well as Reduction square-wave curves of PPDT2FBT, PC₆₁BM, PC₇₁BM, C₆₀, and C₇₀ (RIGHT).

B.7. Solar simulation light curves

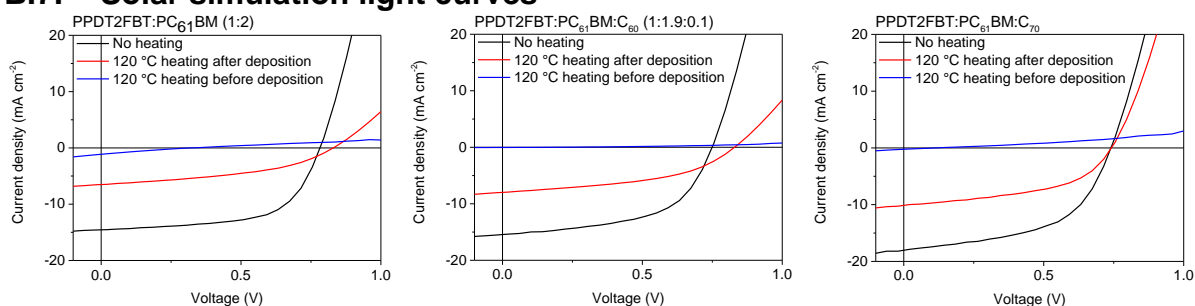


Figure B2: Light current-density / Voltage (JV) curve of PPDT2FBT:PC₆₁BM (1:2) (LEFT), PPDT2FBT:PC₆₁BM:C₆₀ (1:1.9:0.1) (MIDDLE) & PPDT2FBT:PC₆₁BM:C₇₀ (1:1.9:0.1) (RIGHT) after experiencing different heating conditions, prior/post to MoO_x/Al deposition.

B.8. Scanning electron microscopy images

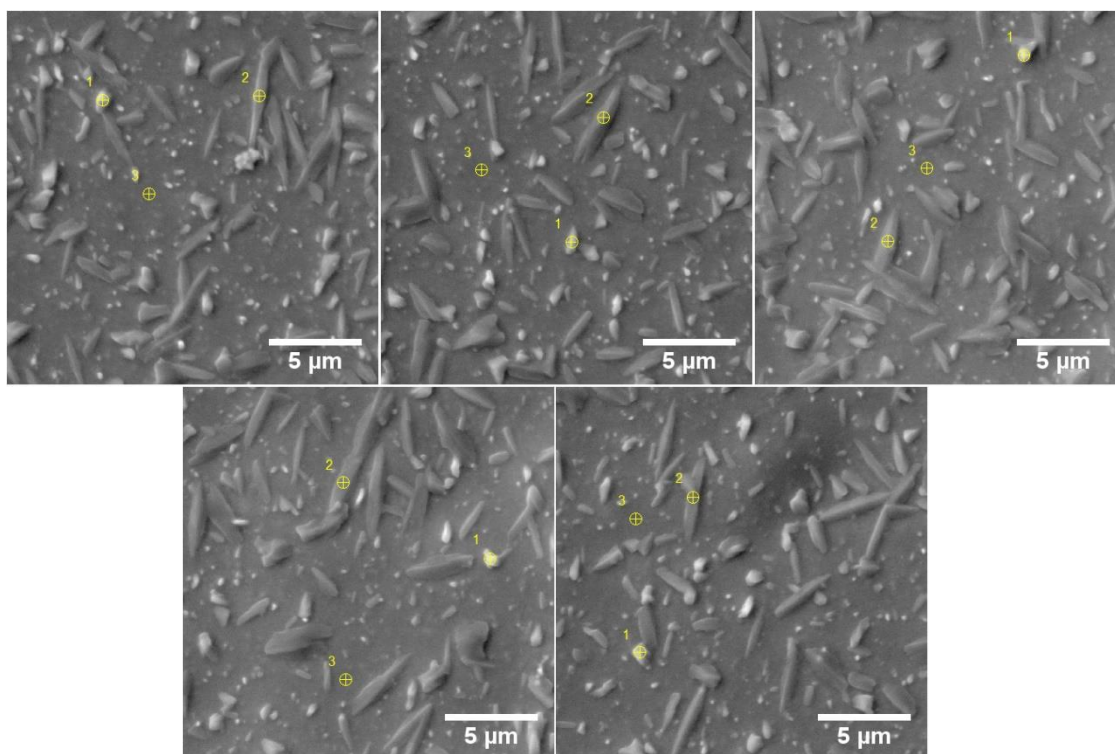


Figure B3: Scanning electron microscopy images of the PPDT2FBT:PC₆₁BM surface after 24 hours at 120 °C with marked locations of Auger electron spectroscopy was measured.

B.9. Auger electron spectroscopy spectra

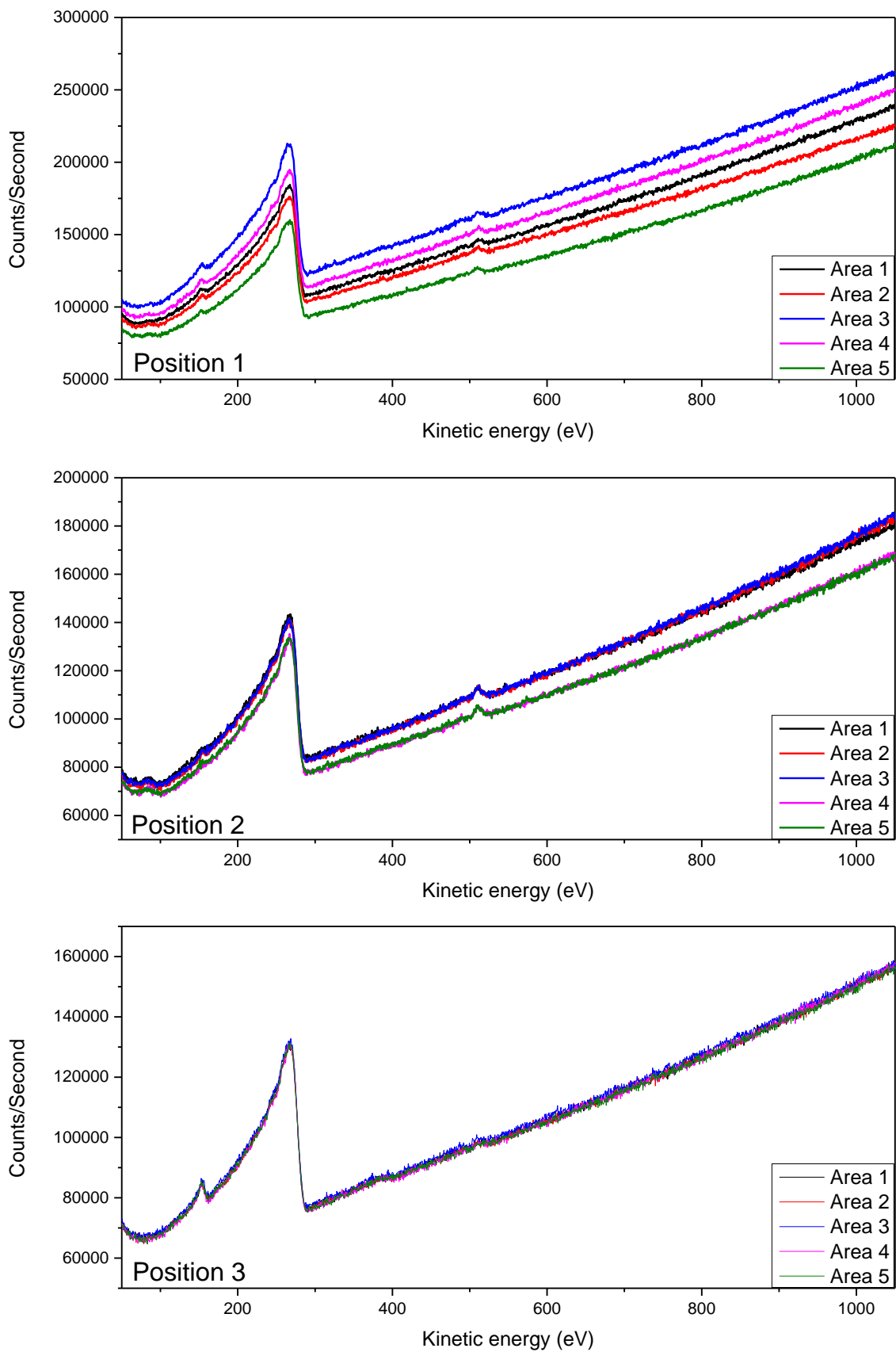


Figure B4: Raw Auger electron spectra of 3 positions (five different point scans per position).

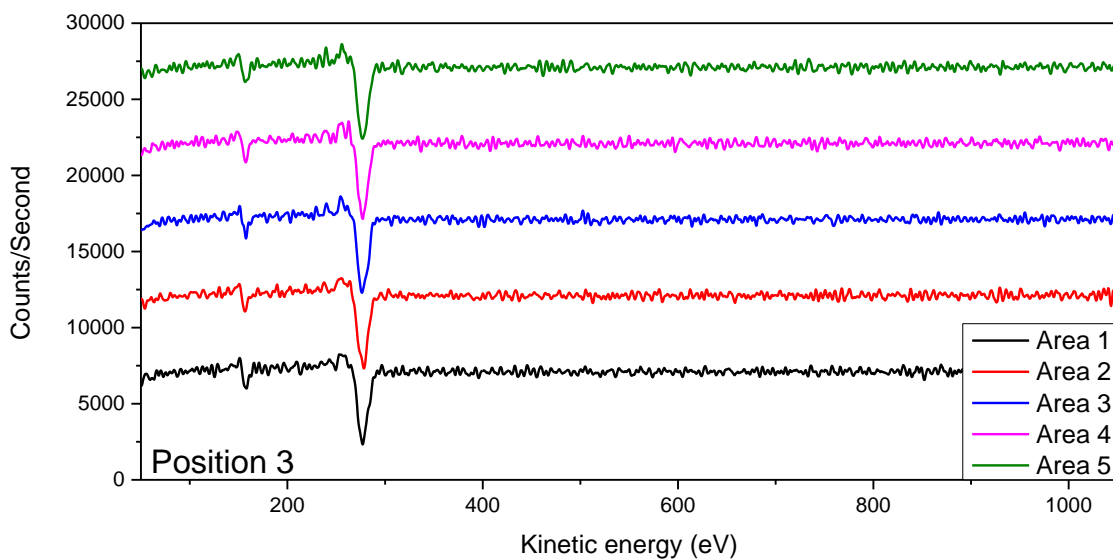
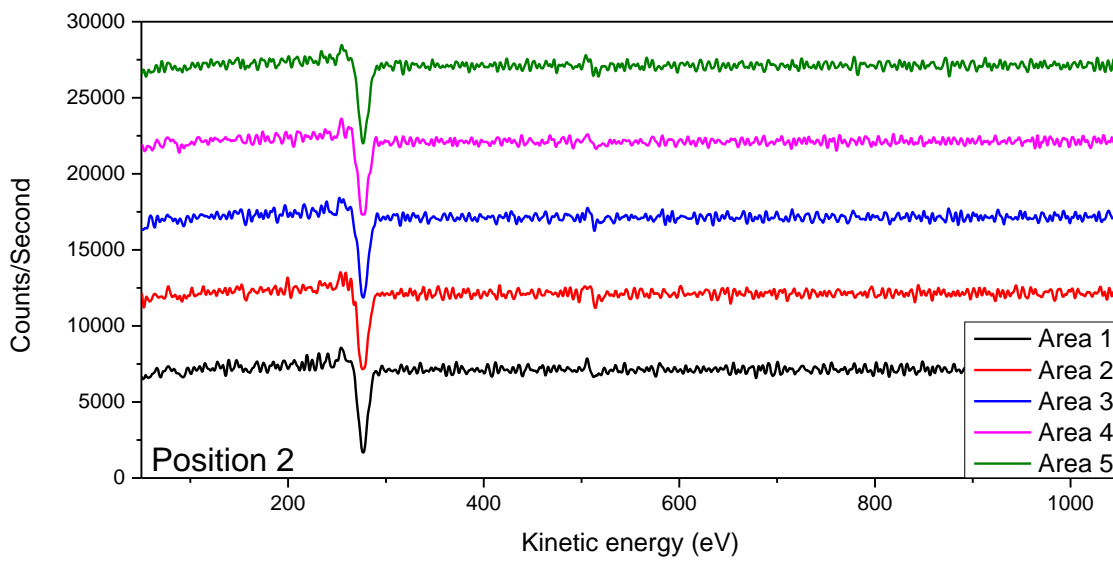
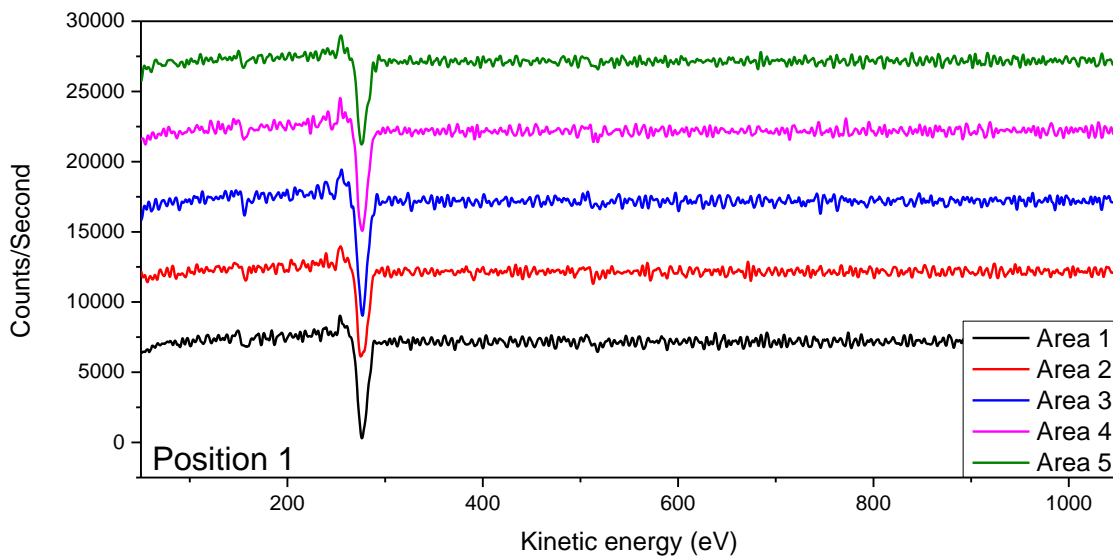


Figure B5: Auger electron spectroscopy scans of 3 positions (five-point scan areas per position). Spectra has been smoothed (9-point Savitzky-Golay) and derived (5-point).

Table B5: Device characteristics of PPDT2FBT:Fullerene devices aging at 120 °C under dark nitrogen conditions.

PPDT2FBT:PC₆₁BM (1:2)				
Aging (hr)	J _{sc} (mA cm ⁻²)	V _{oc} (V)	FF	PCE (%)
0.00	13.8 ± 0.4	0.78 ± 0.00	0.61 ± 0.02	6.52 ± 0.26
1.00	14.9 ± 0.3	0.78 ± 0.00	0.57 ± 0.00	6.56 ± 0.14
4.00	13.7 ± 0.3	0.78 ± 0.01	0.52 ± 0.01	5.49 ± 0.12
24.00	6.3 ± 0.4	0.84 ± 0.02	0.42 ± 0.01	2.22 ± 0.08
42.00	5.7 ± 0.6	0.84 ± 0.02	0.41 ± 0.02	1.98 ± 0.21
66.50	5.5 ± 0.1	0.84 ± 0.00	0.40 ± 0.01	1.83 ± 0.11
137.00	4.5 ± 0.3	0.84 ± 0.07	0.37 ± 0.03	1.38 ± 0.04
155.50	5.0 ± 0.4	0.83 ± 0.01	0.37 ± 0.00	1.54 ± 0.11
180.50	4.7 ± 0.4	0.83 ± 0.01	0.37 ± 0.02	1.46 ± 0.13
PPDT2FBT:PC₆₁BM:C₆₀ (1:1.9:0.1)				
Aging (hr)	J _{sc} (mA cm ⁻²)	V _{oc} (V)	FF	PCE (%)
0.00	15.6 ± 1.1	0.76 ± 0.01	0.57 ± 0.01	6.72 ± 0.24
1.00	14.0 ± 0.9	0.74 ± 0.02	0.49 ± 0.02	5.02 ± 0.22
4.00	10.7 ± 0.4	0.80 ± 0.01	0.47 ± 0.01	4.00 ± 0.08
24.00	7.9 ± 0.2	0.80 ± 0.02	0.45 ± 0.01	2.84 ± 0.11
45.25	7.1 ± 0.3	0.81 ± 0.02	0.43 ± 0.01	2.51 ± 0.03
PPDT2FBT:PC₆₁BM:C₇₀ (1:1.9:0.1)				
Aging (hr)	J _{sc} (mA cm ⁻²)	V _{oc} (V)	FF	PCE (%)
0.00	14.7 ± 0.6	0.74 ± 0.00	0.54 ± 0.02	5.82 ± 0.07
1.00	14.9 ± 0.3	0.74 ± 0.01	0.54 ± 0.01	5.92 ± 0.06
4.00	13.7 ± 0.6	0.73 ± 0.01	0.52 ± 0.01	5.20 ± 0.19
24.00	9.3 ± 0.7	0.74 ± 0.03	0.47 ± 0.01	3.22 ± 0.25
42.00	7.3 ± 0.6	0.78 ± 0.02	0.44 ± 0.01	2.50 ± 0.18
66.50	6.8 ± 0.3	0.79 ± 0.01	0.41 ± 0.01	2.21 ± 0.10
137.00	6.0 ± 0.3	0.81 ± 0.01	0.39 ± 0.02	1.90 ± 0.14
155.50	6.0 ± 0.1	0.80 ± 0.01	0.40 ± 0.01	1.92 ± 0.07
180.50	6.0 ± 0.3	0.80 ± 0.01	0.40 ± 0.02	1.90 ± 0.13

Average Cell No.: 6 cells / Device Area: 0.1 cm²/ Inverted devices

B.10. References

1. Krebs, F. C., Fabrication and processing of polymer solar cells: a review of printing and coating techniques. *Solar energy materials and solar cells*, **2009**. 93 (4), 394-412.
2. Po, R., Bernardi, A., Calabrese, A., Carbonera, C., Corso, G., and Pellegrino, A., From lab to fab: how must the polymer solar cell materials design change? – an industrial perspective. *Energy & Environmental Science*, **2014**. 7 (3), 925-943.
3. Bulle-Lieuwma, C. W. T., Van Gennip, W. J. H., Van Duren, J. K. J., Jonkheijm, P., Janssen, R. A. J., and Niemantsverdriet, J. W., Characterization of polymer solar cells by TOF-SIMS depth profiling. *Applied surface science*, **2003**. 203, 547-550.
4. Frigerio, F., Casalegno, M., Carbonera, C., Nicolini, T., Meille, S. V., and Raos, G., Molecular dynamics simulations of the solvent- and thermal history-dependent structure of the PCBM fullerene derivative. *Journal of Materials Chemistry*, **2012**. 22 (12), 5434-5443.
5. Li, W., Furlan, A., Hendriks, K. H., Wienk, M. M., and Janssen, R. A. J., Efficient tandem and triple-junction polymer solar cells. *Journal of the American Chemical Society*, **2013**. 135 (15), 5529-5532.
6. Pavlishchuk, V. V. and Addison, A. W., Conversion constants for redox potentials measured versus different reference electrodes in acetonitrile solutions at 25 C. *Inorganica Chimica Acta*, **2000**. 298 (1), 97-102.
7. Bard, A. J. and Faulkner, L. R., Fundamentals and applications. *Electrochemical Methods*, **2001**. 2 (482), 580-632.

Appendix C – Methodology and theoretical calculations

This appendix contains supportive information *Chapters 5 – 7*, in connection with the methodology and theoretical calculations. This includes the equation used determining the theoretical wet and dry film thickness from slot-die coating and sample preparation and measurement with the implementation of the Dynamic mechanical thermal analysis technique.

C.1. Active layer material synthesis

Polymer TQ1 was synthesised according to literature [1]. The monomers were purchased from Solarmer® and were purified by recrystallisation before polymerisation. 5,8-dibromo-2,3-bis(3-(octyloxy)phenyl)quinoxaline (12.271 g, 17.616 mmol) and 2,5-bis(trimethylstannyl)thiophene (7.218 g, 17.616 mmol) were dissolved in freshly distilled and pre-degassed toluene (190 mL) and further N₂ gas bubbled for another 30 min after the addition of the monomers.

tris(dibenzylideneacetone)dipalladium(0) (Pd₂(dba)₃) (0.21 g, 0.229 mmol) and tri(o-tolyl)phosphine (0.42 g, 1.374 mmol) were added to the mixture that was further bubbled with N₂ for another 10 minutes. The reaction flask was immersed to an oil bath that was preheated to 100 °C and the reaction was allowed to go for two days.

Then the reaction mixture was poured into 700 mL of ethanol and allowed to stir for a few hours to precipitate the polymer. The solids were filtered and washed with ethanol and acetone. The collected solids were re-dissolved in 500 mL of toluene at 85 °C for 2 h. The solution was passed through a short pad of silica gel to remove the residual catalysts, then precipitated into 2 L of acetone. The dark blue solid was collected using a suction filtration setup with a 0.45 µm PTFE membrane and dried in a vacuum oven. Yield: 10.486 g (95.5%). The molecular weight of TQ1 was determined via Gel Permeation Chromatography using trichlorobenzene at 150 °C, giving a number average molecular weight (M_n) of 52.6 kg/mol with a PDI of 3.29 relative to polystyrene standards.

C.2. Slot-die theoretical thickness

To determine the theoretical thickness of the specific layers coated via slot-die coating, the following equations were employed:

$$d_{wet} = \frac{f}{S w} \quad (C1)$$

$$d_{dry} = \frac{f c}{S w \rho} \quad (C2)$$

Where *d* is the thickness (cm), *f* is the flow rate (cm³ min⁻¹), *S* is the drum rotation speed (cm min⁻¹), *w* is the meniscus guide width (cm), *c* is the solid content in the ink (g cm⁻³) and *ρ* is the density of the dried material [2, 3].

The estimated material density polymer to be 1.0 g mL^{-1} , while the densities for PC₆₁BM & C₆₀ are 1.5 g mL^{-1} [4] and 1.68 g mL^{-1} [5] respectively. The material densities of PC₇₁BM & C₇₀ are similar to PC₆₁BM & C₆₀ respectively.

C.3. Dynamic mechanical thermal analysis

The blend solutions used were the same as the ones used for solar cell fabrication. The prepared samples were dried under high vacuum of approximately 6×10^{-7} torr overnight. The measurements were performed in a strain-controlled tension mode at a heating rate of $3 \text{ }^\circ\text{C min}^{-1}$ from -110 to $300 \text{ }^\circ\text{C}$ under a nitrogen atmosphere at a frequency of 1 Hz . Short-time (30 min) annealing of samples was done in the DMA instrument under a nitrogen atmosphere for 30 min. Whereas long-time (from 1 hour to 1 week) annealing of the sample was done on a hotplate under dark, nitrogen conditions. The storage modulus (E'), loss modulus (E'') and $\tan \delta$ were recorded as a function of temperature for each sample.

C.4. References

1. Wang, E., Hou, L., Wang, Z., Hellström, S., Zhang, F., Inganäs, O., and Andersson, M. R., An easily synthesized blue polymer for high-performance polymer solar cells. *Advanced Materials*, **2010**. 22 (46), 5240-5244.
2. Krebs, F. C., Fabrication and processing of polymer solar cells: a review of printing and coating techniques. *Solar energy materials and solar cells*, **2009**. 93 (4), 394-412.
3. Po, R., Bernardi, A., Calabrese, A., Carbonera, C., Corso, G., and Pellegrino, A., From lab to fab: how must the polymer solar cell materials design change? – an industrial perspective. *Energy & Environmental Science*, **2014**. 7 (3), 925-943.
4. Bulle-Lieuwma, C. W. T., Van Gennip, W. J. H., Van Duren, J. K. J., Jonkheijm, P., Janssen, R. A. J., and Niemantsverdriet, J. W., Characterization of polymer solar cells by TOF-SIMS depth profiling. *Applied surface science*, **2003**. 203, 547-550.
5. Frigerio, F., Casalegno, M., Carbonera, C., Nicolini, T., Meille, S. V., and Raos, G., Molecular dynamics simulations of the solvent- and thermal history-dependent structure of the PCBM fullerene derivative. *Journal of Materials Chemistry*, **2012**. 22 (12), 5434-5443.

Appendix D – Raw spectroscopy, microscopy, and analysis data

In this appendix is the supporting data gathered for chapters 5-7. The data includes images measured from atomic force microscopy (AFM) and scanning electron Microscopy (SEM) images taken from the Auger electron spectroscopy (AES) instrument prior to spectrum scans. The appendix also includes raw data taken from Photo charge extraction by linearly increasing voltage (photo-CELIV), transient photovoltage (TPV) and time-resolved charge extraction (TRCE) for charge carrier dynamics, as well as raw AES spectra for elemental composition investigation.

D.1. Atomic Force Microscopy

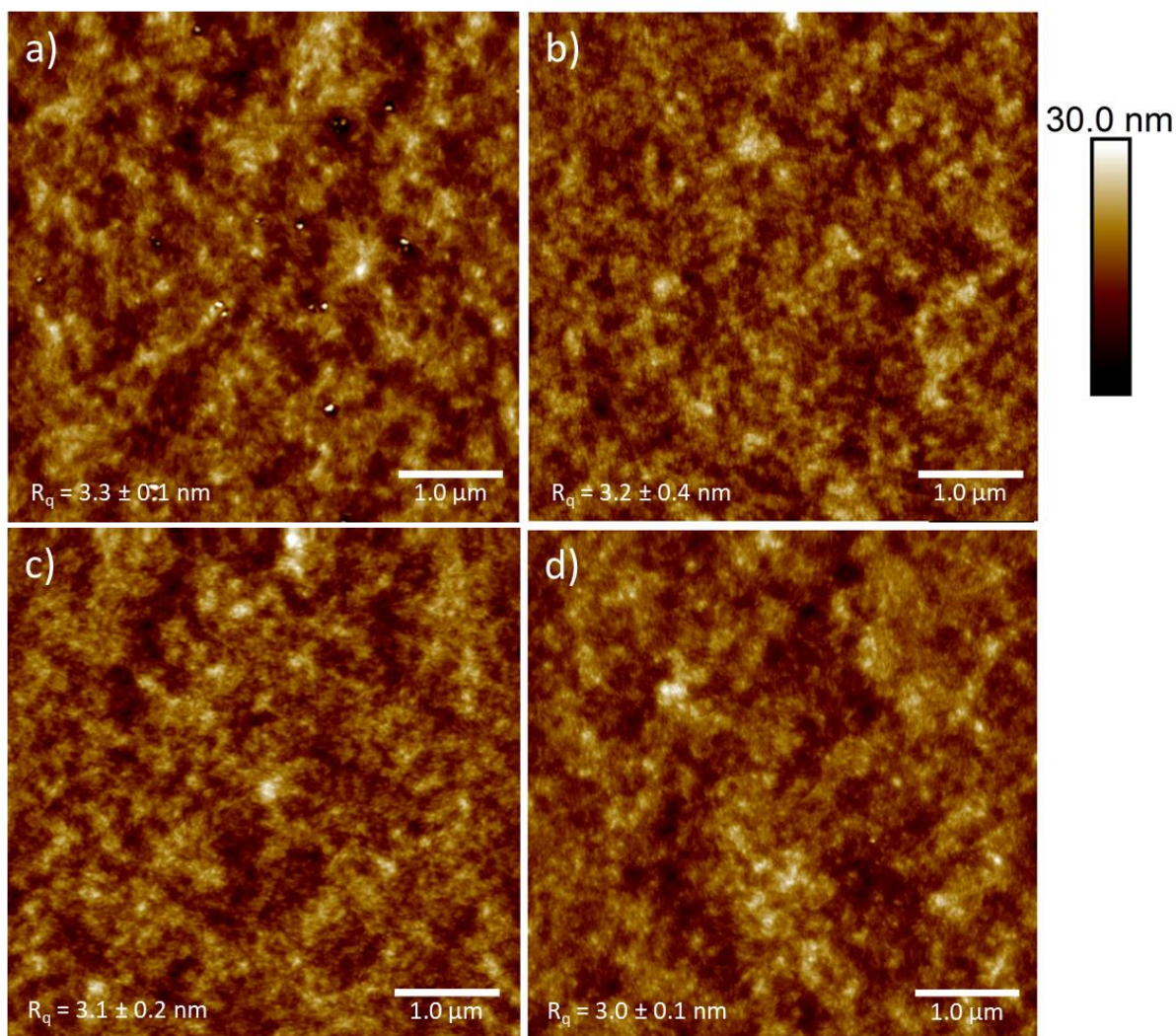


Figure D1: Atomic force microscopy images of surface of PPDT2FBT:PC₆₁BM a), with the addition of either 1.0% w/w PP b), 0.1% w/w BP c) or 1.0% w/w PAN d).

D.2. Scanning Electron Microscopy images from Auger Electron Spectroscopy samples

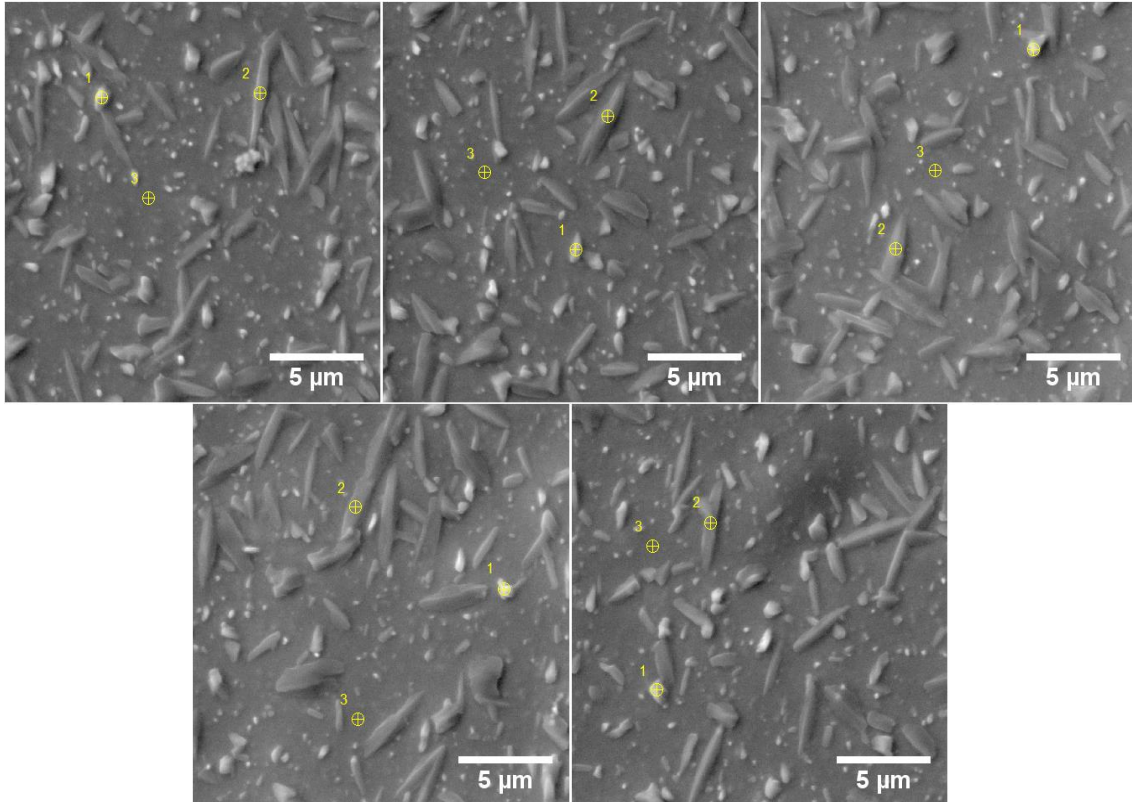


Figure D2: Scanning electron microscopy images of the PPDT2FBT:PC₆₁BM surface after 8 hours at 120 °C with marked locations of Auger electron spectroscopy was measured. Position 1 & 2 is the spot scan location over the short and long crystals, respectively, while position 3 is over the surface of the BHJ.

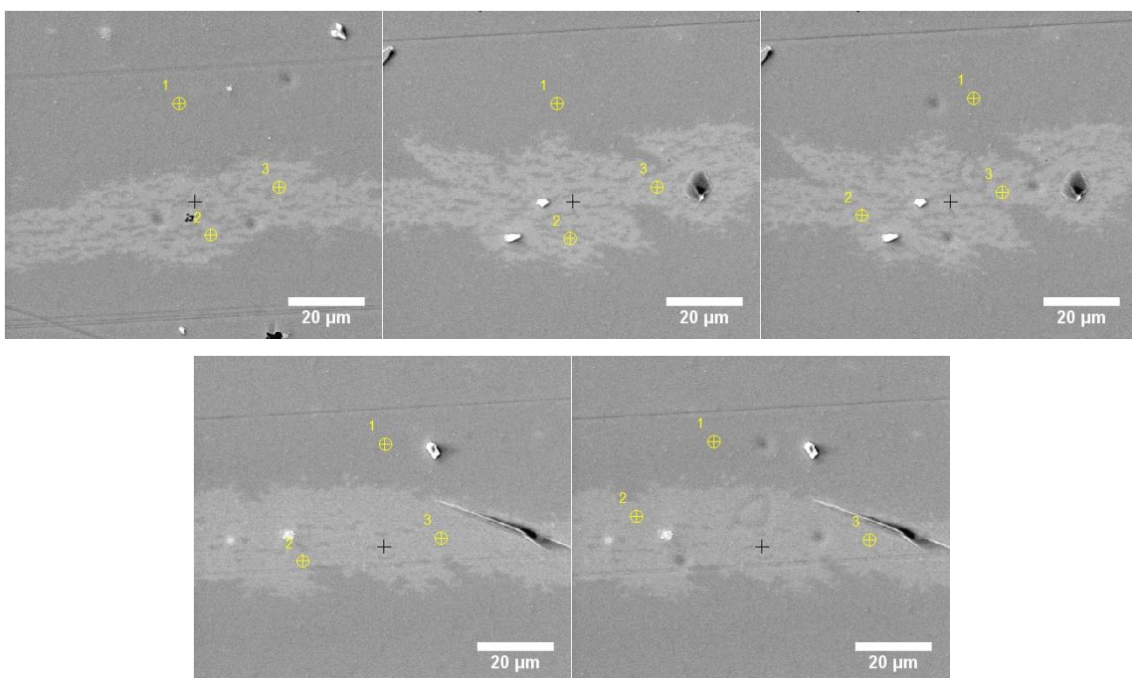


Figure D3: Scanning electron microscopy images of the PPDT2FBT:PC₆₁BM surface after 6 months at 85 °C with marked locations of Auger electron spectroscopy was measured. Position 1 is the surface of the BHJ, while position 2 & 3 is the spot scan location of the flat surface feature.

D.3. Auger Electron Spectra of surface features present on thermally aged PPDT2FBT:PC₆₁BM BHJ

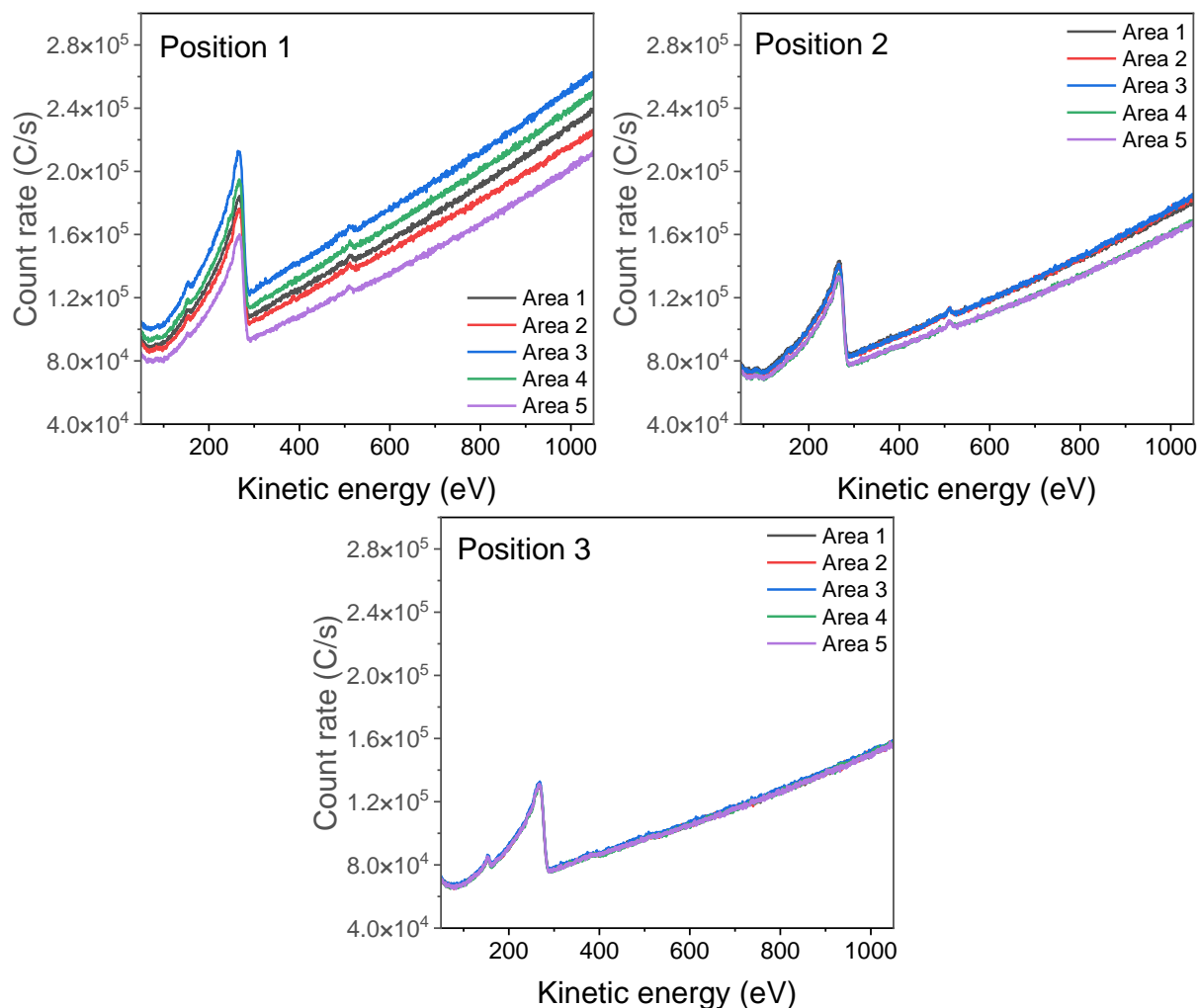


Figure D4: Auger electron spectra of PPDT2FBT:PC₆₁BM surface after 8 hours at 120 °C with marked locations of Auger electron spectroscopy was measured. Position 1 & 2 is the spot scan location over the short and long crystals, respectively, while position 3 is over the surface of the BHJ. Position locations can be seen in Figure D2.

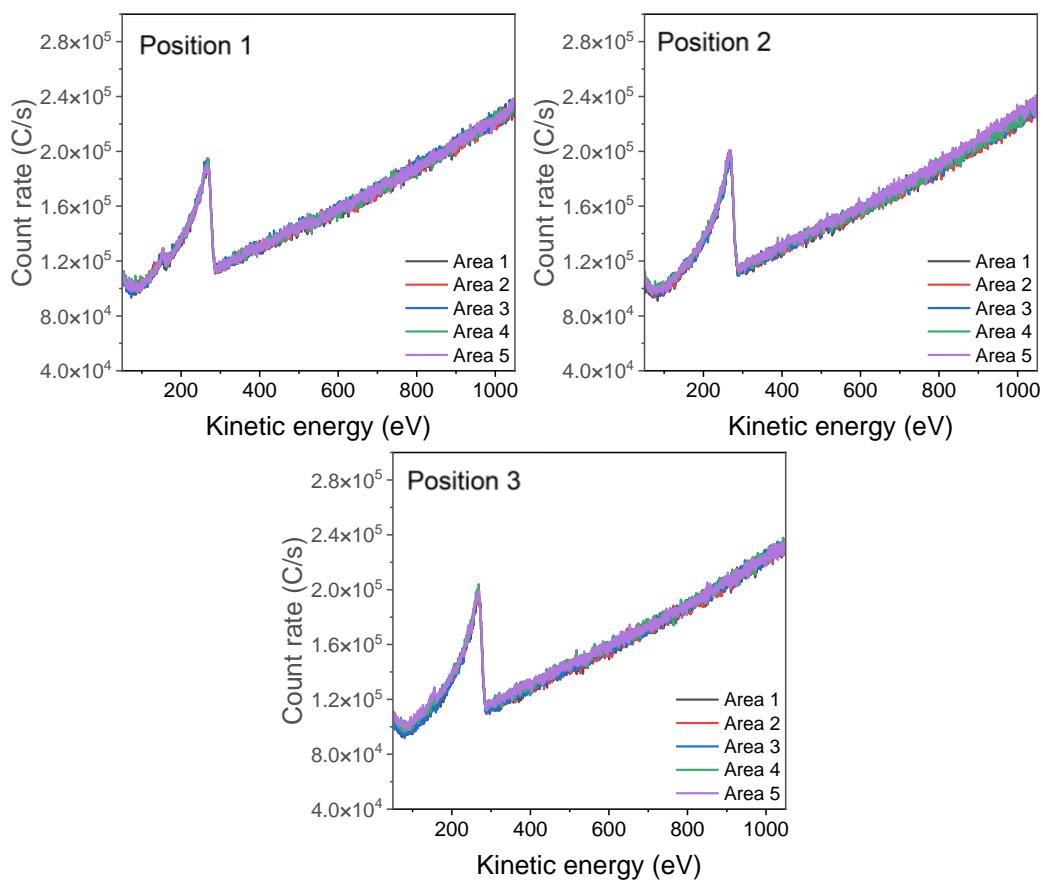


Figure D5: Auger electron spectra of PPDT2FBT:PC₆₁BM surface after 8 hours at 120 °C with marked locations of Auger electron spectroscopy was measured. Position 1 & 2 is the spot scan location over the short and long crystals, respectively, while position 3 is over the surface of the BHJ. Position locations can be seen in Figure D3.

D.4. Charge carrier dynamics of inverted PPDT2FBT:PC₆₁BM devices

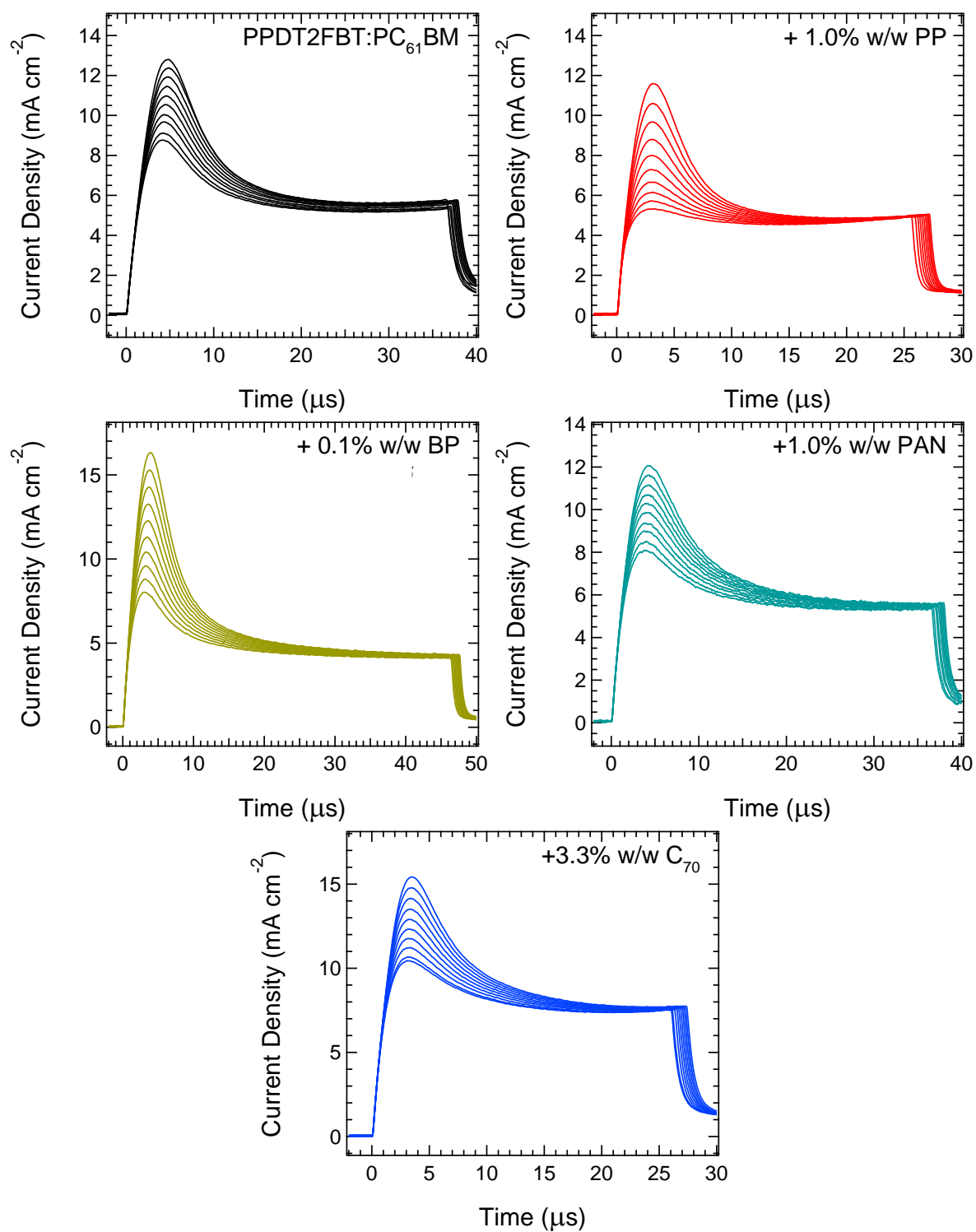


Figure D6: Photo-CELIV results for inverted slot-die fabricated PPDT2FBT:PC₆₁BM devices, with and without solid additives. Additives include neat C₇₀, PP, BP, and PAN.

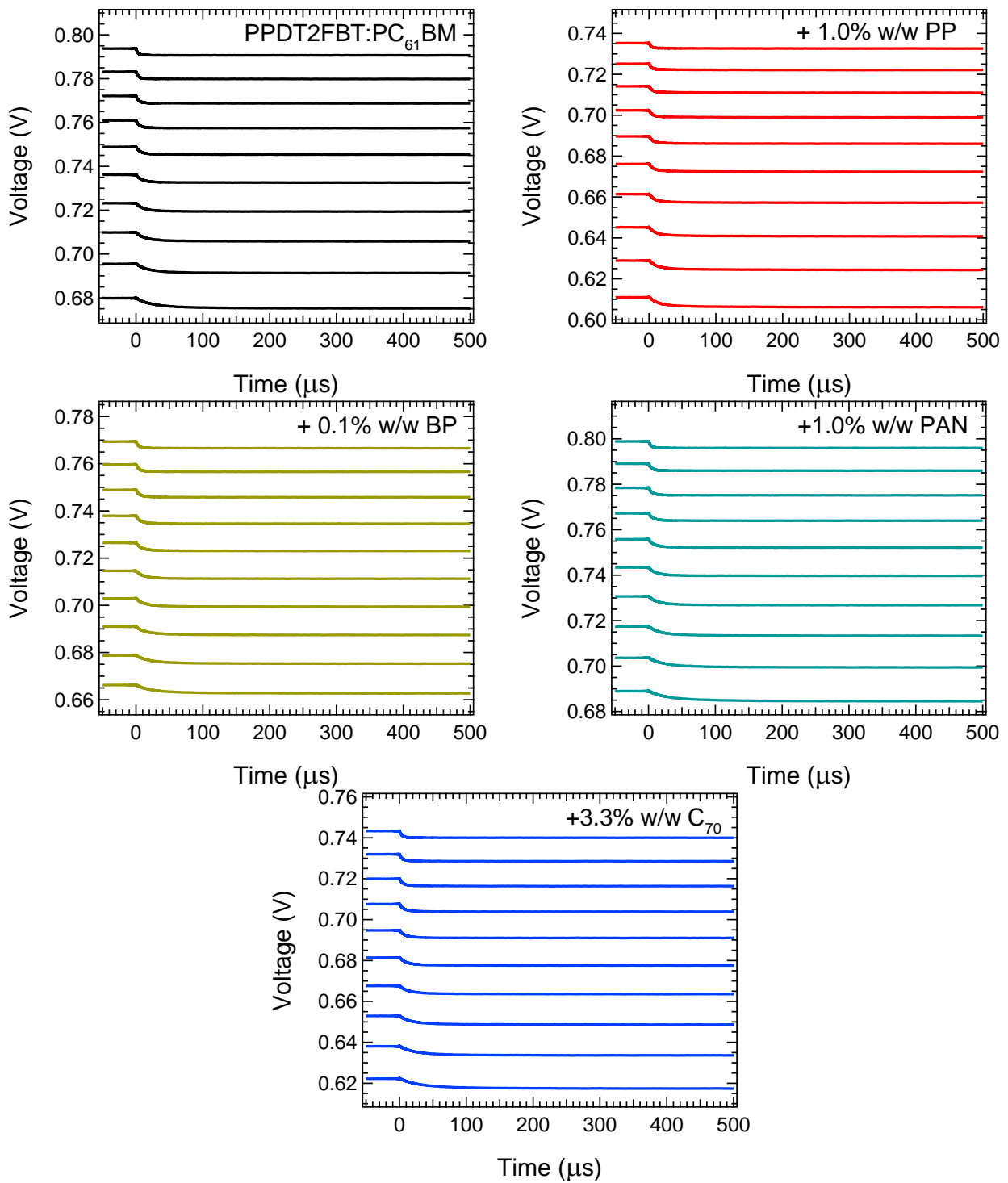


Figure D7: : Transient photovoltage results for inverted slot-die fabricated PPDT2FBT:PC₆₁BM devices, with and without solid additives. Additives include neat C₇₀, PP, BP, and PAN.

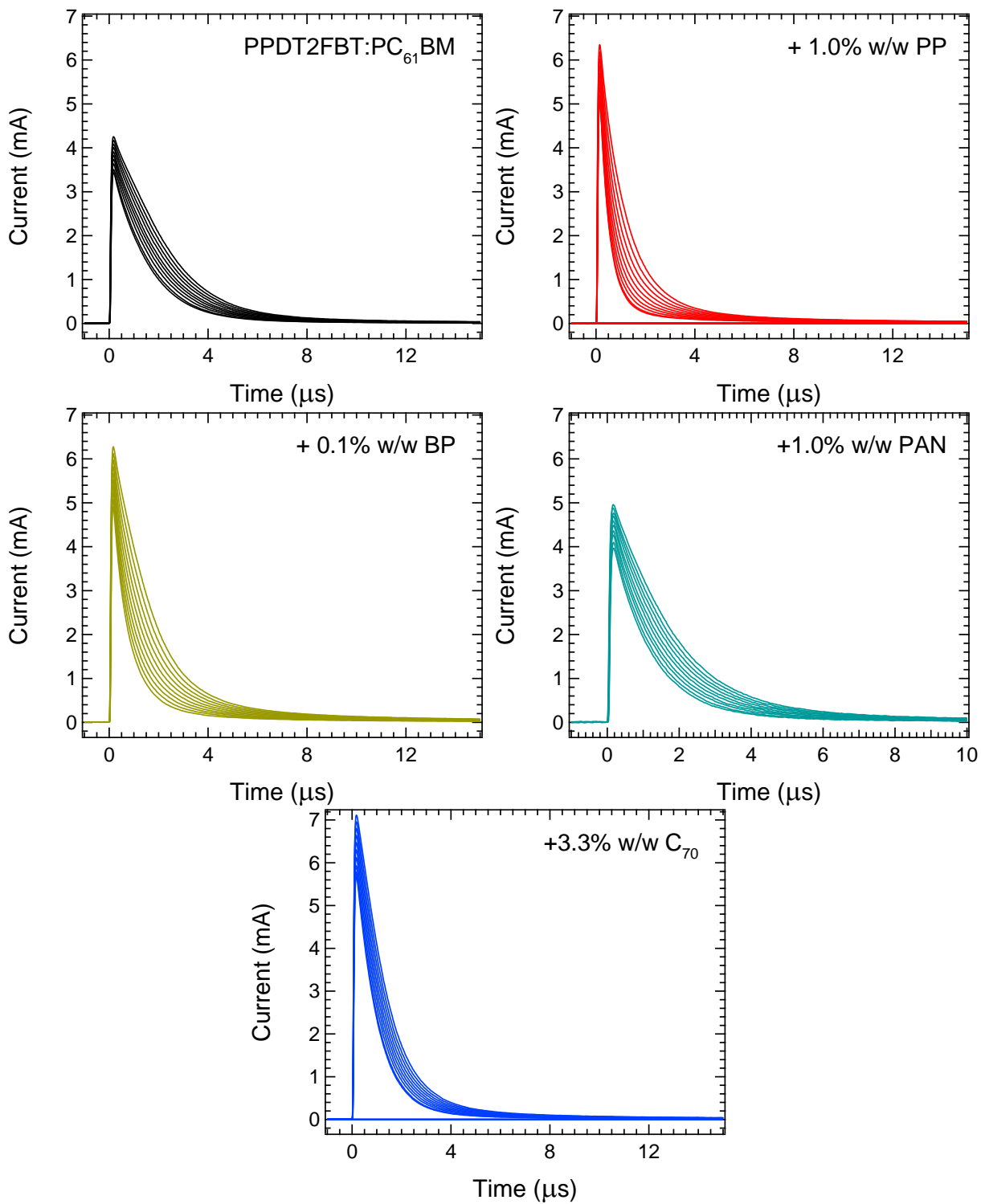


Figure D8: Time-resolved current extraction results for inverted slot-die fabricated PPDT2FBT:PC₆₁BM devices, with and without solid additives. Additives include neat C₇₀, PP, BP, and PAN.